UNIVERSITÄT ZU LÜBECK
INSTITUT FÜR MEDIZINTECHNIK

From the Institute of Medical Engineering
of the University of Lübeck

Director: Prof. Dr. rer. nat. Thorsten M. Buzug

Experimental investigation and validation of CFD simulations of steady flow in stenosis and pharynx using 2D PC-MRI and 4D flow MRI

Dissertation for Fulfilment of
Requirements for the Doctoral Degree
(Dr.rer.nat)
of the University of Lübeck

From the Institute of Medical Engineering

Submitted by
Pragathi Gurumurthy
from Karnataka

Lübeck, 2025

First referee: Prof. Dr. rer. nat. Thorsten M. Buzug
Second referee: Prof. Dr. rer. nat. habil. Heinz Handels
Chairperson: Prof. Dr. Christian Hübner
Date of oral examination:17 October 2025
Approved for printing. Lübeck, the 21st October 2025

Acknowledgement

Completion of this work was possible only due to the guidance and support of many people in my professional and personal life.

My heartfelt thanks to my supervisor Thorsten M. Buzug for all his encouragement, patience, and guidance throughout this work. I am grateful to be a part of an outstanding team of researchers, who are always open to enthusiastic discussions, teaching and collaboration. I am indebted to my colleagues Christina Hagen (geb. Kluck), Dr. Patricia Ulloa, Alina Ibbeken, Vincent Methot, and Dirk Steinhagen for their motivation, time, and invaluable discussions. I wish to express my gratitude to our research collaborators in Universitätsklinikum Schleswig-Holstein (UKSH) Prof. Dr. med. Alex Frydrychowicz, Dr. med. Thekla Oechtering and Prof. Dr. med. Armin Steffen and Prof. Dr.-Ing.Dipl.-Phys. Olaf Jacobs, Dipl. -Ing. (FH). Birgit Schädel from Technische Hochschule Lübeck for their time.

I am blessed to have a beautiful family. My loving husband, Samarth Talanki, and my son Aadhvik Talanki have always been by my side in this process; this would not have been possible without their constant support and understanding. I learned to dream and persevere from my parents, Gurumurthy KK and Poornima GR, my heartfelt gratitude and love to them. It is because of them that I have been able to achieve this. Also, I am very thankful to my in-laws and sister-in-law Sreenivasa Murthy, Sucharitha, and Samagna Talanki for their support.

Pragathi Gurumurthy, 02.05.2025

Abstract

Obstructive sleep apnea (OSA) is a sleep disorder of repetitive disrupted breathing caused by partial or complete closure of the upper airway, despite the effort to breathe. The sleep disorder not only causes social impact on the patient such as daytime sleepiness, fatigue but it has also been linked to several heart conditions. A combination of anatomical variations, impaired neuromuscular functions, ventilatory instability and premature awakening cause OSA. Due to the complex and heterogeneous nature of the disease, the etiology of OSA is not well understood. There are several invasive and non-invasive treatments available for the problem such as uvulopalatopharyngoplasty, maxillomandibular advancement, upper airway stimulation, use of continuous positive airway pressure and dental appliances. However, these have moderate to poor success rate. The identification of the factors contributing to OSA and development of cause driven treatments are not possible with the existing methods. Therefore, more recently numerical simulations or computational fluid dynamics (CFD)is being used to simulate physiological flow to observe the flow phenomena to help identify the problem causing OSA and derive an effective treatment plan. However, the results of the simulations are highly dependent on the mathematical model, boundary conditions, grid size and so on. Hence, a comparison of simulation results with experimental results is important to validate the accuracy of the simulation results.

In-vitro phase-contrast magnetic resonance imaging (PC-MRI) based velocity measurements provides a powerful and non-invasive method to acquire spatially registered fluid velocity. This thesis proposes the use of 2D PC-MRI and 4D flow MRI as an investigative and validation tool for CFD of fluid flow in the upper airway during OSA.

In the current work, two models are chosen for investigation. One is an idealized rigid axisymmeteric stenosis model with 75% occlusion, which is a narrowing in the arteries resulting from plaque build up and also a simplified version of the occlusion occurring in the anatomically complex pharynx model. This model is

primarily used to validate the MRI techniques using previously published laser doppler anemometry (LDA) data and also study the effects and progression of atherosclerosis. The second model is an anatomically accurate and OSA patient individual pharynx model to investigate the flow dynamics in the upper airway during OSA using the above validated 2D PC-MRI and 4D flow MRI. The results are used to understand the cause and effects of OSA. Both 2D PC-MRI and 4D flow MRI are used to measure the velocity in both the models at different boundary conditions. The stenosis model is investigated in laminar and turbulent flow condition. The pharynx model is studied at average inspirational and expiration flow rate. In a statistical framework the results of the velocity measurements in the stenosis and pharynx are compared with computational fluid dynamics (CFD) results to validate the numerical simulation results. Also, with the use of 4D flow MRI other pathophysiological parameters such as wall shear stress and recirculation patterns are quantitatively examined, validated with published data and compared with 2D PC-MRI and CFD data. The role of these parameters in atherosclerosis and OSA are also discussed.

Kurzfassung

Obstruktive Schlafapnoe (OSA) ist eine Schlafstörung mit wiederholten Atemaussetzern, die durch einen teilweisen oder vollständigen Verschluss der oberen Atemwege trotz Atemanstrengung verursacht wird. Die Schlafstörung hat nicht nur soziale Auswirkungen auf den Patienten, wie z. B. Tagesmüdigkeit und Erschöpfung, sondern wird auch mit verschiedenen Herzerkrankungen in Verbindung gebracht. Eine Kombination aus anatomischen Variationen, beeinträchtigten neuromuskulären Funktionen, Atmungsinstabilität und vorzeitigem Erwachen führt zu OSA. Aufgrund der komplexen und heterogenen Natur der Erkrankung ist die Ätiologie der OSA nicht gut erforscht. Es gibt mehrere invasive und nicht-invasive Behandlungsmöglichkeiten für das Problem, wie z. B. Uvulopalatopharyngoplastik, Vorverlagerung des Oberkiefers, Stimulation der oberen Atemwege, Anwendung von kontinuierlichem positivem Atem-wegsdruck und Zahnspangen. Diese weisen jedoch eine mäßige bis schlechte Erfolgsquote auf. Die Identifizierung der Faktoren, die zu OSA beitragen, und die Entwicklung ursachenbezogener Behandlungen sind mit den bestehenden Methoden nicht möglich. Daher werden in jüngster Zeit numerische Simulationen oder die numerische Strömungsmechanik (CFD) eingesetzt, um den physiologischen Fluss zu simulieren und die Strömungsphänomene zu beobachten, um das Problem, das OSA verursacht, zu identifizieren und einen wirksamen Behandlungsplan abzuleiten. Die Ergebnisse der Simulationen hängen jedoch stark vom mathematischen Modell, den Randbedingungen, der Gittergröße usw. ab. Daher ist ein Vergleich der Simulationsergebnisse mit experimentellen Ergebnissen wichtig, um die Genauigkeit der Simulationsergebnisse zu validieren. Die Bewertung der Ätiologie der Schlafstörung war auf klinische Studien beschränkt, und die klinischen Instrumente haben ihre technischen und ethischen Grenzen. Geschwindigkeitsmessungen auf der Grundlage von In-vitro-Phasenkontrast-Magnetresonanztomographie (PC-MRT) bieten eine leistungsstarke und nicht-invasive Methode zur Erfassung räumlich registrierter Flüssigkeitsgeschwindigkeiten. In dieser Arbeit wird die Verwendung von 2D-PC-MRT

und 4D-Fluss-MRT als Untersuchungs- und Validierungsinstrument für die CFD des Flüssigkeitsflusses in den oberen Atemwegen während OSA vorgeschlagen. In der aktuellen Arbeit werden zwei Modelle für die Untersuchung ausgewählt. Eines ist ein idealisiertes, starres, achsensymmetrisches Stenosemodell mit 75% Okklusion, das eine Verengung der Arterien aufgrund von Plaquebildung darstellt und auch eine vereinfachte Version der Okklusion ist, die im anatomisch komplexen Pharynxmodell auftritt. Dieses Modell wird hauptsächlich zur Validierung der MRT-Techniken unter Verwendung von zuvor veröffentlichten Laser-Doppler-Anemometrie-Daten (LDA) sowie zur Untersuchung der Auswirkungen und des Fortschreitens von Atherosklerose verwendet. Das zweite Modell ist ein anatomisch genaues und individuelles Pharynxmodell eines OSA-Patienten zur Untersuchung der Strömungsdynamik in den oberen Atemwegen während der OSA unter Verwendung der oben genannten validierten 2D-PC-MRT und 4D-Flow-MRT. Die Ergebnisse werden verwendet, um die Ursachen und Auswirkungen der OSA zu verstehen. Sowohl die 2D-PC-MRT als auch die 4D-Flow-MRT werden verwendet, um die Geschwindigkeit in beiden Modellen bei unterschiedlichen Randbedingungen zu messen. Das Stenosemodell wird unter laminaren und turbulenten Strömungsbedingungen untersucht. Das Pharynxmodell wird bei einer durchschnittlichen Inspirations- und Exspirationsflussrate untersucht. In einem statistischen Rahmen werden die Ergebnisse der Geschwindigkeitsmessungen in der Stenose und im Pharynx mit den Ergebnissen der numerischen Strömungsmechanik (CFD) verglichen, um die numerischen Simulationsergebnisse zu validieren. Außerdem werden mithilfe der 4D-Fluss-MRT andere pathophysiologische Parameter wie Wandschubspannung und Rezirkulationsmuster quantitativ untersucht, mit veröffentlichten Daten validiert und mit 2D-PC-MRT- und CFD-Daten verglichen. Die Rolle dieser Parameter bei Atherosklerose und OSA wird ebenfalls diskutiert. Diese Parameter helfen bei der besseren Diagnose und Behandlungsplanung von OSA. Die Vorhersage von Blutflussgeschwindigkeiten in patientenspezifischen Geometrien mit Computational FluidDynamics (CFD) kann zusätzliche Daten für die Diagnose und Behandlungsplanung liefern, aber die Lösung kann ungenau sein. Daher ist es wichtig, die Simulationsfehler zu verstehen und das numerische Modell zu kalibrieren. Die In-vitro-Geschwindigkeits-kodierte MRT ist ein vielseitiges Instrument zur Validierung von CFD. Der Vergleich zwischen CFD- und In-vitro-MRT-Geschwindigkeitsdaten und die Analyse des Simulationsfehlers sind die Ziele dieser Studie. Es wird eine dreistufige Routine zur Validierung medizinischer CFD-Daten vorgestellt. Zunächst wird ein korrekt skaliertes Modell der patientenspezifischen Geometrie erstellt, um eine hohe relative Auflösung im MRT-Experiment zu erreichen. Anschließend wird die gemessene Strömungsgeome-

trie mit einem von zwei Algorithmen, Coherent Point Drift und Iterative Closest Point, mit den CFD-Daten abgeglichen. Die abgeglichenen Datensätze werden dann auf ein gemeinsames Raster interpoliert, um einen Punkt-zu-Punkt-Vergleich zu ermöglichen. Drittens werden die globalen und lokalen Abweichungen zwischen CFD- und MRT-Geschwindigkeitsdaten mithilfe verschiedener Algorithmen berechnet, um den Simulationsfehler zuverlässig zu schätzen. Die Routine wurde erfolgreich mit einem patientenspezifischen Modell eines zerebralen Aneurysmas getestet. Zusammenfassend lässt sich sagen, dass die hier vorgestellten Methoden einen Rahmen für die CFD-Validierung unter Verwendung von In-vitro-MRT-Geschwindigkeitsdaten bieten.

Contents

1 Introduction

1.1 Background

1.1.1 Anatomy of human airway

The upper airway is a conduit transporting air from the atmosphere to the lungs. It consists of nasal cavities, pharynx, and larynx (Figure 1.2). The two nasal cavities are divided by the septum and are kept patent by the bone and the cartilaginous framework. They communicate with the external environment via the anterior apertures and nares. Mucosal-lined sinuses surround these cavities. The nasal cavities humidify, warm, filter the inspired air, and protect the respiratory tract from invading particles through the mucociliary system. They also house receptors responsible for olfaction [1] [2].

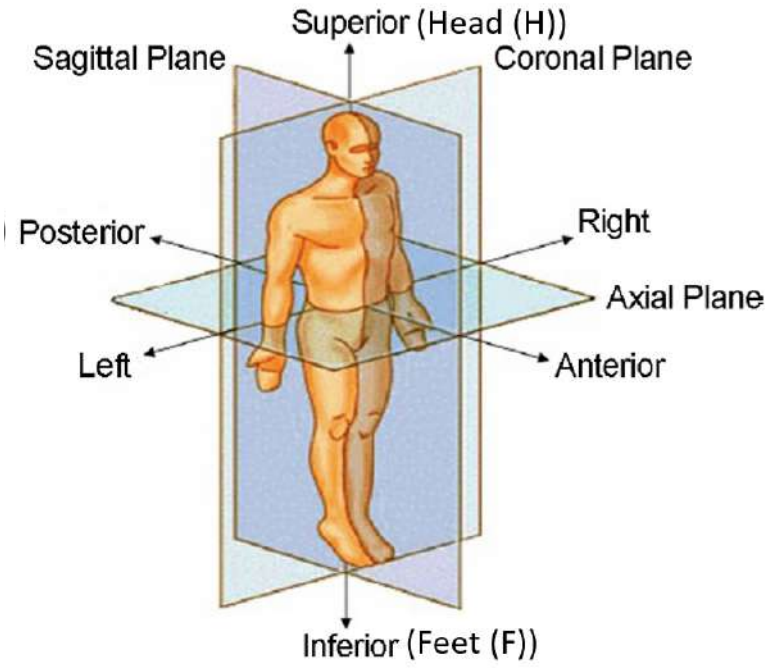

Figure 1.1: Anatomical plane definitions in human body [3].

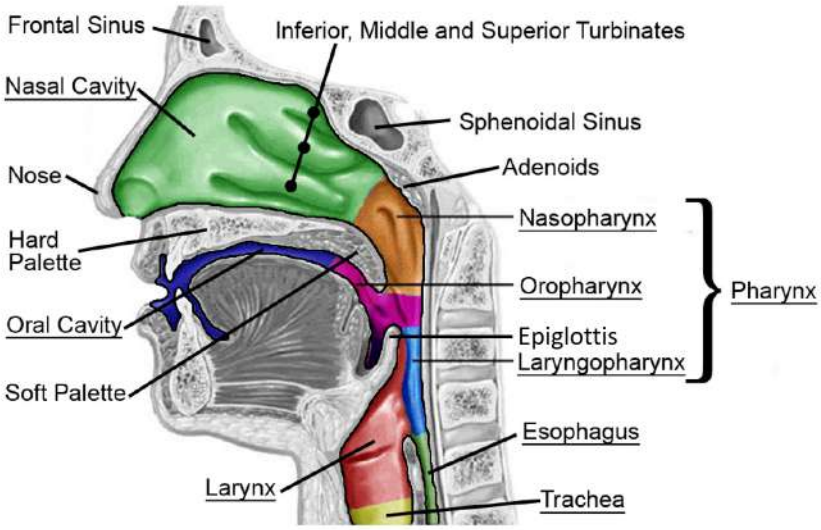

Figure 1.2: Anatomy of the human upper airway [4].

The pharynx is a U-shaped fibromuscular tube that extends from the base of the skull to the cricoid cartilage. It is bounded anteriorly and superiorly by the nasal

cavity, followed more inferiorly by the mouth and then the larynx. The pharynx is comprised of the nasopharynx (the region between nares and the hard palate), velopharynx (the region between the hard palate and the soft palate), oropharynx (the region between the soft palate and the epiglottis), and hypopharynx (the region between the base of the tongue and the larynx). These four structures form the pathway of air from the nose to larynx. They are responsible for physiological functions, such as phonation and swallowing [5] [6] [7]. More than 20 upper airway muscles surround the pharyngeal wall, actively constricting and expanding the upper respiratory tract lumen. The epiglottis is an elastic cartilage covered by mucosa. It is attached superiorly and anteriorly to the larynx and guards the opening to the glottis [8].

The larynx is the passageway for air between the pharynx and the trachea. This dynamic structure is made of several cartilages, muscles, and ligaments. It has a pyramid-shaped cavity that extends from its base, pointing to the tongue and apex to the trachea. The primary function of the larynx in humans is to protect the lower respiratory tract from aspirating food into the trachea while breathing. It also contains the vocal cords and functions as a voice box for producing sounds [9].

1.1.2 Sleep related breathing disorder

Breathing is an essential process of the human body to sustain life. This process provides the oxygen needed for metabolism through inspiration and removes the by-product carbon dioxide during expiration. Breathing affects motor control and postural stability, it helps maintain homeostatic functions, physiological and psychological regulation. Breathing becomes dysfunctional when a person cannot breathe efficiently or when inefficient in responding to environmental conditions and the individual's changing needs. Breathing can also be inefficient due to musculoskeletal dysfunction, disease, chronic psychological stress, or other factors that affect respiratory drive and control. Impairment of breathing functions affects people's lives, challenging homeostasis and compromising health [10].

Sleep is a "physiological state of relative unconsciousness and inaction of the voluntary muscles, the need of which recurs periodically. It is a period of regeneration of the higher nervous system and of muscular tissue, the nutritive and metabolic processes continuing" - as defined in the Stedman's medical dictionary [11]. Sleep is a vital and fundamental biological phenomenon where an average person spends about one-third of their life doing it. It is crucial for the brain's functioning, such as in building new pathways and communication between the neurons. It helps in the

consolidation of memories and aids in learning [12]. It also helps maintain physical health by repairing cells and maintain the balance of the hormone levels in the body [13]. The process of growth and development is also dependent on sleep. Lack of quantity and quality of sleep causes an imbalance in bodily functions. One of the important reasons for the lack of sleep is the sleep-related breathing disorder. These are conditions of abnormal and difficult respiration during sleep. They are classified into central sleep apnea, sleep-related hypoventilation, and hypoxemia disorder.

1.2 Obstructive sleep apnea

Obstructive sleep apnea (OSA) is a sleep disorder in which breathing repeatedly pauses for at least 10 seconds during sleep due to complete or partial collapse of the upper airway despite efforts to breathe (Figure 1.3) [14].

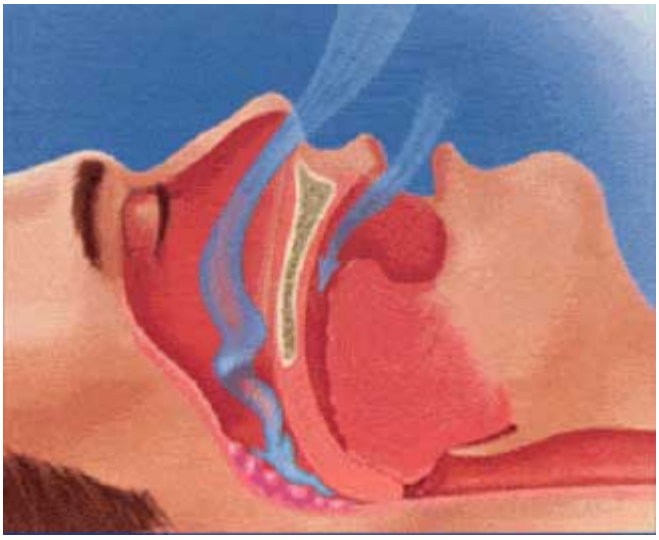

Figure 1.3: Illustration of collapse of soft tissue into the airway passage causing OSA [15].

In a pivotal study using state-of-the-art statistical modeling techniques, Benjafield et al. [16] revealed a heterogeneous distribution of OSA across 193 countries. It estimated more than 936 million people as having OSA, defined by an apnoea-hypopnoea index (AHI), frequency of apneas and hypopneas per hour during sleep of approximately 5 events/h and 425 million people had moderate to severe OSA, defined by an AHI of approximately 15 events/h [17]. The prevalence of OSA ranged from 7.8% (Hong Kong) to as high as 77.2% (Malaysia) for mild OSA, and from

4.8% (Ireland and Israel) to 36.6% (Switzerland) for moderate-severe OSA [18].

Many health conditions are linked to OSA, such as worsening symptoms of asthma and chronic obstructive pulmonary disease (COPD). People with sleep apnea are more likely to develop insulin resistance, causing them to develop type 2 diabetes and is likely to increase blood pressure, low-density lipoprotein (LDL) cholesterol levels, and obesity. Apnea can also worsen heartburn and other gastroesophageal reflux diseases symptoms, which can interrupt sleep even more. OSA also has several personal and societal implications [19]. Untreated OSA is associated with impaired productivity at the workplace and an increased risk of motor vehicle accidents resulting in injury and fatality. Other consequences of OSA include but are not limited to impaired vigilance, daytime somnolence, performance deficits, morning headaches, mood disturbances, neurobehavioral impairments, and general malaise [20]. Majority of the population is undiagnosed or untreated due to a lack of awareness and stigma. Due to its high prevalence and impact on daily life, it is the focus of many research groups.

1.3 Pathophysiology of obstructive sleep apnea

OSA is a multifactorial disease. There are anatomical and non-anatomical causes for the collapse of the upper airway. A combination of these two factors decide whether an individual patient has OSA and its severity.

Anatomical factor

Sleep apnea patients often have a narrow airway and this increases its collapsibility. The observed variability in airway size is probably determined by genetic influences on bony structure, tongue size, tonsillar tissue, and acquired factors such as obesity. Obesity also affects the pharyngeal size by directly depositing fat around the airway or altering muscle orientation and function. Soft tissue enlargement is another reason for airway diameter reduction [21] [22].

In addition to a difference in size, numerous studies have shown apnoeic patients having differences in airway shape. These airways have increased length and have their long axis directed anterior-posterior rather than laterally. This change in shape increase susceptibility to collapse and decrease their ability to maintain patency [23].

Other anatomical factors associated with OSA are craniofacial morphology, the position of the hyoid bone, airway surface tension, tongue scalloping, and tongue

fat [21] [22].

Airway critical closing pressure is a gold standard technique used to quantify the airway collapse. It is the airway pressure at which the airway collapses. It assesses the mechanical properties of the upper airway and its surrounding tissues, and it is primarily thought to reflect anatomical components. Higher critical pressure is correlated with higher OSA severity [24] [25].

Non-anatomical factors

Impaired neuromuscular functions, ventilatory instability, premature awakening to obstruction are non-anatomical factors that might cause OSA.

The neuromuscular factors predisposing patients to OSA are majorly the muscle tone [25]. A dynamic balance of intraluminal pressure and neural drive to the upper airway dilator muscle decide the airway stability. Upper airway dilator muscle genioglossus and palatal muscle tensor palatini are essential in maintaining airway patency. These muscles receive central (from the brain stem) and reflex (pharyngeal receptors) inputs resulting in phasic patterns of activation. During sleep, the genioglossus activity reduces, but the tensor palatini muscle is activated. In patients with OSA, this reduction in muscle activity is more significant, making the airway more susceptible to collapse [24].

The other non-anatomical contributing factor for the pathogenesis of OSA is the instability of ventilatory control. Patients with OSA have periodic fluctuations in upper airway muscle activity, upper airway resistance, and ventilation. This instability in the ventilation can be quantified by loop gain (LG), the ratio of the response to the disturbance. The loop gain model consists of one control component (chemoreceptor: controller gain), one exchange component (lung: plant gain), and one connection component (circulation: circulatory delay). A high loop gain promotes recurrent apnoeas as a response to an initial disturbance, such as a sigh, because it is overcompensated, while a low loop gain dampens subsequent oscillations in breathing. The higher the loop gain, the potentially more unstable the respiratory control system becomes [24] [25].

Arousal from sleep has important implications for OSA pathogenesis. Arousal threshold (AT) is defined as the propensity to wake up from sleep. The immediate physiological changes with cortical arousal help terminate the respiratory events and their consequences. However, a lower arousal threshold causes arousal with the slightest increase in the respiratory disturbance. Low AT prevents the activa-

tion of the muscles and causes unstable breathing, and further contributes to OSA pathophysiology [24] [25].

1.4 Diagnosis of OSA

As reported by up to 90% of patients, excessive sleepiness is the most common symptom of OSA. Patients have also reported fatigue, tiredness, or lack of energy. The gold standard for diagnosis is laboratory-based polysomnography (PSG), during which both sleep and respiratory parameters are monitored. Such a study can establish reliable indices of the disorder derived from the number and type of event per hour of sleep (AHI or respiratory disturbance index (RDI)) to determine the presence and severity of the disease quantitatively. Based on expert consensus, an AHI of less than 5 events per hour is considered no sleep apnea, 5 to 14.9 is considered mild sleep apnea, 15 to 29.9 is considered moderate sleep apnea, and at least 30 is considered severe sleep apnea [26] [27].

A home sleep apnea test is a convenient and cost-effective alternative to PSG for diagnosing OSA. The self-applied sensors measure airflow, respiratory effort, and oxygen saturation, but it lacks electroencephalogram recording. This limitation might lead to the under-recognition of narcolepsy and other hypersomnias. Therefore, a negative home study result must be followed by a PSG in patients with unexplained sleepiness and high clinical suspicion of OSA [27] [28].

Screening questionnaires are simple tools used to identify, ascertain patients in urgent need of PSG. Four screening questionnaires available are the Berlin Questionnaire (used in primary care setting), the STOP/STOP-Bang questionnaire (STOP: snoring, tiredness, observed apnea, and high blood pressure and Bang: body mass index (BMI), age, neck circumference, and gender) (used in preoperative screening), and the epworth sleepiness scale (ESS) (used in clinical practice and research) [29] [30] [31].

Although there are no physical examination findings specific to OSA, the following physical characteristics aid in the diagnosis; increased BMI, neck circumference, and waist-to-hip ratio. Additionally, examining the upper airway may identify anatomic abnormalities, such as tonsillar hypertrophy, macroglossia, or retrognathia. If the clinical evaluation suggests OSA, PSG is performed [31].

1.5 Treatments

There are several treatment options for sleep apnea. Some of the popular treatment options are described below.

Surgical treatments

The purpose of surgical treatments is to reduce resistance to airflow by increasing airway size or improving its patency and respiratory functions. The surgical options include septoplasty, rhinoplasty, turbinate reduction, sinus surgery, uvulopalatopharyngoplasty (UPPP), laser-assisted uvuloplasty (LAUP), tonsillectomy and adenoidectomy (T&A), maxillomandibular advancement (MMA), genioglossal advancement, palatal implants, tracheotomy [32] [33]. UPPP is a procedure that removes or rearranges extra tissue in the throat to increase the airway size [34]. In palatal implant surgery, permanent implants are placed inside the soft palate by increasing its stiffness, reducing palatal vibrations and airway collapse. It is used for treating both snoring and mild OSA. It has less morbidity and low cost with similar success as UPPP [35]. MMA is a less complicated surgical option for severe OSA patients. Here the pharyngeal airway is enlarged by anteriorly pulling the tissue attached to the mandible, maxilla, and hyoid bone. Tracheotomy is often seen as the last option for surgery in severe apnea, where the airway is bypassed through a surgical opening in the trachea [36].

Non-surgical treatments

Continuous positive airway pressure (CPAP): CPAP is the gold standard medical treatment for OSA. It uses a pump to deliver air into the nose or mouth via a mask during sleep. This airflow generates a positive pressure that opens up the airway and prevents the soft tissue from collapsing [33].

Mandibular advancement devices (MAD): It protrudes the mandible forward and advances the tongue. This increases the total pharyngeal area, particularly at the level of the soft palate, and decreases the pressure drop during inspiration to reduce the collapsibility of the airway [33] [37].

Hypoglossal nerve stimulation (HGNS): HGNS, also known as upper airway stimulation (pacemaker for the tongue), is a new treatment that works by stimulating the hypoglossal nerve to stiffen the key tongue muscles to avoid obstruction. The stimulating device and breathing sensor are implanted in the chest and connected to a

stimulation lead that touches the hypoglossal nerve and is controlled by a handheld device [33] [37].

Pharmacological: Pharmacological therapy typically targets certain aspects of pathophysiology, such as pharyngeal collapsibility, obesity, arousal threshold, and loop gain, which supports a personalized approach to treatment. The combination of supplemental oxygen and a hypnotic drugs has been reported to benefit OSA patients with mild/moderate pharyngeal collapsibility, presumably by lowering loop gain and raising the arousal threshold [37].

1.6 Motivation

Due to the complex and heterogeneous nature of the disease, the etiology of OSA is not well understood. Anatomical factors were deemed to be the primary cause of OSA [24]. However, recently, the relevance of physiological, non-anatomical factors has been investigated and it has been shown that it is the combination of these two factors that cause OSA. The cause for OSA in any given patient might be all or a combination of some of the contributing factors. However, the identification of these factors and development of cause driven treatments are not possible with the existing methods.

For instance, the gold-standard method used to diagnose sleep-disordered breathing is an in-laboratory PSG. In-laboratory PSG is comprehensive, but it is also labor-intensive, time-consuming, costly, and intrusive to sleep itself [38]. The AHI is one of the vital sleep variables measured in PSG. Although AHI is a widely used measure of OSA severity, it has several limitations as it does not consider information associated with hypoxemia and the duration of the expiratory event. For example, patients with very long respiratory events may experience significant hypoxemia but have a relatively low AHI. Conversely, another patient may have a much higher AHI but minimal exposure to hypoxemia. In addition, non-apneic respiratory events that do not meet the scoring criteria for hypopnea are associated with heart rate changes and increased expiratory pharyngeal resistance. Breathing disruptions that do not cause significant hypoxemia are also associated with objective daytime sleepiness [39]. Finally, two patients with same AHI but differnt backgrounds may have different clinical maifestations, implying treatment benefits would differ for the two patients [40]. These few examples highlight some limitations of currently used diagnostic methods and the need for a new diagnostic method.

As for the existing treatment methods, the following are the limitations. The upper

airway has multiple collapsible structures (soft palate, lateral walls, tongue, and epiglottis) that interact directly (via soft tissue forces) and indirectly (by modulating the pressure and flow experienced by other structures). Optimal surgical outcomes for obstructive sleep apnea require accurate identification of the primary site of flow limitation in each patient. However, identifying this and developing cause driven therapies is challenging [41].

CPAP is the first-line treatment for most patients affected by OSA and represents the paradigm of a one-size-fits-all therapeutic strategy. However, while some patients highly benefit from CPAP, others have reported mild/ severe side effects, there is no way for clinicians to distinguish between likely responders and non-responders [42].

MAD are a valuable non-surgical treatment option for patients diagnosed with OSA. The most common adverse effects found during the initiation of treatment are temporomandibular joint discomfort, dry mouth, and excessive salivation. Other common adverse effects included halitosis, gingival pain, toothache, intraoral soreness, and problems with retaining and fitting devices. The literature has shown that mandibular protrusion is critical in optimizing MAD efficacy. This is achieved using titration. The titration of the protrusion should be carried out individually, trying to find the most effective protrusion while at the same time respecting the patient's physical limits. The mandible is progressively advanced during sleep each time respiratory events occur throughout the night. However, this is a time-consuming, labor-intensive, expensive and alters natural sleep because of the need for overnight and attended hospital stays [43].

HGNS, a treatment targeting the upper airway muscle is promising. However, a significant dropout rate (28%) after 48 months of follow-up was seen. Although being a responder or non-responder is partly explained by the resulting tongue protrusion or retrusion after hypoglossal nerve stimulation, there is a need for a more precise description of treatment responders based on outcome parameters [44].

Therefore to ensure effective treatment, future research in OSA should examine the relative contributions of different pathophysiological factors in the collapse of the pharynx in individual patients. Furthermore, it should address the increasing need to provide tailored cause driven therapeutic options.

A possible solution to the above-explained problems is numerically studying the aerodynamic characteristics of respiratory flow and its interaction with the soft tissues and muscles in each individual. The central hypothesis is that the outcomes

of numerical simulations help localize the cause of OSA and enable development of biological markers by correlating a simulation parameter for example critical closing pressure to the severity of OSA. Furthermore, studying the airflow characteristics in pre-and post-treatment models provides physicians additional data to choose an appropriate and customized treatment, help optimize the medical device design for higher efficacy and also provide a priori knowledge to aid surgical intervention.

In recent years computational fluid dynamics (CFD), a numerical method has been widely employed to analyze the airflow in both healthy and diseased human airways [45]. With the advancements in medical imaging techniques, unique and realistic geometries of the respiratory tract can be reconstructed from the scanned images, to which they can be converted into a CFD model. Most studies have focused on pollutant transport and drug delivery in respiratory systems, whereas others focused on sleep-disordered breathing. During breathing, the airflow characteristics through the human respiratory tract are very complex. The airflow can be in laminar, transitional, or turbulent conditions. The geometry and boundary conditions are the main factors that significantly affect the airflow in human respiratory tracts. The complex geometry of the human upper airway results in curved streamlines, recirculation/ vortex regions, secondary flow, and jet flow. Therefore, these factors must be considered in the CFD study of respiratory flow [4] [46].

To analyse the flow, CFD employs several mathematical models which solve the governing equations of fluid flow while advancing the solution via space and time. Fluid flow modeling is done assuming rigid boundaries using laminar or turbulence models such as k-epsilon, unsteady and steady large eddy simulation (LES), k-omega, k-omega shear stress transport (SST), renormalization group (RNG) k-epsilon model, and Spallart-Allarmas model. These models are generally used to study the airflow in the upper airway during inspiration and expiration to find the region of minimum pressure, which is the likely spot of collapse. More recently, the rigid boundaries are replaced by more realistic ones; this is the method of fluid-structure interaction (FSI) [46]. However, investigation of airflow in the upper airway using FSI is beyond the scope of this study.

Given the diversity of the models available and the variety of their predictions in the context of the study of OSA, a precise and quantitative assessment of these methods is needed. The methodology needs to be validated with either experimental or benchmark clinical data to gain confidence in the CFD computations. Due to the absence of direct accurate invasive clinical flow measurements in upper airways, the validation of the CFD methodology in the present study is performed by comparing

CFD results with experimental flow data measured in an identical physical model of the airway at the same flow conditions.

Experimentally, flow can be measured with hot-wire anemometry or laser-based methods such as laser doppler anemometry (LDA), and particle image velocimetry (PIV). This, together with the ability of 3D printers (3- dimensional printer) to accurately fabricate complex anatomical structures, has paved the way for flow dynamics studies in vessels and the airway. However, laser techniques are inherently constrained by optical access to the 3D model. As for hot-wire anemometry measurements, they are unreliable in zones with recirculation and secondary flows. Due to these constraints, the proposed experimental method to validate CFD results are 2D phase-contrast magnetic resonance imaging (PC-MRI) and 4D flow MRI. PC-MRI is a versatile and non-invasive tool for cardiovascular blood flow assessment and can be applied anywhere in the human body. Conventional PC-MRI velocity mapping measures the mean velocity in each voxel and is used clinically mainly for accurate volume flow measurements. These days, 4D flow MRI (3D time-resolved PC-MRI) is extensively used to comprehensively evaluate complex blood flow patterns by 3D blood flow visualization and quantification of flow parameters.

1.7 Objective

This work aims to demonstrate the use of 2D PC-MRI and 4D flow MRI as an investigative tool for in-vitro study of flow dynamics in arteries or airway and as a validation tool for CFD simulation of the same. To achieve this two models are chosen, one a stenosis model used for the purpose of validation of the measured MRI data with published LDA data and to also to study the effects/ progression of atherosclerosis. The second is an anatomically accurate pharynx model for the investigation of flow parameters in the pharynx during OSA to study its etiology.

The main goals of the thesis are listed below.

The first goal is to showcase the feasibility of fabricating MRI compatible physical models of an idealized stenosis and an anatomically accurate pharynx using 3D printers and develop a reliable experiment setup mimicking idealized flow in the models for MRI measurements.

The second goal is to assess test-retest reliability of 2D PC-MRI and 4D flow MRI velocity measurements.

The third goal is to validate the stenosis velocity measurements at steady flow

obtained from 2D PC-MRI and 4D flow MRI with published LDA results and to establish a statistical framework to compare it with CFD results. Additionally, the wall shear stress (WSS) values obtained in 4D flow MRI are also validated with published data.

The fourth goal is to extend the validated method of 2D PC-MRI and 4D flow MRI to the complex, anatomically accurate pharynx model during steady inspiration. The experimental results are further used to validate the CFD results.

The fifth goal is to use the results from the flow analysis to understand the pathophysiology and effects of atherosclerosis and OSA using the stenosis model and pharynx model respectively.

1.8 Published work

During her doctoral studies, the author published research in the area of PC-MRI and 4D flow MRI at several international conferences. Research on flow patterns in the pharynx using PC-MRI was presented during the 33rd annual scientific meeting of the European Society for Magnetic Resonance in Medicine and Biology (ESMRMB) (September 2016, Vienna - Austria) and at the annual conference of the DGBMT (September 2016, Basel - Switzerland). The work presented in the 33rd annual scientific meeting of the European Society for Magnetic Resonance in Medicine and Biology (ESMRMB 2016) as a poster earned the author a Magna Cum Laude P[1].

The comparative study of the flow patterns in the pharynx of a obstructive sleep apnea patient studied using CFD and PC-MRI was presented at the 51st annual conference of the DGBMT (September 2017, Dresden - Germany) P[2]. The results of the flow pattern investigation in the pharynx during obstructive sleep apnea was presented at the 34th annual scientific meeting of the ESMRMB (October 2017, Barcelona - Spain.

Additionally, the author participated in other collaborative projects in the investigation of flow pattern in the upper airway using MRI techniques (P[3] P[4] P[5] P[6]).

1.9 Structure of the thesis

This section describes the structure of the thesis and a summary of the contents of each chapter.

- Chapter 1 begins with the rationale for this research, description of airway anatomy followed by brief background about obstructive sleep apnea, current diagnosis and treatment procedure. The motivation and goals for the thesis are outlined in the chapter.
- Chapter 2 presents a literature review of the analytical and experimental studies in airway research.
- Chapter 3 briefly explains the theory behind PC-MRI, physical modeling and CFD.
- Chapter 4 discusses in detail the experimental result of velocity measurement using the 2D PC-MRI method in the rigid axisymmetric stenosis, its validation with published LDA data and its comparison with numerical simulation.
- Chapter 5 extends the methodology used in chapter 4 to the pharynx model. It discusses in detail the pharyngeal flow physics during inspiration and expiration and the validation of CFD results with the measurements obtained from 2D PC-MRI.
- Chapter 6 presents the results of 4D flow MRI obtained from stenosis and pharynx models. A thorough discussion of validation of the flow parameters with published data and application of 4D flow MRI as a validation tool is given.
- Chapter 7 gives the discussion and conclusion of the research work along with recommendations for future work.

2

Literature review

The current research work focuses on the potential use of 2D PC-MRI and 4D flow MRI as an investigation tool and experimental validation technique for numerical simulations. In this chapter, a brief literature review of all the experimental techniques used over the years to study the airway is presented.

2.1 Review of analytical studies

2.1.1 Mathematical models

The human respiratory system is a complex network consisting of several components. Mathematical models aim to describe the relationship of the main variables of this system, namely flows, pressures, and volumes. The earliest theoretical models were zero-dimensional or lumped parameter models in which the relevant variables were functions of only time and satisfied non-linear ordinary differential equations (ODEs). These models are based on schematization of the respiratory system and known constitutive functions of the main components such as collapsible airway resistances, lung elastic recoil, or transmural pressure [48]. Although the model show oscillations in the flow, it cannot describe many mechanical features. The next level of models are one-dimensional models in which the pressure and longitudinal veloc-

ity, both averaged across the tube cross-section are regarded as the functions of the longitudinal coordinate and time. This model includes a set of partial diffdrential equations (PDEs) describing mass and momentum conservation, coupled with tube law relation [49]. Similarly, two-element models sufficiently predicts inspiratory and expiratory airway obstruction during sleep [50] [51]. The three-dimensional models in development are the finite element models used in simulations.

2.1.2 Starling resistor

As the airway is a flexible conduit, earlier studies used collapsible tubes to study the airflow. This phenomenon is best described with a starling resistor experimental setup (Figure 2.1a) [52].

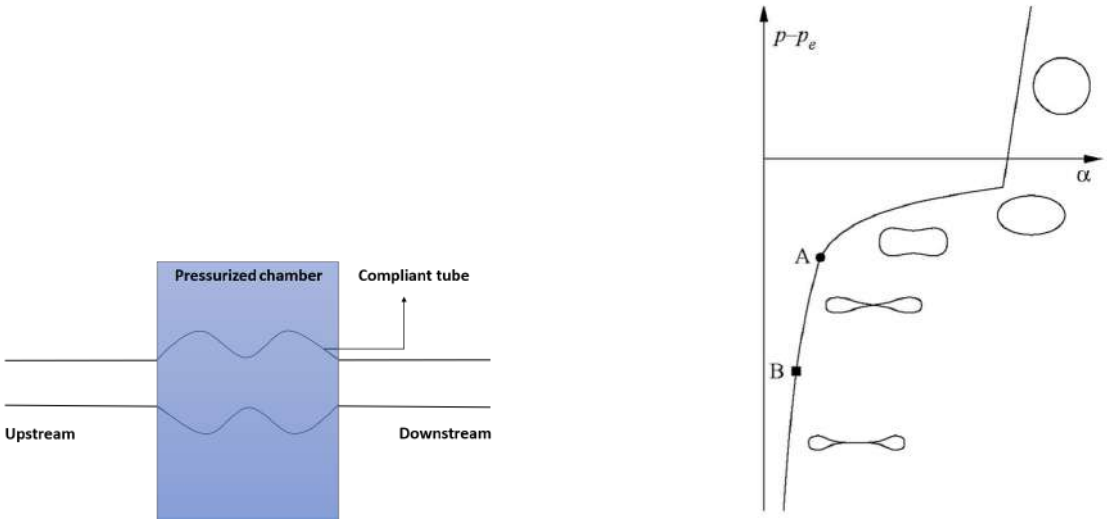

(a) (b)

Figure 2.1: (a) Setup of starling resistor to study airflow mechanism in flexible tubes [52]. (b) Relationship of transmural pressure (y-axis) to the cross-sectional area (x-axis) in flexible tube given by tube-law [53].

The experiment comprises a collapsible tube placed inside a pressurized chamber. When a flexible tube is subjected to a change in external pressure, the internal pressure varies. The transmural pressure (internal minus external pressure) changes the cross-sectional shape and causes wall deformations, and this relation is known as tube law (Figure 2.1b). It also helps explain the following non-linear behavior: the

waterfall effect (effect where prior to the collapse of the tube, the flow becomes independent of the pressure downstream), and the self-excited oscillations. Although a starling resistor can help understand the collapsibility mechanisms in an airway, it is not sufficient to characterize the flow features in real airway anatomy. The actual anatomy of an airway is more complex in shape than a simple collapsible tube.

2.2 Review of in-vivo experiments

In the late 1800s, the focus was on understanding the respiratory functions of the airway, in particular the nose (Figure 2.2). Effect of stenosis, airway tensions, and collapse were some of the subjects of investigations. In earlier attempts, this was achieved by studying parameters measured from apparatus connected to the nose with tubing and the mouth with mouthpieces [54]. However, the tubing and mouthpieces introduced airflow resistance, invalidating natural breathing conditions. These experiments majorly studied the effect of pathology on respiratory functions, however this changed in the 1900s to the study of flow dynamics in the airway.

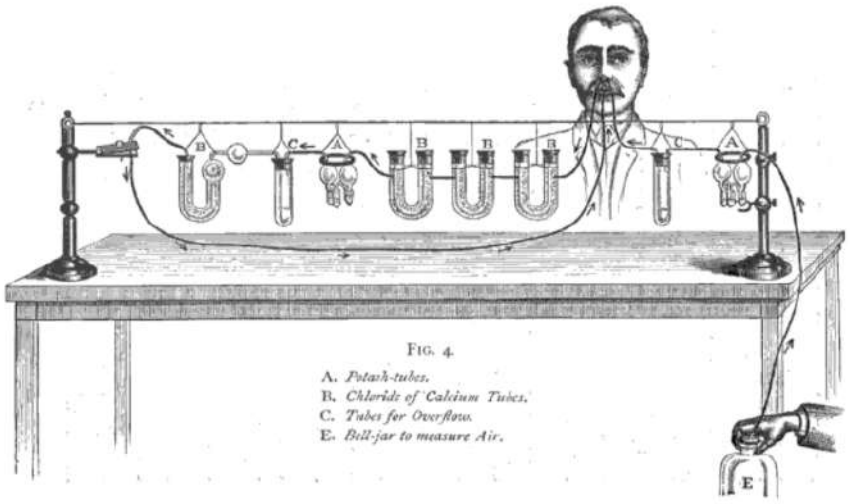

Figure 2.2: Experimental setup with bell jars, flexible tubings and large calcium-chloride vessel used for airflow measurements [54].

In 1901, Parker [55] investigated airflow patterns during respiration by studying

the distribution of lycopodium filled in Kabierskie's insufflator (instrument used to distribute powders in nose or throat) during inspiration. Expiration was studied by making the subjects smoke cigarettes and exhaling the smoke, and watching it utilizing nasal speculum. These were done for both nose in normal condition and nose with rhinitis and deflections. Several developments were done in the pneumotachograph to record the inspiration and expiration in the 1940s in an effort to understand the changes that occur in the velocity of airflow during normal breathing in healthy volunteers and abnormal breathing in patients suffering from diseases such as asthma and tuberculosis [56] [57] [58]. A mask was then introduced instead of a mouthpiece to ensure normal respiration. Additionally, some studies focused on measuring the pressure gradients in the nose or the lungs using manometers or calculations done based on the law of flow of gas [59]. In 1973 Shevrygen lined up the airway with litmus paper to measure the direction and distribution of inspired flow by measuring the regional cooling caused by incoming air (ammonia gas) with electro-thermometer probes [60]. In 1974 Schleslinger, monitored particle deposition by aerosol by rectilinear scanners to study the airflow pattern and distribution in the airway [61]. Due to the complex geometry of the airway, visualization of the airflow and wall deformation without the introduction of aerosol or other particles is challenging. In the case of introducing such particles, care has to be taken not to disturb the natural breathing and the ethical restrictions due to radiation exposure.

2.3 Review of ex-vivo experiments

Ex-vivo anatomical models offer an interesting alternative to the in-vivo models. From 1930s, the focus turned to study airflow patterns and their effects on the pathobiology of the airway and to study particle deposition using nasal molds from cadavers. In 1951, Proetz used a cadaver and sent smoke through the airway to visualize the flow through a glazed window. Manometers were used to measure the pressure [62]. In 1967 Masing, Proctor 1966, 1977 Swift and Proctor did quantitative measurements of local velocities with a miniature angle meter in a half-nasal model [63] [64] [65]. This study showed that air stream patterns of quiet inspiration are almost independent of the flow rate. In 1987 Hornung, casted an anatomically accurate model from autopsy and to studied the distribution of the radioactivity of xenon in the airway to understand the flow and deposition of particles [66]. In 1983 with Girardin came a breakthrough in the experimental investigation of airflow patterns in a model of human nasal fossa using LDA [67]. In 2004 Churchill stud-

ied the airflow across physiological flow rates using water and dye flowing through anatomically accurate acrylic models of human nasal air passageways. The models were derived from a direct casting of the nasal passageways of 10 Caucasian cadavers (six male, four female) [68]. While cadaver-based models are relatively easy to create, postmortem specimens suffer inevitably from uncontrollable tissue shrinkage, which renders the airways excessively patent and possibly distorted. Therefore, plastination a newer form of preservation in which the dehydration procedure (freeze-substitution in acetone) claiming to result in less than 10% shrinkage was introduced (Figure 2.3) [69].

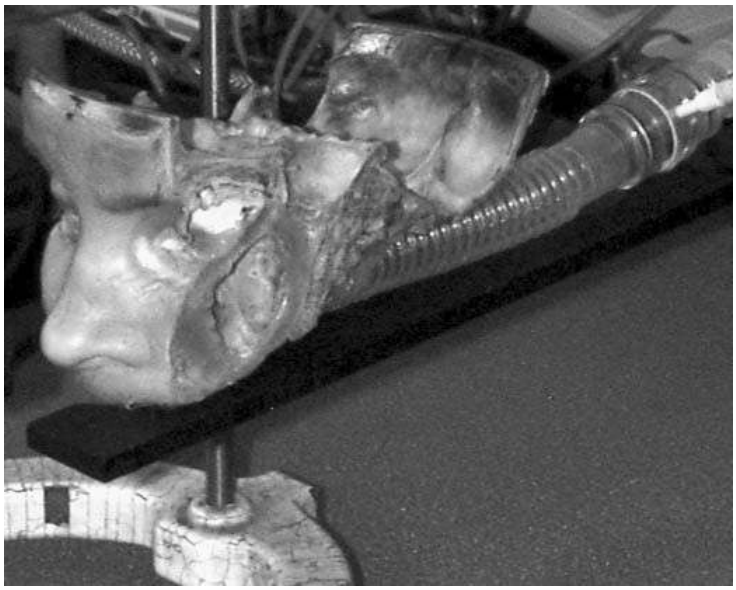

Figure 2.3: The human plastinated nasal cavities and maxillary sinuses connected by a tube to the negative pressure generator was used to study the pressure drop in the model during inspiration [70].

2.4 Review of in-vitro experiments

Here are some of the prominent in-vitro experiments performed over the years. In 1989 Scherer generated a nasal model from CT images, and used hot wire anemometer to measure velocity in the model [71]. An interesting approach was used by Leiter in 1992 to study the pharyngeal resistance and genioglossal electromyography (EMG) activity. A model of orifice was used to analyze the relationships among pressure, flow, and genioglossal EMG activity in the human pharynx during inspiration. Different airway shapes (circular and elliptical) and orientations (major axis

anteroposterior and lateral) were incorporated into the model calculations. It was shown that in an elliptical airway the genioglossus muscle shortening increases the pharyngeal area which in turn reduces the airway resistance [72]. In 1993, Schreck studied the relationship between the pressure losses within the nasal airways in a 3:l scale MRI based model. Pressure measurements, flow visualization, and hot-wire anemometry studies were performed. Digitized coronal sections of the left nasal airways were enlarged three times and formed into templates used to cut clear plastic (plexiglas) plates of 12 mm thickness. The influence of nasal congestion and the collapse of the external nares were well examined here but due to the high thickness of the plate the complicated geometry of the nasal airway was represented in less resolution [73]. Similarly Hahn in 1993 constructed an anatomically accurate, 20 times enlarged scale model of a healthy human adult nasal cavity from computerized axial tomography scans to study nasal airflow patterns. In this experiment detailed velocity profiles for inspiratory and expiratory flow through the model and turbulence intensity were measured with a hot-film anemometer probe with 1 mm spatial resolution [74]. Brucker and Park, in 1999, were the first to use this PIV technique to study nasal airflow patterns. The nasal cavity model used was reconstructed using low-resolution anatomical data, and hence, they observed high velocities, which is uncommon in the olfactory regions (Figure 2.4 [75]).

In 2000, Stapleton used a mouth-throat replica from a hand-carved wooden model of the geometry as a form for a fiberglass cast. Air was run through the cast, and the pressure drop was measured with a differential pressure transducer attached via pressure taps at the inlet and the exit of the trachea. A nebulizer was used as an aerosol generator and attached to the inlet of the model via heat-shrink tubing to examine the particle deposition predictions. The outlet was attached directly to a Marquest filter and a vacuum pump. The measured pressure and particle deposition were compared with CFD simulated data [76]. Later, Kelly et al., in 2000, measured flow field distribution in a half nasal cavity model (2:1 scale), reconstructed from better resolutions anatomical scans of subjects. To better the resolution of the physical models, new fabrication methods such as rapid prototyping started being used [77].

In 2000, Hopkins et al. were the first to use rapid prototyping to build a transparent model of the nasal cavity for PIV measurement. The general procedure of which is described below. Nasal airway geometry was segmented from medical image data to create a computer model. The negative of the model was printed using a water soluble material. This was then dissolved to get the nasal airway model. This

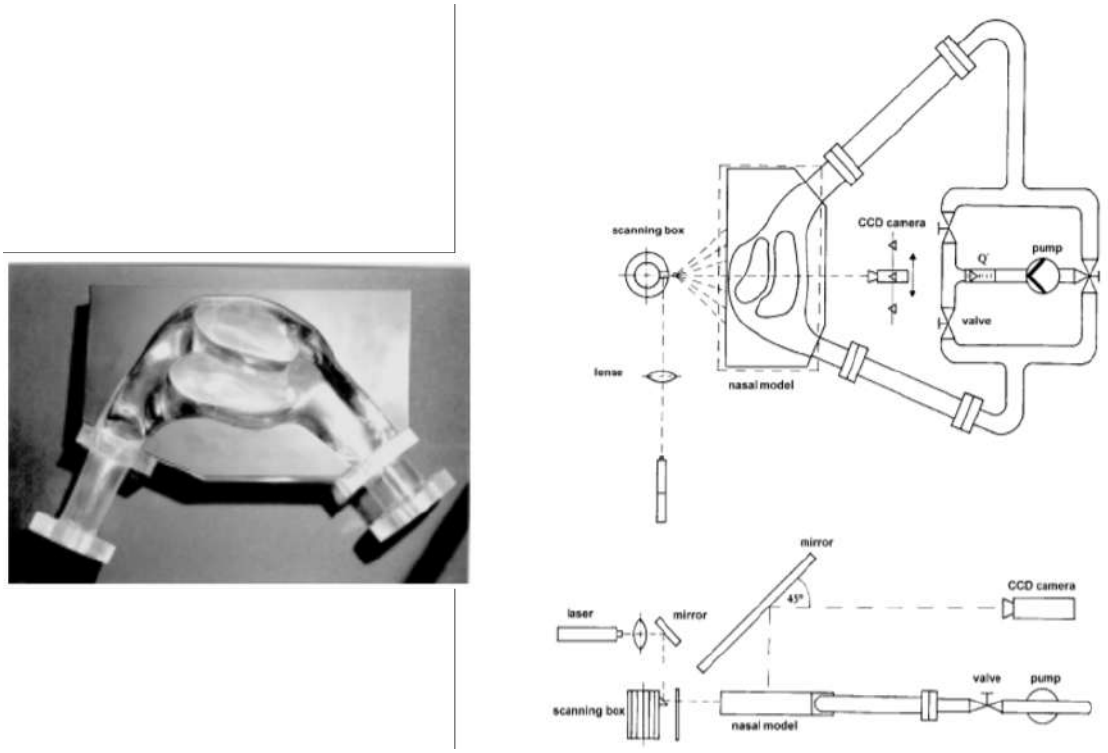

Figure 2.4: Setup for digital PIV (DPIV) study of flow patterns within the scaled human nasal cavity model of epoxy resin [75].

method allowed larger than life-size artificial models to be produced from geometries of live subjects with high resolution [78].

An advancement was done in 2003 by Heenan in measuring the velocity field in the central sagittal plane of an idealized representation of the human oropharynx (HOP) during steady inspiration through an inhaler mouthpiece using endoscopic PIV. The PIV data indicated the complex nature of HOP flow, with three-dimensionality and several regions of separation and recirculation [79]. Kim and Chung, 2004 used tomographic PIV (TPIV) to measure detailed velocity flow fields in normal and abnormal nasal cavity models. TPIV, is an extension of the stereoscopic 3D concept of PIV and it measures all three components of velocities in a 3D control volume. A nasal cavity model of an abnormal subject obtained from high resolution computed tomography (CT) images was reconstructed using rapid prototyping in 2:1 scale. The average and root mean square (RMS) distributions of the velocities in both sagittal and coronal planes were obtained. A concept of virtual surgery using experimental models was well demonstrated in this experiment [80]. Hörschler et al. in 2006, investigated the impact of geometry in different nasal cavity models

with both simulations and DPIV at peak inspiration and expiration [81].

Fewer studies reported in-vitro measurements in pharyngeal airway compared to nasal and lower airways. In 2006, Brouns et al. studied flow dynamics in an idealized and simplified oropharyngeal airway model at three different inhalation flow conditions. CT scans from several subjects were taken, and a normalized airway model was reconstructed. An experimental replica was fabricated from this geometry. Three major recirculation zones were seen at the mouth, pharynx, and trachea and a laryngeal jet attached to the anterior side of the trachea was observed. This was contrary to the observations made by other authors that the laryngeal jet is either attached to the posterior side or is found in the center of the trachea. The authors corroborate this anomaly to the oropharyngeal inlet and the absence of nasal cavity in their geometry [82]. In 2006, Xu studied the pressure in healthy and OSA patients using CFD and in-vitro model. 85% scale models were used for the experiment. The models were developed from the segmented upper airway image of OSA patient and constructed from transparent polymer via rapid prototyping stereolithography. The study showed the strong relationship between the pharyngeal shape and the internal pressure distribution [83].

In 2008, Doorly et al. used both dye and bubble flow visualization with PIV to examine the flow dynamics in a human cavity model. The finding using both techniques were complimentary. They observed from PIV and flow visualization that airflow accelerates in the nasal vestibule region and impacts the middle turbinate [84]. The low flow was found near inferior meatus, as reported by other studies by Kelly et al [77]. In 2009, Kim and Chung again worked on creating accurate, transparent flow passages to analyze the flow inward a geometrically complex flow passage like human airway by PIV. Phase averaged mean and RMS velocity flow field distributions in coronal and sagittal planes were obtained during 7 temporal points along the respiratory cycle [85]. In 2009, Mylavarapu constructed an anatomically accurate human upper airway model from multiple axial MRI scans. CFD simulation investigated the fluid flow in the airway regions susceptible to collapse. A physical model was fabricated from the digitized airway model using stereolithography to experimentally measure the pressure and velocity (Figure 2.5) [86].

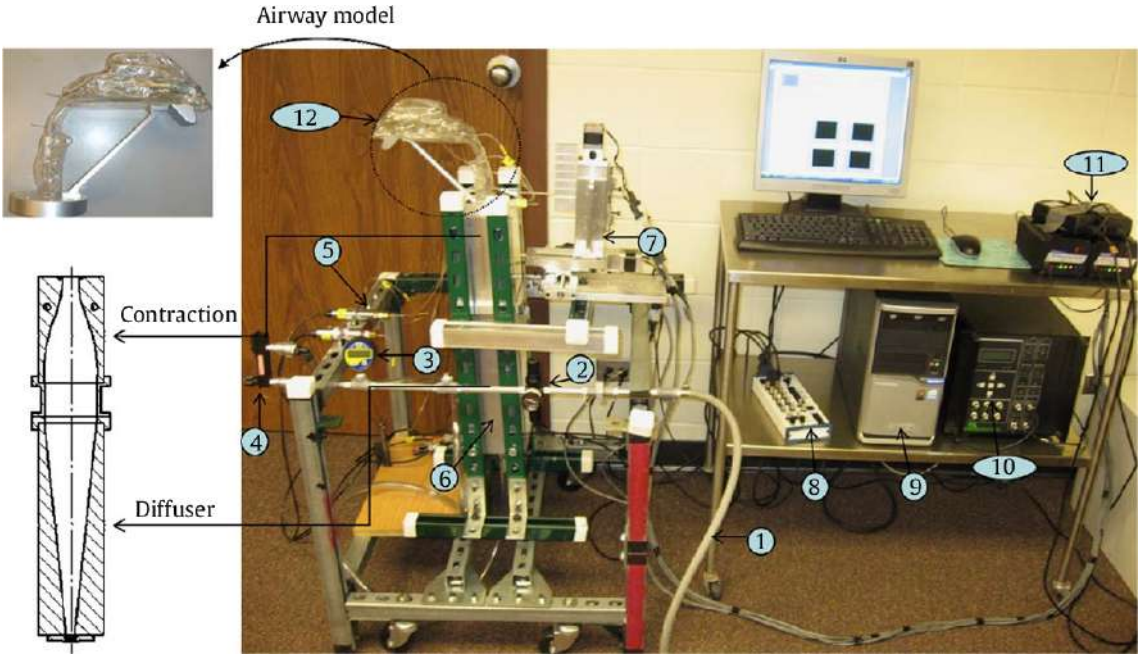

Figure 2.5: Experimental setup for pressure and velocity measurements in the 3D printed airway model [46].

In 2010, Pollard used the geometry of the idealized oro-pharyngeal-laryngeal (OPL) human airway developed based on information from MRI and CT scans and data in the archival literature. The idealized geometry was constructed using simple geometric shapes that possess all the basic anatomical features of actual OPL geometries. Hot-wire anemometry, smoke wire visualization, and PIV were used for the measurements and a review of the results obtained from all the methodologies was provided [87]. One of the early experimental study using a flexible model to investigate airflow dynamics was by Chouly et al. in 2009 [88]. This was a validation study to their numerical FSI study Chouly et al. in 2008 (Figure 2.6). An over-simplified representative model of airway anatomy was considered in both numerical and experimental studies. The tongue was represented by a latex tube filled with water. This study shows the flow induced collapse of the pharyngeal airway [89].

The 2012 paper by Shineeb and Pollard, reports an experimental investigation of the vortical structures in the pharynx/larynx region of an idealized human extrathoracic airway obtained using PIV [90]. In 2011, Spence airflow velocity during natural and assisted breathing was investigated using planar and stereo PIV in steady and oscillatory flow conditions. The investigations on anatomically accu-

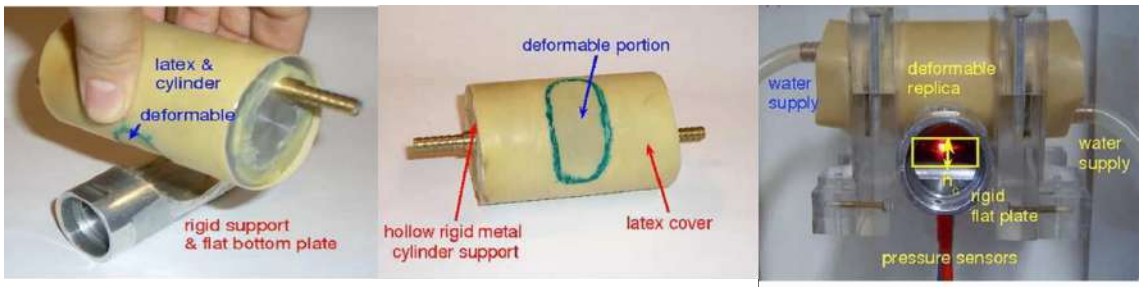

Figure 2.6: In-vitro flexible model of the idealized airway to study collapse at the base of the tongue [88].

rate transparent silicone models of the human nasal cavity using rapid prototyping. Breathing flow rates and waveforms were measured in-vivo and dimensionally scaled by Reynolds number (Re) and Womersley number matching to reproduce physiological conditions in-vitro [4].

In 2013, Zhao constructed a flexible in-vitro airway model from airway geometry of patient pre- and post- dental appliance treatment for OSA to validate the FSI simulations. The model was fabricated using stereolithography. The deformation of the wall was recorded using a high speed camera and a linear variable differential transformer sensor. This study showed less deformation (less occlusion) with the use of dental appliance [91]. In 2019, Le used MRI images of the head and neck of a healthy individual to develop a model. It included the geometry of the nasal cavity, pharynx, larynx, and trachea. An identical physical, flexible model of the upper airway was fabricated using a combination of 3D printing and silicone molding. A pressure catheter was used to measure pressure at the model outlet, while a flow meter was used to measure the flow rate. The impact of elastic properties of the pharyngeal wall on the pressure-flow curve was investigated and revealed that the peak inspiratory flow rate increased as the modulus of elasticity increased. These results were used to then validate FSI simulation data [92]. In 2020, Fan investigated the fluid dynamics inside the pharyngeal airway using numerical simulations and PIV. A real sized 3D cast replica was manufactured using 3D printing technique. These measurements showed flow acceleration after the pharynx bending with high velocities in the posterior pharyngeal wall [93]. In 2020, Xu investigated the flow in during inspiration and expiration in a 3D model of the airway using PIV (Figure2.7). This investigation provided key differences in jet formation and region recirculation during inspiration and expiration [94].

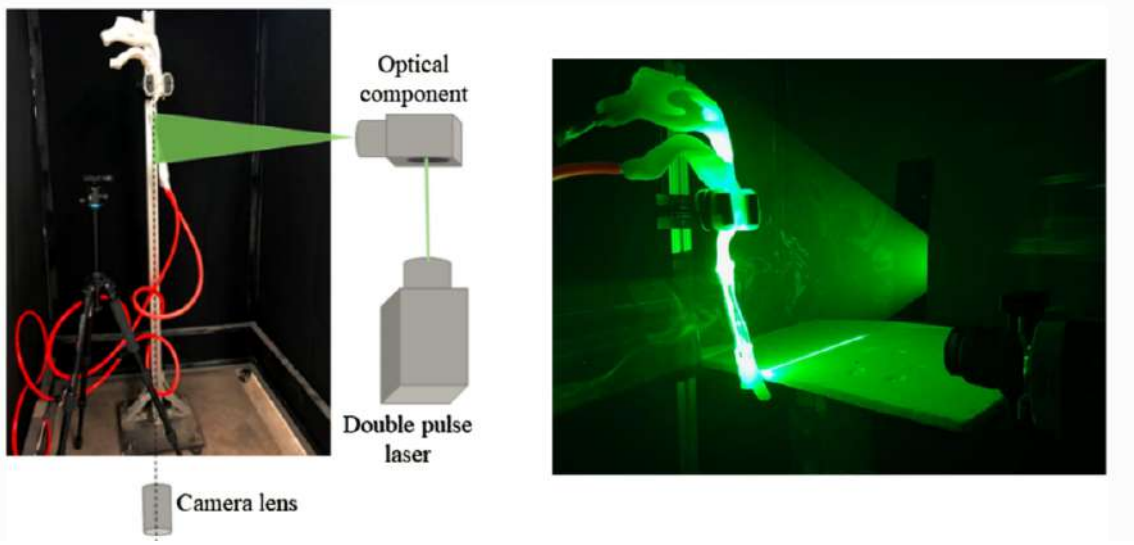

Figure 2.7: PIV measurement setup for airflow study in the 3D model of the airway during inspiration and expiration [94].

2.4.1 Review of in-vitro experiments using MRI based techniques

In 2006, Rochefort's paper described a technique that combines radial MRI and phase-contrast to map the velocities of hyperpolarized gases (3He) in the airway. The method was evaluated on well-known geometries straight and U-shaped pipes. The three velocity components measured helped visualize the vortices and localize characteristic points, such as the maximum velocity and vortex center positions. These results were then compared with the results from numerical simulations [95].

In 2018, Collier developed two human airway models, including and excluding the oral cavity and upper airways derived from MR and CT imaging, were 3D printed (Figure 2.8). 3D phase contrast velocimetry - magnetic resonance imaging (PCV-MRI) was used for velocity measurements in these models at different flow conditions. A comparison of 3D velocity maps measured with flow MRI and predicted by computational fluid dynamics simulations was done and was seen to have an excellent agreement (linear regression R-squared values ranging from 0.39 to 0.94) [96].

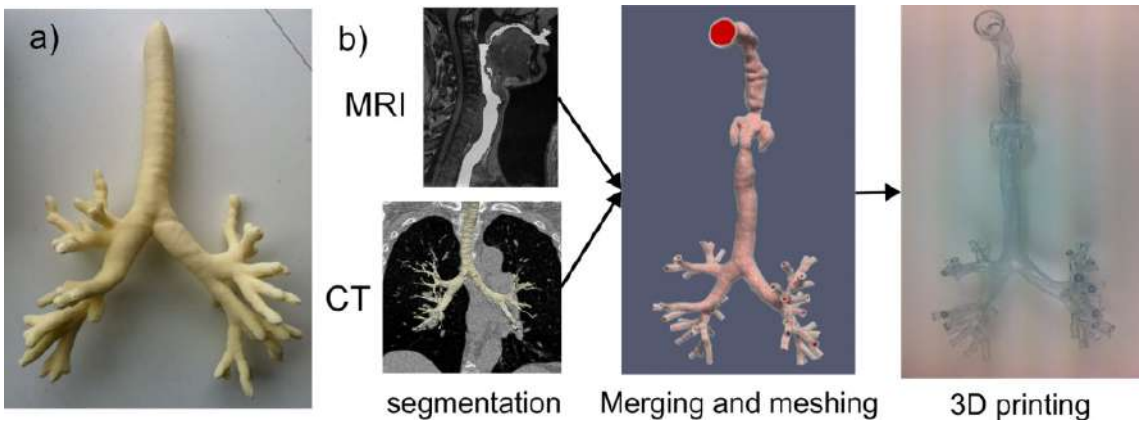

Figure 2.8: 3D printed model of patient specific lung model used for velocity measurement with PC-MRI [96].

To the author's knowledge, Collier's 2018 paper is the only other similar research work focusing on using 3D PCV MRI to measure velocity in airway models to validate CFD results.

The uniqueness of this research work is that the airflow in the upper airway is dynamic, changing in space and time. There is a complex interdependent interaction between the airway walls and the airflow. Hence, it is essential to understand these variations. Only few experimental techniques study these variations and compare them with CFD data.

3

Theory

3.1 Theory and fundamentals

3.2 Basics of MRI

MRI is a non-invasive imaging technique to produce high-quality images of the inside of the human body. MRI is an application of nuclear magnetic resonance (NMR) principles, a spectroscopic technique used to determine the structure of a material by measuring the interaction of nuclear spins in the presence of a strong magnetic field [97].

Different scan sequences enable various applications, for example, standard sequences like T1 and T2 weighted scans provide a good contrast in soft tissue and fluids. Functional MRI (fMRI) facilitates the measurement of neuronal activity. Diffusion tensor imaging (DTI) allows obtaining directions of fiber bundles in the brain. PC-MRI, the central topic of this thesis, enables the measurement of blood flow directions and velocities in the cardiovascular system, the head, and the liver. MRI has significant advantages over other imaging modalities. MRI uses strong magnetic fields but exposure to such fields has no known side effects. It is completely non-invasive and provides good contrast between soft tissues. Additionally,

MRI allows for multiplanar imaging which is impossible with radiography and CT.

3.3 Working of the MRI

An atomic nucleus, composed of protons and neutrons can be described by spin angular momentum and spin quantum number. Atomic nuclei with an odd number of protons and neutrons, such as hydrogen, which has only a single proton in its nucleus, possess a non-zero spin quantum number ($\pm 1/2$) and interact with the magnetic field. Also, as hydrogen is abundantly available in the human body it is used for MR imaging [98] [99].

Without an exterior magnetic field, the spins orient randomly. However, the presence of an external static magnetic field, B_0, produces a spin about the direction of the external magnetic field, $\vec{B_0}$ in parallel or anti-parallel direction. The Boltzmann distribution states that the spins will statistically prefer a parallel direction due to favorable energy contribution rather than an anti-parallel direction [100]. The interaction between the proton's spin and the external magnetic field generates torque. The rotation induced by this torque is called precession. The angular frequency of this precession is given by Larmor frequency, ω_0 and is proportional to the strength of the external magnetic field connected by the gyromagnetic ratio γ (Figure 3.1) (Equation 3.1)[101].

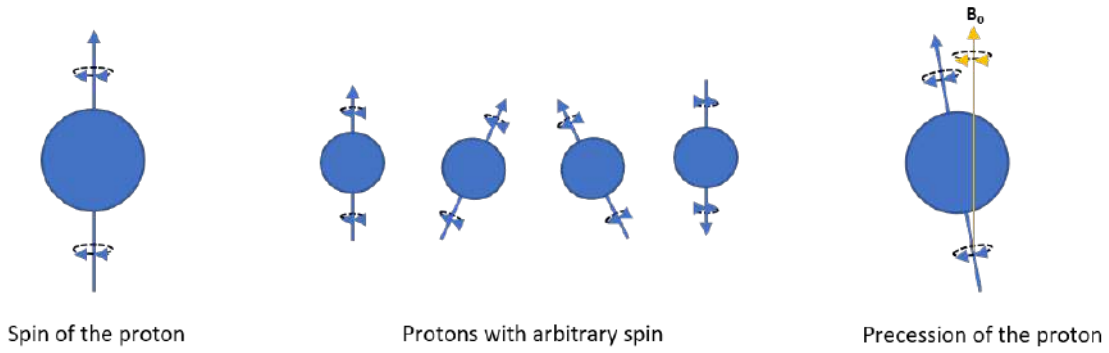

Figure 3.1: Spin and precession of the protons.

$$\omega_0 = \gamma B_0 \tag{3.1}$$

Since many atoms are considered in the NMR process, the behavior of a sample of spins included in volume V can be described at the macroscopic scale (following

the classical laws of mechanics) by summing the contribution of each magnetic moment. Net magnetization $\vec{M}$ is composed of a longitudinal part $\vec{M}_z$, parallel to $\vec{B}_0$, and a transversal component $\vec{M}_{xy}$, orthogonal to $\vec{M}_z$ (Figure 3.2). The transversal component becomes 0 at equilibrium [102]. The equations describing the macroscopic evolution of the magnetic response that arises when a set of spins are subjected to an external magnetic field were introduced by Bloch in 1946 [103]. This set of spins is called an isochromat and is defined as an ensemble of spins with the same phase.

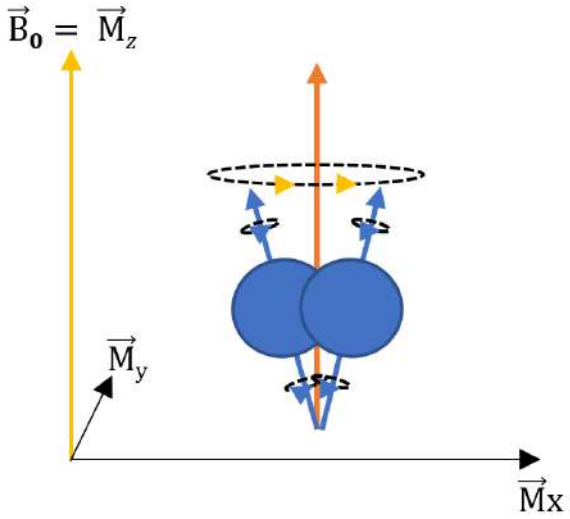

Figure 3.2: The sum of unmatched protons magnetic moments provides a net magnetization $\vec{M}$.

3.3.1 Excitation and relaxation

An NMR experiment consists of two steps, excitation and relaxation. In the excitation step an oscillating magnetic field $\vec{B}_1$ is applied to disturb the net magnetization from equilibrium. This magnetic field called the radio frequency (RF) pulse is applied by a transmit coil transverse to the static field during a short period of time. When the protons are excited with a RF equal to their Larmor frequency and perpendicular to direction of the external field, about half of the protons spin axes flip by 180°. This causes phase coherence (synchronization of the precession) (Figure 3.3)).

When the RF signal is turned off, relaxation or return to equilibrium of net magnetization begins. During relaxation the transverse magnetization decays (spin-spin

relaxation) and the longitudinal magnetization recovers (spin-lattice relaxation). Transverse magnetization decay is described by an exponential curve, characterized by the time constant T2. T2, transverse magnetization looses 63% of its original value. The recovery rate is characterized by the tissue-specific time constant T1. After time T1, longitudinal magnetization returns to 63% of its final value. During relaxation the electromagnetic energy is retransmitted to provide an RF signal. The intensity depends on the amount of hydrogen protons in the tissue, the B_0 magnetic field strength, the T1 and T2 relaxation times. The RF coil detects these signals switched to the receiver (Figure 3.3).

To acquire MR image, RF excitation is done as a pulse sequence, where the signal is rapidly switched on and off again. The time between two excitations (a scan parameter), during which the longitudinal magnetization can recover, is called the repetition time (TR). Then a demodulation of the signal is performed to remove the rapid oscillations at the frequency ω_0 [104].

3.3.2 Spatial encoding

Prior to the signal detection, spatial encoding is done to localize the magnetic contribution coming from each isochromat. In order to distinguish the spatial location of the signal, the magnetic gradient linearly alters the unique resonance frequency to a continuous bandwidth. That is, three spatially varying magnetic fields superimposed on the B_0 field with direction of each gradient perpendicular to the other two are employed. First, the z-gradient oriented from head to feet encodes the image slice. Slice distances result from the steps in which the RF for excitation is incremented during the scan. Second, the y-gradient facilitates the selection of a specific column within a slice. It is turned on and off for a short period of time, directly after the RF, and causes a phase shift of the precessing spin axes. Therefore, it is also called a phase-encoding gradient. The frequency-encoding x-gradient encodes the row by causing a shift in the precession frequencies within the column. This gradient is active with the z-gradient when the signal is received [102].

3.3.3 Image reconstruction

The data from the MRI signal during data acquisition is stored in the data matrix, k-space. It represents the spatial frequency and phase information of the object. Different k-space trajectories can be adopted to fill the k-space, depending on the signal and pixel width required. The path adopted greatly influences the result-

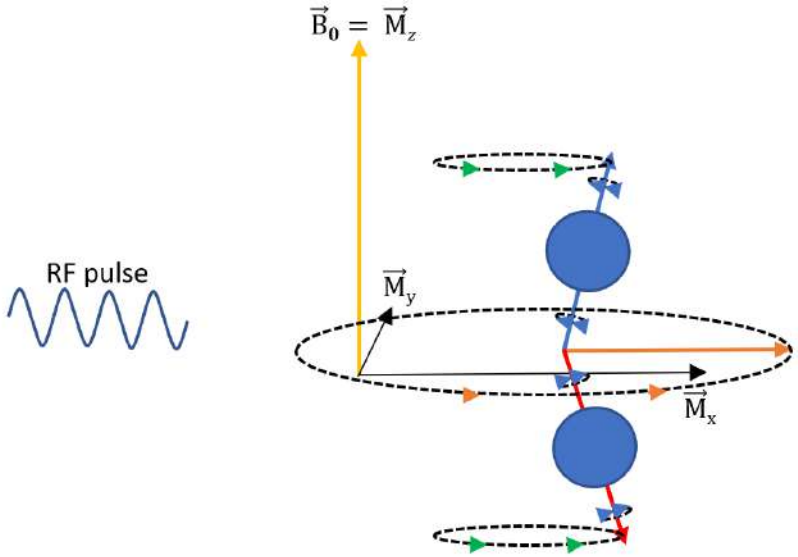

Figure 3.3: The overall magnetization vector (orange) is rotating in the $\vec{M}_{xy}$ plane perpendicular to $\vec{B}_0$ (yellow). Excited with the correct RF, the unmatched protons spin axes synchronize their precession (green). That is about half of the spin axes are flipped by 180° (red) and the transversal magnetization component increases (longitudinal component decreases) until $\vec{M}$ rotates in a plane perpendicular to $\vec{B}_0$ to cause phase coherence. When the RF is turned off, the transversal magnetization gradually decreases and the longitudinal magnetization is restored (T1 relaxation). Also, the protons phases desynchronize (T2 relaxation). During this processes, a measurable RF is released, which is the energy the protons absorbed from the excitation.

ing imaging artifacts. A common and straightforward strategy covers the k-space following a cartesian trajectory. To fill the k-space progressively, an MR imaging sequence consists of the sequential repetition of many pulse sequences with each pulse sequence usually filling one line of the k-space. A particular type of sequence might be preferred depending on the type of tissues/organs or functionality of to image. For instance, spin-echo sequences are characterized by 180° refocusing RF pulse and will be preferred to measure the T2 accurately. On the contrary, gradient echo sequences (GRE) are usually characterized by a lower flip angle and a unique RF pulse per pulse sequence, such that it results in a fast MR acquisition. The relationship between k-space data and image data is the Fourier transformation. An inverse Fourier transform allows converting this data matrix into an image.

3.4 Velocity measurement: standard 2D PC-MRI

During a standard MRI acquisition, a phase difference is caused due to various movements within the body, such as breathing, vessel pulsations, swallowing, and moving fluids. Such a phase difference leads to artifacts like blurring or ghosting (noise appearing as repeated version of the image). However, this phase shift is proportional to velocity and can be used to quantify moving fluids. The central idea of flow measurements is to encode velocity using phase information. Alternatively, PC-MRI is based on the principle that in the presence of moving spins, the phase of the spatially encoded signal could be expressed as a function of the velocity of these spins. 2D PC-MRI allows for the one-directional velocity measurement of fluid in a 2D slice.

The principle of velocity measurement is explained below with an example of measurement of blood flow velocity in a vessel (Figure 3.4). The velocity encoding is achieved using bipolar gradients. Bipolar means the gradients have the same strength but in opposite directions. After a slice selecting z-gradient is applied, two bipolar gradients are superimposed on the B_0 field causing phase coherence. Application of the first of the bipolar gradient causes a position dependent phase shift in the vessel (stationary) and the blood. Then the application of second of the bipolar gradient removes the phase shift in the stationary vessel. However, as the protons in the blood have travelled a certain distance, it experiences a different part of the gradient. Subtraction of two images acquired from two acquisitions, one with the first and one with the second of the bipolar gradients active results in phase difference is directly related to the flow velocity [102].

3.4.1 Velocity encoding parameter

Velocity encoding parameter (Venc) is an essential user defined scan parameter chosen to encompass maximum measurable blood flow velocity between ±Venc m/s per dimension. Venc adjusts the strength of the bipolar gradients so that the maximum velocity correspond to ±180° phase shift of data. Venc influences the image contrast and quantitative precession. Also, as signal-to-noise (SNR) is inversely proportional to the chosen Venc value, choosing a high Venc value causes lower SNR and measurement quality. On the other hand, choosing a low Venc value, causes velocity aliasing. Thus, adjusting the scan to the flow in a specific region is crucial for a

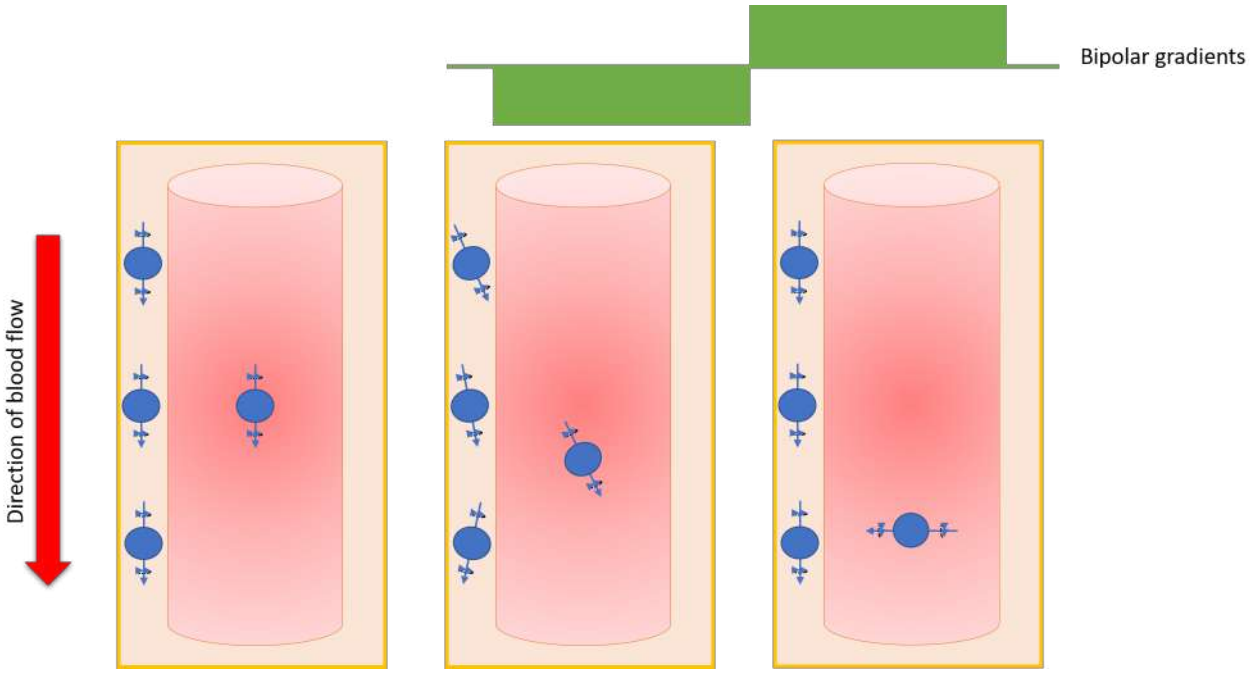

Figure 3.4: From left to right: The protons in the stationary tissue (orange) and vessel (red) aligns with $\vec{B}_0$ which is pointing in the direction of the reader. Application of the first bipolar gradient causes position dependent shift in the stationary tissue and the vessel. A phase difference is then caused due to the application of the same gradient in the opposite direction and encodes velocity in the blood.

successful acquisition (Figure 3.5).

Standard techniques use PC-MRI velocity maps with two spatial dimensions obtained by one-directional (through plane) velocity encoding along the flow direction. For complex flows, the velocity can be encoded in all three flow directions in a given 2D slice. In 4D Flow MRI, by encoding the velocity in all three directions in a three-dimensional volume, the temporal evolution of the flow can be measured and visualized.

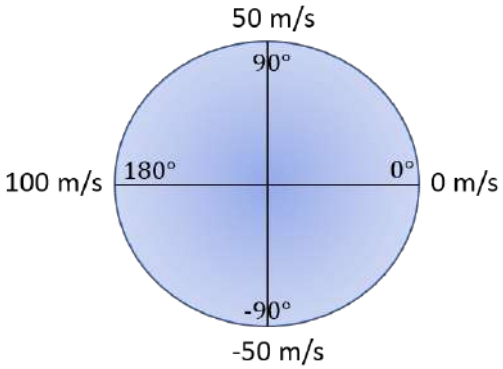

Figure 3.5: The Venc parameter adjusts the strength of the bipolar gradients so that the maximum velocity selected corresponds to a 180° phase shift in the data. For instance, for a given Venc value of 100 m/s, the bipolar gradient is adjusted to encoded velocities ±100 m/s. If the actual velocity is 150 m/s, it would be mapped to 270° which instead would represent -50 m/s.

3.5 4D flow MRI

The first 3D cine PC-MRI sequence with three-directional velocity encoding was first developed by Firmin et al [105]. This technique images the time-varying anatomy with high contrast and measures the temporal variations in hemodynamic parameters. Thus, it constitutes as a promising tool for clinicians.

3.5.1 Velocity encoding

In 4D flow MRI, velocity is encoded in all three directions throughout a specified time duration. There are several approaches to encode velocity in all three directions. The earliest approach was the six-point method. Like in one-directional velocity encoding (Section 3.4), this uses one flow compensated and one flow encoded measurement per direction. In the flow compensation technique, the reference image is acquired with vanishing zero and first gradient moments, and a second image performs velocity encoding with added bipolar gradients with identical parameters. Subtracting of the two scans allows for the quantification of flow. Later, more time-efficient four-point techniques were introduced where one reference image and three velocity-encoded images along three orthogonal directions are acquired. Interleaved velocity encoding requires the successive acquisition of the same phase encoding line with four different velocity encoding gradients.

3.5.2 Data acquisition

Due to the large amount of data that has to be collected (three spatial dimensions, three velocity directions and over time), efficient data acquisition is necessary to achieve practical scan times for 4D flow MRI. Advancement in hardware such as, the availability of high performance gradients, introduction of phased-array coils, multi-receiver channels, and parallel imaging technology have reduced the total scan time. Other methodological improvements to reduce scan time include the use of advanced accelerated imaging approaches such as k-t BLAST, k-t SENSE, k-t GRAPPA, or compressed sensing [106]. An alternative technique that is increasingly used to accelerate 4D flow MRI is radial data sampling combined with undersampling. Radial acquisition schemes have been shown to permit 4D flow imaging with improved scan time while providing large spherical volumetric coverage with high spatial resolution [107].

3.6 Signal-to-Noise Ratio

Noise is always present in MR imaging and can be a non-negligible source of errors. It generally originates from the electromagnetic interaction within the MRI scan room (receiver coils) or patient body electronic charges. The signal-to-noise ratio (SNR) is a measure that compares the true signal to the background noise. It is mostly used for quality assurance, image evaluation and pulse sequence comparison. SNR is proportional to the voxel size and the square root of the acquisition time. The noise also impacts the phase of the MR signal. Low signal intensities can apparent bias due to the acquisition noise.

Phase contrast velocity images also suffer from noise and introduce errors in the acquired velocities. The noise in velocity encoded images is defined as the standard deviation of the phase differences in a region with no flow or motion and is inversely related to the SNR in the corresponding magnitude images (Equation 3.2) [108]. For a given SNR, the velocity noise, σ is determined by the Venc value, resulting in a trade-off between the minimum detectable velocity sensitivity needed to avoid aliasing. The Venc should always be selected as small as possible for optimal noise performance.

$$\sigma = \frac{\sqrt{2}}{\pi} \frac{Venc}{SNR} \tag{3.2}$$

3.7 Limitations of PC-MRI

3.7.1 Motion related artifacts

Flow misregistration is an important flow induced artifact. It occurs when the moving spins change position between the frequency- and phase-encoding gradients times. This artifact is most prominent for in-plane flows.

3.7.2 Technique related artifacts

Velocity aliasing: When the chosen Venc value is lower than the maximum velocity of blood flow the values appear flipped in the image data. This is termed as phase wrap.

Wrap around: A wrap-around artifact results when the chosen field of view (FOV) is smaller than the object's size. It is caused by non-linear gradients or undersampling of the frequencies (violation of the Nyquist theorem).

Gibbs artifact: The Gibbs artifact or truncation artifact occurs due to undersampling of high spatial frequencies at sharp boundaries. It appears as a series of lines in the MR image. Theoretically, reconstruction of the image by a Fourier transform from a finite sampled signal causes the truncation effect.

Partial volume effect: Partial volume effects appear when a voxel lies at the interface of two tissues with different resonance properties. In such a voxel, the signal would be contributed from both the interfaces. Additionally, if the object is smaller than the voxel a loss of detail and spatial resolution occurs.

Chemical shift: This an artifact that occurs at water and fat interface in the frequency encoding direction due to the difference between the resonance frequencies of fat and water.

Magnetic susceptibility: The magnetic susceptibility is intrinsic to each material property and corresponds to its ability to either disperse the surrounding magnetic field (diamagnetic) or concentrate it (paramagnetic, ferromagnetic). For example, magnetic field distortions appear due to the magnetic susceptibility differences at the interface around metal implants and air-tissue interfaces.

3.7.3 Hardware related artifacts

Eddy-currents artifacts: Eddy currents are caused due to the rapid switch on and off the gradient fields. This causes deviations of the gradient waveform profile, perturbs the spatial encoding and therefore causes an offset of the true velocity

Static field inhomogeneities: Imperfections in the homogeneity of the static field are natural and can be additionally caused by the object to image.

Gradient field non-linearities: Gradient field non-linearities produce the most significant distortions. It is caused when the magnetic fields are not able to produce an accurate field causing inhomogeneous distribution.

3.8 Physical modeling

The following section describes the several steps involved in physically modeling and manufacturing a 3D model from a given set of medical image.

3.8.1 Segmentation

Segmentation of a digital image is the process of its division into several small regions to reduce the complexity of the image and to make further image processing simpler. One of the most common segmentation algorithms used in processing medical images is a watershed algorithm. It is a region-based method where an image is regarded as a topographic landscape with ridges and valleys defined with gray values. The segmentation decomposes an image into catchment basins and watershed lines with elevation of the landscape representing the brightness of the point [109]. There are several algorithms available to perform watershed algorithm. One of the commonly used watershed algorithm is Meyer's flooding algorithm [110]. This algorithm works on a gray scale image and the flooding is performed on the gradient image.

The general procedure for the segmentation is as follows,

1. Local minimums are chosen as a starting marker for flooding and all labelled differently.
2. Neighboring pixels of each marked area with priority level corresponding to the pixel gradient value is inserted into a hierarchical queue.

3. The pixel with the highest priority level (lowest gray level) is extracted from the hierarchical queue. If the neighbors of the extracted pixel is marked with the same label, then the pixel is marked with their label. All non-marked neighbors not yet in the hierarchical queue are put into the hierarchical queue.
4. Step 3 is repeated until the hierarchical queue is empty. Non-labeled pixels form the watershed lines.

3.8.2 Surface triangulation and smoothing

Surface triangulation is done to represent a segmented surface. Popular algorithm used to achieve this is the marching cube algorithm by Lorensen and Cline [111]. The marching cube considers a cube defined with eight data values (one value at each vertex of the cube) and locates the isosurface within this cube. If the data value at the vertex of the cube is higher than the isosurface-value (i.e., inside the surface), then it receives one, while it is lower (outside), it receives a zero. This binary labeling (8 bit string) is used to create an index. There are 256 (2^8=256) possible configuration of the cube (256 ways the isosurface can intersect the cube) depending on whether the vertices lie inside or outside the surface. By considering symmetries, the 256 configurations are brought down to 15 configurations (Figure 3.6). For a given index, a lookup table is generated for edge-isosurface intersection. Linear interpolation is used to place the vertex of the isosurface in the appropriate position along the cube's edge. In the final step, a unit normal for each cube vertex is calculated. These are essential for lighting and shading of the resulting mesh. All the individual cubes make the surface. This completes the surface triangulation process.

In principle, more number of triangles translates to a more accurately represented model. However, it is the quality of the mesh that determines the accuracy of the model. The surface might appear faceted with more triangles and contain triangles with minimal angles. These can be removed, and the mesh quality can be increased by mesh smoothing. A smoothing of the surface can be achieved by reducing the number of triangles. That is, two triangle vertices are contracted to one vertex if they share an edge. Then the edge and the two belonging triangle faces are removed. The contraction is performed until a prescribed percent of triangle reduction is reached. The contracting vertices are chosen based on a quadratic error estimate described by Garland and Heckbert [112]. Secondly, Laplacian smoothing can be performed. The Laplacian smoothing technique changes the position of nodes without modifying the topology of the mesh. In the process of Laplacian smoothing,

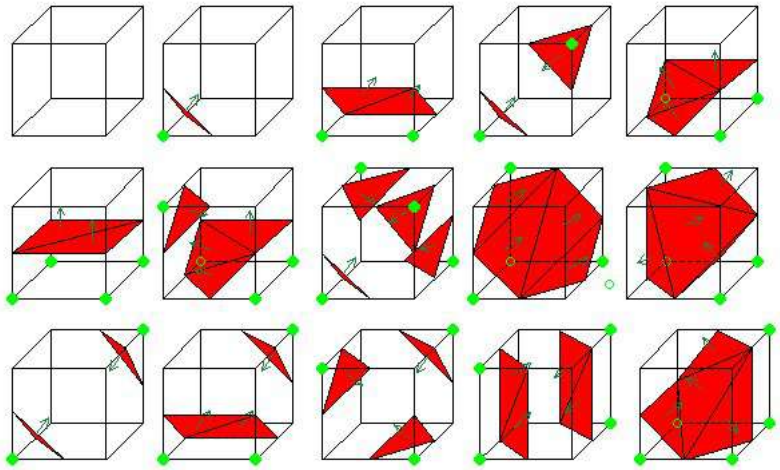

Figure 3.6: 15 basic cases of the marching cube technique [111].

each vertex moves to a new position defined by taking the average position of its neighbors [113].

3.8.3 Fabrication with 3D printing

3D printing, or additive manufacturing, fabricates a 3D object from a computer aided design (CAD) or digital 3D model. The term "3D printing" can refer to a variety of processes in which material is deposited, joined, or solidified under computer control to create a 3D object, with the material being added together (such as plastics, liquids, or powder grains being fused), typically layer by layer. Multijet printing (MJP) is a new rapid prototyping process that constructs high resolution, hard plastic parts with complex geometries. It uses piezo printhead technology to deposit either photocurable plastic resin or casting wax materials layer by layer. MJP printers offer high z-direction resolution with layer thickness as low as 16 microns [114].

3.9 Computational fluid dynamics

Computational fluid dynamics (CFD) analyzes fluid flows using numerical solution methods. CFD can analyze complex problems involving fluid-fluid, fluid-solid, or fluid-gas interaction. Engineering fields where CFD analyses are frequently used are aerodynamics and hydrodynamics.

3.9.1 Mathematical modelling

The following conservation laws of physics give the governing equations of fluid flow:

1. The mass of fluid is conserved (Equation 3.3).
2. The rate of momentum change equals the sum of the forces on a fluid particle (Newton's second law) (Equation 3.4).
3. The rate of change of energy is equal to the sum of the rate of heat addition to and the rate of work done on a fluid particle (first law of thermodynamics) (Equation 3.5).

The molecular structure of matter and molecular motions may be ignored to analyze fluid flows at macroscopic length scales.

$$\frac{\partial \rho}{\partial t} + \rho \cdot (\nabla \cdot v) = 0 \tag{3.3}$$

$$\frac{\partial (\rho v)}{\partial t} + \nabla \cdot (\rho v v) = -\nabla p + \nabla(\tau) + \rho g \tag{3.4}$$

$$\rho \left[\frac{\partial h}{\partial t} + \nabla \cdot (hv) \right] = \frac{\partial p}{\partial t} + \nabla \cdot (k \nabla T) + \theta \tag{3.5}$$

with ∇ as the gradient operator ρ the density, v the fluid velocity, τ the viscous stress, g the acceleration due to gravity, p the pressure, T the temperature, θ the source term.

The above equations (3.3, 3.4, 3.5) are the governing equations of CFD.Conservation of momentum (Equation 3.4)is also known as the Navier-Stokes equation. Navier-Stokes equations are PDEs used to describe motion of viscous fluid.

CFD solvers transform these laws into algebraical equations and are able to efficiently solve these equations numerically [115].

3.9.2 Discretization

The strategy of CFD is to replace the continuous problem domain with a discrete domain using a grid. In the continuous domain, each flow variable is defined at every single point in the domain and in discrete domain the flow variable is defined only at the grid points (Figure 3.7). Different techniques such as the finite element method (FEM), finite difference method (FDM), and finite volume method (FVM)

are available to discretize the governing differential equations into algebraic form. This produces a system of ODEs for unsteady problems and algebraic equations for steady problems [116].

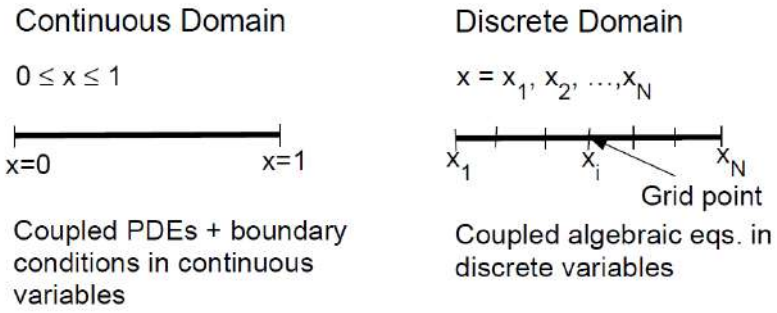

Figure 3.7: Discretization [116].

3.9.3 Turbulence modelling

A flow regime can be described as laminar, transitional, and turbulent. Most flows encountered in nature are turbulent. Reynolds number (Re) is used to determine the flow regime (Equation 3.6).

$$Re = \frac{\rho v d}{\mu} \tag{3.6}$$

where v and d are characteristic velocity and length scale and μ is the dynamic viscosity of the fluid.

A turbulent flow is described as an irregular and random motion both spatially and temporally. Some techniques have been developed to describe turbulent flow with less computational costs by introducing approximations. Those are generally divided into averaged Navier-Stokes Equations (RANS) and Large-eddy simulations (LES). RANS is based on a statistical treatment of stationary or slowly varying flow fluctuations. The dependent variables are broken into two parts: a mean, time- or ensemble-averaged part of the flow, and a fluctuating component representing deviations from this mean. This approach gives time averaged mean value for velocity field. The advantage of RANS is that it is fast and available in most CFD codes and is streamlined to handle unstructured complex grids. An alternative to RANS model is LES where filtering rather than averaging is performed. That is spatially filtered governing equations are used to capture the large flow structures depending on the filter size and subgrid scale model is used to model the small scale

flow structures. LES has the potential of giving more accurate results. Although the technique is computationally expensive, using parallel computing has helped bring down the time.

3.9.4 Numerical solutions and post-processing

After obtaining the discrete equations, boundary conditions such as velocity and pressure are applied at the grid points of the boundary. Solving this is a matrix inversion problem. There are millions of unknowns in the discrete system therefore optimization of the matrix inversion is done to reduce CPU time and memory. For instance, the matrix to be inverted is sparse and the CFD code stores only non-zero values to minimize memory usage. An iterative procedure to invert the matrix is employed; the longer one iterates, the closer one gets to the true solution for the matrix inversion. An important step in finding the solution is also checking for grid convergence. It is essential to check the grid convergence in CFD, i.e. examining the convergence is a method for determining the discretization error. As the grid is refined (grid cells become smaller and the number of cells in the flow domain increase) and the time step is refined (reduced), the spatial and temporal discretization errors, respectively, should asymptotically approach zero [116].

Turbulence introduce additional non-linearities in the governing equations. This makes obtaining accurate numerical solutions for complex flows challenging. To adapt with non-linearity, the equations are linearised about a guess value of the solution and are iterated until the guess agrees with the solution to a specified tolerance level. A direct or an iterative solver can be used to find the linear solution in such instances. A direct solver (eg. PARDISO in comsol) is based on LU decomposition (lower-upper decomposition) and are very efficient, fast and robust. An iterative solver (eg. General Minimal RESidual (GMRES) in comsol) contrary to direct solvers, iterative methods approach the solution gradually, rather than in one large computational step. Such iterative solvers are robust at the same time use less memory space.

Post-processing of the simulation results is performed to extract the desired information from the computed flow field. Reliability of a CFD simulation result depends on the degree of uncertainty and the cumulative effect of errors. Some of the prominent errors are modeling errors, discretization errors and convergence errors. Modeling errors can be defined as the difference between the actual, real flow and the simulated flow resulting from the exact solution of the mathematical model. Discretization errors is the difference between the exact solution of the

mathematical model and the exact solution of the algebraic system resulting from the discretization and iteration errors. Convergence errors is the difference between the exact solution and the iterative solution of the algebraic system.

Therefore, verification and validation is done to ensure that the CFD code produces accurate and reliable results for a specific range of flow problems.

4

Experimental investigation of flow in axisymmetric stenosis: 2D PC-MRI

4.1 Introduction

This chapter aims to establish the test-retest reliability and accuracy of the 2D PC-MRI technique. The application of the technique as an investigation tool to study flow dynamics and as a validation tool for numerical simulation is demonstrated using a case study.

Stenosis is an abnormal narrowing in a compliant vessel such as carotid and renal arteries or tubular organs like the trachea, and spinal canal caused due to build-up of plaque, fat deposition, disease, injury, or narrow anatomy [117] [118]. This change in the vessel's or the tubular organ's geometry alters the flow conditions and restricts normal body functions. Arterial stenosis caused due to atherosclerosis alters the blood flow pattern and vessel wall shear stress (WSS) to contribute to thrombus formation or compromised blood flow. This causes severe medical conditions such as stroke, blood clots, aneurysms, and ischemia [119].

Arteries and the pharynx both have a tubular structure. In the anatomy of the pharynx, the lumen narrows at the end of the soft palate and also at the beginning

of epiglottis (Chapter 1, figure 1.2). The narrowing of the airway lumen and the presence of stenosis in the artery produce comparable flow phenomenons. Like the airflow in the pharynx, blood flowing through stenosis is in the laminar-turbulent transition regime. The changes in pressure and WSS in the airway post the narrow region are analogous to the effects observed in an artery with stenosis. However, the geometry of stenosis is more straightforward than the geometry of the pharynx. Therefore, it is chosen to assess the experimental technique and design's reliability, accuracy, and validity.

The goals of the chapter are listed below,

1. Investigation of flow dynamics in the stenosis model at laminar and turbulent flow conditions.
2. Assessment of reliability of the 2D PC-MRI measurements using three sets of data acquired at the same condition and by the same operator at different time points and statistically quantifying the test results with intraclass correlation coefficient (ICC).
3. Evaluation of the accuracy of 2D PC-MRI velocity values by validating it with previously published data by Ahmed and Giddens [120] using Bland-Altman plot and linear regression analysis.
4. Validation of numerical simulations with 2D PC-MRI data.

4.2 Phantom design, fabrication and experiment setup

4.2.1 Geometry

The rigid axis-symmetric stenosis phantom is an idealized representation of physiological stenosis. Ahmed and Giddens, in their paper, measure velocity in the stenosis model during steady flow. The study was conducted at laminar and turbulent flow in various models with different degrees of occlusions. In this thesis, stenosis with 75% degree constriction was considered for the investigation. The stenotic phantom in Ahmed and Giddens paper had a diameter of 50.4 mm and a length of over 6 m. Due to the restricted space available in the MRI room, the phantom in the current study was scaled down. All the phantom's length measures were considered as dimensionless properties proportional to the unoccluded tube

diameter to ensure uniform downscaling that maintained the shape of the phantom. The stenotic phantom used in this study has an unoccluded diameter of 25.9 mm and a stenosis length of 50 mm. The constriction follows a cosine curve given by the equation below (Equation 4.1, unit in mm). omputer aided design (CAD) tool, SolidWorks (Dassault Systems SolidWorksCorp., Waltham, Massachusetts) was employed for precise geometry definition. Small extensions were placed at the inlet and the outlet of the stenosis to ensure smooth flow of the fluid at the transition from pipe to stenosis inlet and stenosis outlet to the pipe (Figure 4.1).

$$y = 6.475 \cos(\frac{\pi}{51.8}x) - 12.95 \tag{4.1}$$

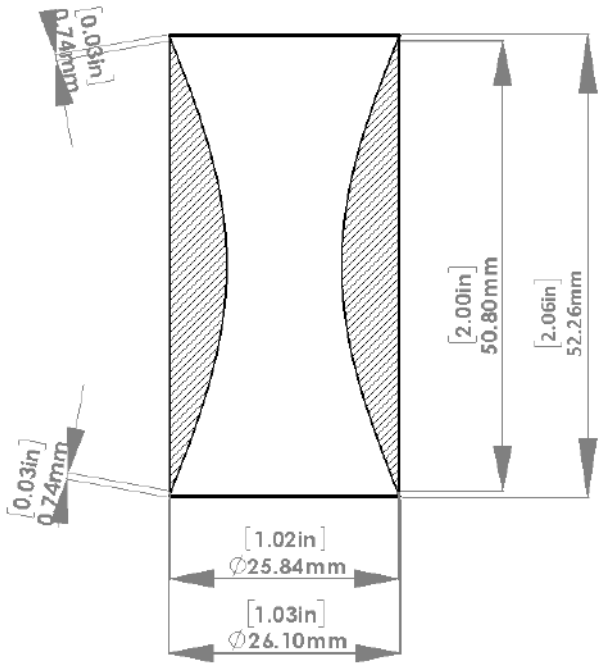

Figure 4.1: CAD geometry of the stenotic phantom.

4.2.2 Fabrication

The CAD-defined geometry is fabricated using the 3D printer, ProJet 3510HD by 3D systems, California, USA. This printer uses MultiJet 3D printing technology. This technique printed a thin layer of UV-curable liquid plastic on the platform with wax as support material. The model, after fabrication, was placed in the oven

at 60° to melt the wax. Once the model cooled down to room temperature, it was placed in an ultrasonic bath for about 30 to 45 minutes with baby oil to clean the model. The model was slightly polished and smoothed to remove staircase effects. The material used to print the stenotic phantom was Visijet X. Visijet X has a tensile strength of 49 MPa, a tensile modulus of 2168 MPa, and flexural strength of 65 MPa, and a heat distortion temperature of 88° at 0.45 MPa. The stenosis was printed in high definition (HD) resolution with a layer thickness of 32 μm, resolution of 375 x 375 x 790 dots per inch (DPI) in xyz direction, and an accuracy of 0.001-0.002 inch per inch of part dimension.

4.2.3 Experiment setup

A closed-loop flow system was used for the experiment (Figure 4.2). The flow system consisted of the phantom, flexible tubing, MR compatible flow pump, and a fluid reservoir. The details of the flow system are as follows. The 3D printed stenosis was placed inside the plexiglass pipe with a comparable inner diameter to avoid any disturbance in the flow at the boundary. The entrance length for the stenosis was 965 mm, and the post-stenotic region length was 400 mm. The plexiglass pipe was connected at the inlet and outlet to the MR-compatible pump and the fluid reservoir via flexible tubings. The model setup was done such that there were no kinks in the pipes to ensure straightforward implementation of the inlet flow conditions. The MR-compatible computer-controlled gear pump (CardioFlow 5000 MR, Shelly Medical Imaging Technologies, Toronto, Canada) generates a steady flow with an accuracy of ±3%. The trials were performed on a whole-body MR clinical system with Ingenia 3 Tesla (T) scanner (Philips Healthcare, Best, Netherlands) using a 108-channel body coil. The center of the stenosis was positioned at the isocenter of the bore of an MRI scanner.

4.2.4 Test fluid

To preserve the dynamic similarity of the experimental setup, the test fluid properties were scaled to that of the geometry of the stenosis; that is, an aqueous glycerol solution (55.27% by weight) was used. The fluid's density and viscosity were calculated from the empirical formula as given by equations 4.4 to 4.11 [121]. The values obtained from the formula were validated with Ubbelholde viscometer, type II, calibrated with capillary constant of 0.1 mm^2/s^2 (Lauda Scientific GmbH, Lauda-Kö nigshofen, Germany). The formula and the viscometer results are given in the ta-

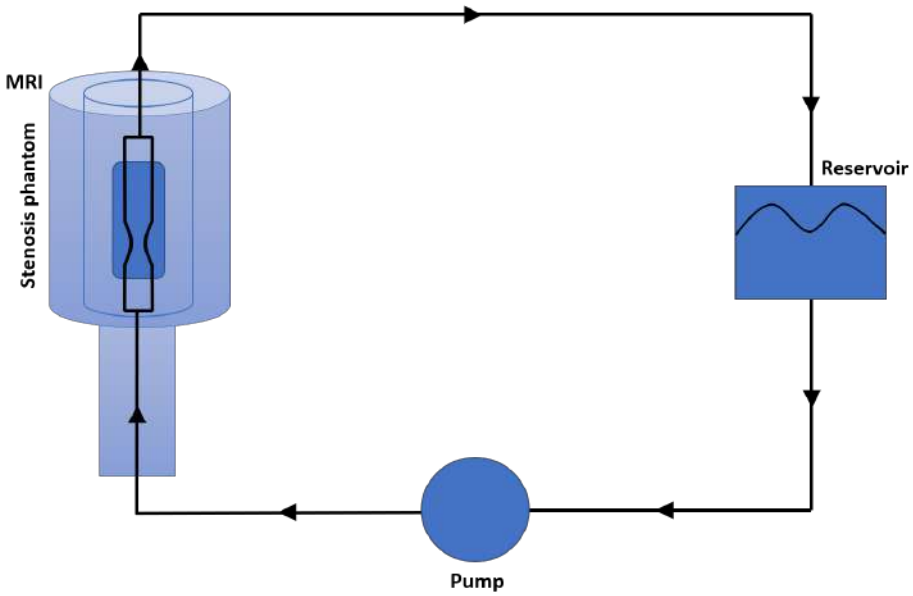

Figure 4.2: Schematic drawing of the experimental setup used for studying flow in the stenosis model. The region of stenosis under study is placed on the MRI table (dark blue rectangle box) as shown in the figure.

ble (Table 4.1). Table 4.1 shows that the values obtained from the formula and the experiment agree. Therefore, the values from the empirical formula were used in all further trials to maintain consistency. In the current set of trials, the test fluid was used at a temperature of 25°C (the temperature maintained in the MRI room) with density value 1144 kg/m^3, absolute viscosity 5.818 mm^2/s and relative viscosity 6.6563 mPas (mPas = cP).

Calculation of the density of the water-glycerol mixture is given by the following equations,

$$\rho_g = 1277 - 0.654T \tag{4.2}$$

$$\rho_w = (1 - \frac{(T-4)^{1.7}}{622}) \times 1000 \tag{4.3}$$

$$\rho = (\rho_w \times (1 - C)) + (\rho_g C) \tag{4.4}$$

where, ρ_w is the density of water in kg/m^3, ρ_g is the density of glycerol in kg/m^3, ρ is the density of the mixture in kg/m^3, T is the temperature in °C.

$$a = 0.705 - 0.0017T \tag{4.5}$$

$$b = (4.9 + 0.036T) \times a^{2.5} \tag{4.6}$$

$$\alpha = 1 - C + \frac{(abC(1-C))}{(aC + b(1-C))} \tag{4.7}$$

where, a and b are coefficients, T is the temperature in °C, C is the glycerol concentration in mass in percentage, α is the weighting factor from 0 to 1.

Equations below describe the calculation of dynamic and kinematic viscosity of the water-glycerol mixture.

$$\mu_{\mathrm{w}} = 1.79 \times e^{((-1230-T)\times T/(36100+360\times T))} \tag{4.8}$$

$$\mu_{\mathrm{g}} = 12100 \times e^{((-1233+T)\times T/(9900+70\times T))} \tag{4.9}$$

$$\mu = \mu_w^{\alpha} \times \mu_g^{(1-\alpha)} \tag{4.10}$$

$$\nu = \frac{\mu}{\rho} \times 10^3 \tag{4.11}$$

where, μ_{w} is the dynamic viscosity of water in cP, μ_{g} is the dynamic viscosity of glycerol in cP, μ is the dynamic viscosity of the mixture in cP, ν is the kinematic viscosity in m^2/s.

Table 4.1: Comparison of viscosity values obtained from Ubbelohde viscometer and empirical formula.

Method	**Weight (%)**	**Temp(°C)**	**Density ($\mathbf{kg/m^3}$)**	**Absolute viscosity ($\mathbf{mm^2/s}$)**	**Dynamic viscosity (mPas)**
Ubbelohde viscometer	55.27	25	1159	5.344	6.195
Empirical formula	55.27	25	1144	5.818	6.6563

4.3 Investigation of flow at laminar and turbulent condition

4.3.1 Inlet flow conditions

The trials were conducted at two inlet flow conditions, laminar and turbulent, given by Re = 500 and Re = 2000. These were achieved by a flow rate of 59.17 ml/s and 236.7 ml/s, respectively. The flow rates are calculated from the continuity equation 4.12, for which the velocity value is obtained from Reynolds number equation (Chapter 3.1, equation 3.6).

$$Q = A \times v \tag{4.12}$$

where, Q is the flow rate in m^3/s, A is the area in m^2 and v is velocity in m/s.

4.3.2 MRI acquisition

All 2D PC-MRI trials were performed with a Ingenia 3T scanner (Philips Healthcare, Best, Netherlands) using a 108-channel flexible body coil. The system provides a maximum gradient strength of 45 mT/m with a maximum slew rate of 120 mT/m/ms. 3D quantitative flow with one-directional velocity encoding and cartesian readout was used to measure the through-plane velocity in the transverse slice (slice perpendicular to the flow) of the phantom. The frequency encoding direction was perpendicular to the flow to avoid displacement artifacts. The long axis of the phantom was placed parallel to the B_0 magnetic field with the throat of the stenosis (center of the stenosis) at the isocenter of the magnet by moving the patient table with the MRI built-in laser pointer.

Imaging parameters used for the scan were as given in table 4.2.

Venc = 70 cm/s and 250 cm/s for the flow rates 59.17 ml/s and 236.7 ml/s were used. The velocity encoding value was chosen 10-20% higher than the maximum velocity in the phantom to avoid aliasing [122]. The FOV in trial 1 was 100 x 100 x 220 mm and in trials 2-3 was 100 x 100 x 350 mm. It is to be noted that the model was rotated in trial 2-3 from its original position in trial 1. No local phase correction was chosen, as the phantom was surrounded only by air. Corrections for background phase errors and eddy currents were not performed.

Table 4.2: Imaging parameters used for the 2D PC-MRI experiment.

Scan mode	3D	**Scan technique**	Fast field echo
Contrast enhancement	T1	**Acquisition mode**	Cartesian
Fast imaging mode	Turbo field echo	**Gradient mode**	Enhanced
Flow compensated	Yes	**SMART**	Yes
Quantitative flow	Yes	**Local phase correction**	No
Flow direction	FH	**Voxel size**	$1 \times 1 \times 1$ mm^3
Number of averages	4	**TE**	6 ms
TR	10 ms	**Flip angle**	7°

4.3.3 Post-processing

The Phase Contrast (PC) series (magnitude, phase difference, and velocity images) acquired in the trials were saved in classic DICOM format. The 2D PC-MRI pixel values (stored values (SV)) represent normalized intensities, not velocity values. These SV are converted to velocity values using conversion parameters rescale intercept (RI), rescale slope (RS), and scale slope (SS) stored in the DICOM headers (Table 4.3). The conversion was performed as per equation 4.13 in MATLAB R2020b (MathWorks Inc., Natick, MA, USA) [123]. Before calculating the velocity value in each pixel, masking based on the magnitude image was done to remove calculation errors due to the variation in the area.

Table 4.3: Description of DICOM attributes and their corresponding tag numbers.

Attribute name	**Tag**
Rescale intercept	0028,1052
Rescale slope	0028,1053
Rescale type	0028,1054
Scale slope	Private 2005 100e

$$v = \frac{(SV * RS + RI)}{SS * RS} \tag{4.13}$$

After calculating the velocity values, a hexahedral mesh was generated from the image data. The calculated velocity value of each pixel was stored in each mesh element. This list of points and elements of the mesh with the velocity values was then converted into an unstructured grid in .vtu file format. The .vtu file was read in an open-source software of Paraview (Sadia National Laboratory, Kitware Inc., Los Alamos National Laboratory) for the visualization and analysis of the velocity values.

4.3.4 Numerical simulation

For validation, flow in the stenosis model at Re = 2000 was simulated with LES at Re 2000. LES is a turbulence model used in CFD. In LES, the large-scale motions of the large eddies of turbulent flow are computed directly, and only small-scale or sub-grid-scale motions are modeled. The LES simulation was performed in the fully independent open-source CFD solver OpenFOAM.

The axisymmetric flow model used in the simulation is the same as in the experiment. At the inlet, a parabolic velocity profile with turbulences of 5% turbulence intensity was imposed. A zero pressure boundary condition was specified at the outlet. The vessel walls are rigid, with no-slip boundary conditions for velocity. Blood is assumed to be Newtonian. A time-step of 0.5 ms was employed for simulations. Total simulation time was 15 s. The PIMPLE algorithm with default settings by OpenFOAMv1612 was used to solve the governing equations. A hexahedral mesh with a cell size of 0.5 mm and a refined cell size of 0.25 mm in the most constricted part was used, with 3 layers of wall refinement resulting in a grid of in total 7015716 elements was used.

4.3.5 Statistical analysis

Reliability is the extent to which measurements can be replicated [124]. To analyze the reliability of the PC-MRI measurements, the experiment at each boundary condition was performed in triplicate (the three experiments are named trial 1, trial 2 and trial 3 in the remainder of the work), on the same phantom, at identical conditions, by the same operator at different time points. The individual voxel velocity value of a trial was compared with the corresponding voxel velocity of the other two trials. This comparison was quantitatively evaluated using the intraclass

correlation coefficient (ICC), a measure of reliability that reflects both degrees of correlation and agreement between measurements. A 2-way mixed-effects model with the absolute agreement (95% confidence interval) was the most suited to calculate the ICC for the repeatability test [125]. ICC was calculated using IBM SPSS Statistics version 28 (IBM Corp., Armonk, NY, USA).

To assess the agreement between two quantitative methods of measurements such as LDA and 2D PC-MRI and 2D PC-MRI and LES, Bland-Altman chart and linear regression were used (both analyses done using MATLAB R2020b). A one-sample t-test is run on the difference of the method to evaluate the p-value. A p-value greater than 0.001, is a statistically non-significant result that would allow to continue with the Bland-Altman plot. In this thesis, a p-value of less than 0.001 (two-sided) was considered statistically significant. No adjustment of p-values was done for multiple testing.

The Bland-Altman chart is a scatter plot of the difference between the two measurements for each sample on the vertical axis, and the average of the two measurements on the horizontal axis [126]. Three horizontal reference lines are superimposed on the scatter plot: one line at the average difference between the measurements and two lines to mark the upper and lower control limits of plus and minus $1.96^{*}\sigma$, respectively, where σ is the standard deviation of the measurement differences. If the two methods are comparable or when the reference method can be replaced by the new method, then differences are minor, with the mean of the differences close to 0, showing no systematic variation with the mean of the two measurements. Also, the Bland-Altman plot helps identify any proportional bias that is present. A proportional bias is present when the difference of the two measurements increase or decrease as a function of the average of the methods. To further investigate this a linear regression analysis of the difference and average of the two methods and replotting the Bland-Altman plot with difference of the two methods in percentage is done [127] [128] [129].

Correlation is a statistical technique that can show whether and how strongly correlated pairs of variables are. Linear regression finds the best line that predicts one variable from another. It quantifies goodness of fit with R^2, the coefficient of determination. In MATLAB, an A component ANOVA (Analysis of variance) table from a linear regression model gives the coefficients necessary for the analysis.

4.4 Results and analysis

The measurements were performed in triplicate (named trial 1, trial 2 and trial 3) at two inlet conditions, Re 500 and Re 2000. These measurements are named as trial 1, trial 2 and trial 3. The acquired MR images were saved as classic DICOM images. These images were processed in MATLAB to get a 3D meshed model with velocity values. The analysis of the reliability using ICC in the SPSS software, velocity analysis in MATLAB and its visualization in Paraview is discussed in the following section. Further, to validate the velocities measured by the 2D PC-MRI technique, the obtained results were compared with the published LDA data by Ahmed and Giddens [120]. Additionally, at Re 2000, the published LDA and 2D PC-MRI data were compared with the LES data. Non-dimensional measures of velocity (normalized with inlet velocity) and length (normalized with an unoccluded diameter of the pipe) are used to plot the results. The flow characteristics were analyzed in specific locations, i.e., at -1d (inlet), 0d, 1d, 2.5d, 4d, 5d, and 6d, where d is the unoccluded diameter of the stenosis (Figure 4.3).

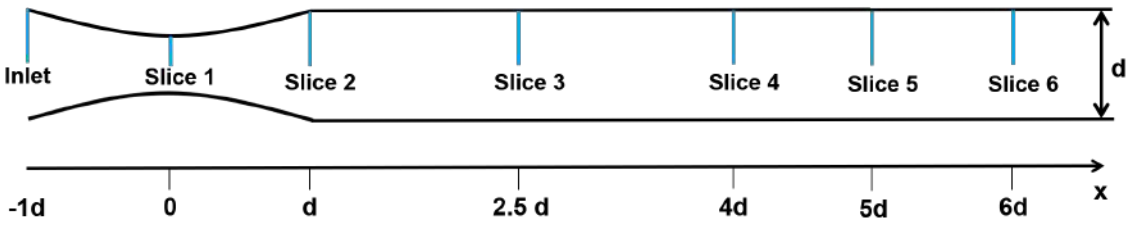

Figure 4.3: Position of the chosen slices in the stenosis model.

4.4.1 Reliability analysis

To demonstrate the reliability of the 2D PC-MRI technique, the velocity value at every voxel in a chosen slice at all three trials was statistically compared with each other using ICC. This comparison for Re 500 and Re 2000 is presented below in tables 4.4 and 4.5 respectively.

The reliability of velocity was characterized as excellent (ICC $>$ 0.80), good (ICC 0.60 - 0.79), moderate (ICC 0.40 - 0.59), fair (ICC 0.20 - 0.39), or poor (ICC $<$ 0.20) [130]. At both the inlet conditions the ICC values are above 0.930, indicating an excellent reliability. Also, 95% of all the samples have ICC values between 0.936 - 0.991 (the lower and upper bound).

Table 4.4: ICC with lower and upper bound (LB and UB) values at Re 500 for chosen slices.

Slice	ICC	LB	UB
Inlet	0.993	0.987	0.995
0d	0.979	0.943	0.947
1d	0.945	0.987	0.987
2.5d	0.987	0.994	0.994
4d	0.994	0.994	0.994
5d	0.944	0.963	0.965
6d	0.964	0.963	0.965

Table 4.5: ICC with lower and upper bound values (LB and UB) at Re 2000 for chosen slices.

Slice	ICC	LB	UB
Inlet	0.970	0.955	0.978
0d	0.983	0.981	0.984
1d	0.990	0.990	0.991
2.5d	0.965	0.964	0.966
4d	0.947	0.946	0.948
5d	0.939	0.936	0.942
6d	0.949	0.947	0.950

4.4.2 Flow investigation at Reynold's number 500 - 2D PC-MRI

The 3D model of the stenosis generated in MATLAB and visualized in Paraview is presented in the figure (Figure 4.4). Each mesh element has a velocity value (in m/s) calculated from MATLAB and is represented with the figure's color map. The colormap shows that the velocity at the stenosis is relatively higher than that in the pre- and post-stenotic region. It is to be noted that the velocities at the boundary should ideally be null. However, as the size of the voxel is big (1 x 1 x 1 mm), it represents the flow not only at the boundary but also the flow within.

Figure 4.5 and 4.6 depicts the velocity distribution and the velocity profile at the inlet of the stenosis across all the three trials.

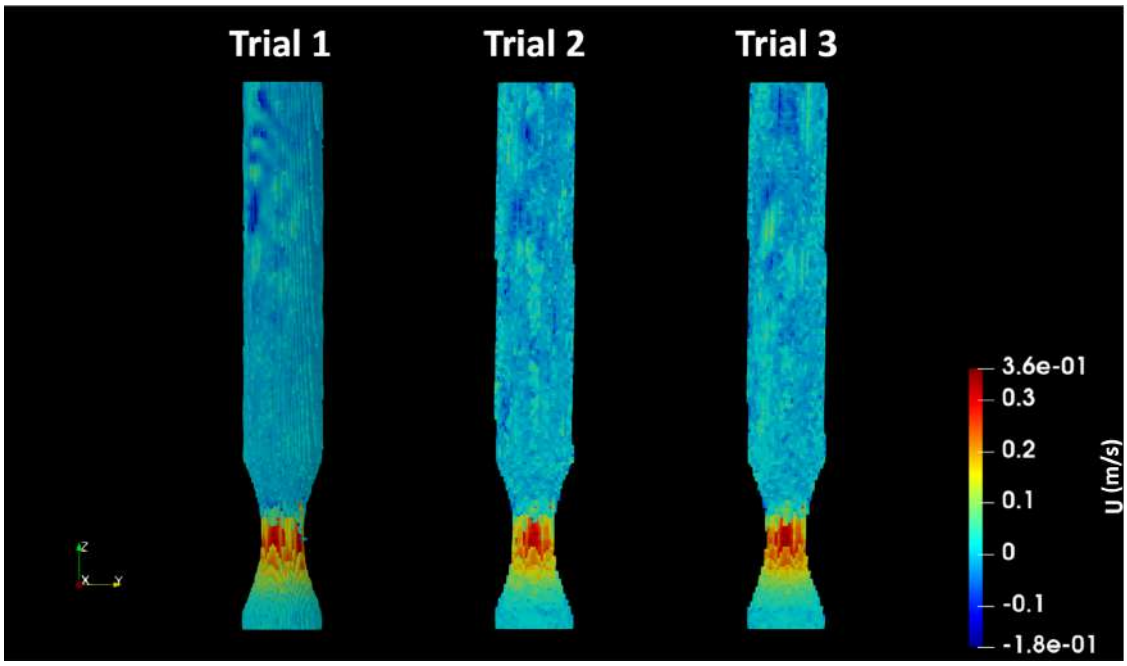

Figure 4.4: 3D model of the stenosis model at Re 500 obtained from the three trials as visualized in Paraview.

As explained in subsection 4.3.2, the model in trials 2 and 3 were rotated from the trial 1 position. Therefore, in the Paraview analysis, the trial 1 model was rotated to match the position of trials 2 and 3. Therefore a difference in the inlet slice images between trial 1 and trials 2 and 3 is observed. Additionally, the voxels at the boundary of inlet slices in all three trials are different. This is due to the presence of bubbles or loss of voxel data during thresholding.

As seen in figure 4.6, the velocity profile along the x-axis is parabolic, with the maximum velocity at the center indicating a laminar flow (since the stenosis model is axisymmetric, the velocity profile in x- and y- direction remain the same. Hence, velocity profile only along the x-axis is depicted). The average velocity at the inlet across all three trials was 0.106 m/s. As the flow at the inlet is fully developed and steady, velocity calculated theoretically from equation 4.12 is used to verify the 2D PC-MRI measured velocity value. The theoretical value of the velocity at the inlet is 0.112 m/s. Compared to the theoretical value, the measured average velocity value is lower by 5.7%. It is observed that with the same flow rate prescribed at the pump, the velocity at the inlet was slightly different in the three trials. Measured velocity closest theoretical value was obtained in trial 1: 0.111 m/s, 1.5% lower than theoretical. In trial 2: 0.101 m/s, the velocity was lower than the theoretical value

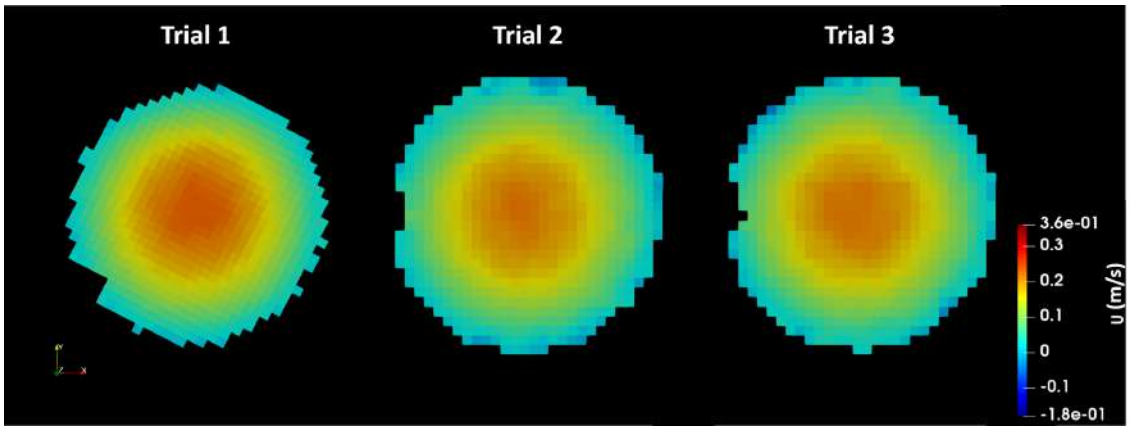

Figure 4.5: Velocity distribution in the inlet slice of the stenosis model at Re 500 at all three trials.

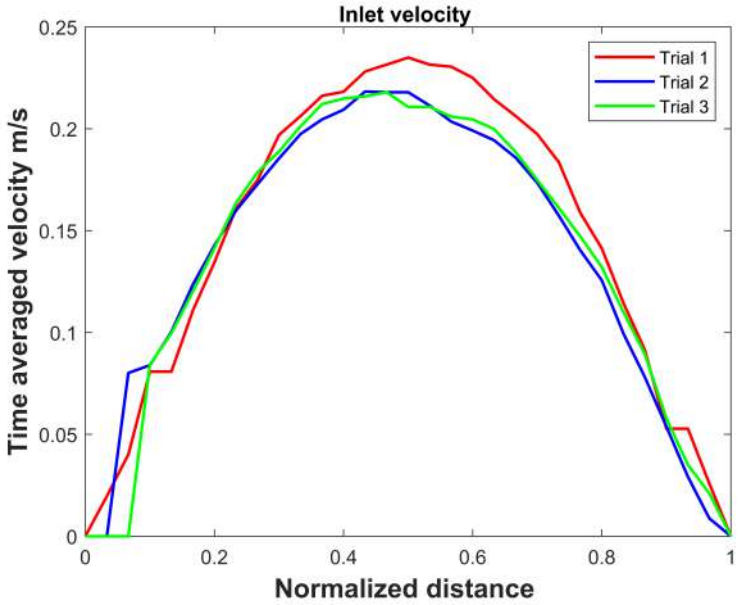

Figure 4.6: Plot of the inlet velocity profile at Re 500 obtained in all three trials.

by 9.2%, and in trial 3: 0.105 m/s it was lower by 6.2%.

Figure 4.7 shows the velocity map in the sagittal slice of the stenosis phantom in the y-z plane. At the inlet, the velocity profile is parabolic. The flow accelerates as it enters the stenosis and reaches a peak value at the throat, where the cross-sectional area is minimum. As the fluid leaves the stenosis, the area increases abruptly and causes flow separation. Flow separation is the condition where the actual flow detaches itself from the body of the stenosis to create a low-pressure area and causes a reversal of flow at the base of stenosis. The low-pressure area sucks the fluid back from the main flow, creating vortices (recirculation). The detached flow continues upstream in the form of a jet before reattaching to the main wall. Although the jet is axisymmetric, in the y-z plane, it is observed that around 5.5d shear layer on one side of the jet leans towards the pipe till 6d before dissipating into a uniform flow (Figure 4.8). In the x-z plane, the jet travels through the center of the phantom before dissipating into a uniform flow after 7d (Figure 4.9). The total length of the jet in the model is approximately 9d. Difference in the length of the trial 1 model and trials 2, 3 model is seen in figures 4.8 and 4.9. This is due to different FOV's for trial 1 and trials 2, 3. The centerline velocity profile was plotted from 0d to 6d (Figure 4.10). The plot shows a gradual decrease in the velocity from 0d to 6d.

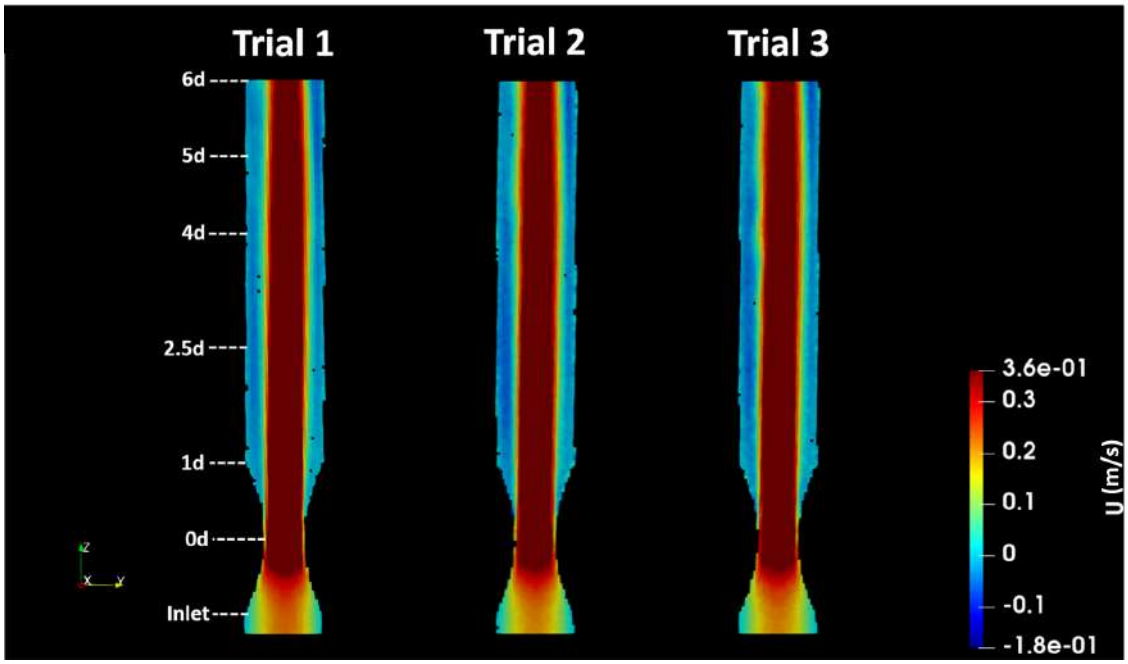

Figure 4.7: Velocity distribution showing flow separation in the sagittal slice (y-z view) of the stenosis model at Re 500 at all three trials.

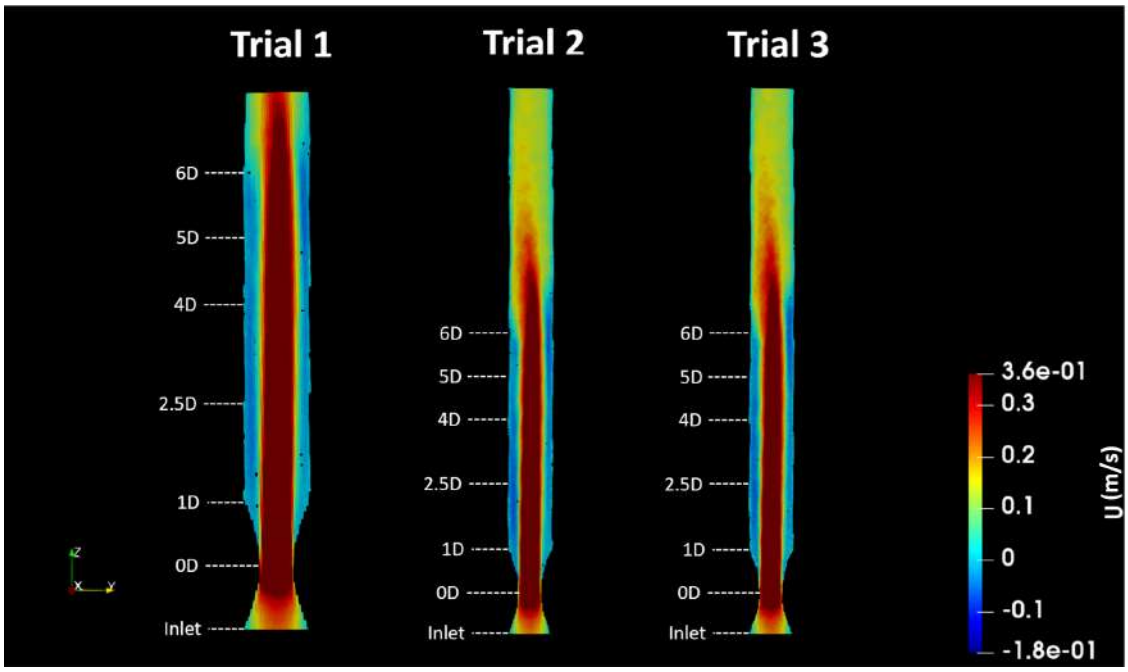

Figure 4.8: Affinity of the jet towards one side of the pipe at Re 500 observed in the sagittal slice (y-z view) of the stenosis model at all three trials.

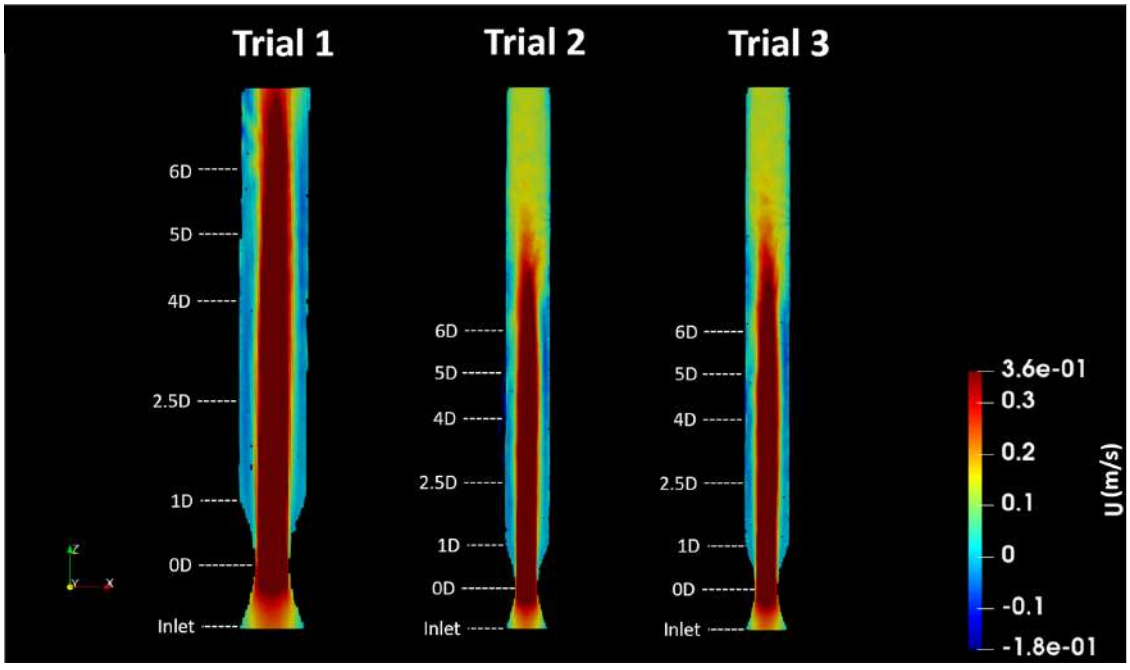

Figure 4.9: The sagittal slice (x-z view) shows the axisymmetric jet traversing through the model at Re 500 at all three trials.

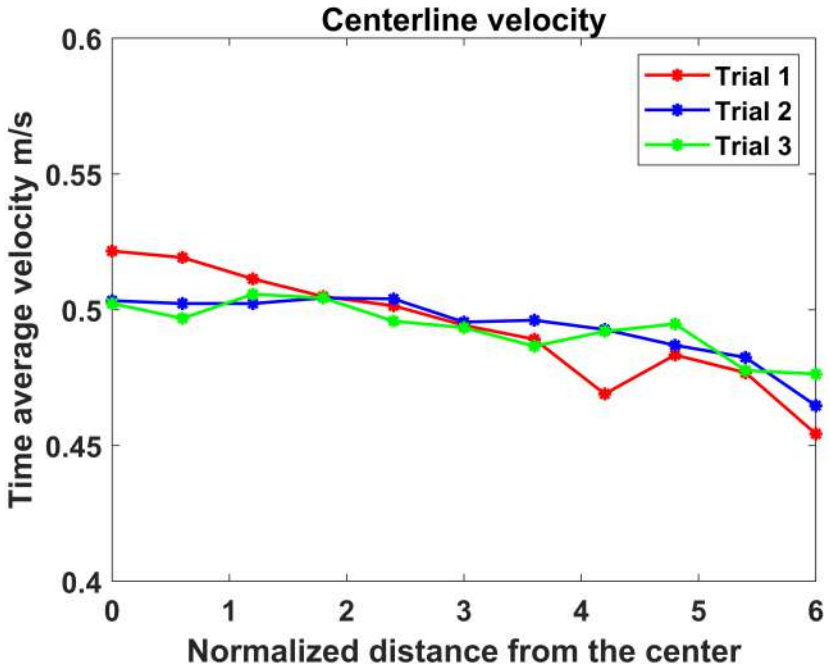

Figure 4.10: Centerline velocity profile of all three trials plotted from 0d to 6d of the stenosis model at Re 500.

At individual slices, the observations are as follows. At 0d (Figure 4.11), the velocity is at maximum, and, at the boundaries, the velocities are low due to frictional forces. In the 1d slice (Figure 4.12), the velocity at the center is high (jet), but around the jet, velocity is negative due to the recirculation of flow. At 2.5d and 4d (Figure 4.13 and 4.14), the same flow phenomenon seen at 1d follows, but the recirculation regions reduces. Also, the cross-sectional view of the jet is elliptical, unlike at 1d, where it is circular. At 5d (Figure 4.15), a part of the jet branches out in the southeast direction. Further at 6d (Figure 4.16), the jet branches into three main branches (southwest, southeast, and east direction). In some slices, some voxel data (particularly in the recirculation regions) are missing (represented by the black voxels) due to the artifacts in the phase image.

Average velocity at each of the chosen slices from three trials with standard deviation is given in the table 4.6.

The velocity at 0d exceeds the inlet velocity by a factor of 4. This agrees with the theoretical solution, i.e., the velocity is inversely proportional to the square of the diameter (Equation 4.12). Therefore, as the diameter at the stenosis's throat is half

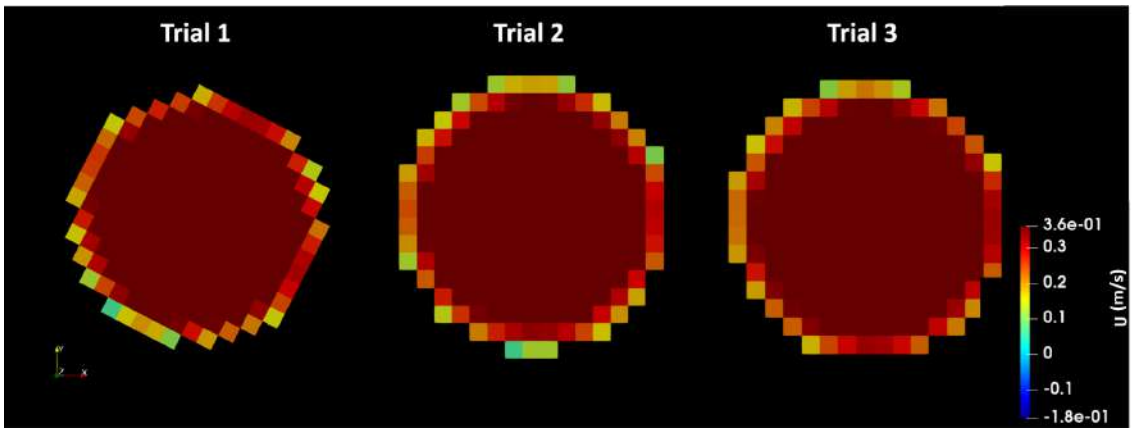

Figure 4.11: Velocity distribution at slice 0d in all three trials.

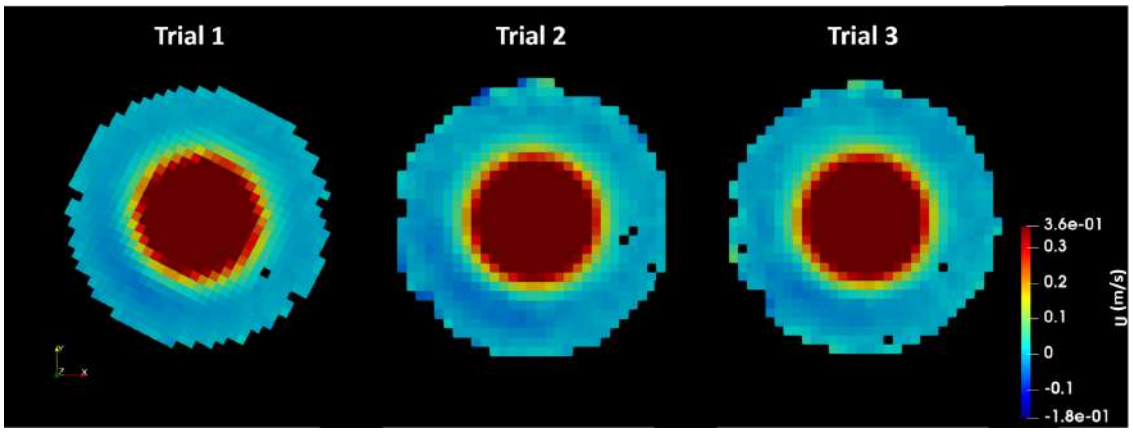

Figure 4.12: Velocity distribution at slice 1d in all three trials.

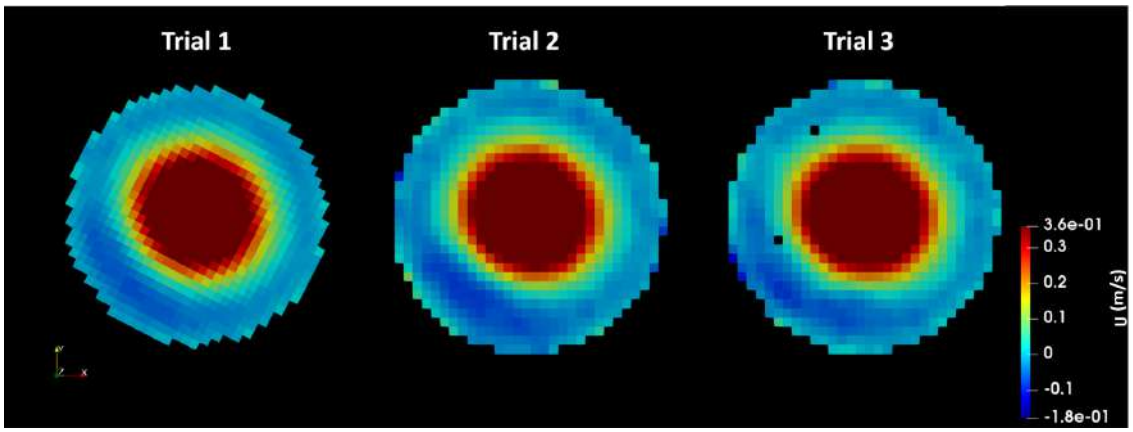

Figure 4.13: Velocity distribution at slice 2.5d in all three trials.

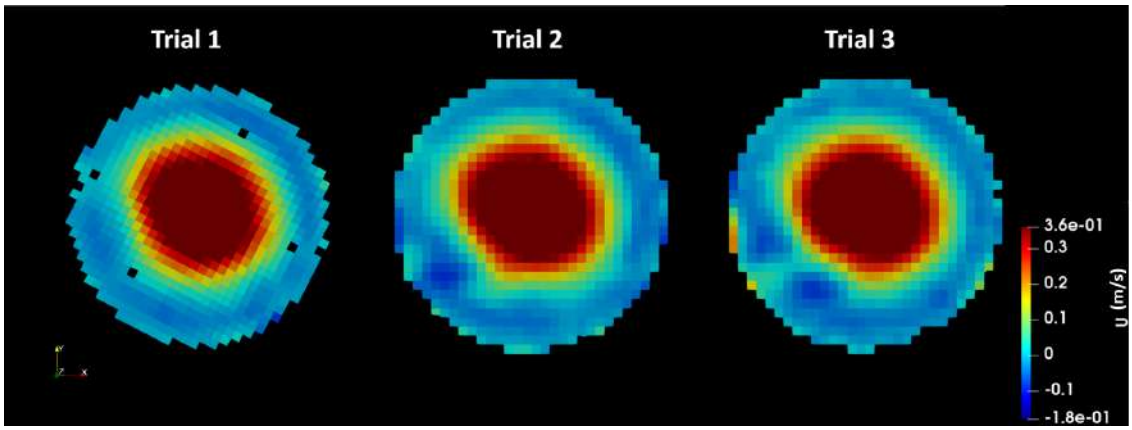

Figure 4.14: Velocity distribution at slice 4d in all three trials.

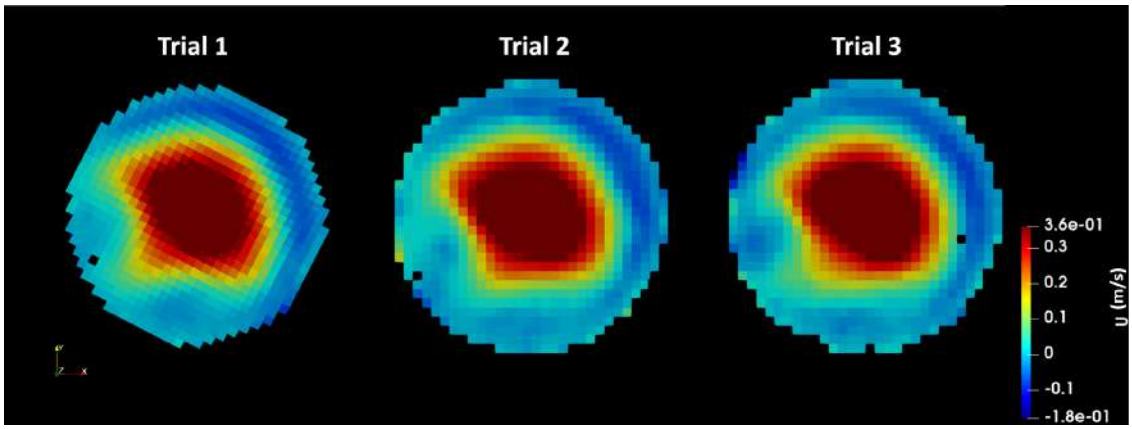

Figure 4.15: Velocity distribution at slice 5d in all three trials.

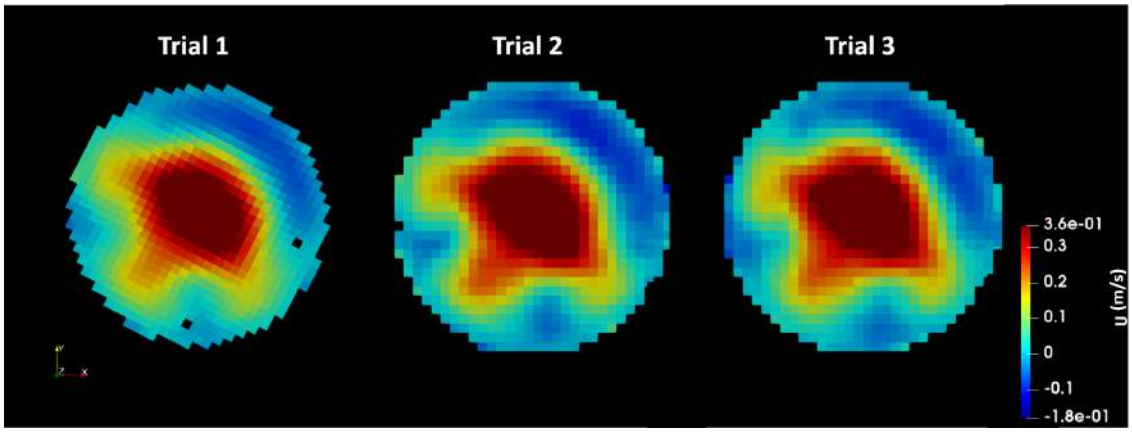

Figure 4.16: Velocity distribution at slice 6d in all three trials.

Table 4.6: Average velocity and standard deviation values measured at Re 500 by 2D PC-MRI in all three trials.

Slice number	**Trial 1, m/s**	**Trial 2, m/s**	**Trial 3, m/s**	**Average, m/s**	**Standard deviation**
0d	0.423	0.397	0.409	0.410	0.013
1d	0.105	0.104	0.108	0.106	0.002
2.5d	0.113	0.104	0.105	0.107	0.005
4d	0.116	0.088	0.891	0.098	0.016
5d	0.111	0.105	0.097	0.104	0.007
6d	0.110	0.111	0.111	0.111	0.000

the inlet diameter, the velocity is four times higher. Downstream to the stenosis, where the diameter of the pipe is the same as that at the inlet, the velocity values are again in the range of inlet velocity.

4.4.3 Comparison of PC-MRI and LDA data

In their paper [120], Ahmed and Giddens presented the plots of axial velocity profiles obtained from LDA at the chosen slice locations. This data is digitized by using GRABIT function that extracts data points from the image [131]. In the current work, the velocity profile data at the chosen slice location is extracted from Paraview and is plotted against the digitized LDA data from Ahmed and Giddens in MATLAB (Figure 4.17).

The velocity profile obtained in each chosen slice in 2D PC-MRI and LDA shows a good resemblance. At 0d, both LDA and PC-MRI have a plug-like velocity profile. However, the PC-MRI values are higher than LDA by 9% at the center. At 1d and 2.5d, the PC-MRI values are again higher than LDA values at the center of the slice, but the values show a good match in the recirculation region. At 4d, 5d, and 6d, values at the center are higher. However, around 3 mm from the center of the slice, the PC-MRI values become lower than that of LDA.

To further analyze the similarities and differences quantitatively. A one-sample t-test was performed on the difference of the methods and all the slices had a statistically non-significant p-value ($p>0.001$): making them eligible for a Bland-Altman analysis. Therefore, a linear regression on the two methods and a Bland-Altman plot with linear regression of the difference and the average of the two

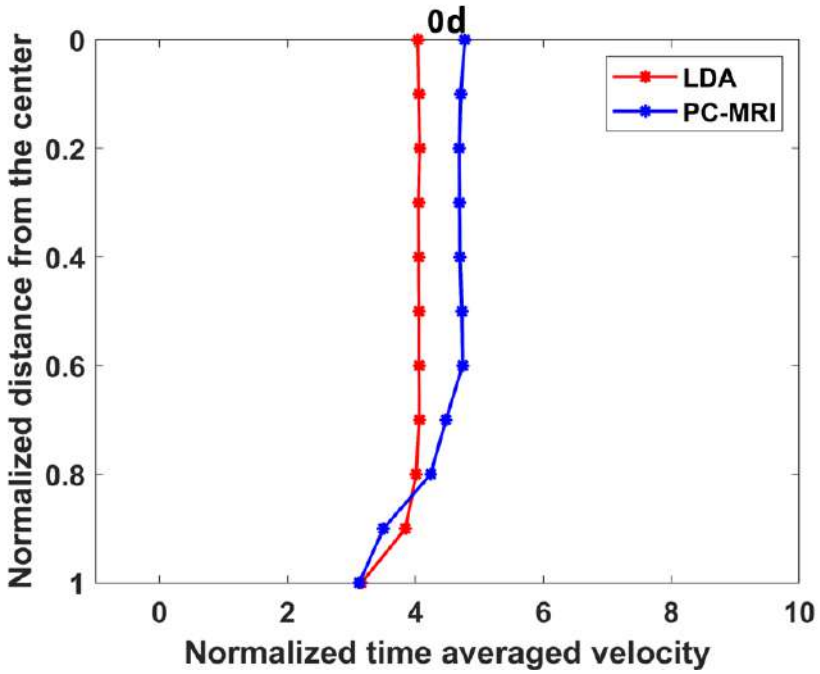
0d
LDA
PC-MRI
Normalized distance from the center
0
0.2
0.4
0.6
0.8
1
0
2
4
6
8
10
Normalized time averaged velocity

(a)

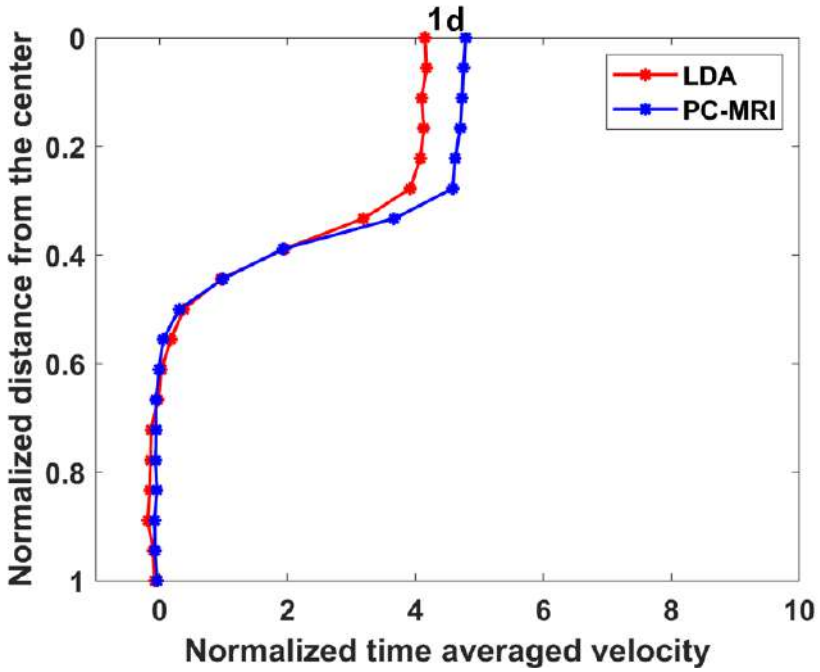
1d
LDA
PC-MRI
Normalized distance from the center
0
0.2
0.4
0.6
0.8
1
0
2
4
6
8
10
Normalized time averaged velocity

(b)

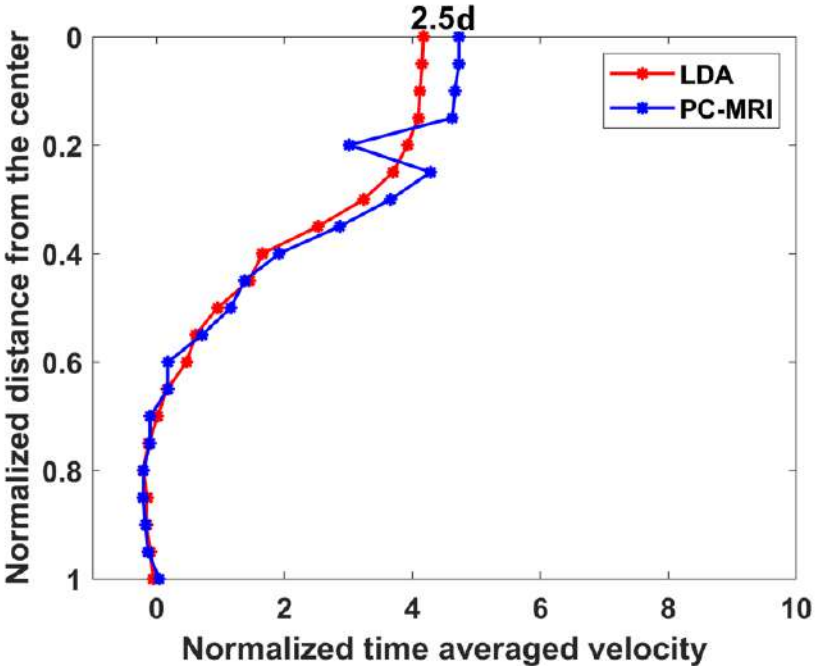
2.5d
LDA
PC-MRI
Normalized distance from the center
Normalized time averaged velocity
0
0.2
0.4
0.6
0.8
1
0
2
4
6
8
10

(c)

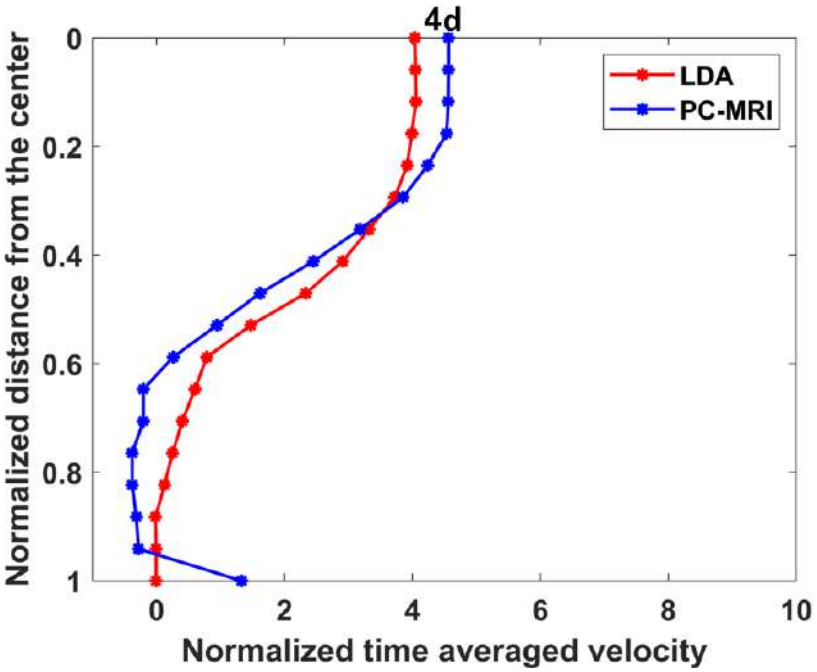
4d
LDA
PC-MRI
Normalized distance from the center
Normalized time averaged velocity
0
0.2
0.4
0.6
0.8
1
0
2
4
6
8
10

(d)

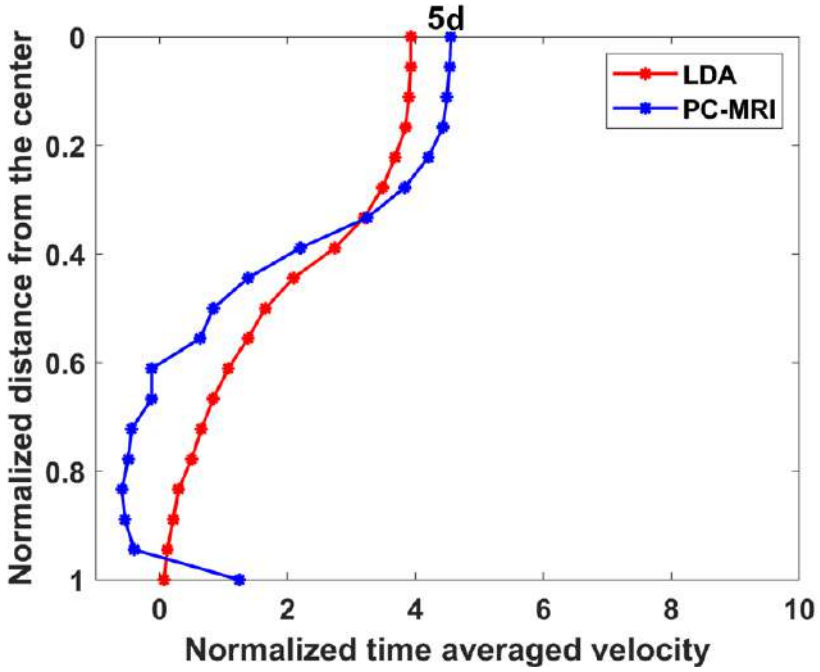

(e)

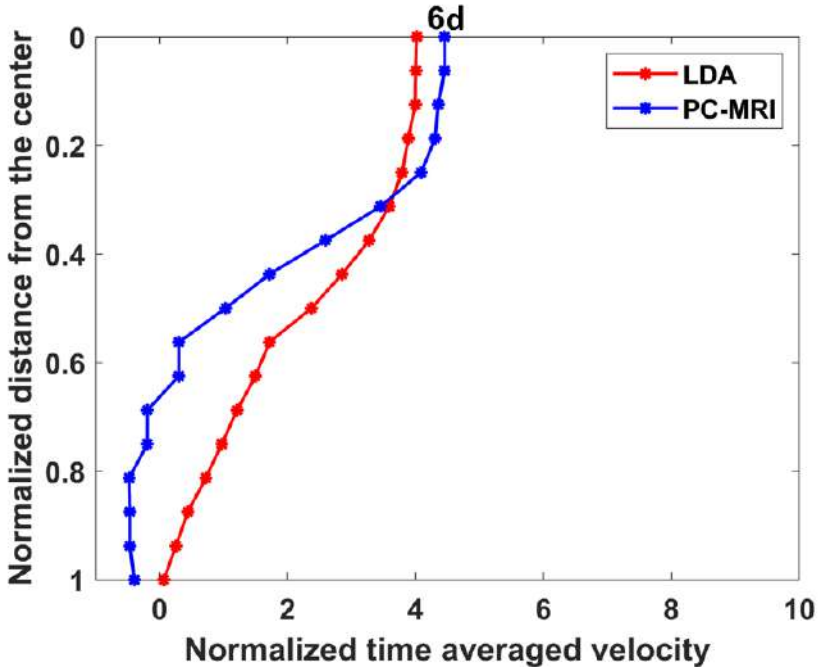

(f)

Figure 4.17: Figures a to f presents the axial velocity profile along the radius of the chosen slices at Re 500 obtained from 2D PC-MRI (average of the three trials) and LDA.

methods were done (Table 4.7 and Figure 4.18).

Table 4.7: Linear regression values from the comparison of 2D PC-MRI (average of the three trials) and LDA velocity values at Re 500.

Slice number	**Slope**	**Intercept, m/s**	**R^2**	**p-value**
0d	1.824	-2.808	0.767	<0.001
1d	1.140	0.002	0.998	<0.001
2.5d	1.092	-0.020	0.974	<0.001
4d	1.153	-0.395	0.934	<0.001
5d	1.311	-0.865	0.920	<0.001
6d	1.347	-1.370	0.940	<0.001

The slope of the regression line from slices 1d to 6d were all close to unity with R^2 values ranging from 0.920 - 0.998 with $P < 0.001$, confirming a good agreement between PC-MRI and LDA data. Only at 0d the correlation was low (slope: 1.82, R^2: 0.767) as the PC-MRI values were higher than the LDA values.

The Bland-Altman difference plot (Figure 4.18, slices od to 6d) shows good agreement with low bias. However, a downward trend is seen from slices 1d to 6d. That is a decrease in the difference of the measurement was found with increasing average value. Therefore, a linear regression was performed on the difference and the average of the measurement to detect any proportional bias present (Figure 4.18. The coefficient of determination (R^2) and p-value of the linear regression is given in the table below (Table 4.8).

For the slices 2.5d and 4d, a statistically non-significant (p>0.001) result implies no proportional bias. In slices 0d, 1d, 5d and 6d with a statistically significant result a proportional bias may have occurred and therefore for further analysis a percentage plot with linear regression is plotted (Figure 4.19). The percentage plot is calculated as the ratio of difference and average of the measurements multiplied by 100. The R^2 and p-value is calculated and presented in table below (Table 4.9). In this case, a statistically non-significant result shows that the earlier detected bias is just a linear bias. However, a statistically significant result indicates a non-linear source of errors are present. The slices under investigation 0d, 1d, 5d and 6d have a statistically non-significant result and therefore the earlier detected dependency of difference on the average of the measurement is a linear bias.

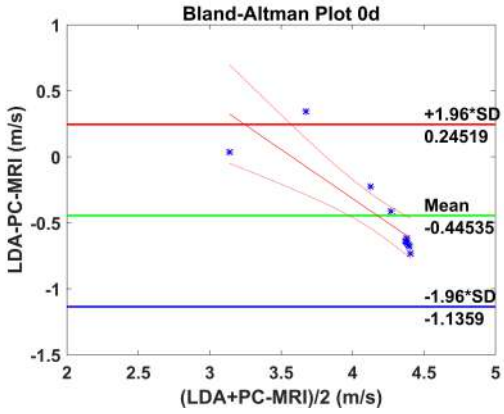
Bland-Altman Plot 0d
LDA-PC-MRI (m/s)
(LDA+PC-MRI)/2 (m/s)
+1.96*SD
0.24519
Mean
-0.44535
-1.96*SD
-1.1359

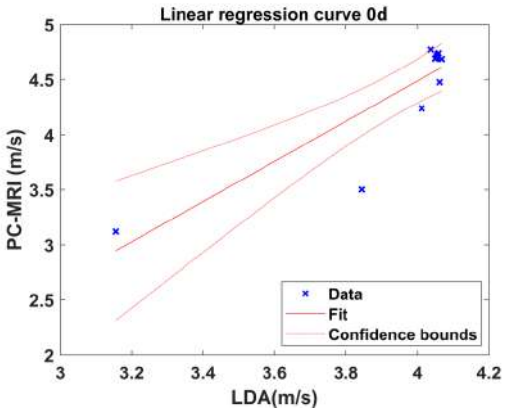
Linear regression curve 0d
PC-MRI (m/s)
LDA(m/s)
Data
Fit
Confidence bounds

(a)

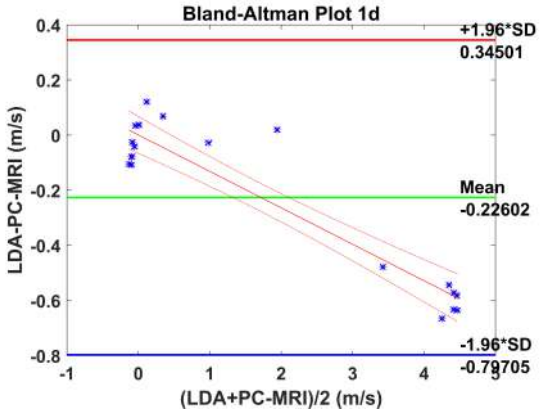
Bland-Altman Plot 1d
LDA-PC-MRI (m/s)
(LDA+PC-MRI)/2 (m/s)
+1.96*SD
0.34501
Mean
-0.22602
-1.96*SD
-0.79705

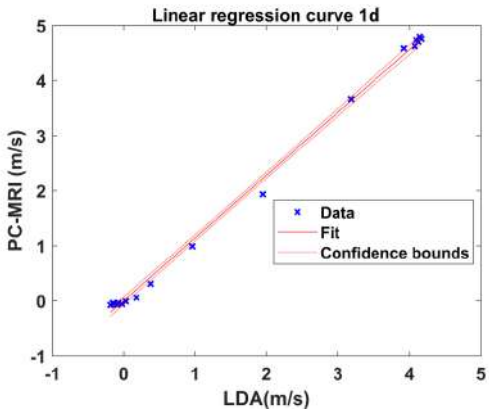
Linear regression curve 1d
PC-MRI (m/s)
LDA(m/s)
Data
Fit
Confidence bounds

(b)

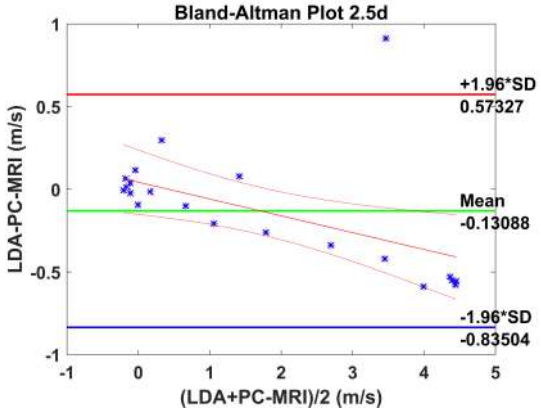
Bland-Altman Plot 2.5d
LDA-PC-MRI (m/s)
(LDA+PC-MRI)/2 (m/s)
+1.96*SD
0.57327
Mean
-0.13088
-1.96*SD
-0.83504

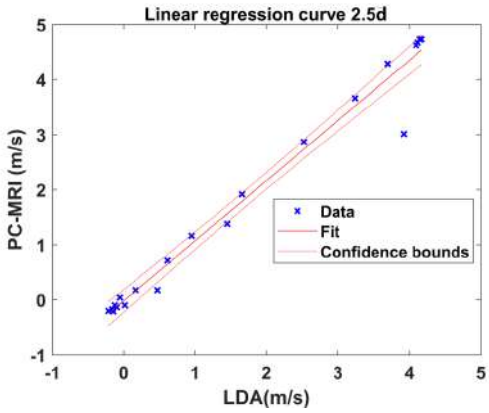
Linear regression curve 2.5d
PC-MRI (m/s)
LDA(m/s)
Data
Fit
Confidence bounds

(c)

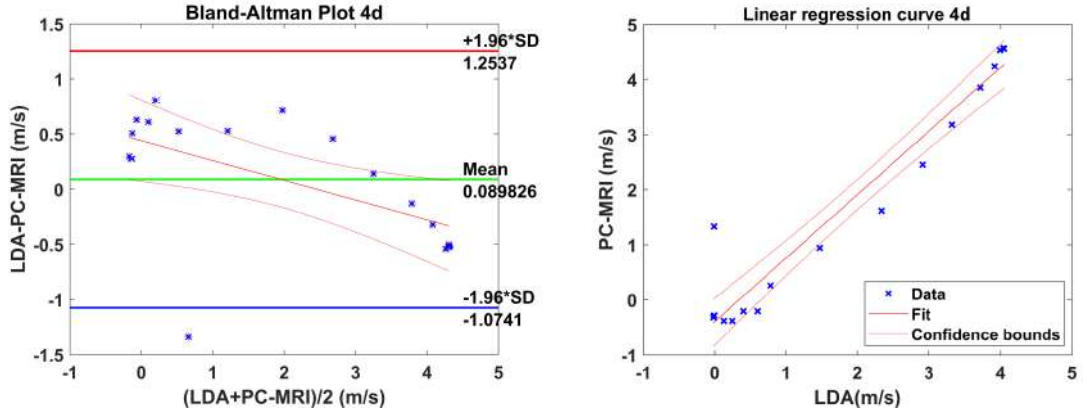

(d)

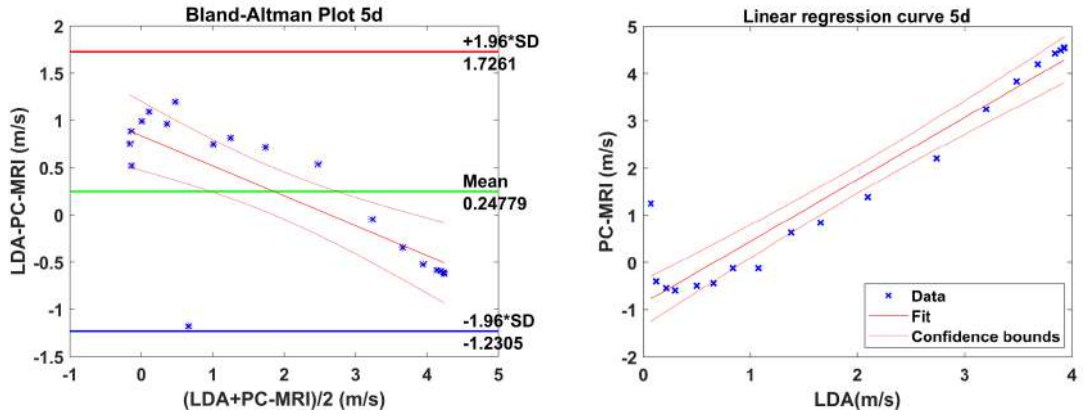

(e)

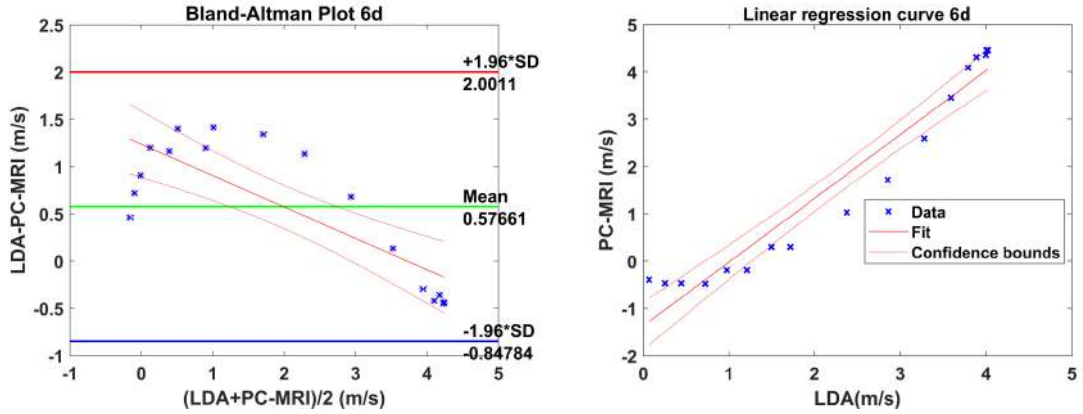

(f)

Figure 4.18: Figure a to f presents the Bland-Altman with linear regression plot and linear regression line of comparison of 2D PC-MRI (average of the three trials) and LDA velocity values at chosen slices at Re 500.

Table 4.8: Table of bias and linear regression values from the Bland-Altman comparison of 2D PC-MRI (average of the three trials) and LDA velocity values at Re 500.

Slice number	**Bias, m/s**	**R^2**	**p-value**
0d	-0.455	0.733	=0.001
1d	-0.226	0.877	<0.001
2.5d	-0.131	0.283	>0.001
4d	0.090	0.322	>0.001
5d	0.248	0.558	<0.001
6d	0.577	0.652	<0.001

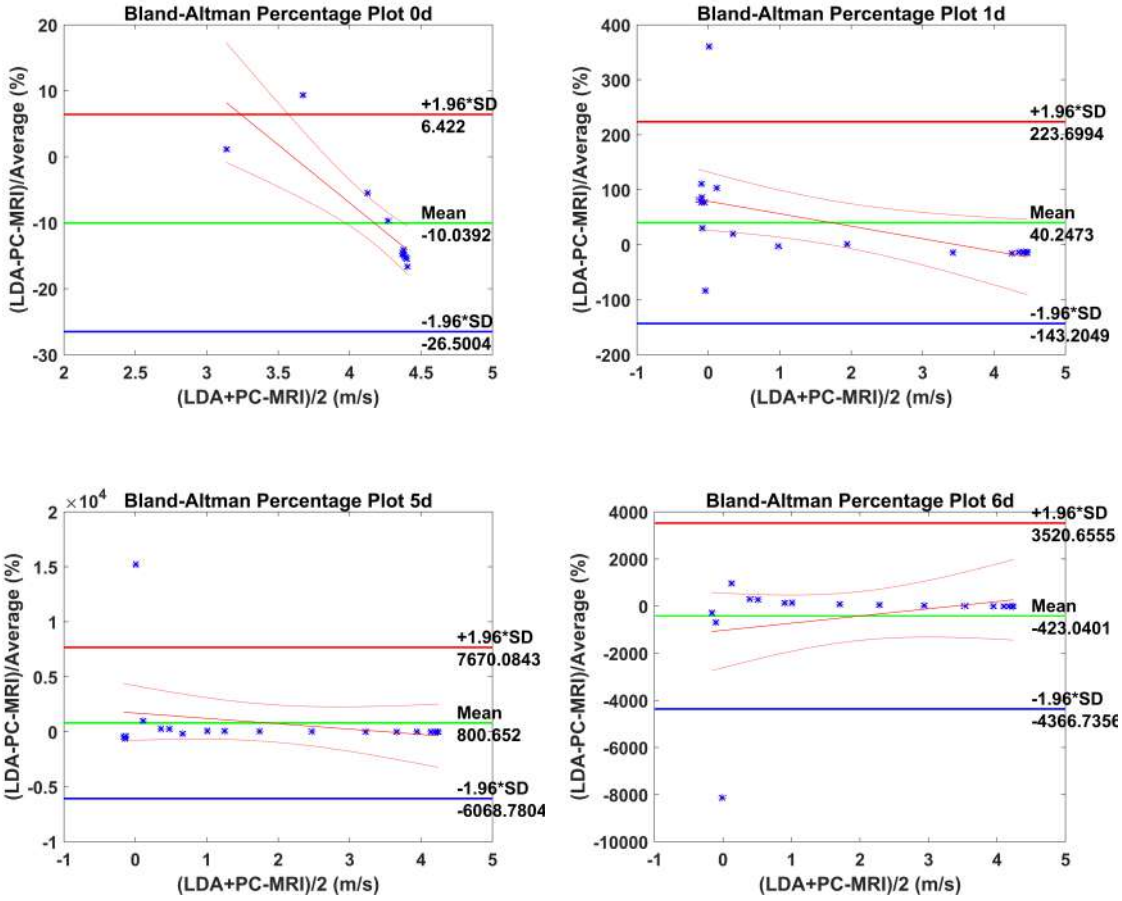

Figure 4.19: Bland-Altman percentage plot and linear regression line of comparison of 2D PC-MRI (average of the three trials) and LDA velocity values at chosen slices at Re 500.

Slice number	R^2	p-value
0d	0.725	=0.001
1d	0.251	>0.001
5d	0.066	>0.001
6d	0.072	>0.001

Table 4.9: Linear regression values from the Bland-Altman percentage comparison of 2D PC-MRI (average of the three trials) and LDA velocity values at Re 500.

4.4.4 Flow investigation at Reynolds number 2000 - 2D PC-MRI

The 3D volume of the stenosis in all three trials, as seen in Paraview, is given below (Figure 4.20). Figure 4.20 shows the 3D model surrounded by noise. However, these are removed during the analysis using thresholding. Similar to Re 500, the velocity is maximum at the center of the stenosis.

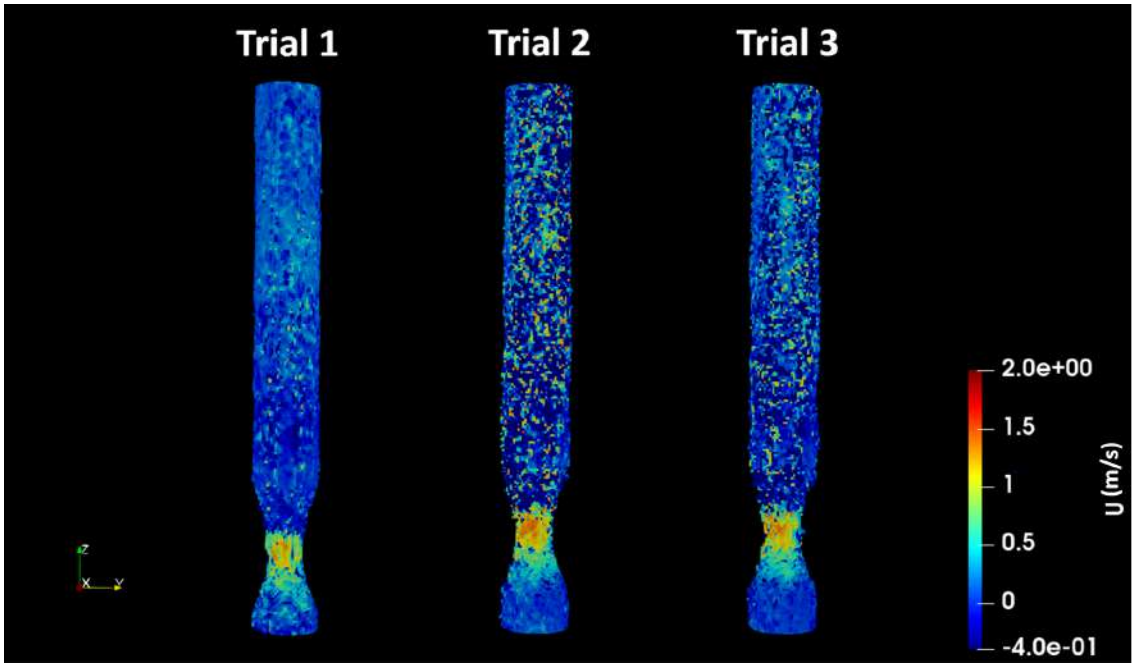

Figure 4.20: 3D model of the stenosis model at Re 2000 obtained from the three trials as visualized in Paraview.

Figure 4.21 shows the inlet slices at all three trials. The velocity profile along the

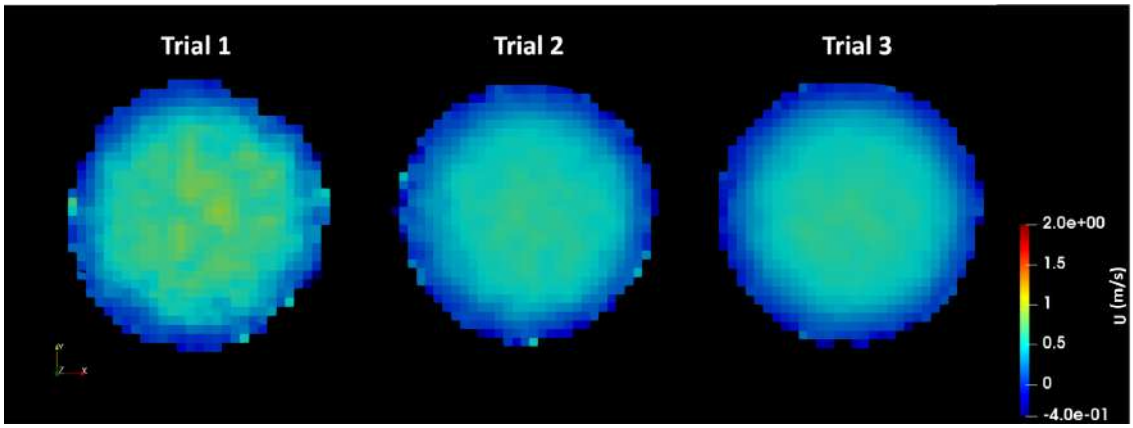

Figure 4.21: Velocity distribution in the inlet slice of the stenosis model at Re 2000 in all three trials.

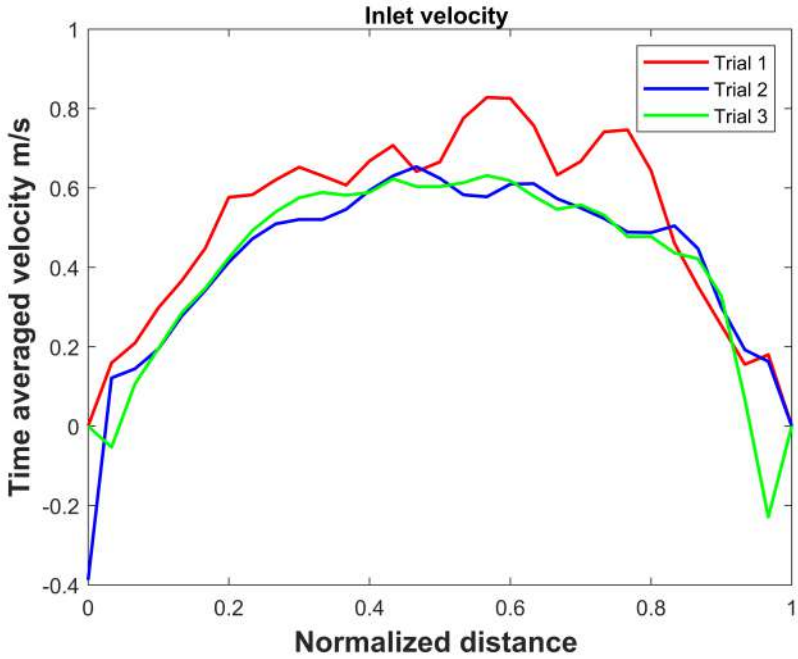

Figure 4.22: Plot of the inlet velocity profile at Re 2000 obtained in all three trials.

x-axis at the inlet in trials 2 and 3 is parabolic, however a slightly top-hat profile in trial 1, indicates a little turbulence (Figure 4.22). The measured average velocity of the inlet slice was 0.369 m/s, while the velocity value obtained from the theoretical calculation was 0.449 m/s (4.12). The measured average value at the inlet was lower by 18% as compared to the theoretical value. The velocity at trial 1 is in good agreement with the theoretical value and is only 5% lower. However, the velocities obtained in trials 2 and 3 were lower by 22.3% and 26.5% compared to the theoretical value.

The velocity distribution in the sagittal slice is shown in the figure 4.23. The flow profile at Re 2000 is similar to that observed at Re 500. The velocity as it enters the stenosis is developed, and as the area contracts at the throat of the stenosis, the fluid accelerates. Due to the sudden expansion of the area, a region of recirculation and a jet forms downstream to the throat. A distinct region of recirculation is observed till 2.4d in the figure. A short axisymmetric jet of length 3-4d is formed as opposed to the long jet formed at Re 500. Beyond this, the jet dissipates, and uniform flow resumes downstream. The centerline velocity profile is shown in the figure 4.24. Here, it is observed that the velocity holds steady up to 2d and then decreases steeply till 5d. After 5d the velocity is uniform till 6d.

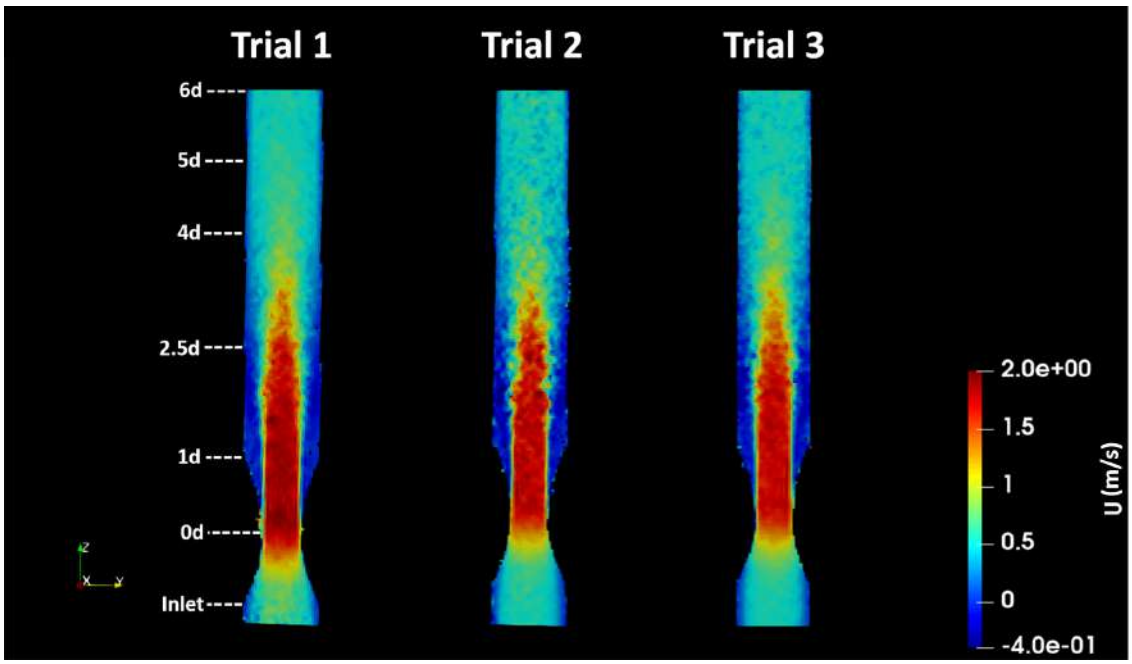

Figure 4.23: Velocity distribution showing flow separation in the sagittal slice (y-z view) of the stenosis model at Re 2000 in all three trials.

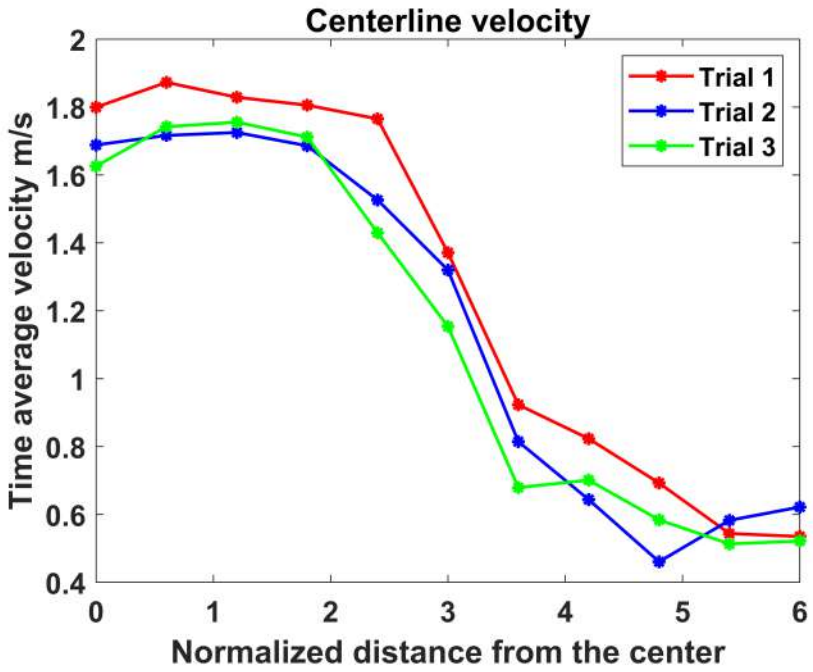

Figure 4.24: Centerline velocity profile of all three trials plotted from 0d to 6d of the stenosis model at Re 2000 for all three trials.

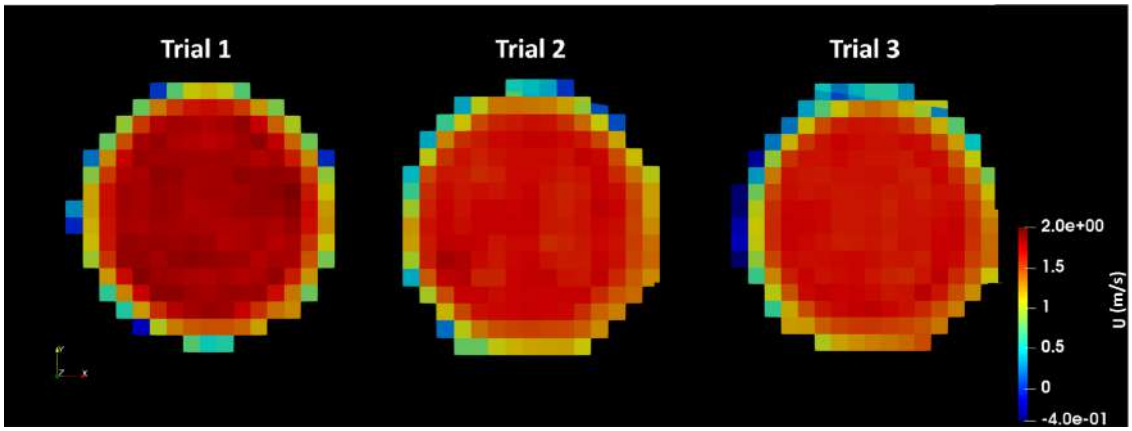

Figure 4.25: Velocity distribution at 0d in all three trials.

The velocity distribution in individual slices is presented in figures 4.25 to 4.30. The velocity value is maximum at slice 0d (Figure 4.25). At 1d (Figure 4.26), a reversal of flow around the jet is observed due to flow separation and the transversal view of the jet is circular. At 2.5d (Figure 4.27), the recirculation region remains, but the instability in the jet is seen.

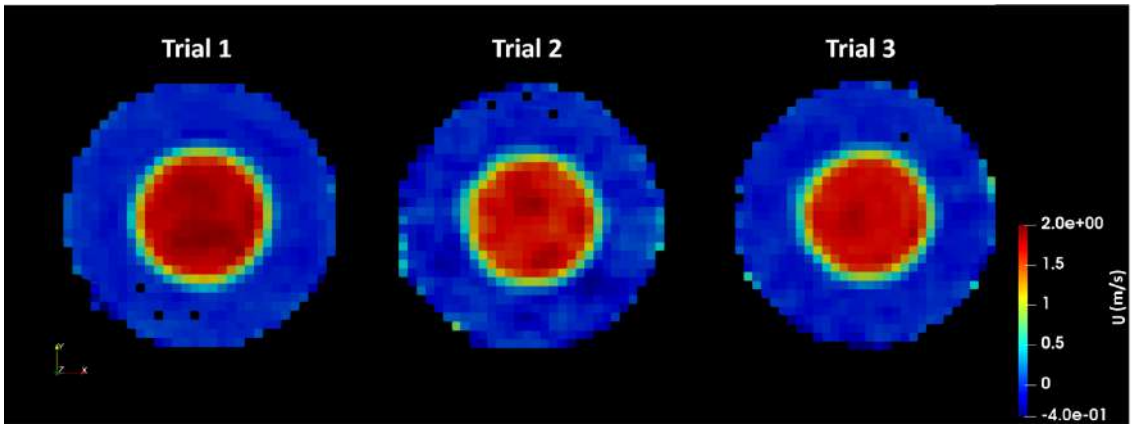

Figure 4.26: Velocity distribution at 1d in all three trials.

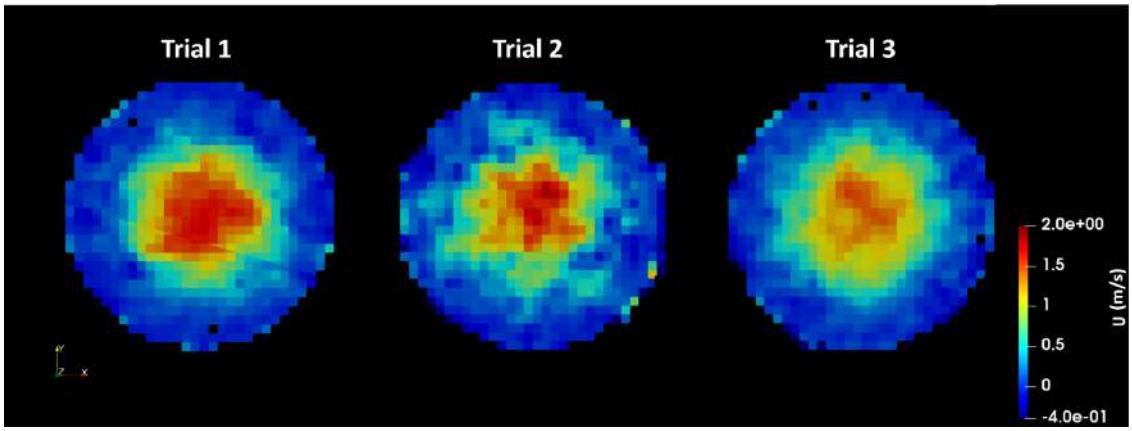

Figure 4.27: Velocity distribution at 2.5d in all three trials.

The velocity distribution at 4d, 5d and 6d (Figures 4.28, 4.29 and 4.30) is turbulent, but the flow separation here has ends. The table 4.10 presents the average velocities with standard deviation at chosen slices across all three trials. The velocity at the throat of the stenosis in all three trials is four times higher than their respective inlet velocity. In trial 1, the velocity in the post-stenotic region is in the same range as the inlet velocity. The values in trials 2 and 3 are slightly higher than inlet velocities.

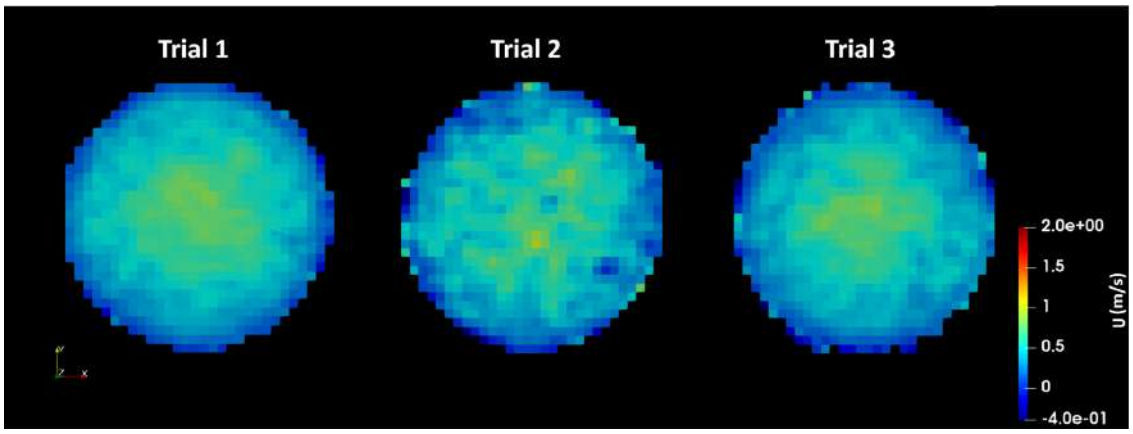

Figure 4.28: Velocity distribution at 4d in all three trials.

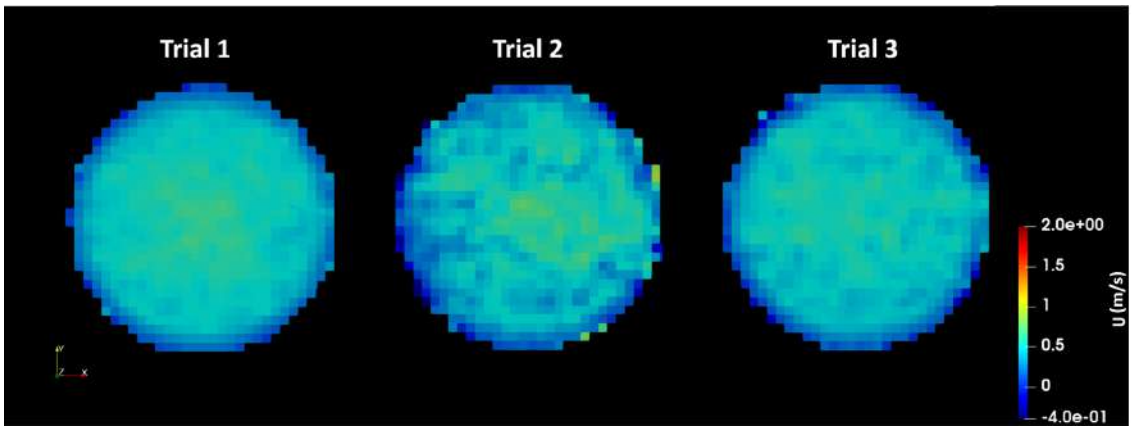

Figure 4.29: Velocity distribution at 5d in all three trials.

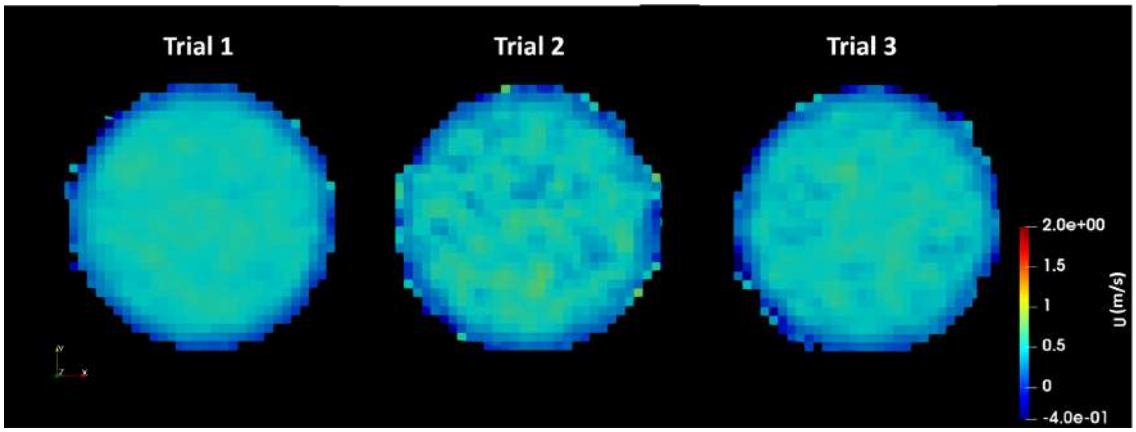

Figure 4.30: Velocity distribution at 6d in all three trials.

Table 4.10: Average velocity and standard deviation values measured at Re 2000 by 2D PC-MRI in all three trials.

Slice number	**Trial 1, m/s**	**Trial 2, m/s**	**Trial 3, m/s**	**Average, m/s**	**Standard deviation, m/s**
0d	1.538	1.394	1.350	1.427	0.098
1d	0.389	0.356	0.352	0.366	0.020
2.5d	0.415	0.372	0.377	0.388	0.023
4d	0.430	0.403	0.389	0.407	0.021
5d	0.440	0.398	0.407	0.415	0.022
6d	0.428	0.416	0.402	0.415	0.012

4.4.5 Comparison of 2D PC-MRI and LDA data

To validate the PC-MRI results at Re 2000, it is qualitatively and quantitatively compared with the classic stenotic flow experiment by Ahmed and Giddens [120]. Given below is the plot of the velocity profile of digitized LDA and PC-MRI data (Figure 4.31).

The velocity profile obtained from LDA and 2D PC-MRI shows a good correlation. At 0d, the plug-like velocity profile is evident in both modalities, but the PC-MRI measured value is higher by 15% compared to LDA measurements. At 1d, the velocity at the center of the slice is higher than LDA, but the values are in agreement at the recirculation region. At 2.5d, 4d, 5d, and 6d, the profile of both modalities match. However, slight variations in values are seen along the radius. A statistically non-significant result obtained from the one-sample t-test performed on the difference of the velocities measured by the two methods allows for the further quantitative analysis of the data using linear regression on the two methods and Bland-Altman and linear regression on the difference and average of the two methods (Table 4.11 and figure 4.32).

The slope of the linear regression line is close to unity at 1d and 2.5d with R^2 0.939 and 0.983, respectively, showing a good correlation of the values. At 4d, 5d, and 6d, where flow is turbulent, the slopes were not close to unity and had R^2 values ranging from 0.955, 0.827, and 0.899, respectively.

The Bland-Altman plot shows a good agreement with low bias. In comparison to the Bland-Altman analysis in the laminar flow condition (Figure 4.18), there were more

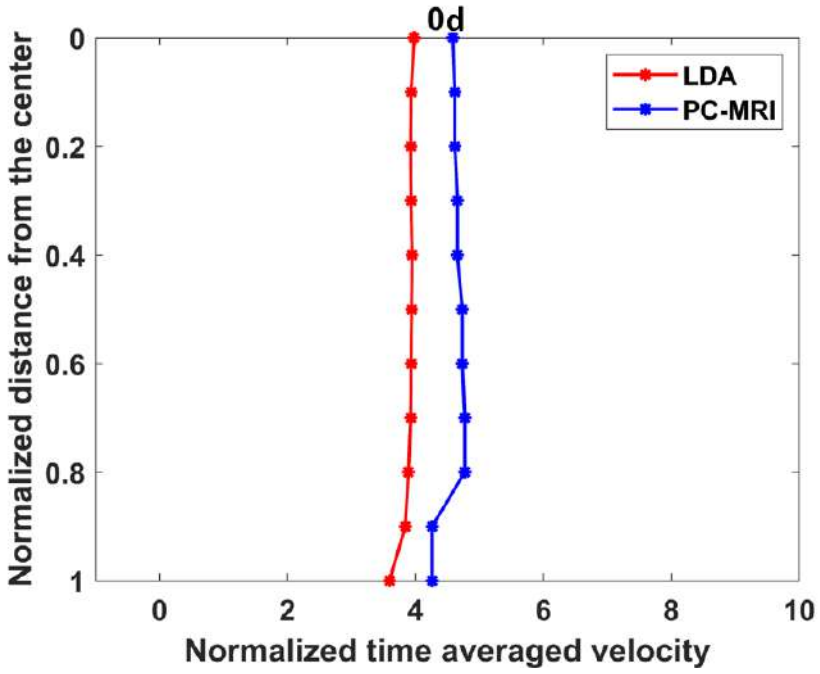
0d
LDA
PC-MRI
Normalized distance from the center
0
0.2
0.4
0.6
0.8
1
0
2
4
6
8
10
Normalized time averaged velocity

(a)

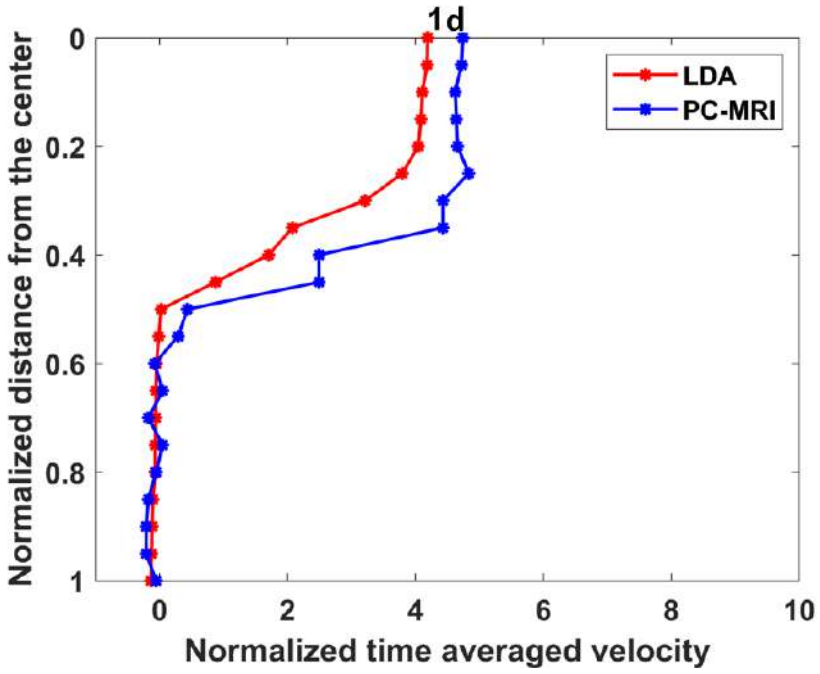
1d
LDA
PC-MRI
Normalized distance from the center
0
0.2
0.4
0.6
0.8
1
0
2
4
6
8
10
Normalized time averaged velocity

(b)

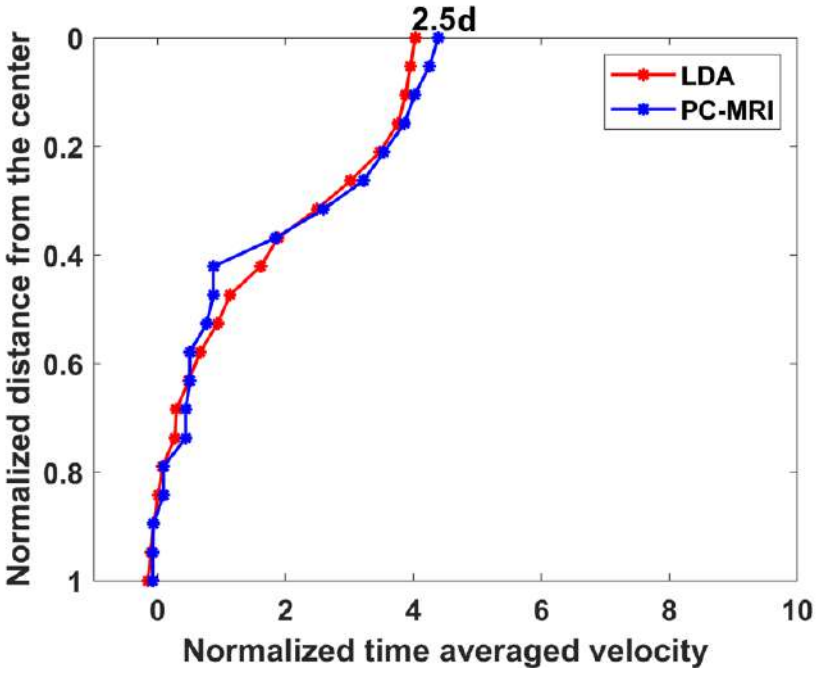
2.5d
LDA
PC-MRI
Normalized distance from the center
Normalized time averaged velocity
0
0.2
0.4
0.6
0.8
1
0
2
4
6
8
10

(c)

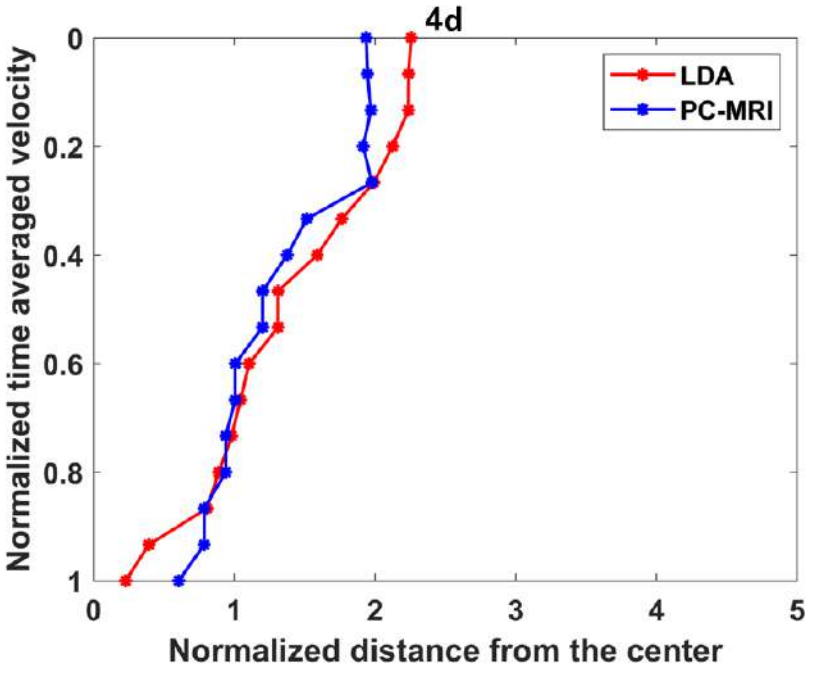
4d
LDA
PC-MRI
Normalized time averaged velocity
Normalized distance from the center
0
0.2
0.4
0.6
0.8
1
0
1
2
3
4
5

(d)

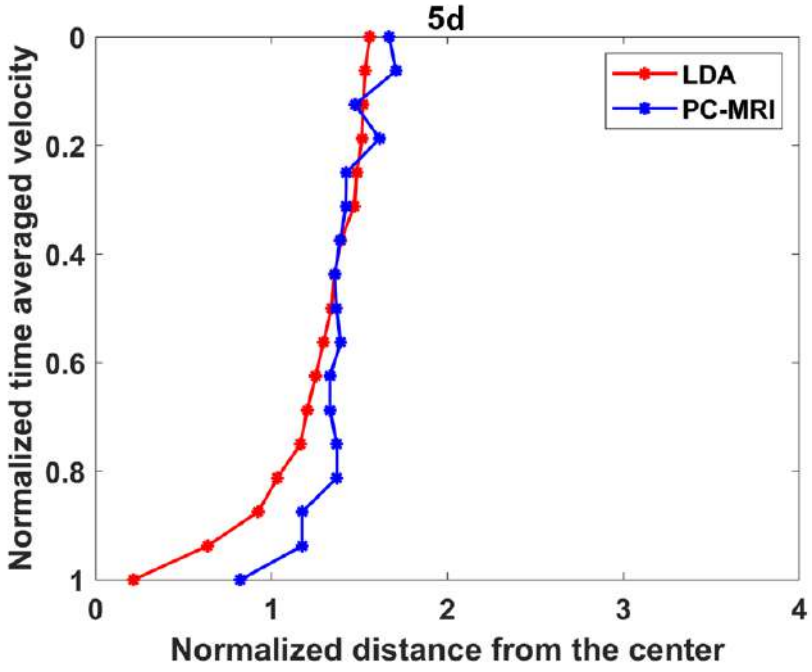

(e)

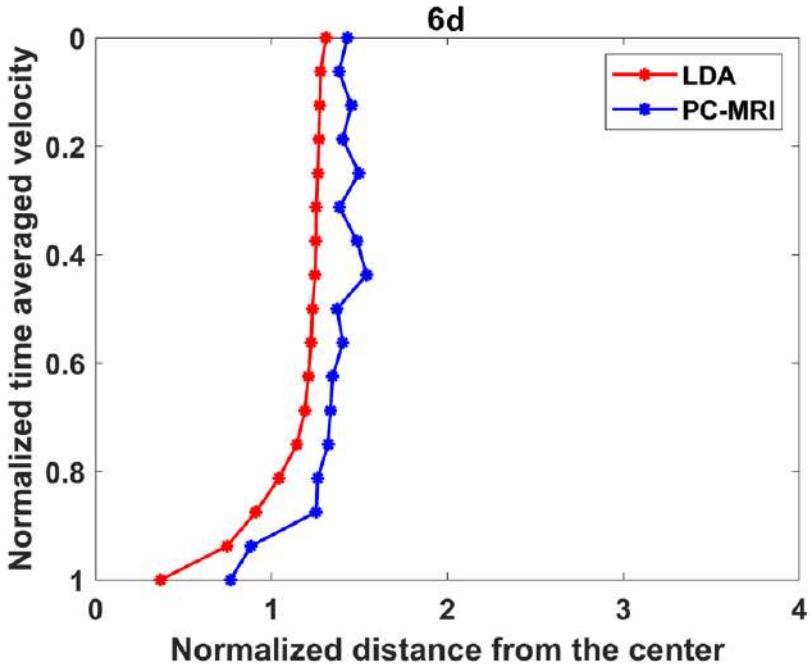

(f)

Figure 4.31: Figures a to f presents the axial velocity profile along the radius of the chosen slice at Re 2000 obtained from 2D PC-MRI (average of the three trials) and LDA.

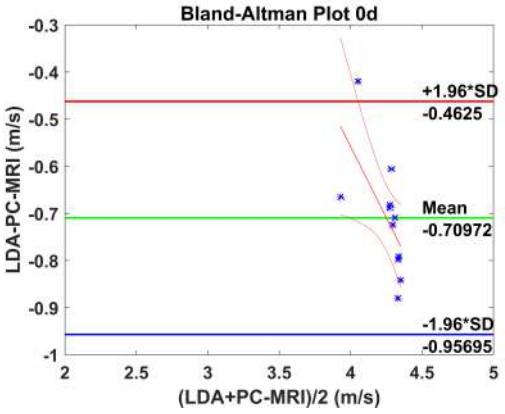
Bland-Altman Plot 0d
+1.96*SD
-0.4625
Mean
-0.70972
-1.96*SD
-0.95695
LDA-PC-MRI (m/s)
(LDA+PC-MRI)/2 (m/s)

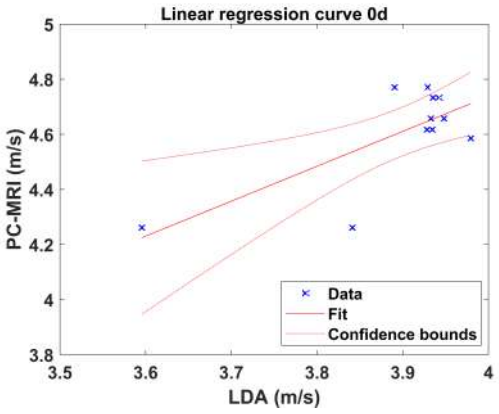
Linear regression curve 0d
Data
Fit
Confidence bounds
PC-MRI (m/s)
LDA (m/s)

(a)

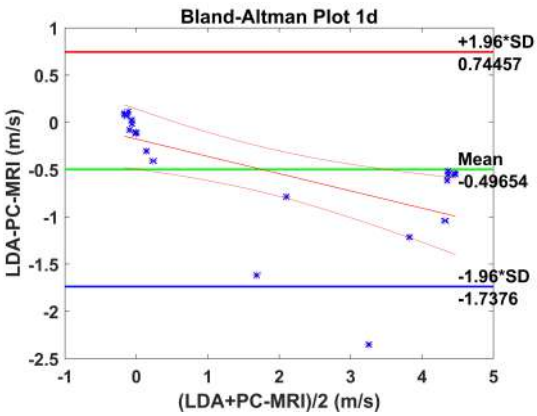
Bland-Altman Plot 1d
+1.96*SD
0.74457
Mean
-0.49654
-1.96*SD
-1.7376
LDA-PC-MRI (m/s)
(LDA+PC-MRI)/2 (m/s)

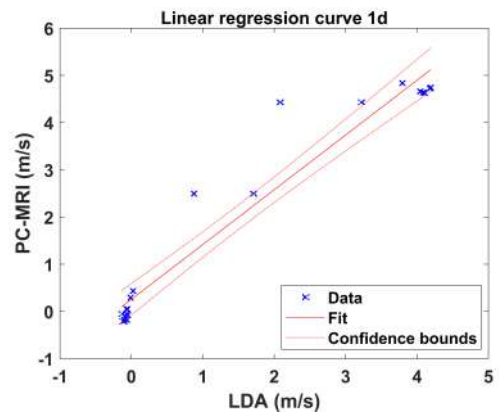
Linear regression curve 1d
Data
Fit
Confidence bounds
PC-MRI (m/s)
LDA (m/s)

(b)

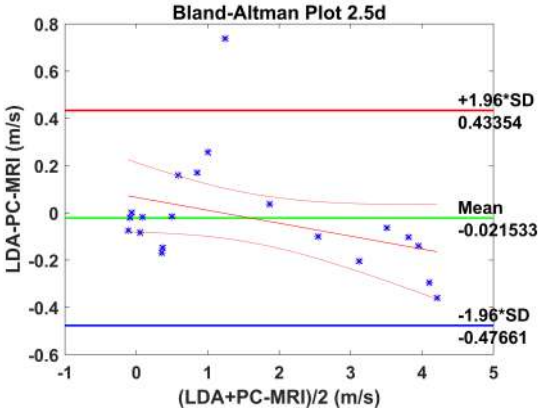
Bland-Altman Plot 2.5d
+1.96*SD
0.43354
Mean
-0.021533
-1.96*SD
-0.47661
LDA-PC-MRI (m/s)
(LDA+PC-MRI)/2 (m/s)

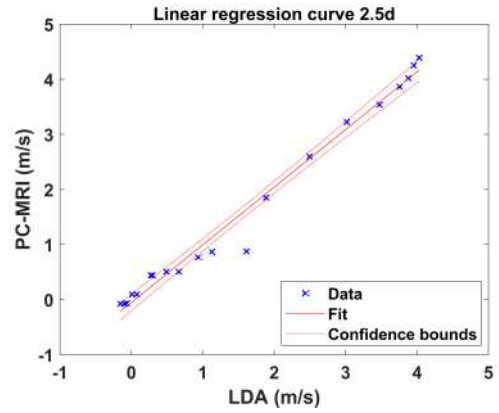
Linear regression curve 2.5d
Data
Fit
Confidence bounds
PC-MRI (m/s)
LDA (m/s)

(c)

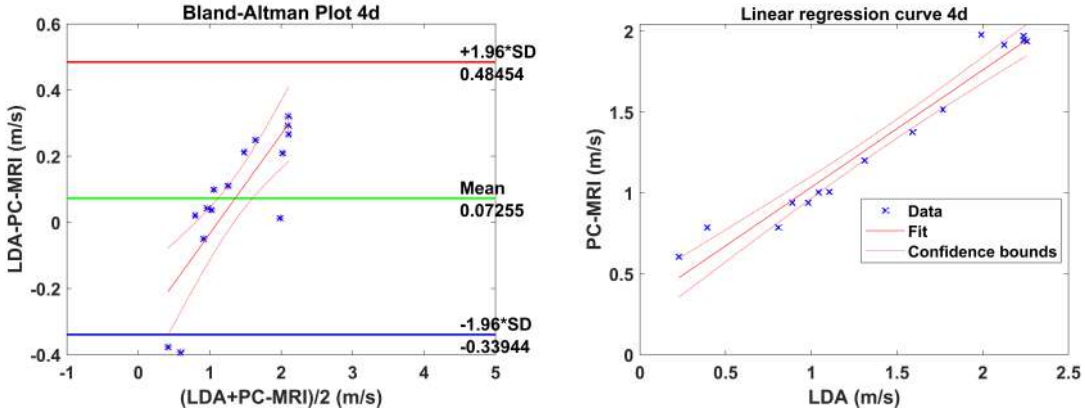

(d)

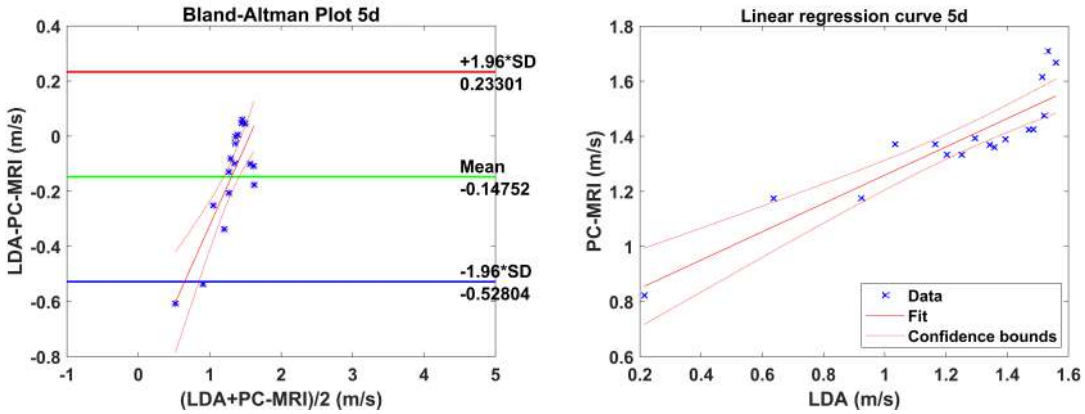

(e)

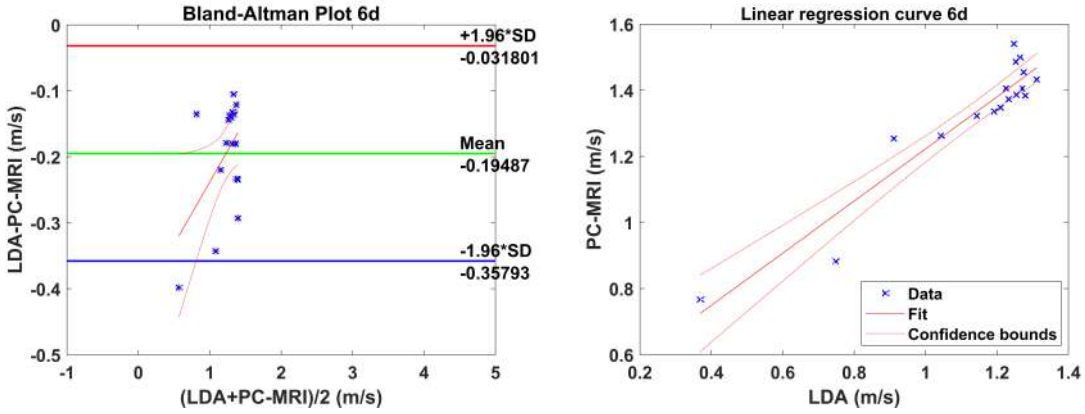

(f)

Figure 4.32: Figures a to f presents the Bland-Altman plot with linear regression plot and linear regression line of comparison of 2D PC-MRI (average of the three trials) and LDA velocity values at chosen slices at Re 2000.

Table 4.11: Linear regression values from the comparison of 2D PC-MRI (average of the three trials) and LDA velocity values at Re 2000.

Slice number	**Slope**	**Intercept (m/s)**	**R^2**	**p-value**
0d	1.268	-0.334	0.543	<0.001
1d	1.160	0.255	0.939	<0.001
2.5d	1.047	-0.053	0.983	<0.001
4d	0.725	0.311	0.955	<0.001
5d	0.514	0.745	0.827	<0.001
6d	0.788	0.434	0.899	<0.001

outliers in the turbulent flow condition (Figure 4.32). Although no definite trend was visually observed in the Bland-Altman plot, a linear regression analysis was done for the difference and the average of the values. Table 4.12 gives the R^2 and p-value. This shows that 4d and 5d might have a proportional bias as indicated by the statistically significant p-value ($p<0.001$). Therefore, a Bland-Altman percentage plot with linear regression is plotted for slice 4d and 5d (Figure 4.33).

Table 4.12: Bias and linear regression values from the Bland-Altman comparison of 2D PC-MRI (average of the three trials) and LDA velocity values at Re 2000.

Slice number	**Bias, m/s**	**R^2**	**p-value**
0d	-0.710	0.415	>0.001
1d	-0.496	0.349	>0.001
2.5d	-0.021	0.146	>0.001
4d	0.072	0.671	<0.001
5d	-0.147	0.678	<0.001
6d	-0.195	0.256	>0.001

The linear regression resulting from the percentage plot (Figure 4.33) is given in table 4.13. The p-value >0.001 eliminates the possibility of the proportional bias in the measurements.

At the centerline (Figure 4.34), the velocity profile of both modalities match. As observed before, the PC-MRI velocity values from constriction to 2.5d are higher than LDA data. Downstream to 2.5d, where the flow separation stops, the variation

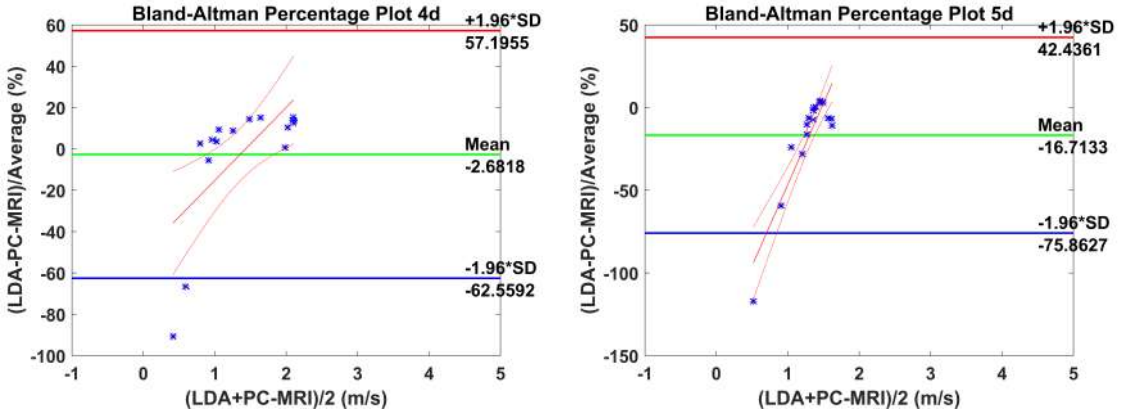

Figure 4.33: Bland-Altman percentage plot and linear regression line of comparison of 2D PC-MRI (average of the three trials) and LDA velocity values at chosen slices at Re 2000.

Table 4.13: Linear regression values from the Bland-Altman percentage comparison of 2D PC-MRI (average of the three trials) and LDA velocity values at Re 2000.

Slice number	**R^2**	**p-value**
4d	0.439	>0.001
5d	0.807	<0.001

Table 4.14: Bland-Altman and linear regression values from the comparison of 2D PC-MRI and LDA centerline velocity values at Re 2000.

Method	**Slope**	**Intercept (m/s)**	**R^2**	**p-value**
PC-MRI - LDA	-0.265	0.950	<0.001	-0.235

Table 4.15: Linear regression values from the Bland-Altman percentage comparison of 2D PC-MRI (average of the three trials) and LDA velocity values at Re 2000.

-	**Bias (m/s)**	**R^2**	**p-value**
BA	1.173	0.411	>0.001

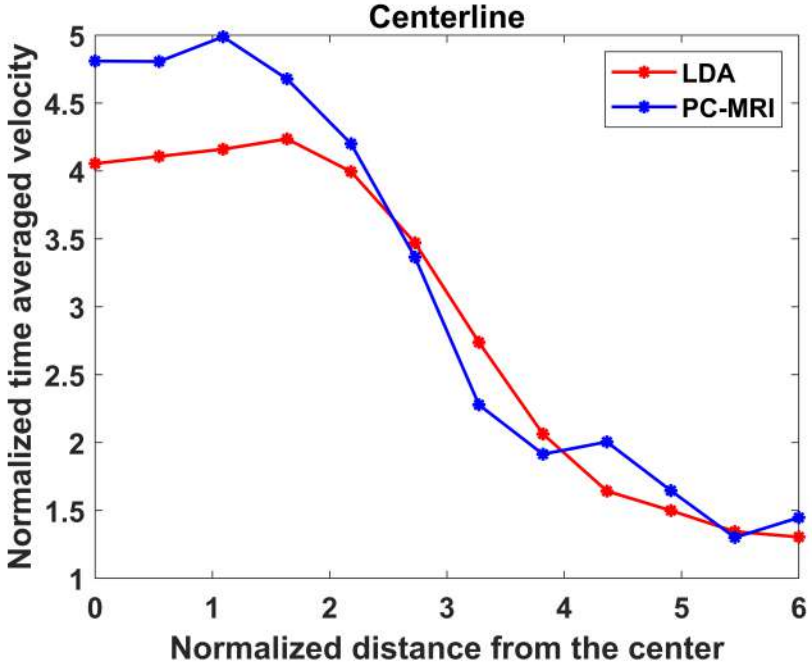

Figure 4.34: Comparison of velocity profiles from 0d to 6d at centerline measured with 2D PC-MRI (average of the three trials) and LDA.

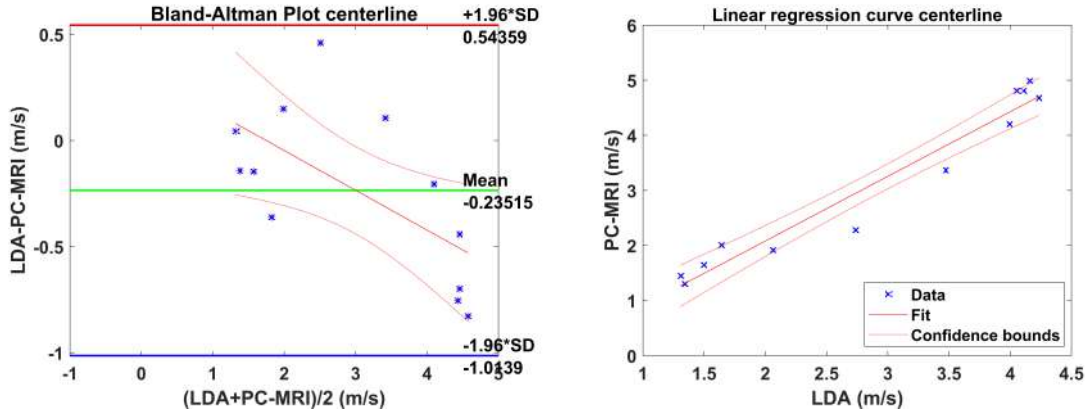

Figure 4.35: Bland-Altman plot and linear regression line of comparison of 2D PC-MRI (average of the trials) and LDA centerline velocity values at Re 500.

reduces. The quantitative comparison using Bland-Altman and linear regression (Figure 4.35 and table 4.14) shows that the slope of the regression line is 1.173, and R^2 is 0.95. Statistically significant p-value (p>0.001) indicates no proportional bias in the centerline velocity.

The previous two sections have established the reliability and accuracy of the PC-MRI measurements at laminar and turbulent inlet conditions. Therefore, the following section shows the application of PC-MRI as a validation tool for numerical simulation.

4.4.6 Flow investigation at Reynolds number 2000 - LES

The flow in the stenosis at Re=2000 was simulated using an LES simulation. The results of the LES simulations are presented below (Figure 4.36). It is to be noted that only the velocity values along the z-direction are taken for the analysis with 2D PC-MRI. The figure 4.36 shows that the velocity on the model's surface is null.

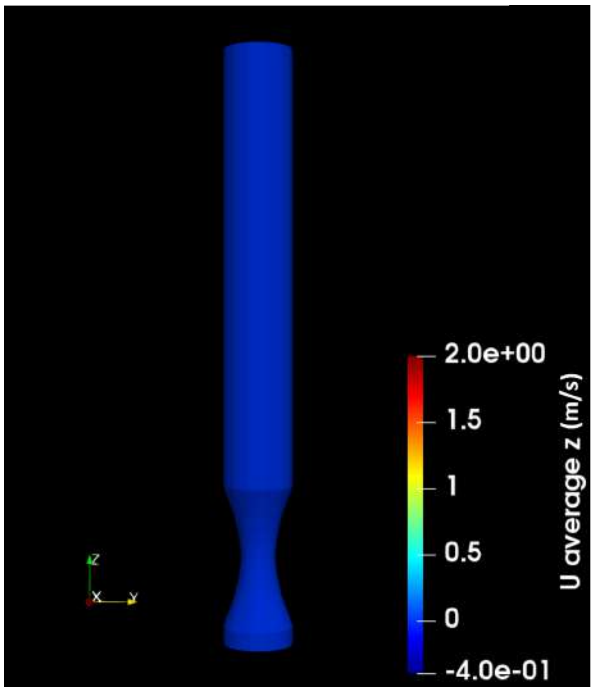

Figure 4.36: 3D model of the stenosis model at Re 2000 obtained from LES as visualized in Paraview.

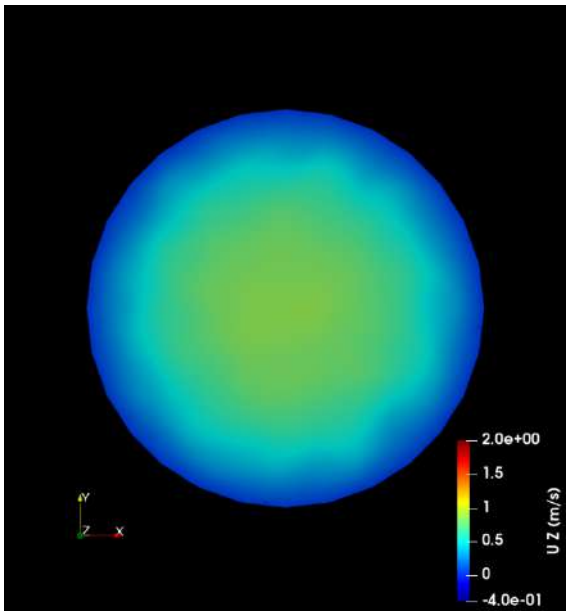

Figure 4.37: Comparison of LES and 2D PC-MRI velocity distribution in the inlet slice of the stenosis model at Re 2000.

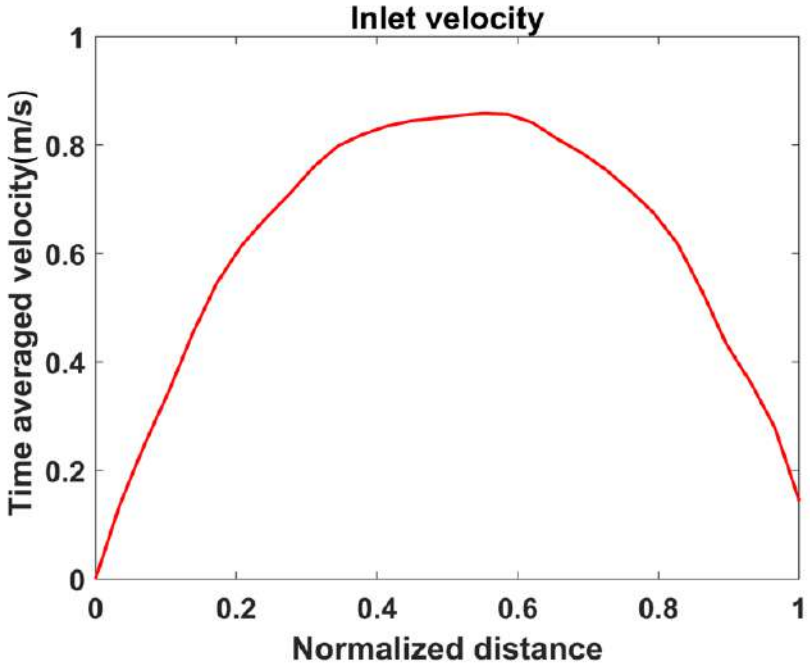

Figure 4.38: Plot of the inlet velocity profile at Re 2000 obtained from LES.

A fully developed flow is observed in the inlet slice is plotted in figure 4.38. The

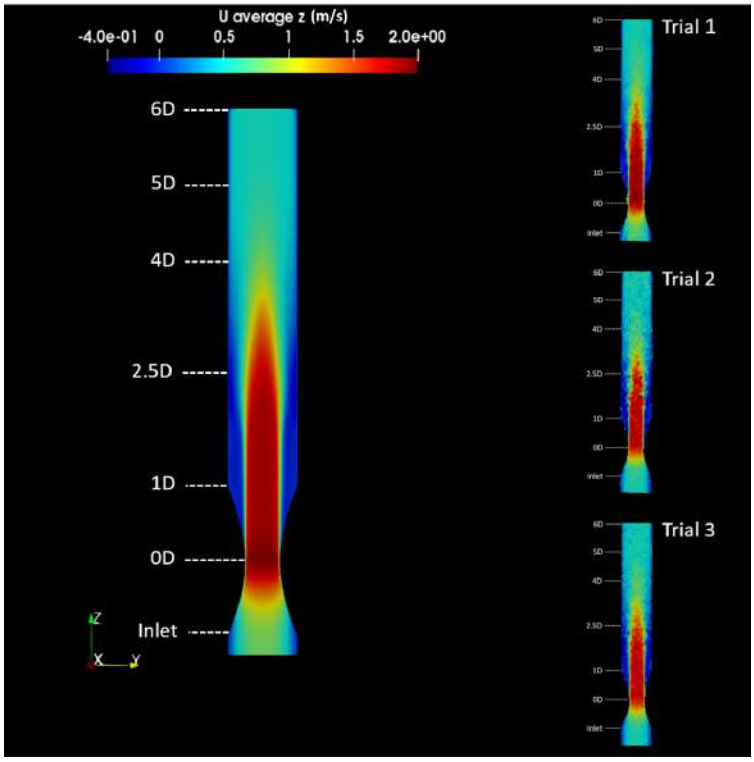

Figure 4.39: Sagittal slice of the LES and 2D PC-MRI stenosis model (y-z view) showing flow separation at Re 2000.

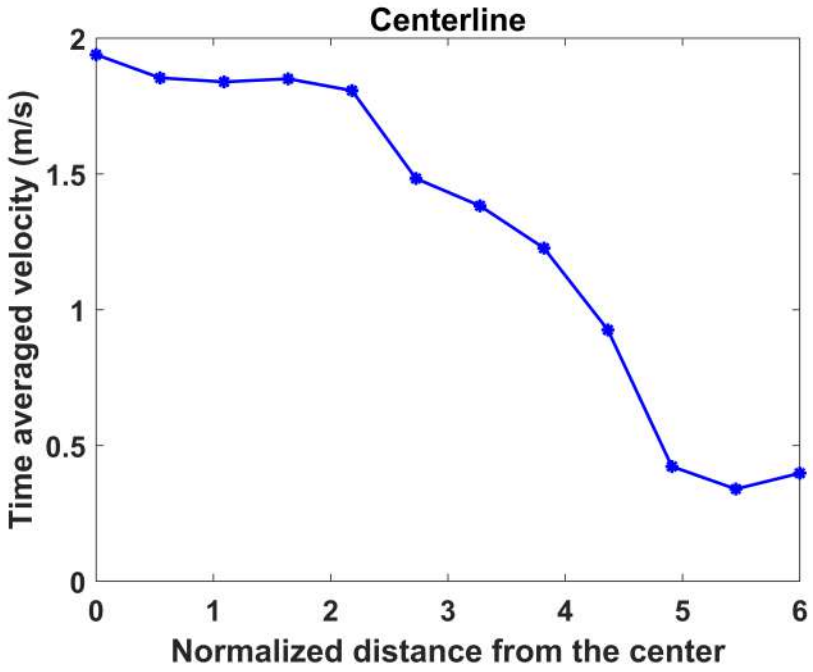

Figure 4.40: LES calculated centerline velocity profile plotted from 0d to 6d of the stenosis model at Re 2000.

inlet velocity obtained from the simulation was 0.449 m/s (considering only the z-component value).

In the sagittal slice (Figure 4.39), the same flow phenomenon of acceleration and deceleration of fluid in the converging and diverging stenosis with flow separation downstream of the end of stenosis observed in the trials is seen here. The recirculation region ends at 1.63d, and a jet of length 3.6d was observed. From the centerline profile (Figure 4.40), it is observed that around 2.1d, the velocity starts dropping down until 5d. Downstream to this, the values remain uniform.

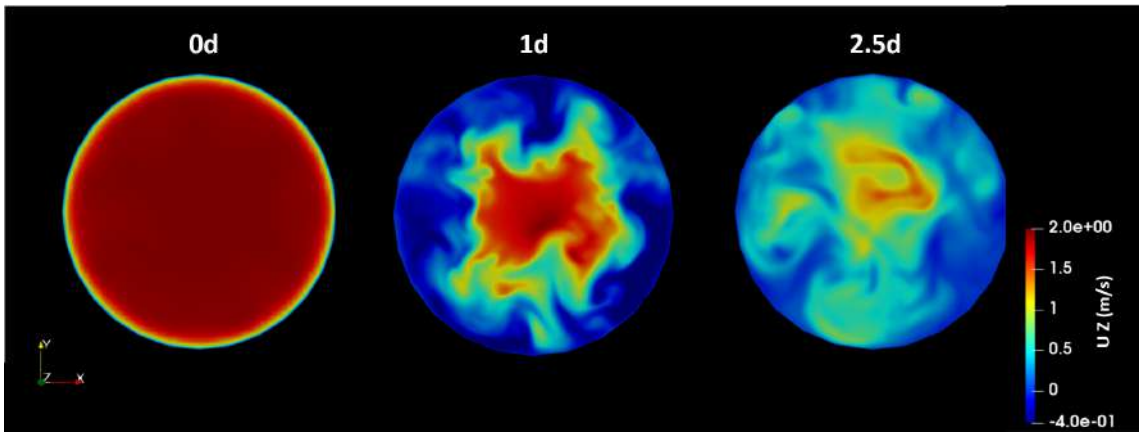

Figure 4.41: LES simulated velocity distribution in slices 0d to 2.5d.

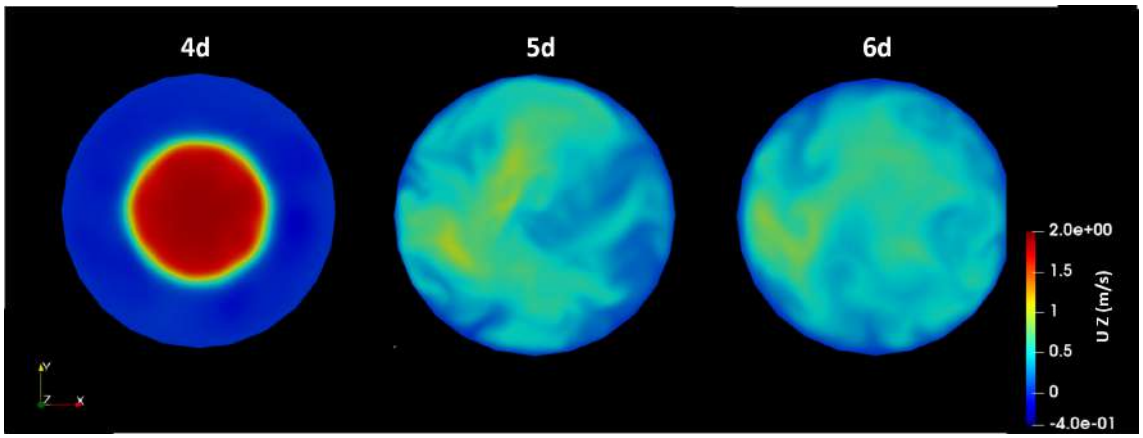

Figure 4.42: LES simulated velocity distribution in slices 4d to 6d.

The velocity distribution in individual slices is presented in Figure 4.42. At 0d, the velocity at the center is high, and the at the borders is low. At 1d, the flow separation is observed. At 2.5d, the flow appears to be more turbulent. Further downstream at 4d, 5d, and 6d, the flow is unsteady.

4.4.7 Comparison of PC-MRI and LES data

Table 4.16 presents the comparison of the average velocity values of PC-MRI and LES at Re 2000. The results from both methods show excellent agreement in all the slices.

Table 4.16: Comparison of 2D PC-MRI measured and LES calculated average velocities and standard deviations at Re 2000.

Slice number	**2D PC-MRI, m/s**	**LES, m/s**	**Standard deviation, m/s**
Inlet	0.366	0.449	0.108
0d	1.427	1.760	0.004
1d	0.366	0.449	0.005
2.5d	0.378	0.449	0.009
4d	0.407	0.449	0.002
5d	0.415	0.449	0.002
6d	0.415	0.444	0.019

The LES data has a much higher spatial resolution than the PC-MRI data. Therefore, for a detailed comparison, the LES data is resampled to the spatial resolution of the PC-MRI data. The qualitative and quantitative analysis of the LES and PC-MRI data is presented. Figure 4.43 presents a difference plot (difference of the velocity measured by LES in z direction and the 2D PC-MRI). Supporting the data seen in table 4.16, the difference plot shows that velocity values at the inlet from the LES simulation is higher by approximately 0.08 m/s. Consequently the velocity downstream is marginally higher in the LES simulation compared to the velocity measured by the 2D PC-MRI technique. At slice 1d, 2.5d, the difference plot is inhomogeneous due to the flow separation. From 4d to 6d as the flow homogenizes, the velocity value obtained from both the methods reduces.

Figure 4.44 shows the axial velocity profile along the radius of the chosen slice.

At 0d, it is seen that the LES and PC-MRI have the same profile, but the LES values are higher throughout the profile. At 1d and 6d, an excellent agreement between the two is observed. At 2.5d and 4d, high LES values are seen at the center except at the border. At 5d, the LES values were lower than PC-MRI values. The comparison of the centerline velocity also shows a fair agreement, although LES has a slightly

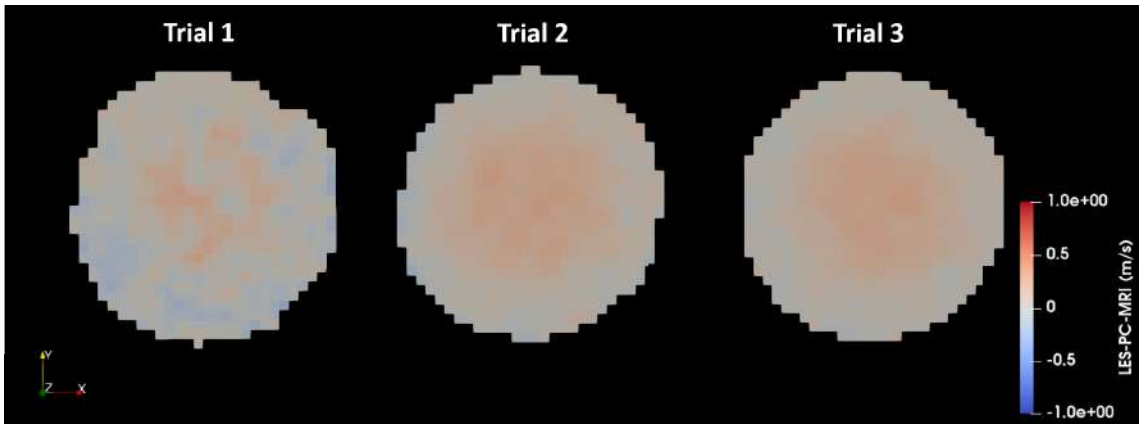
Trial 1
Trial 2
Trial 3
1.0e+00
0.5
0
-0.5
-1.0e+00
LES-PC-MRI (m/s)

(a)

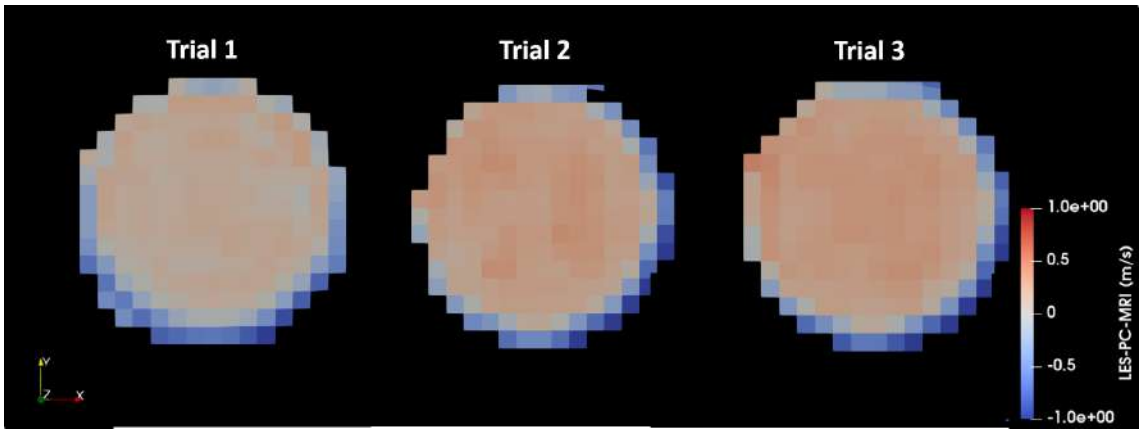
Trial 1
Trial 2
Trial 3
1.0e+00
0.5
0
-0.5
-1.0e+00
LES-PC-MRI (m/s)

(b)

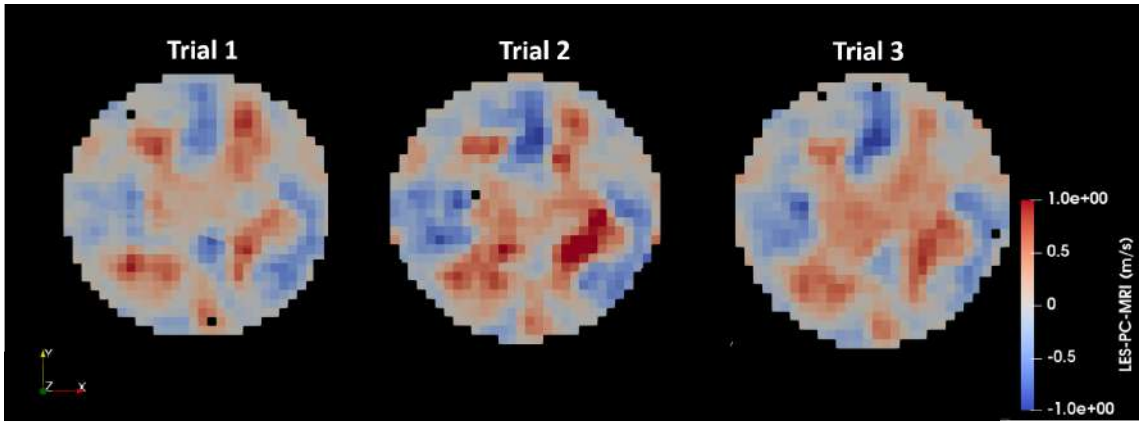
Trial 1
Trial 2
Trial 3
1.0e+00
0.5
0
-0.5
-1.0e+00
LES-PC-MRI (m/s)

(c)

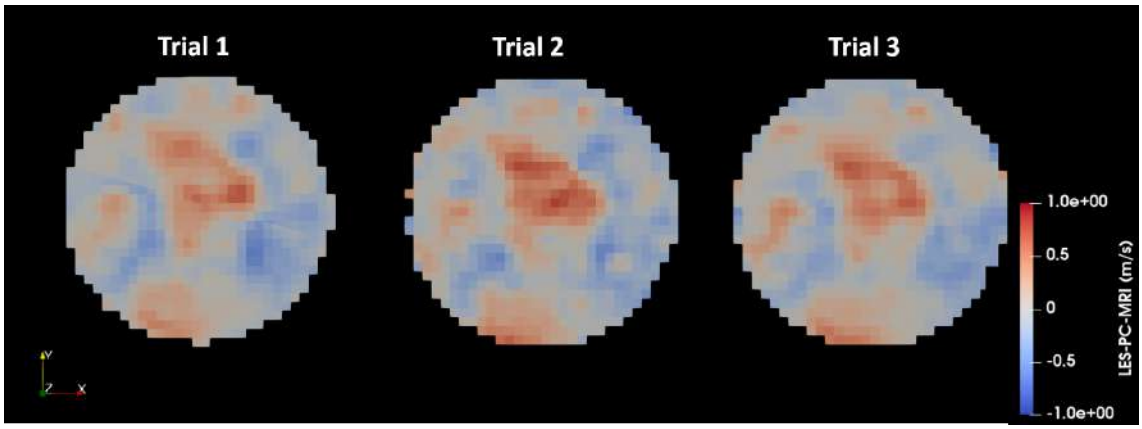
Trial 1
Trial 2
Trial 3
1.0e+00
0.5
0
-0.5
-1.0e+00
LES-PC-MRI (m/s)

(d)

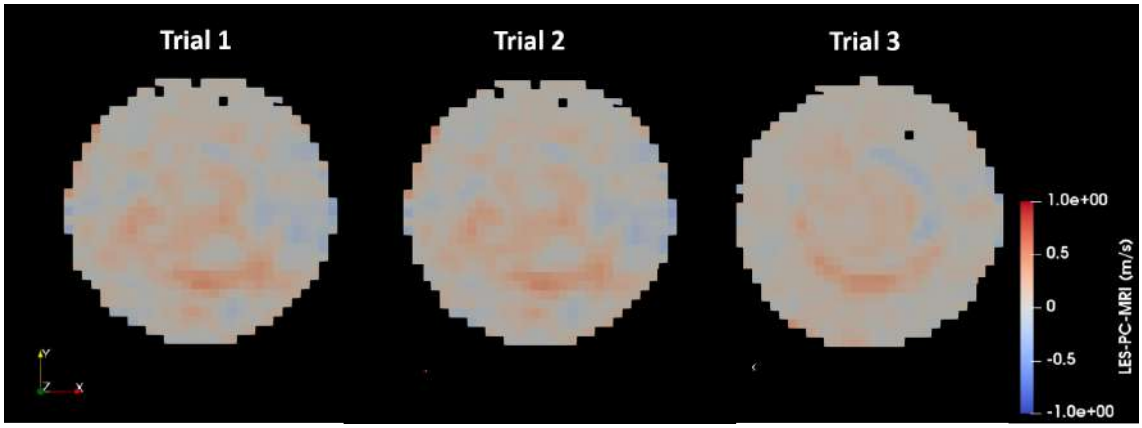
Trial 1
Trial 2
Trial 3
1.0e+00
0.5
0
-0.5
-1.0e+00
LES-PC-MRI (m/s)

(e)

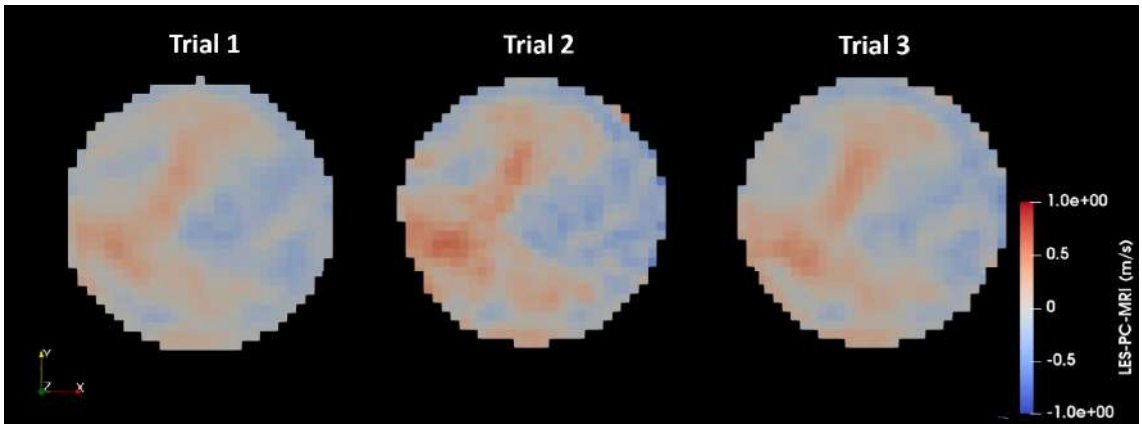
Trial 1
Trial 2
Trial 3
1.0e+00
0.5
0
-0.5
-1.0e+00
LES-PC-MRI (m/s)

(f)

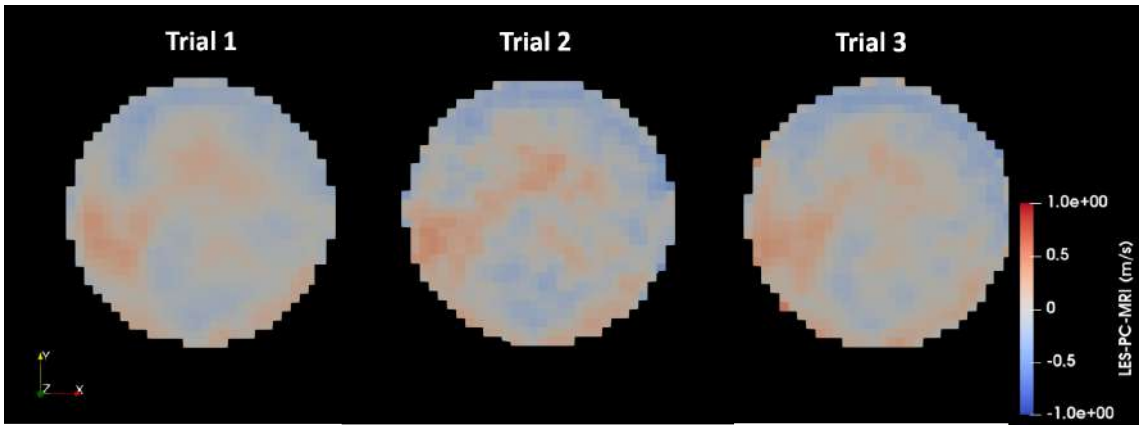

(g)

Figure 4.43: Figure a to g presents the difference plot of velocity value obtained from LES and 2D PC-MRI in inlet, slice 0d, 1d, 2.5d, 4d, 5d and 6d.

Table 4.17: Table of linear regression values from the comparison of 2D PC-MRI (average of the three trials) and LES velocity values for the entire model at Re 2000.

Method	**Slope**	**Intercept (m/s)**	**R ^{2}**	**p-value**
PC-MRI - LES	1.308	-0.110	0.778	=0.001

higher velocity value after the end of the jet.

The quantitative analysis for the entire model using linear regression is provided below. As the one-sample t-test had p-value < 0.001, therefore no Bland-Altman analysis was considered.

A good agreement between the LES and the PC-MRI data was seen with the R^2 value of 0.827. Further, the same quantitative analysis was extended to the chosen slices.

The R^2 value lies between 0.992 - 0.331. The higher R^2 correspond to 1d with a slope close to unity. However, a low R^2 was observed in the region downstream to the reattachment zone.

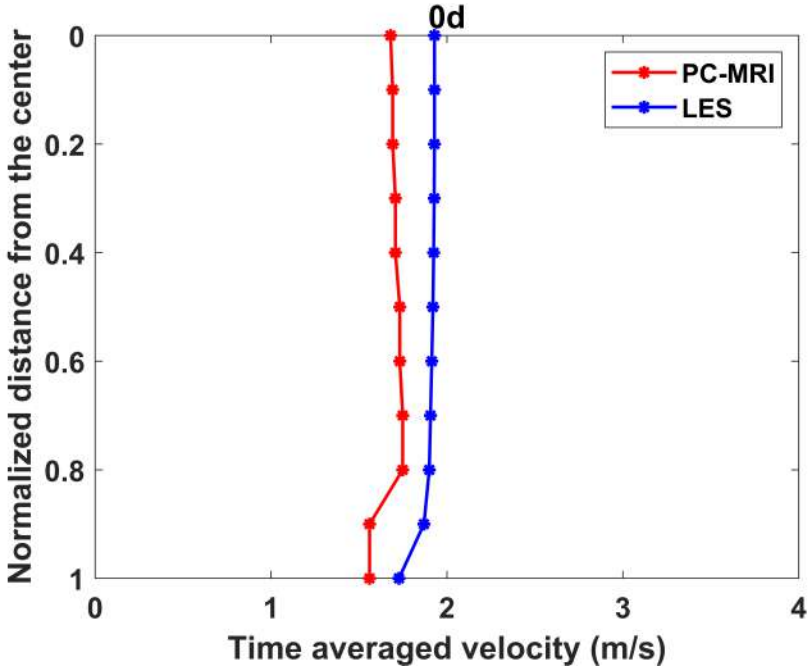
0d
PC-MRI
LES
Normalized distance from the center
Time averaged velocity (m/s)
0
0.2
0.4
0.6
0.8
1
0
1
2
3
4

(a)

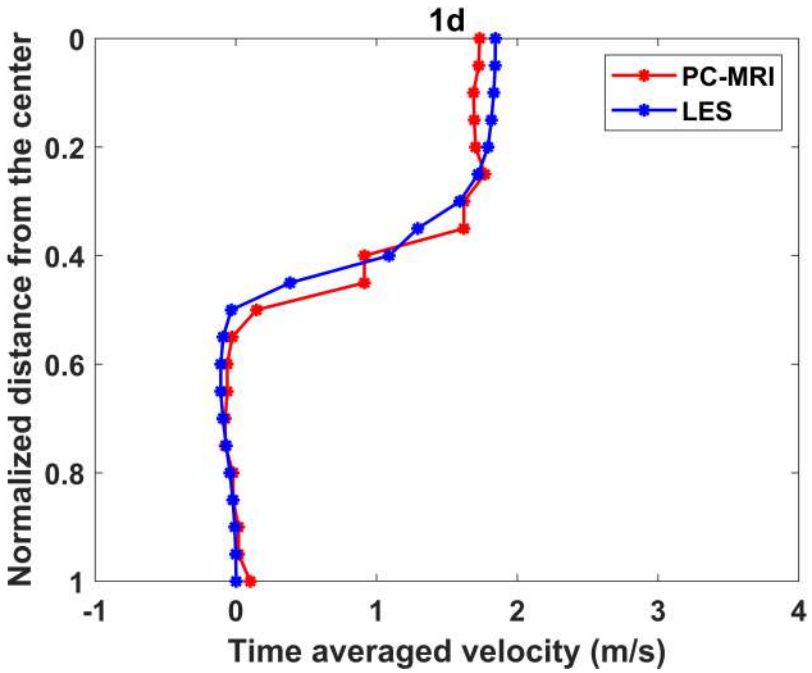
1d
PC-MRI
LES
Normalized distance from the center
Time averaged velocity (m/s)
0
0.2
0.4
0.6
0.8
1
-1
0
1
2
3
4

(b)

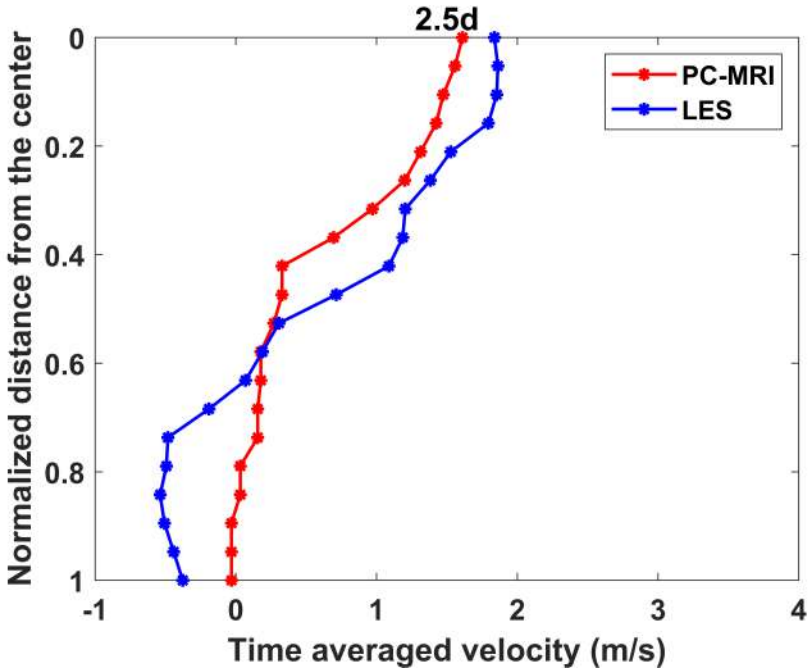
2.5d
PC-MRI
LES
Normalized distance from the center
Time averaged velocity (m/s)
0
0.2
0.4
0.6
0.8
1
-1
0
1
2
3
4

(c)

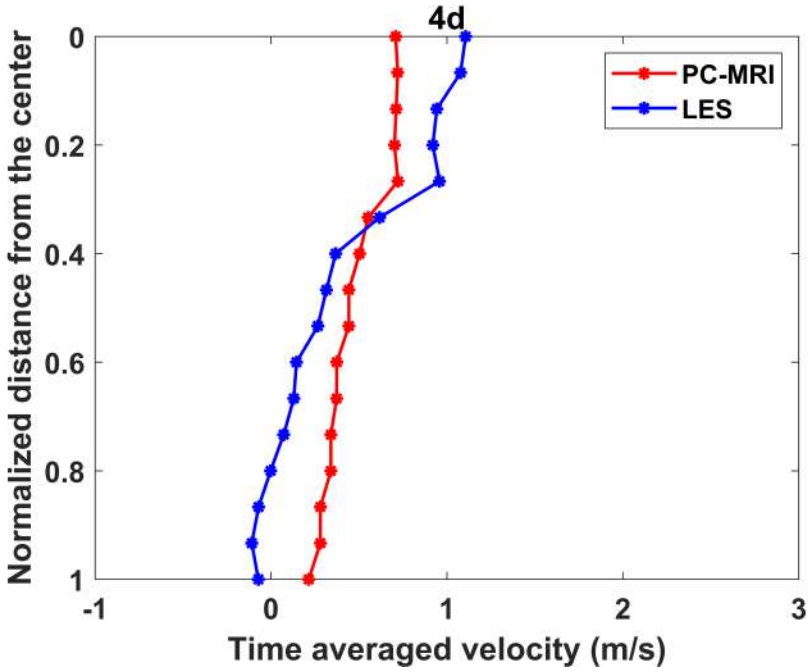
4d
PC-MRI
LES
Normalized distance from the center
Time averaged velocity (m/s)
0
0.2
0.4
0.6
0.8
1
-1
0
1
2
3

(d)

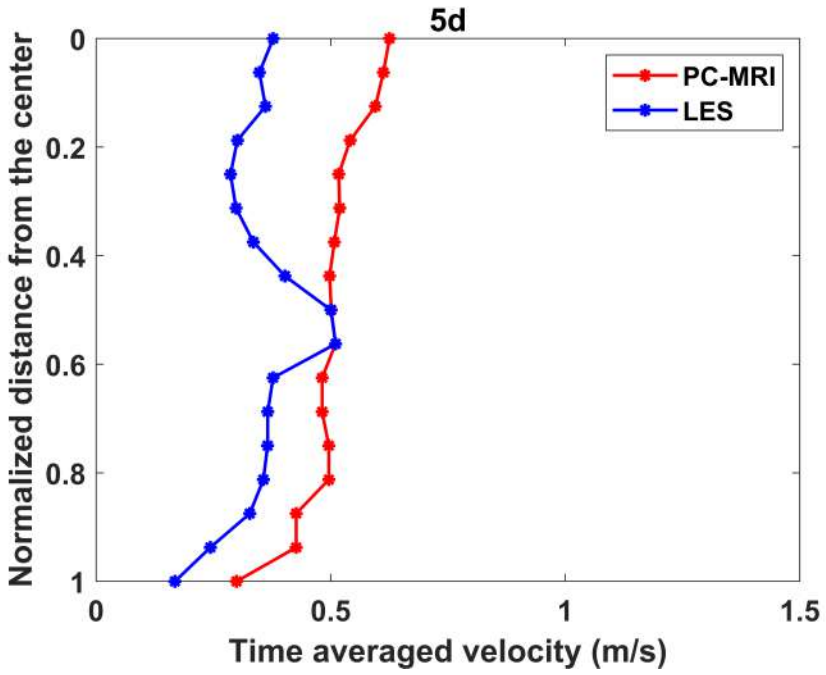

(e)

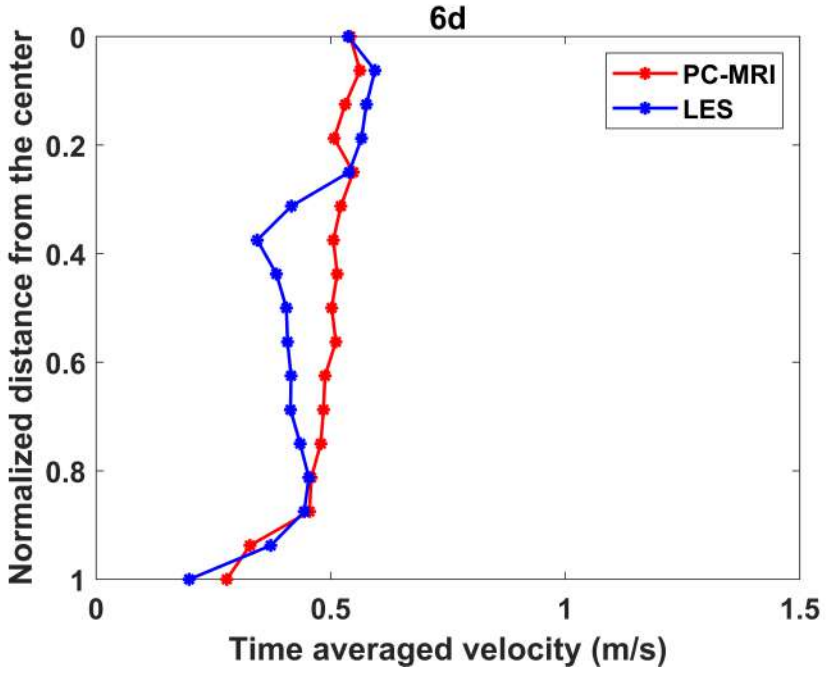

(f)

Figure 4.44: Axial velocity profile along the radius of the chosen slice at Re 2000 obtained from 2D PC-MRI (average of the three trials) and LES.

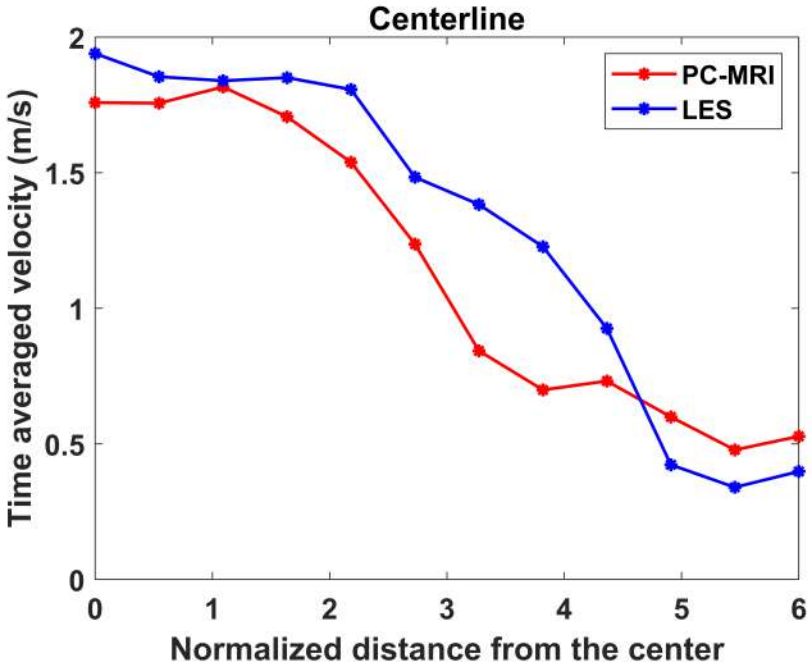

Figure 4.45: Comparison of LES and 2D PC-MRI centerline velocity values plotted from 0d to 6d of the stenosis model at Re 2000.

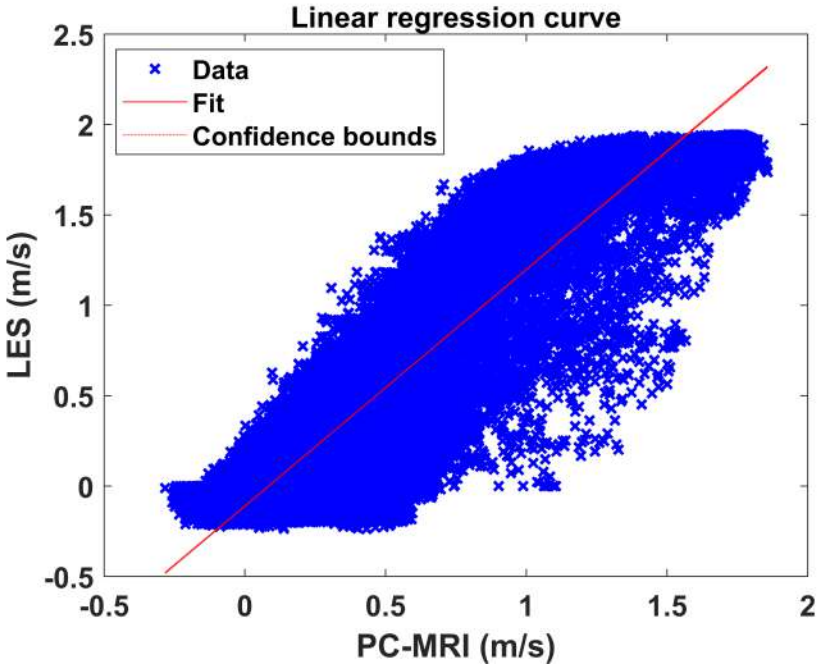

Figure 4.46: Linear regression line of comparison of 2D PC-MRI (average of the three trials) and LES velocity values of the entire model at Re 2000.

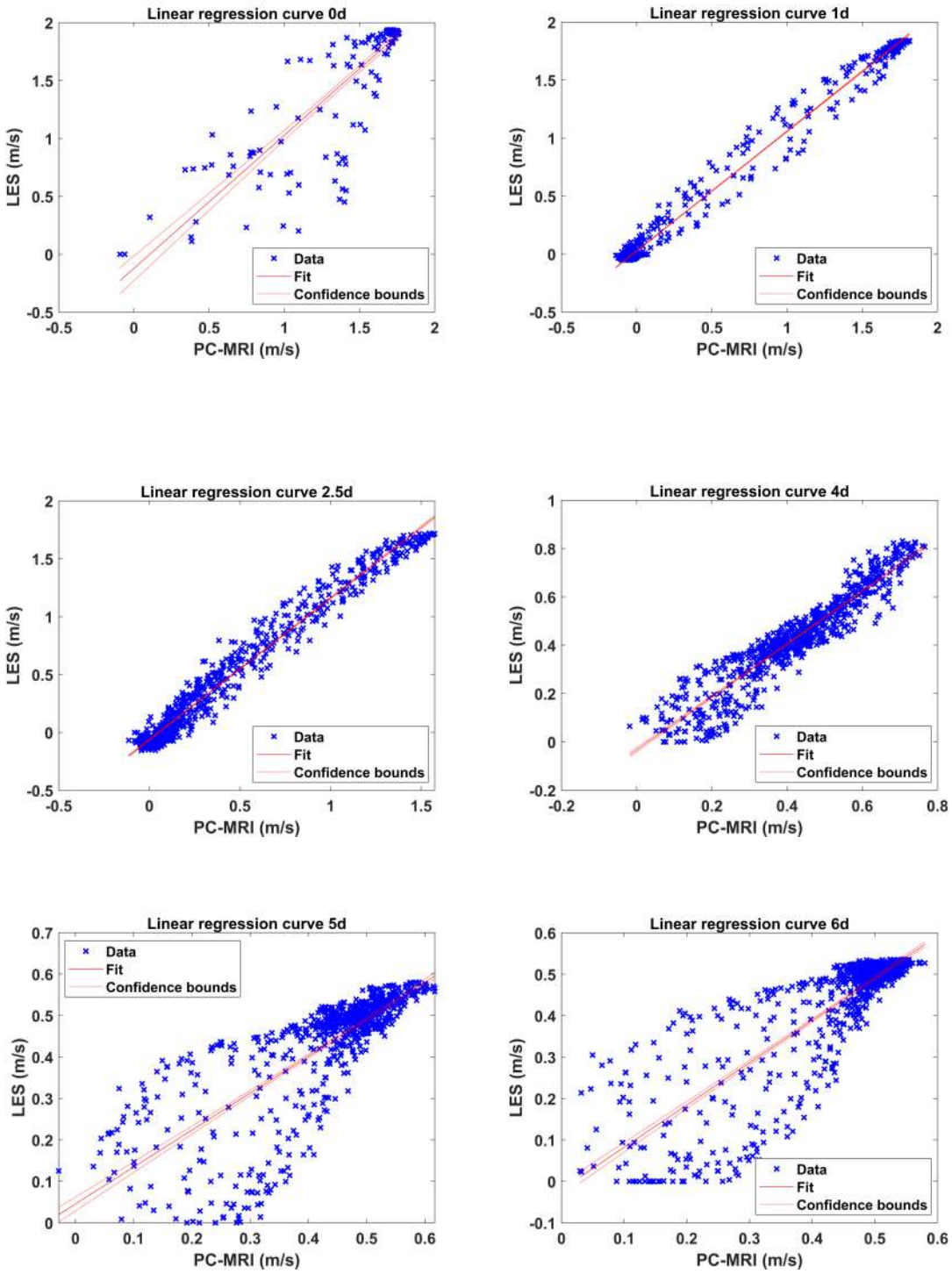

Figure 4.47: Linear regression line of comparison of 2D PC-MRI and LES velocity values at chosen slices at Re 2000.

Table 4.18: Table of Bland-Altman and linear regression values from the comparison of 2D PC-MRI (average of the three trials) and LES velocity values at chosen slices at Re 2000.

Slice number	**Slope**	**Intercept (m/s)**	**R ^{2}**	**p-value**
0d	1.149	-0.122	0.736	p<0.001
1d	1.031	0.027	0.990	p<0.001
2.5d	1.222	-0.063	0.970	p<0.001
4d	1.094	-0.032	0.886	p<0.001
5d	0.892	0.045	0.602	p<0.001
6d	1.020	-0.019	0.705	p<0.001

4.5 Discussion

This section discusses the interpretation and inference of the results in the axisymmetric stenosis model.

Reliability: Measurement technique and experimental setup

This chapter evaluated the reliability and accuracy of the 2D PC-MRI technique along with the technique's feasibility as a validation tool for numerical simulation to investigate flow dynamics was demonstrated. As a first step to achieving this, test-retest reliability was examined. At both the inlet conditions, the ICC values obtained for the voxel-by-voxel comparison of velocity at chosen slices for the three trials show excellent reliability, with all the values above 0.939. The values show that the velocity values at both boundary conditions all three times at different periods measured using the 2D PC-MRI technique were consistent, illustrating the experimental setup's stability and the technique's ability to measure consistently.

However, at both the inlet conditions, the inlet velocity in all the three trials, although uniform, was slightly different despite prescribing the same flow rate. The area of the inlet slice at both inlet conditions, when measured in Paraview, was the same as designed and fabricated, implying a variation in the flow rate generated by the flow pump or an underestimation of velocity measured by 2D PC-MRI.

To check this, the flow volume at the inlet slice was calculated using the continuity equation (Equation 4.12), where area and velocity values are taken from Paraview.

A value of 58.37 ml/s, 52.01 ml/s, and 52.97 ml/s was obtained for the three trials, respectively, at Re 500. Further, the velocity value at the stenosis was also calculated using the area measured and above newly calculated flow rate. The values obtained from this calculation correlated very well with the measured velocity at stenosis, implying that the variation in the flow rate generated by the pump caused the changes in the values. At Re 2000, a flow rate of 177.37 ml/s, 188.12 ml/s, and 185.45 ml/s were calculated from the equation for the three sets of trials, respectively. Nevertheless, unlike Re 500, the measured velocity value was lower than the new flow rate values calculated. So there appears to be an underestimation of PC-MRI measured values during turbulent flow due to higher noise. Thus, the differences seen at the inlet can be explained by the lower flow rate generated by the pump at Re 500 and the underestimation of velocity by 2D PC-MRI at Re 2000.

Flow dynamics in stenosis

The results show that the flow dynamics in the stenosis are well defined by the 2D PC-MRI technique and agree well with previously published LDA data. At Re 500 and Re 2000, a fully developed flow enters the stenosis. As the area decreases, the velocity values peak. As the fluid flows out of the constriction, the sudden increase in the area causes the formation of the recirculation region and the jet. At Re 500, a long axis-symmetric jet of length 8-9d is formed with a strong shear layer in all three trials, but the shear layer at the trailing edge of the jet leans towards one side of the pipe. Also, the axial view at slice 5d shows the branches emerging from the jet presumably occurring due to the oscillation of the jet. The linear instability mechanism might cause this deflection to a weak coanda wall attachment [132] [133]. The Coanda wall attachment refers to the tendency of the fluid to attach itself to the surface and flow along it. Such instability might be caused due to the variation in flow rate occurring during the scan duration, causing perturbations in flow components, or by the oscillations of the shear layer. At Re 2000, the length of the jet is approximately 4d, which correlates well with previously published data. The jet length at Re 2000 is much shorter than at Re 500 due to the higher turbulence in Re 2000. In this case, no affinity of the jet or the shear layer towards the pipe was observed.

Comparison of the PC-MRI and LDA data

Qualitatively and quantitatively, the velocity profiles obtained in 2D PC-MRI and LDA match well at Re 500 and Re 2000. A significant deviation in the numerics was observed at 0d at both the inlet conditions. The average velocity measured th PC-MRI and LDA at 0d, as expected, is higher by 4. However, comparing the velocity values at individual voxels, the values at the center were higher by almost a factor of 5 in 2D PC-MRI measurements. High velocity at the center of the slice was consistently seen in all the slices. Additionally, lower values obtained in the PC-MRI in the recirculation regions were lower than in the LDA values. The results have shown that the velocity at the inlet is lower than the expected value, and the plot shows the ratio of time average velocity to mean average time velocity at the inlet. The above two reasons owes to the variation seen in the plot. An additional deviation observed on the plot is in the distance at which the recirculation region begins. The recirculation region ends earlier than the 2D PC-MRI measurements in LDA measurements. Varghese also observed this deviation in [134]. Here, it is suggested that the turbulence downstream of the shear layer can shift the reattachment point from that observed for a purely laminar flow field, thereby causing the deviation. A similar trend was also seen for Re 2000 in slices 0d, 1d, and 2.5d. However, between 4d and 6d, a good correlation of the values was seen. The Bland Altman and linear regresions plots for both the flow conditions provided robust evidence for the agreement of values between PC-MRI and LDA. In the both flow conditions the R^2 was greater than 0.920 and in the cases where a possibility of proportional bias was detected a linear regression in the percentage plot was performed. The results obtained here clearly dismissed the non-linear bias present and hence the systematic disagreement between the methods.

One of the main concerns in using the 2D PC-MRI technique or velocity measurement is the low spatial resolution and its effect on the accuracy of the measured velocity. The voxel size chosen in the current experiment is 1 mm. A smaller voxel size would be preferable to describe more accurate flow dynamics. However, this would also reduce the signal received, making the velocity measurement inaccurate. Therefore, a delicate balance between the signal received and voxel size must be achieved. This balance is also essential for the SNR and the amount of noise available during velocity measurement. The higher the noise, the lesser the signal and the less precise the velocity measurement. The SNR values in both trials were calculated to analyze the noise in the velocity image using equation 3.2 in chapter 3.1.

Table 4.19: SNR and error propagation in velocity images at Re 500 and Re 2000.

Re	**SNR**	**Noise in velocity image(σ_v)(m/s)**
Re 500 trial 1	10.2488	0.033
Re 500 trial 2	10.263	0.037
Re 500 trial 3	8.820	0.043
Re 2000 trial 1	6.400	0.214
Re 2000 trial 2	3.895	0.341
Re 2000 trial 3	6.227	0.217

In the equation, the SNR is the measured SNR based on the signal magnitude within the model and the background noise, and Venc is the velocity sensitivity. The SNR and the noise in the velocity image are presented in table 4.19.

A higher SNR was observed for Re = 500 in comparison to Re = 2000 where the noise in the velocity image was higher.The partial volume effect and SNR might explain the discrepancy observed in the numerics.

Comparison of the PC-MRI and LES data

The LES velocity data showed perfect agreement with the theoretical data. At the inlet the average velocity was 0.449 m/s, at the center of the stenosis the velocity was four times the velocity value at the inlet and post the stenosis the velocity value was back at 0.449 m/s. Since the spatial resolution of LES is much higher than PC-MRI, a resampling of simulation data was done before the quantitative comparison of the two methods. The average inlet velocity obtained from the PC-MRI was lower in comparison to the LES inlet velocity value (2D PC-MRI: 0.369 m/s and LES: 0.449 m/s). Consequently at 0d, the LES velocity values were slightly higher than the PC-MRI velocity range. The average values calculated at the center of the stenosis and downstream were per the expected values for the given flow rate (Lower than the prescribed flow rate was found in the experiments leading to lower inlet velocity and subsequently lower velocity values through the pipe). Additionally, the length of the jet in the experiment was slightly longer owing to the lower flow rate (less turbulent). Further higher noise in the PC-MRI velocity images could have contributed to the difference seen in the quantitative comparisons.

Conclusion

This chapter establishes the reliability of the 2D PC-MR technique with an ICC value range of 0.944-0.993 for Re 500 and 0.939-0.990 for Re 2000 in the test-retest evaluation. The flow dynamics in the stenosis, including flow instabilities such as Coanda flow, were well visualized and measured. A good correlation was obtained between the 2D PC-MRI and LDA measurements with linear regression values ranging from 0.767-0.998 for Re 500 and 0.543-0.983 for Re 2000. The feasibility of the 2D PC-MRI technique as a tool for reliable velocity measurement was demonstrated, and a statistical framework was provided for further comparisons. The voxel-by-voxel comparison of 2D PC-MRI and LES data in the stenosis model showed agreement with a slope and R^2 values of 1.030 and 0.827, respectively. These results support using 2D PC-MRI as an investigative tool for studying flow dynamics and a validation tool for numerical simulations.

5

Experimental investigation of flow in a pharynx model: PC-MRI

In chapter 4, the PC-MRI technique's reliability and accuracy were demonstrated. This chapter uses the same technique to measure the velocity in a 3D printed pharynx model to understand the flow dynamics and study the etiology of OSA.

The goals of the chapter are as follows,

1. Investigation of flow dynamics in the pharynx model at average inspirational and expiration flow rates.
2. Check of reliability of 2D PC-MRI technique in the complex anatomical structure of pharynx by conducting repeatability tests and statistically analyzing the results using intraclass correlation coefficient (ICC).
3. Validation of the numerical simulation with PC-MRI data at an average inspirational flow rate.

5.1 Phantom design, fabrication and experiment setup

5.1.1 Geometry

Cone-beam computed tomography (CBCT) is a commonly used 3D imaging technique in dentistry. When utilizing a large FOV protocol, the upper airway is visible within the CBCT volume; thus, CBCT is a useful diagnostic tool for evaluating the airway. The basis for the digital model of the pharynx is two CBCT images of the patient suffering from OSA. The imaging was done with the patient in the upright position, and data were acquired without treatment of the disease (Left figure 5.1). The chosen region of interest in the upper airway is the pharynx (Right figure 5.1). The region between the two landmarks, the nasopharynx's hard palate and the second cervical's lower end, was segmented. The images, as well as the segmentation, are courtesy of the SICAT GmbH and Co. KG. The images have a size of 512 x 512 x 512 voxels, with a voxel extension of 0.3 mm in each direction. The segmentation was performed in a reduced resolution of 128 x 128 x 128 voxels to save computational costs. A watershed algorithm performed the segmentation. On the segmented pharynx lumen, a surface triangulation was performed to represent the surface shape of the patient's pharynx using the marching cube algorithm in MeVisLab (MeVis Medical Solutions AG and Fraunhofer MEVIS).

Figure 5.1: CBCT image of the patient suffering from OSA and segmentation of the pharynx from the image

Further, surface triangulation of the pharyngeal lumen was smoothed by reducing the number of triangles using the software, Meshmixer (Autodesk Inc., San Rafael, California, United States). After smoothing and reducing triangles in Meshmixer, the pharynx model was sent to Solidworks. The boundary conditions play an important role in numerical simulation. Therefore, small inlet and outlet adapters designed with CAD tools were attached to the pharynx model.

Further, the negative model of the pharynx was created by placing the pharynx model inside a solid cylinder of diameter 44 mm and a length of 110 mm. The basic pharynx model was subtracted from the main solid cylinder (Figure 5.2). The so-created negative model was placed inside a plexiglas pipe diameter of 44 mm and then connected to the flow rig.

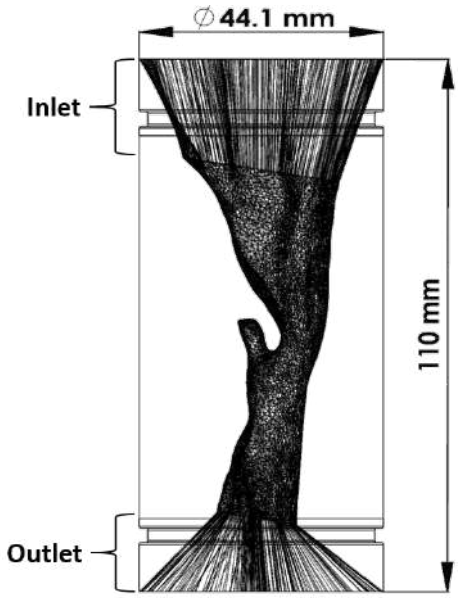

Figure 5.2: CAD geometry of the pharynx model.

5.1.2 Fabrication

The 3D volume file from Solidworks is saved as an STL file and is sent for fabrication. The rigid pharynx model was fabricated from the digital model using a 3D printer, ProJet 3510HD using MJP 3D printing technology, and photopolymer Visijet X. The procedure for fabrication is as in chapter 4, section 4.2.2. The pharynx was printed with HD resolution, a layer thickness of 32 μm, and the print resolution is 375 x 375 x 790 DPI in the xyz direction, respectively.

5.1.3 Experiment setup

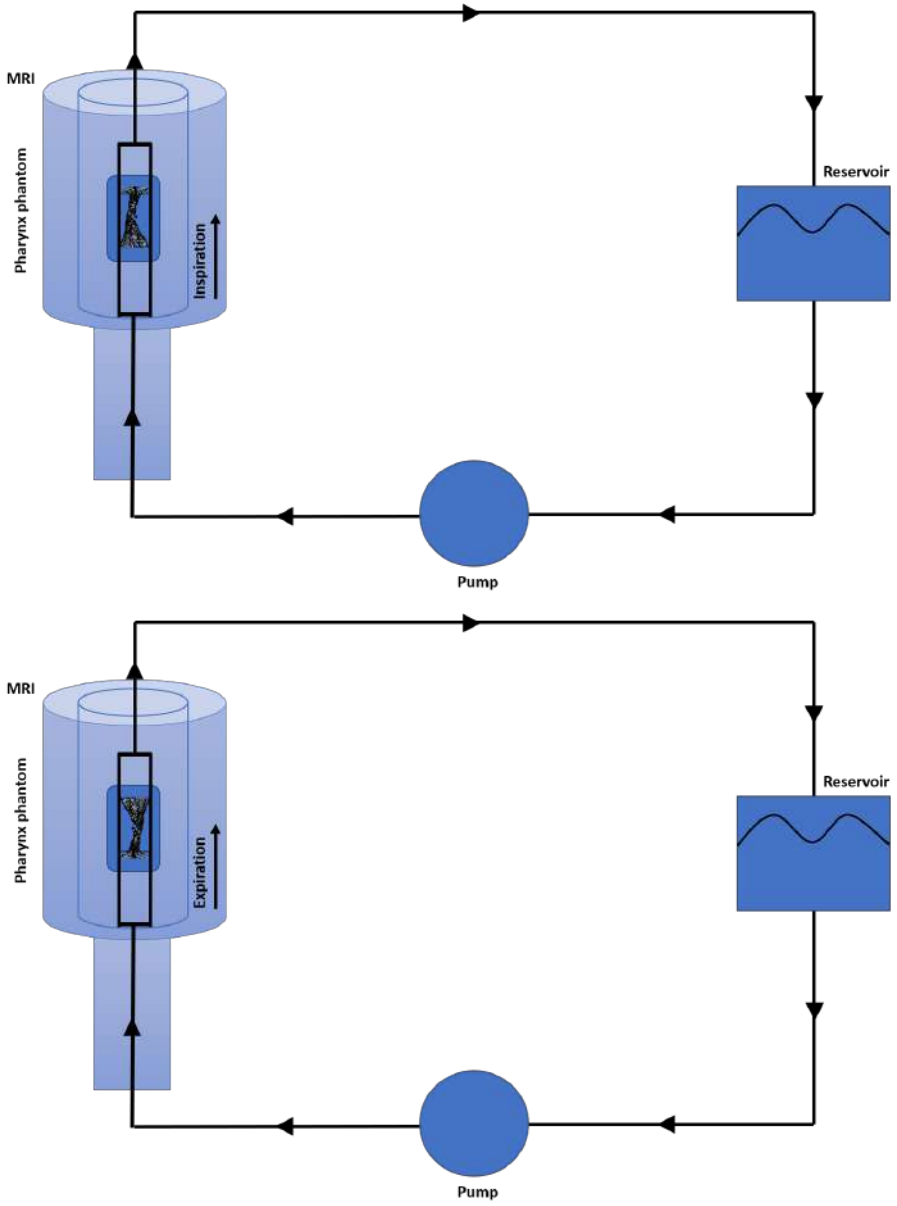

Figure 5.3: Schematic drawing of the experimental setup used for studying flow during inspiration (top) and expiration (bottom) in the pharynx model. The black rectangle represents the pipe within which the model is placed and the dark blue box represents the MRI table.

A closed-loop setup was used for the trials. A schematic diagram of the flow rig

for inspiration and expiration experiment is shown in figure 5.3. As seen in the figure, the flow system for both trials remains the same, with only a change in the direction of placement of the pharynx model for the expiration experiment. The 3D printed pharynx model was placed inside a plexiglass pipe of 44 mm diameter. To ensure a fully developed flow at the entrance of the model, a 450 mm long straight, rigid plexiglas tube was placed upstream of the test section. The inlet of this pipe was connected to a pump, CardioFlow 5000 (Shelley Medical Imaging Technologies, London, Canada). The pipe outlet was connected to a header tank, and its other outlet was connected to the pump's inlet. All the components were connected via flexible tubings. The test fluid used was a mixture of water and glycerol (55.27% by weight). The test fluid was used at a temperature of 25°C with density value 1144 kg/m^3, absolute viscosity 5.818 mm^2/s and relative viscosity 6.6563 mPas. These values were calculated from the empirical formula in chapter 4, equation 4.11.

The trials were performed on a whole-body MR system with the Ingenia 3T scanner (Philips Healthcare, Best, Netherlands) using a 108-channel body coil. The center of the model was positioned at the isocenter of the bore of an MRI scanner. OSA is mainly observed when the patient is asleep in the supine position. Therefore, to replicate that, the model was placed in this position.

5.2 Investigation of airflow during inspiration and expiration at average flow rate

5.2.1 Inlet flow conditions

Studies show that the average inspirational flow rate in the upper airway is approximately 250 ml/s [135] [79] [136]. To replicate this flow condition in the experiment that uses a water-glycerol mixture, a flow rate of 88.62 ml/s was prescribed. This value was calculated from Reynolds number equation (Equation 3.6) and the continuity equation (Equation 4.12). The same inlet flow condition was also used for the velocity measurement in the model during expiration.

5.2.2 MRI acquisition

All 2D PC-MRI trials were performed with a 3T Ingenia Philips MR system using a 108-channel flexible body coil. The system provides a maximum gradient strength of 45 mT/m with a maximum slew rate of 120 mT/m/ms. A standard two-dimensional

(2D) phase-contrast sequence with a cartesian readout was used to measure the velocity in the transverse slice of the phantom.

Imaging parameters used for the scan were as given in table 5.1.

Table 5.1: Imaging parameters used for the 2D PC-MRI experiment.

Scan mode	3D	**Scan technique**	Fast field echo
Contrast enhancement	T1	**Acquisition mode**	Cartesian
Fast imaging mode	Turbo field echo	**Gradient mode**	Enhanced
Flow compensated	Yes	**SMART**	Yes
Quantitative flow	Yes	**Local phase correction**	No
Flow direction	Feet-Head (FH)	**Voxel size**	$1 \times 1 \times 1$ mm^3
Number of averages	4	**TE**	6 ms
TR	10 ms	**Flip angle**	7°

Velocity encoding value of Venc = 160 cm/s for the flow rates 88.62 ml/s was used. The velocity encoding value was chosen 10-20% higher than the maximum velocity in the model to avoid aliasing. The FOV for all the three trials was $100 \times 100 \times 150$ mm. The model position in trials 2 and 3 was slightly rotated compared to the model position in trial 1. No local phase correction was performed as the phantom is surrounded by air and no water or fluid. Also, no corrections for background phase errors and eddy currents were performed.

5.2.3 Post-processing

The images acquired from the MRI in classic DICOM format were processed in MATLAB R2020b (MathWorks, Natick, MA, USA). A threshold based on magnitude images was used on the images to remove any variations in the geometry of the images. The velocity for each voxel was calculated from normalized intensities using the equation 4.13. A hexahedral mesh with velocity values was generated in MATLAB and converted into a .vtu file format to be analyzed in the open platform software Paraview.

5.2.4 Numerical simulation

The same Solidworks 3D model used for the experiment was also used for the simulations. The airflow in a human pharynx can be described by the stationary Navier-Stokes equations, a set of non-linear PDEs of second order prescribing mass and momentum conservation of fluid.

COMSOL Multiphysics was used for simulating airflow in the model with incompressible Navier-Stokes equations and no turbulence modeling. The mesh of the model consists of 76722 elements, of which 44324 tetrahedra and 32398 prisms.

The simulation chooses all the physical properties of the air corresponding to a temperature of 20°C. All other boundaries were chosen to be no-slip walls. The simulations were performed only during inspiration.

5.2.5 Statistical analysis

A voxel-by-voxel comparison of velocity values between the three trials was made at all chosen slices to check the agreement (performed only for experiments replicating inspiration). The agreement of the values was quantified with ICC using a 2-way mixed-effects model with an absolute agreement (95% confidence interval) in IBM SPSS software (version 28). Bland-Altman chart and linear regression in MATLAB R2020b were used to assess the agreement between 2D PC-MRI and numerical simulation results.

5.3 Results and analysis

The in-vitro experiment for flow in the pharynx was performed at the average inspiration and average expiration settings. The velocity values in the inspiration and expiration experiment were calculated in MATLAB. A reliability study to evaluate the test-retest reliability during inspiration was performed by conducting the trials three times. No reliability test was performed for the expiration experiment. The meshed model with velocity value generated in MATLAB was used for analysis and visualization in Paraview. The results of the analysis are discussed in this section.

Eleven uniformly distributed slices are chosen within the pharynx phantom for the analysis (Figure 5.4).

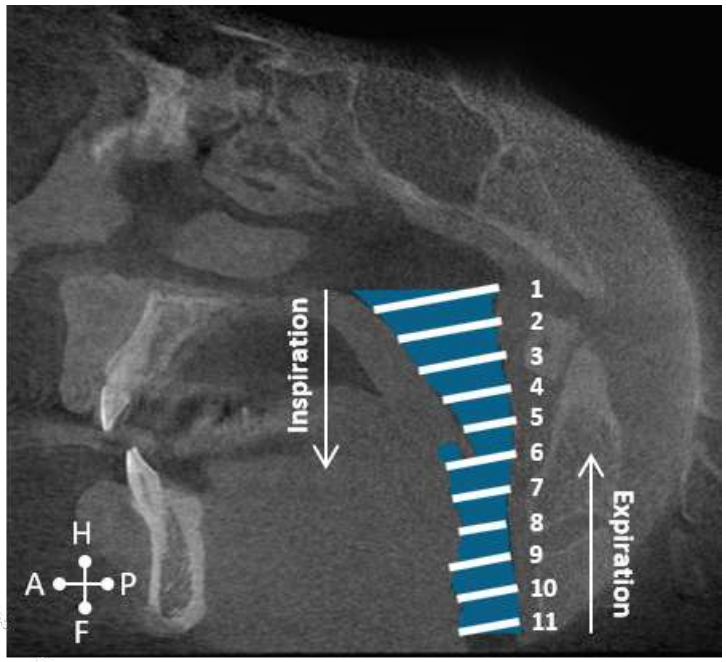

Figure 5.4: Position of the chosen slice in the pharynx model.

5.3.1 Reliability analysis during inspiration

The comparison of the velocity values between the three trials at average inspirational flow rate and chosen slices is presented in the table (Table 5.2).

As in chapter 4, the reliability of velocity was characterized as excellent (ICC > 0.80), good (ICC 0.60 - 0.79), moderate (ICC 0.40 - 0.59), fair (ICC 0.20 - 0.39), or poor (ICC < 0.20) [130]. The ICC values obtained for the chosen slices all lie between 0.950-0.986, indicating excellent reliability.

5.3.2 Pharyngeal flow investigation during inspiration - 2D PC-MRI

The 3D surface model of the pharynx with velocity values visualized in Paraview is shown in figure 5.5. The outer surface of the pharynx model should represent no flow; however, as the size of the voxels is big, they also represent the flow within the model. A qualitative analysis of the 3D model shows that the flow at the inlet of the model (at the adapter just before the beginning of the pharynx) is uniform. Moving downstream, the velocity increases due to the reduction in cross-sectional

Table 5.2: ICC with lower and upper bound (LB and UB) values during inspiration at chosen slices.

Slice number	ICC	LB	UB
1	0.975	0.973	0.977
2	0.954	0.950	0.957
3	0.984	0.983	0.985
4	0.986	0.986	0.987
5	0.972	0.971	0.972
6	0.977	0.977	0.978
7	0.983	0.982	0.983
8	0.977	0.976	0.979
9	0.980	0.979	0.980
10	0.981	0.981	0.982
11	0.977	0.976	0.978

area. However, as the cross-sectional area increases downstream to the constriction, the velocity reduces except on the anterior wall, where the velocity value remains high.

A parabolic inlet velocity profile is seen across all three trials (Figure 5.7). The average inlet velocity value for the three trials was 0.042 m/s. This value compared to the theoretical velocity value 0.058 m/s obtained from equation 4.12 was lower by 28%. The inlet velocities in the three trials are as follows, trial 1: 0.047 m/s, trial 2: 0.037 m/s, and trial 3: 0.041 m/s. Due to the presence of air bubbles, an unevenness in the boundaries of the inlet slice is observed in figure 5.6. Additionally, the figure shows voids (black spots). These represent zero velocity value caused due to artifacts in the phase images.

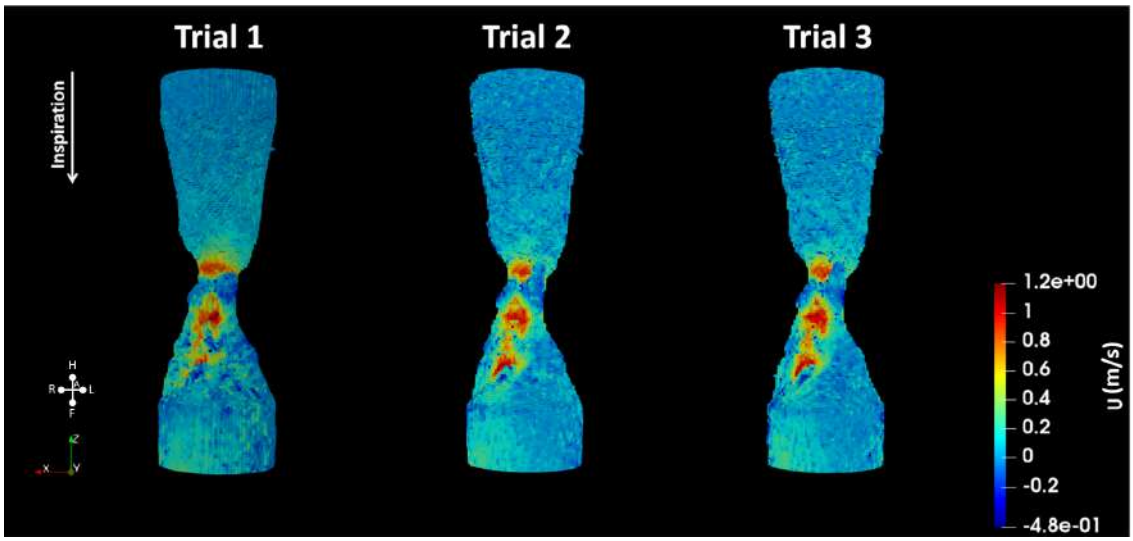

Figure 5.5: 3D model of the pharynx during inspiration obtained from all three trials as visualized in Paraview.

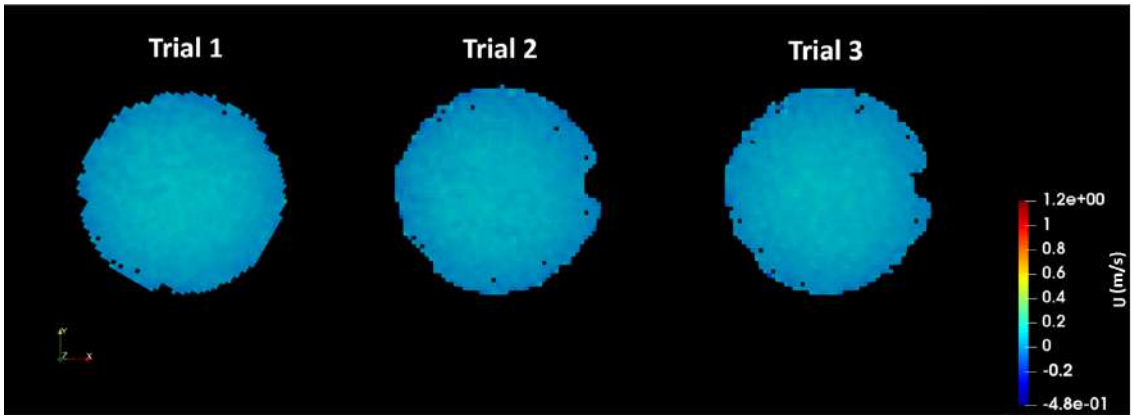

Figure 5.6: Velocity distribution in the inlet slice of the pharynx model during inspiration at all three trials.

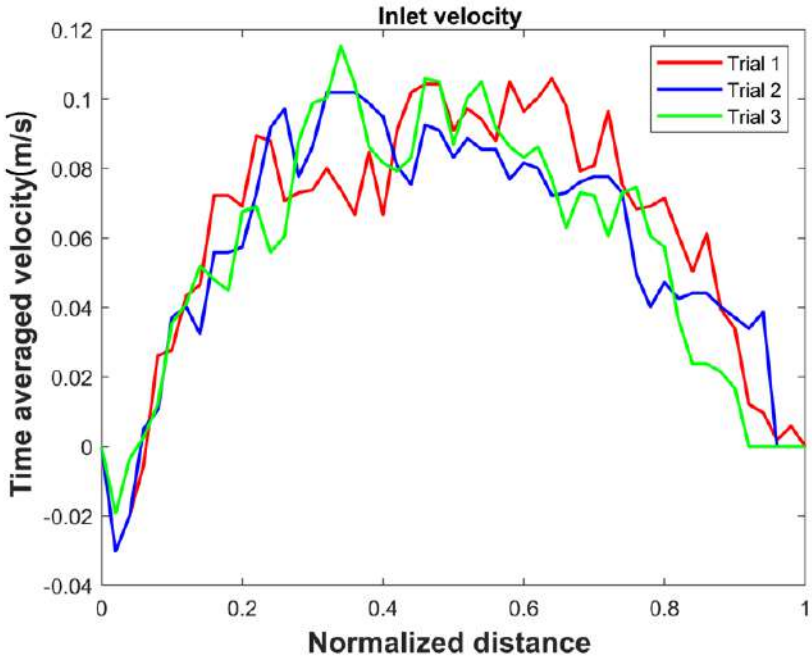

Figure 5.7: Plot of the inlet velocity profile during inspiration obtained in all three trials.

Figures 5.8 and 5.9 represents the flow patterns in the sagittal and coronal slice of the model. The flow entering the pharynx is laminar and fully developed. From the nasopharynx to the oropharynx, the cross-sectional area reduces gradually and accelerates the flow. The pharynx has a minimum cross-sectional area at the tip of the soft palate; therefore, the maximum velocity value is attained here. The cross-sectional area increases downstream to the soft palate and decelerates the flow. This causes the flow to separate, as seen in the stenosis model in chapter 4. However, due to the geometry of the pharynx, the jet produced is not axisymmetric to the model; it instead impinges on the anterior side of the pharynx in the region above the epiglottis. At the epiglottis, a second reduction and expansion of the cross-sectional area are observed, leading to the second acceleration and deceleration of the flow. The jet formed still impinges on the anterior airway. Downstream to the second constriction, the flow becomes uniform again.

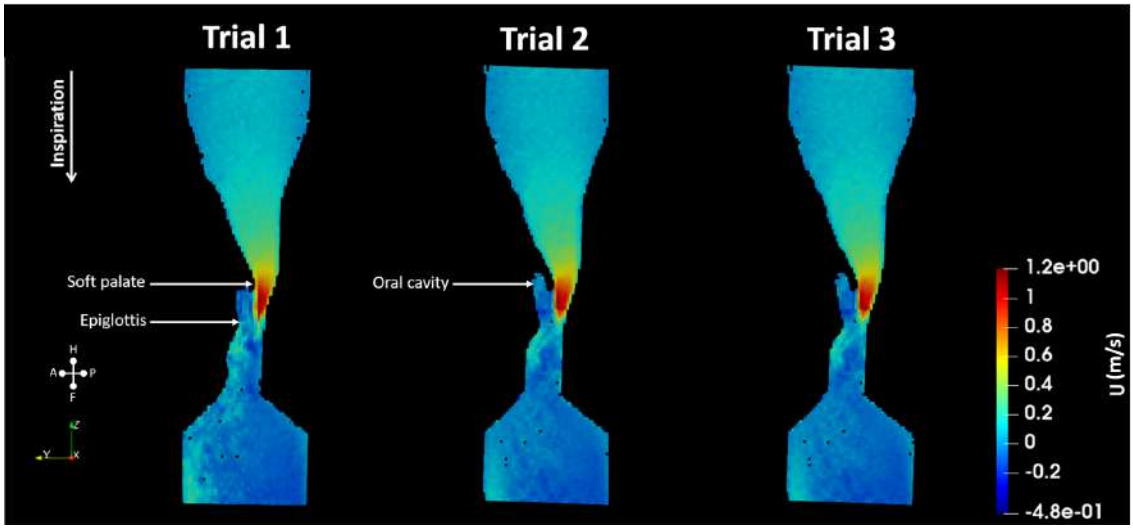

Figure 5.8: Velocity distribution showing flow separation in the coronal slice of the pharynx model during inspiration at all three trials.

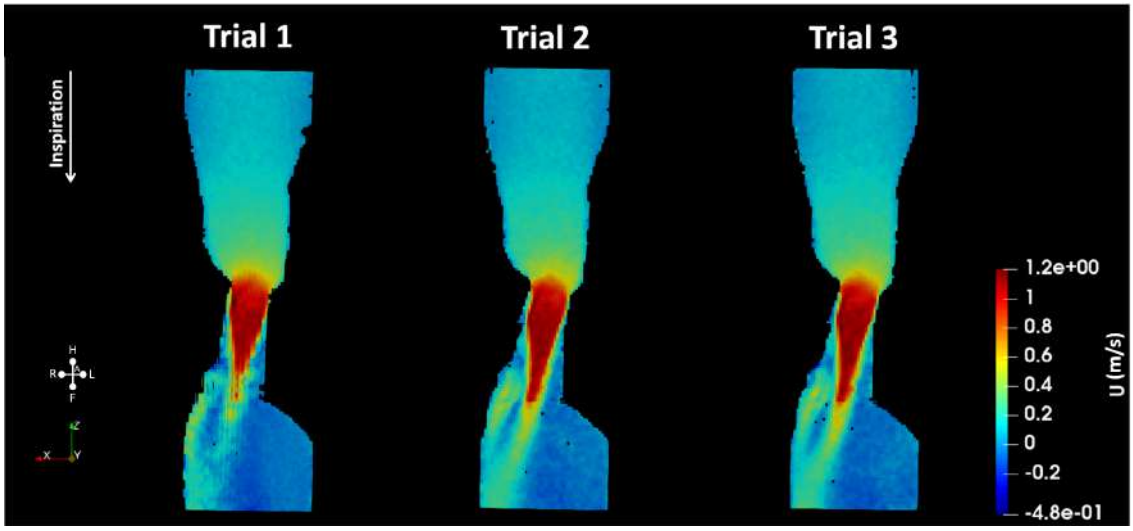

Figure 5.9: Velocity distribution showing flow separation in the sagittal slice of the pharynx model during inspiration at all three trials.

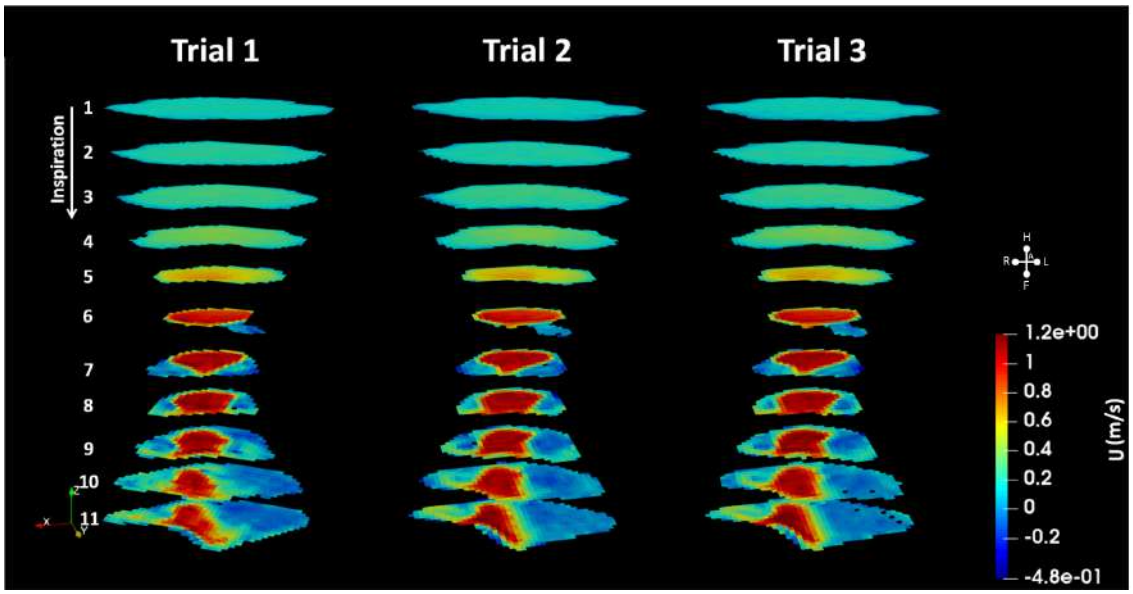

Figure 5.10: Velocity distribution in all chosen slices of the pharynx model during inspiration at all three trials.

Table 5.3: Average velocity and standard deviation values measured during inspiration by 2D PC-MRI in all three trials.

Slice number	**Trial 1 m/s**	**Trial 2 m/s**	**Trial 3 m/s**	**Average m/s**	**Standard deviation m/s**
1	0.142	0.122	0.121	0.128	0.012
2	0.177	0.162	0.160	0.166	0.010
3	0.209	0.194	0.188	0.197	0.010
4	0.303	0.265	0.257	0.275	0.024
5	0.541	0.469	0.470	0.494	0.041
6	0.633	0.634	0.536	0.634	0.001
7	0.542	0.515	0.507	0.522	0.018
8	0.570	0.595	0.587	0.584	0.013
9	0.365	0.415	0.400	0.393	0.026
10	0.284	0.309	0.307	0.300	0.014
11	0.232	0.285	0.270	0.263	0.027

To further analyze the flow patterns in the pharynx, velocity in the chosen slices is

examined (Figure 5.10). Slices 1 to 5, the flow steadily accelerates, and as the cross-sectional area reduces at slice 6, the velocity peaks. In slice 7, the flow separation is observed. The jet formed from the flow separation impinges on the anterior wall of the pharynx, and on both sides of the jet, left-anterior and right-anterior sides, a recirculation region is observed. From slice 7 onwards, the vortical structures around the circumference of the slice on the left-anterior and right-anterior walls are seen. In slice 8, a second decrease in the cross-sectional area causes the velocity values to increase briefly before dropping down as the area increases. On slices 10 and 11, the jet impinges more towards the left of the model, and the strong vortex is seen on the right as compared to the left. The measured velocities at chosen slices averaged across three trials are presented in the table (Table 5.3).

5.3.3 Pharyngeal flow investigation during inspiration - CFD

The airflow in the pharynx is simulated using model in COMSOL Multiphysics software. The results of the same are discussed below. It is to be noted that only the velocity values along z-direction is taken for the comparison with 2D PC-MRI. In figure 5.11, the 3D surface model of the pharynx is presented. As defined by the boundary conditions, the velocity on the surface model is null.

A parabolic flow was observed at the inlet of the model (Figure 5.12 and 5.13). The inlet velocity obtained was 0.169 m/s, which coincides with the theoretical velocity value of 0.164 m/s (please note that the simulation is performed for a 250 ml/s airflow in the pharynx).

In the sagittal and coronal view (Figure 5.14 and 5.15) of the model, flow acceleration in the first half of the model and flow separation downstream to the minimum cross-sectional area due to the sudden deceleration is observed. The jet impingement on the anterior wall is also observed in the figures.

The next section qualitatively assesses the flow pattern in the individual slices across the pharynx. As the cross-sectional area reduces from slice 1, the flow accelerates and peaks at slice 6. In slice 7, as seen in the experiment, the flow separation produces a jet in a region of recirculation. The jet is impinging on the anterior wall (from slices 7-11). However, unlike in the flow measured by PC-MRI, no vortices are observed in the recirculation region as no turbulence model is used.

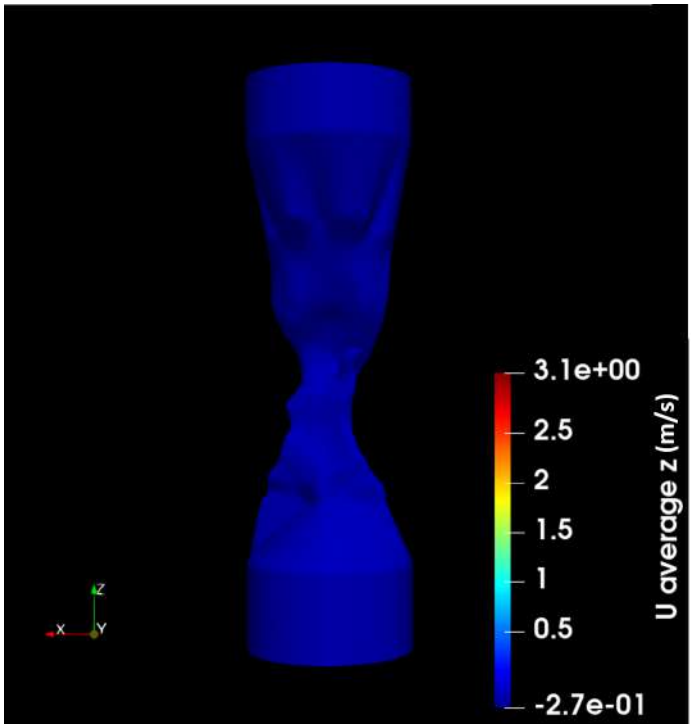

Figure 5.11: 3D model of the pharynx during inspiration obtained from CFD as visualized in Paraview.

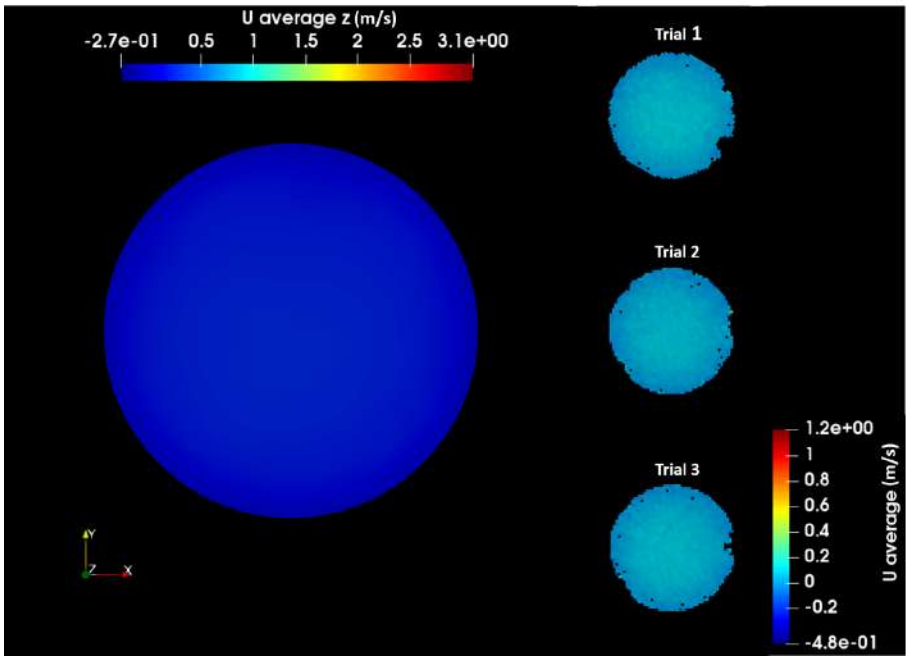

Figure 5.12: Comparison of CFD and 2D PC-MRI velocity distribution in the inlet slice of the pharynx model during inspiration.

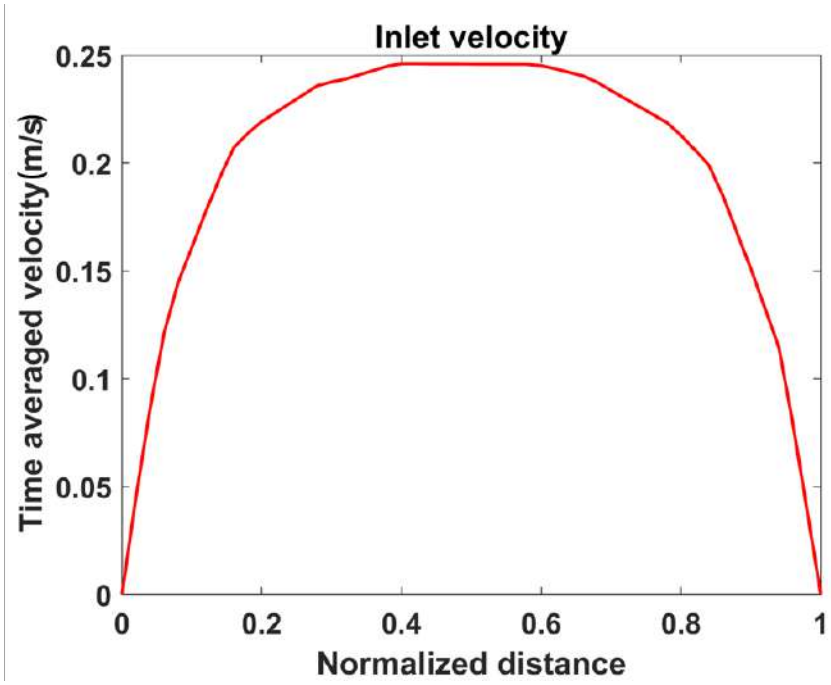

Figure 5.13: Plot of the inlet velocity profile during inspiration obtained from CFD.

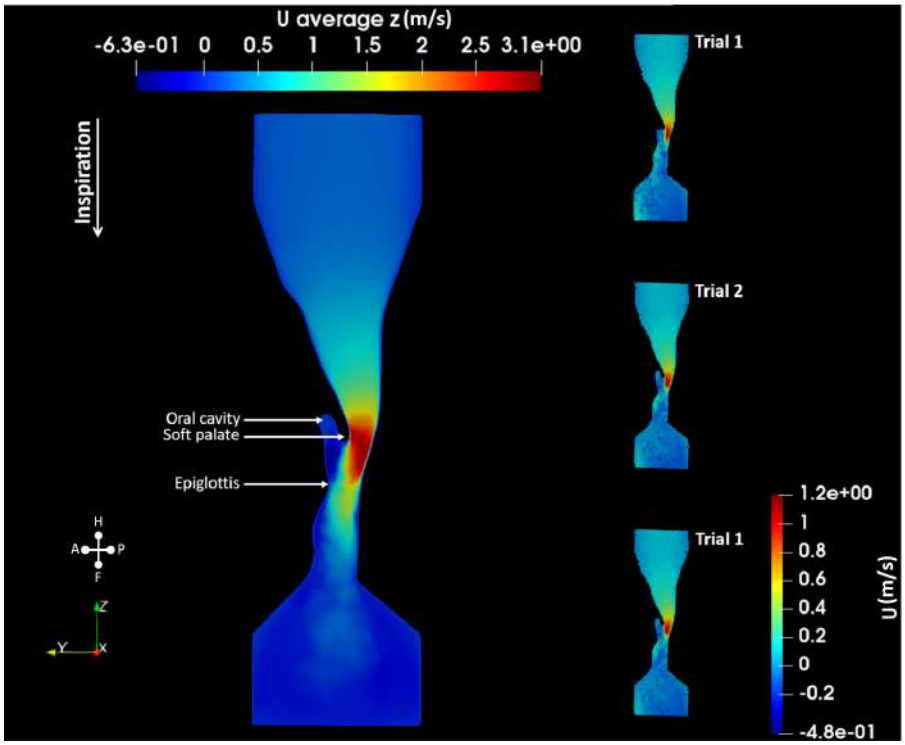

Figure 5.14: Sagittal slice of the CFD and 2D PC-MRI pharynx model showing flow separation during inspiration.

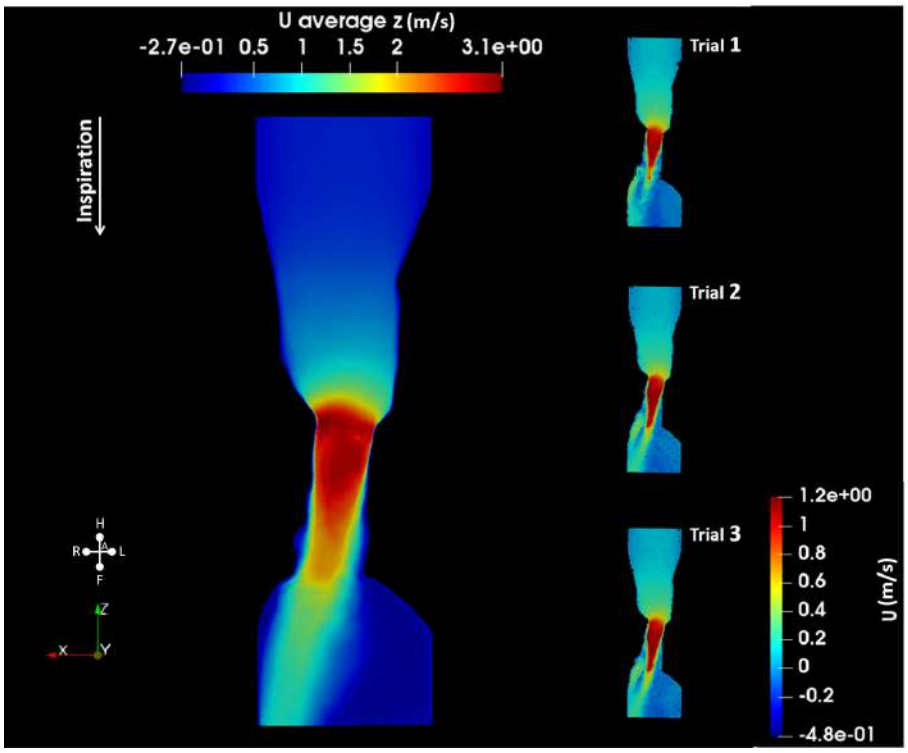

Figure 5.15: Coronal slice of the CFD and 2D PC-MRI pharynx model showing flow separation during inspiration.

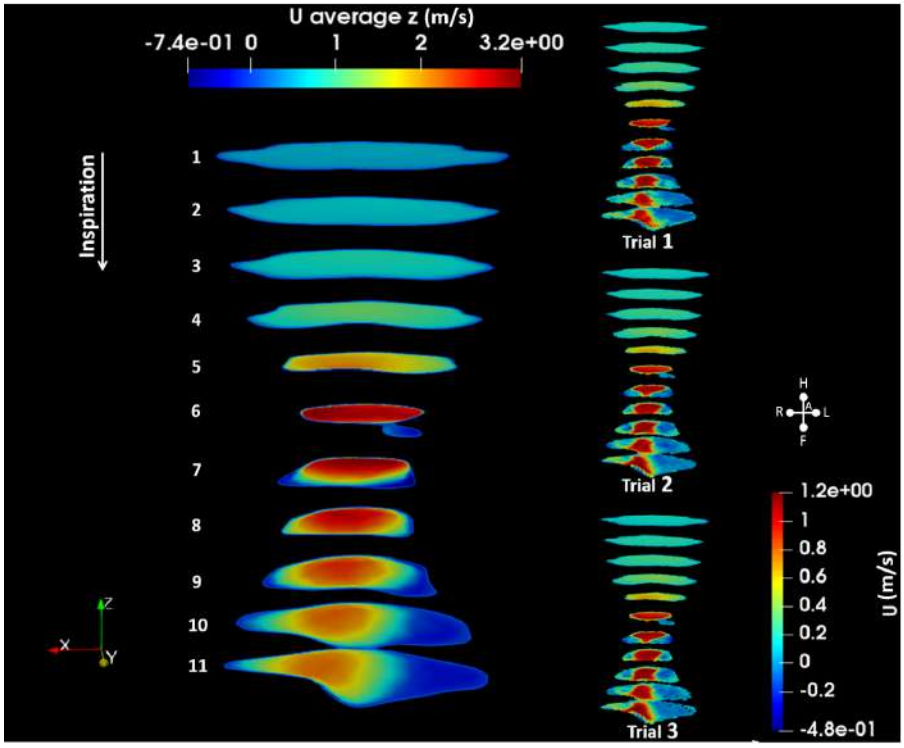

Figure 5.16: Velocity distribution in all chosen slices of the pharynx model during inspiration in CFD and 2D PC-MRI trials.

5.3.4 Comparison of PC-MRI and CFD results

A quantitative comparison between CFD simulation of airflow and PC-MRI measurements of water-glycerol mixture mimicking airflow in the pharynx model is presented below. The normalized time-averaged velocity measured by 2D PC-MRI and Uz velocity from CFD is shown in table 5.4. The 2D PC-MRI and CFD velocities are normalized with their respective inlet velocities. The table shows that overall flow pattern from slice 1 to slice 11 is the same in both: the highest velocity is seen at slice 6 at the smallest surface area, then a dip of velocity value in slice 7 and rise of velocity in slice 8. However, the normalized velocity values were lower in CFD in comparison to the 2D PC-MRI measured velocity values. This is consequence of the lower than expected inlet velocity in the experiment.

Table 5.4: Comparison of normalized 2D PC-MRI measured (average of the three trials) and CFD calculated average velocities in the pharynx model during inspiration.

Slice number	**2D PC-MRI (m/s)**	**CFD (m/s)**	**Standard deviation (m/s)**
1	3.050	2.521	0.374
2	3.960	3.195	0.541
3	4.691	3.787	0.639
4	6.539	5.183	0.958
5	11.751	9.355	1.694
6	15.104	12.769	1.651
7	12.418	9.964	1.735
8	13.900	11.503	1.694
9	9.359	7.811	1.095
10	7.148	5.621	1.080
11	6.253	5.148	0.782

The computational datasets from CFD simulations were imported into Paraview, registered manually to the experimental dataset, and resampled to match the MRI images' resolution. The difference between the velocity measured by simulation awith each of the PC-MRI data set is presented in figure 5.17.

A voxel-by-voxel comparison of both flow velocity fields in the entire model was per-

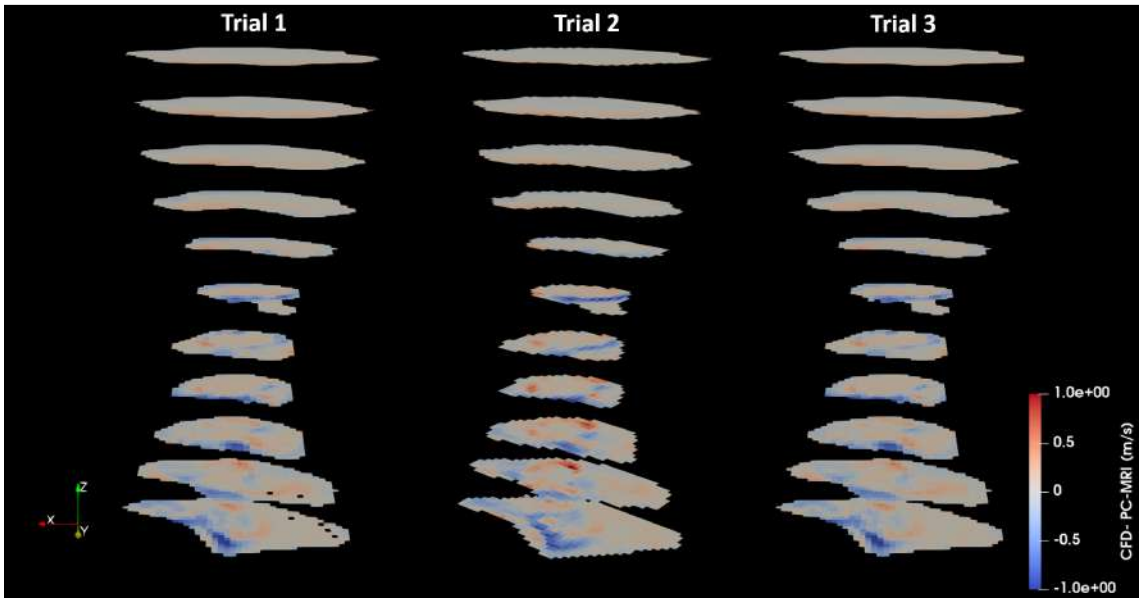

Figure 5.17: Difference plot

formed using linear regression of two methods and Bland-Altman on the difference and average of the two methods in MATLAB (Figure 5.18 and table 5.5).

Table 5.5: Linear regression values from the comparison of 2D PC-MRI (average of the three trials) and CFD velocity values for the entire model during inspiration.

Method	**Slope**	**Intercept (m/s)**	**R^2**	**p-value**
PC-MRI - LES	-1.901	-0.010	0.633	<0.001

The Bland-Altman analysis for the velocity values in the entire pharynx model shows a lot of outliers. This is further seen with low R^2 value of 0.633. Further only a linear regression analysis was used on the eleven chosen slices to assess the agreement (Figure 5.19 and table 5.6).

The comparison shows that all the R^2 values lie between 0.415 - 0.793. A good agreement of the values is seen at the beginning of the model, where the flow is laminar. As the flow separates and becomes unsteady, the drop in the R^2 value is also observed.

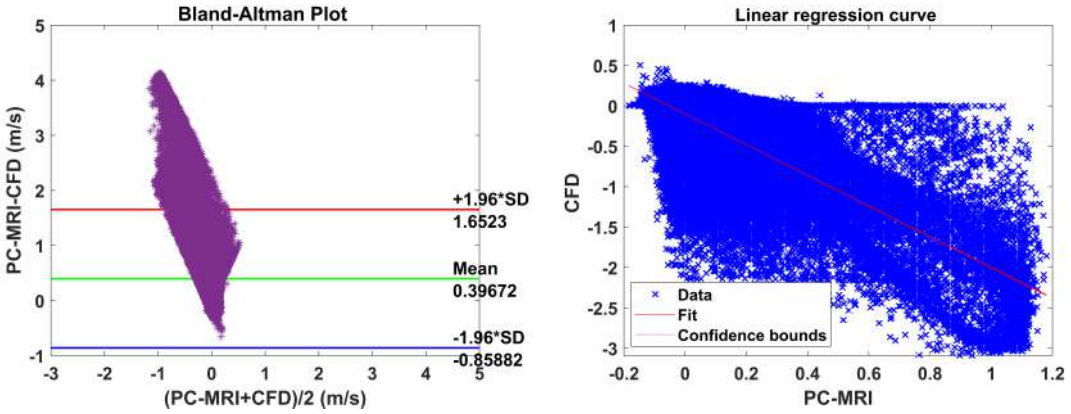

Figure 5.18: Bland-Altman plot and linear regression line of comparison of 2D PC-MRI (average of the three trials) and CFD velocity values of the entire model during inspiration.

Table 5.6: Linear regression values from the comparison of 2D PC-MRI (average of the three trials) and CFD velocity values at chosen slices during inspiration.

Slice number	**Slope**	**Intercept (m/s)**	**R^2**	**p-value**
1	-2.850	-0.010	0.620	p<0.001
2	-3.368	0.093	0.747	p<0.001
3	-3.056	0.052	0.688	p<0.001
4	-3.281	0.179	0.674	p<0.001
5	-3.439	0.396	0.793	p<0.001
6	-2.470	0.187	0.66	p<0.001
7	-2.220	-0.235	0.638	p<0.001
8	-1.626	-0.465	0.489	p<0.001
9	-1.398	-0.453	0.415	p<0.001
10	-1.632	-0.290	0.574	p<0.001
11	-1.568	-0.234	0.498	p<0.001

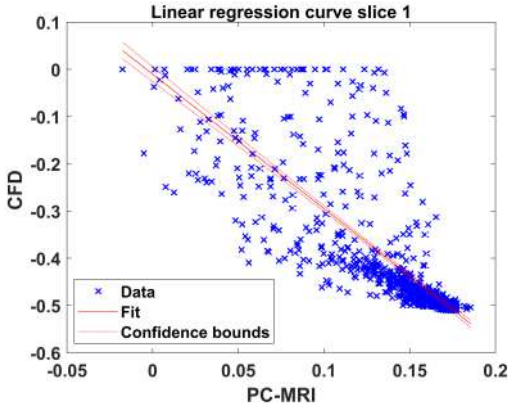
Linear regression curve slice 1
CFD
PC-MRI
Data
Fit
Confidence bounds

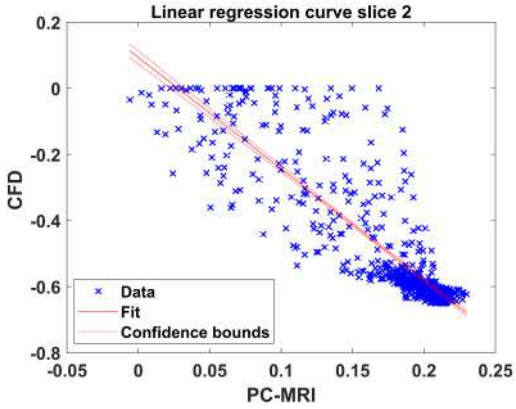
Linear regression curve slice 2
CFD
PC-MRI
Data
Fit
Confidence bounds

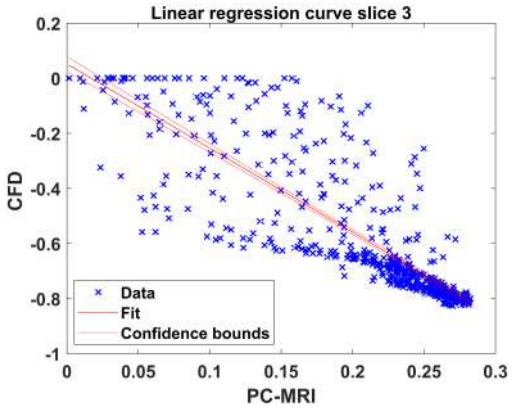
Linear regression curve slice 3
CFD
PC-MRI
Data
Fit
Confidence bounds

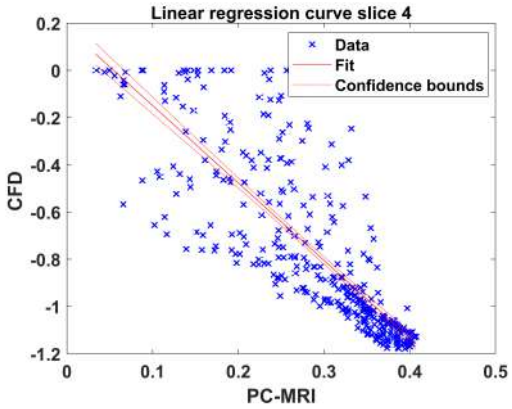
Linear regression curve slice 4
CFD
PC-MRI
Data
Fit
Confidence bounds

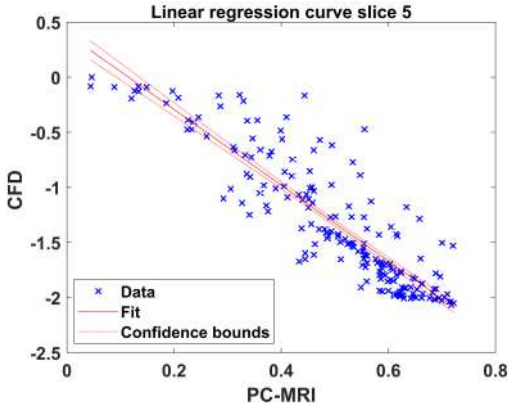
Linear regression curve slice 5
CFD
PC-MRI
Data
Fit
Confidence bounds

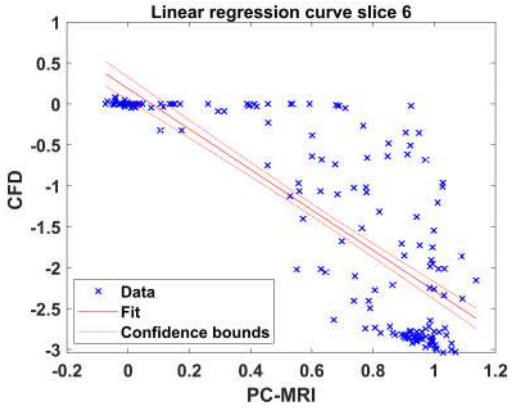
Linear regression curve slice 6
CFD
PC-MRI
Data
Fit
Confidence bounds

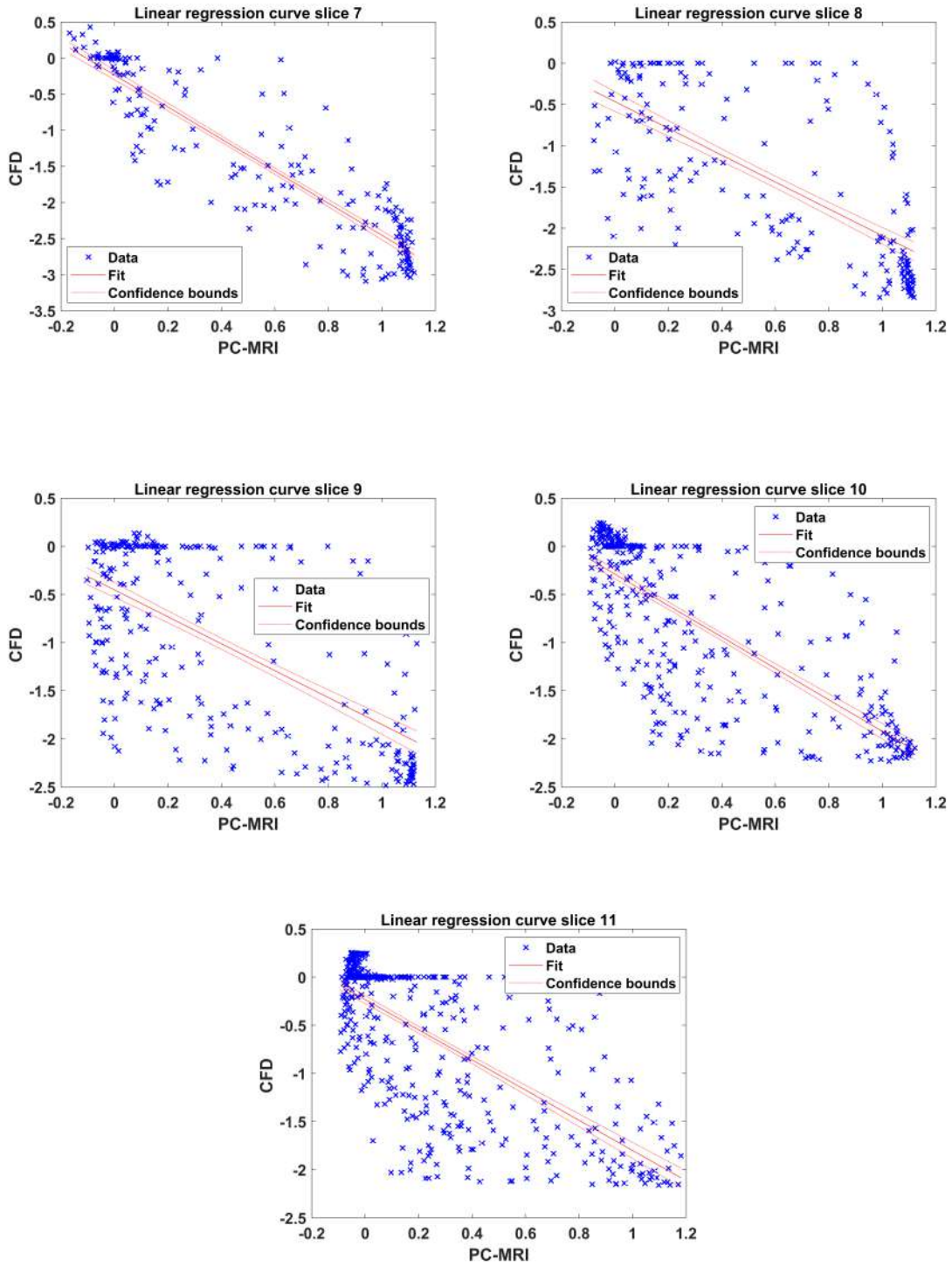

Figure 5.19: Linear regression line of comparison of 2D PC-MRI (average of the three trials) and CFD velocity values at chosen slices during inspiration.

5.3.5 Pharyngeal flow investigation during expiration - 2D PC-MRI

This section illustrates the flow patterns in the pharynx during expiration at a flow rate of 88.62 ml/s. The 3D model of the pharynx during expiration is given in figure 5.20 (The outer surface area is again not zero as in the pharynx model during inspiration). The fluid enters the model uniformly from the laryngopharynx. Unlike in the inspiration model, the anterior region of the model has no region with high velocities (Figure 5.20 left). However, regions with high velocities are observed in the posterior of the model (Figure 5.20 right).

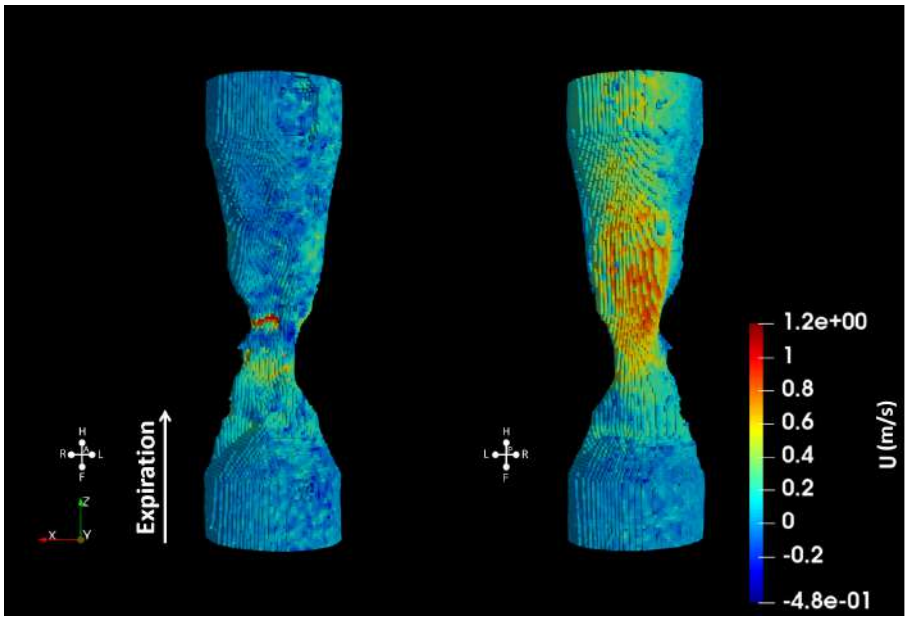

Figure 5.20: 3D model of the pharynx during expiration obtained from 2D PC-MRI as visualized in Paraview (left: front view and right: back view).

The velocity profile at the inlet is studied to ensure the inlet conditions are full-filled. A top-hat profile, instead of parabolic profile, is seen in figure 5.21. The average velocity at the inlet was 0.073 m/s (20% higher than the theoretical value of 0.058 m/s).

The difference in the flow pattern during expiration is visible in the sagittal view of the pharynx (Figure 5.22). The uniform flow at the inlet accelerates as the cross-sectional area reduces from inlet to oropharynx. The velocity reaches its maximum value at the minimum cross-sectional area (at the end of the soft palate). As the cross-sectional area increases, flow separation occurs. However, during expiration,

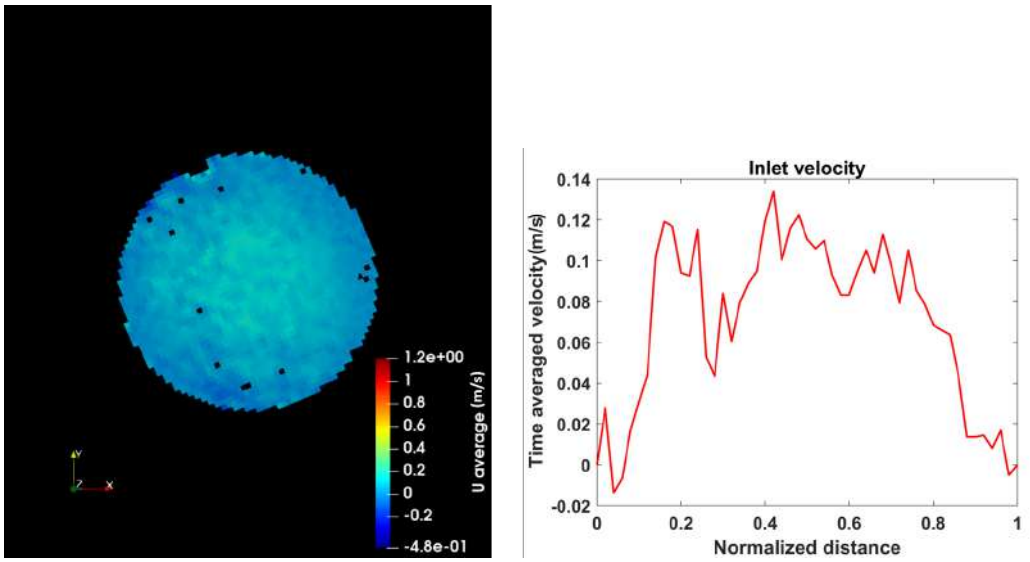

Figure 5.21: Velocity distribution (left) and velocity profile (right) in the inlet slice of the pharynx model during expiration.

the jet formed in flow separation impinges on the posterior wall of the pharynx, and the region of recirculation is formed on the anterior wall. Downstream of the oropharynx, the flow becomes uniform.

The velocity patterns and values are further studied in the individual chosen slices along the pharynx (Figure 5.23 and table 5.7).

The flow is steady and uniform as the fluid enters slice 11 at the bottom. At slice 7, the velocity reaches its maximum. The flow downstream decelerates and forms a jet that impinges on the model's posterior. The jet produced is long and extends beyond slice 1. Large recirculation regions are seen from slices 4 to 1 with the vortex-like structure on both right-anterior and left-anterior. Comparing the average inspiration and expiration velocities (table 5.3 and 5.7) in the chosen slices shows comparable and consistent results. Additionally, the same flow phenomenon is observed as in the case of inspiration, but the jet's location and the recirculation region differ.

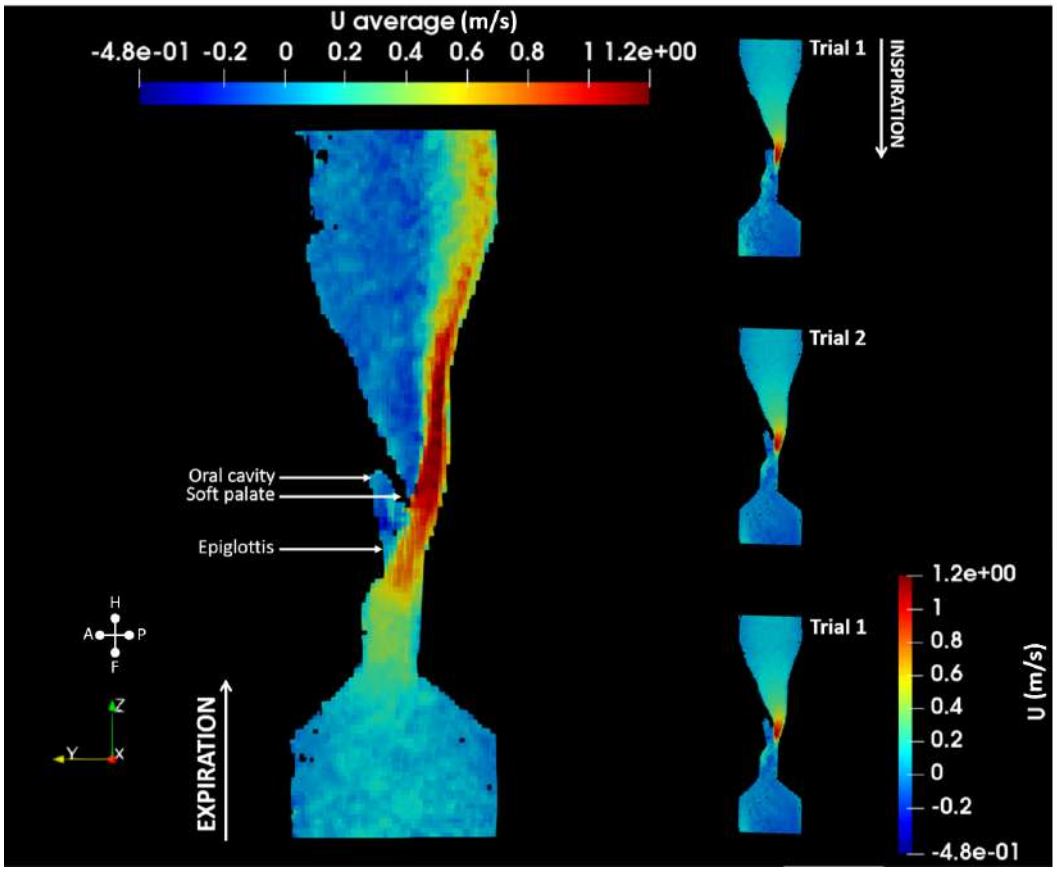

Figure 5.22: Sagittal slice of pharynx model during expiration and inspiration obtained from 2D PC-MRI.

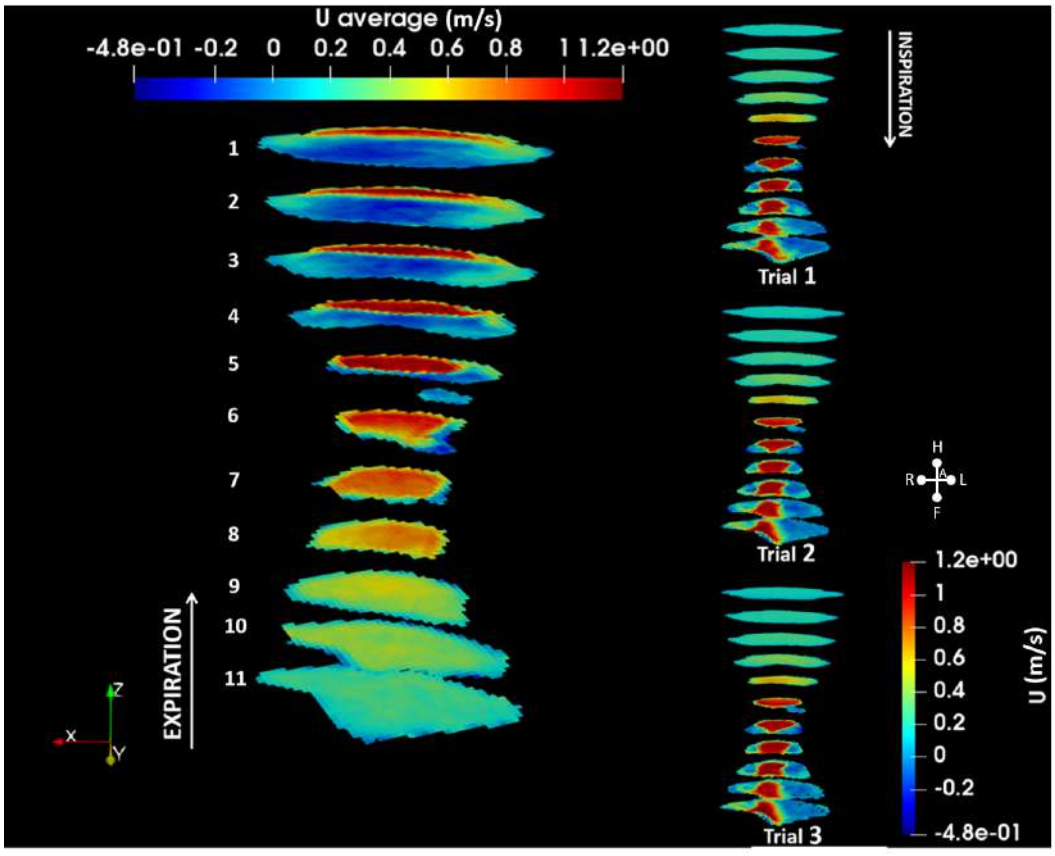

Figure 5.23: Velocity distribution in all chosen slices of the pharynx model during

Table 5.7: Average velocity values measured during expiration by 2D PC-MRI.

Slice number	**Velocity (m/s)**
11	0.212
10	0.306
9	0.370
8	0.582
7	0.606
6	0.529
5	0.481
4	0.318
3	0.231
2	0.199
1	0.167

5.4 Discussion

This section presents a thorough discussion of the results presented in the previous section.

Reliability: Measurement technique and experimental setup

The ICC values obtained for voxel-by-voxel comparison of velocities at chosen slices for the three trials show excellent reliability, with all the values above 0.900. It shows that the velocity measured all three times at different time periods using the 2D PC-MRI technique was consistent despite having a complex geometry and transitional flow regime. As observed in chapter 4, the inlet velocities in all three trials varied from each other and the theoretical value. Also, the inlet velocity was again different from the prescribed value during expiration. The presence of bubbles and the variations produced by the MR-compatible flow pump in the delivery of the prescribed flow rate could have led to the lower velocity value. In general, the results in all chosen slices showed a consistent pattern. An additional change that could improve the reliability of the experimental setup is increasing the entrance length to the model to ensure complete laminarization of the flow to give out more consistent inlet conditions and, therefore, more reliable results.

Pharyngeal flow dynamics

From the analysis of the experiment, it is evident that the model geometry dictates the flow phenomenons in the pharynx, and the flow phenomenons affect the surrounding regions (Figure 5.24). The experimental results for inspiration show the acceleration of the flow as the area reduces at the end of the soft palate. Below the soft palate, the area increases abruptly, causing the flow separation. The flow separation below the soft palate causes recirculation of the flow on the anterior wall of the airway below the oral cavity and at the oral cavity itself. The negative pressure zone in this recirculation region can make the anterior airway (oropharynx and tongue region) more susceptible to collapse. Additional cause for the collapse is, contrary to the posterior airway, where the spine supports the soft tissues, the anterior airway has no solid support. Unlike in axisymmetric stenosis, the jet does not travel through the center of the model but is instead dictated by the geometry of the oropharynx; the pharyngeal jet impinges on the anterior wall of the pharynx above the epiglottis. As the flow stabilizes downstream above the epiglottis, the area reduces and increases abruptly, causing a second acceleration and flow separation at the laryngopharynx. Slices with flow separation show the vortex formation on either side of the jet. These generated vortices might be associated with snoring or soft tissue damage.

The expiration process causes the same flow phenomenon as inspiration but in the opposite direction. The velocity increases from the inlet of the model as the area gradually reduces from the laryngopharynx to the epiglottis. In this case, the maximum velocity occurs at the level of epiglottis. Downstream to the minimum cross-sectional area, the flow separation occurs due to the abrupt change in the area. It causes the formation of the recirculation region above the oral cavity and the pharyngeal jet. During expiration, a recirculation region is formed in the anterior region of the airway, and the pharyngeal jet impinges on the posterior wall of the upper airway. As the spinal cord supports the posterior wall, the likeliness of the collapse during expiration is reduced compared to inspiration. A second reduction in the area is found at the end of the soft palate, but the flow separation continues unchanged. The recirculation region is formed on the anterior wall at the soft palate, which might cause a change in the pressure values enough to cause disturbance in the soft palate region.

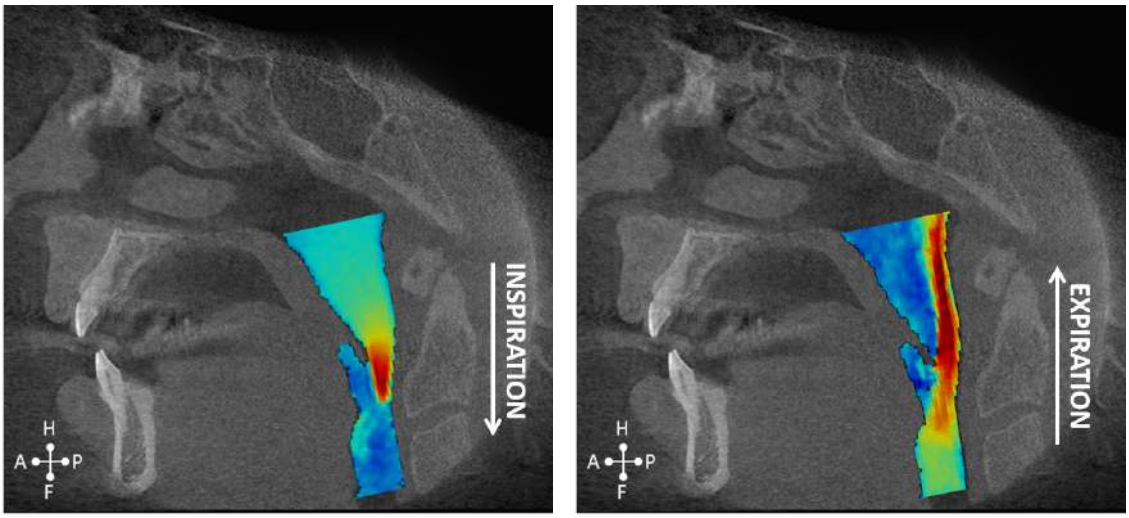

Figure 5.24: Velocity distribution in the pharynx during inspiration and expiration.

Comparison of the PC-MRI and CFD data

This chapter demonstrates the feasibility of using in-vitro PC-MRI as a validation tool for CFD simulations of airflow in the pharynx. A qualitative and quantitative comparison of the CFD and the 2D PC-MRI data was done. Qualitatively, the flow phenomenon occurring and flow pattern from CFD and 2D PC-MRI looks very similar. Except it was observed that the jet produced in CFD was qualitatively longer than that of the experiment. This could arise from the turbulence seen at the inlet profile of the experiments which causes shorter jet. The recirculation region seen in CFD and trials were comparable with one distinct difference that vortices seen in the trials were not visible in the simulation.

Quantitatively comparing the normalized average velocity values of the two methods same flow pattern was observed but the CFD values were lower. This is owed to the normalization of the values with their respective inlet velocities and as discussed before the inlet velocity of the experiment was lower than the excepted value for the prescribed flow rate.

To further analyse the fit of the two data, a linear regression was performed on the 2D PC-MRI and resampled CFD model. A fair agreement between the velocity measured by 2D PC-MRI and those predicted by CFD simulations was achieved with R^2 value of 0.633. For the voxel-by-voxel comparison of velocity values in chosen slices, R^2 value between 0.620 - 0.793 was obtained for slices 1-5. Lower R^2 value, 0.498 - 0.660 was obtained for slices 6-11. These slices correspond to flow

Trial	**SNR**	$\sigma_{\mathbf{v}}$ **(m/s)**
1	7.025	0.235
2	8.945	0.159
3	9.269	0.154

Table 5.8: SNR and error propagation in velocity images.

separation.

This could be because the 2D PC-MRI values are lower due to the partial volume effect at a small cross-sectional area or due to high turbulence that is not well captured by the low spatial resolution of the experiment. Since the geometry of the model is complex, the spatial resolution does have a considerable impact on the results. Therefore, the SNR and velocity error propagation are calculated (Table 5.8).

Residual differences between the CFD simulations and PC-MRI measurements can be attributed to the slight disagreements with the inlet conditions or the noise in the velocity image at regions with high turbulence.

5.5 Conclusion

In conclusion, this chapter illustrated the excellent reliability (ICC value 0.972 - 0.986) of the 2D PC-MRI technique in measuring the velocities of a complex pharynx model during inspiration. The flow analysis during inspiration and expiration gave an understanding of the interdependent roles of the flow phenomenon and the structure of the airway causing OSA. That is, in the pharynx model of the patient suffering from OSA, it was seen that during inspiration, a negative pressure zone in the recirculation region on the anterior wall caused due to the geometry of the airway; this coupled with the intrinsic lack of solid support in the anterior wall-flow phenomenon makes the anterior airway more susceptible to a collapse. Conversely, during expiration, a negative pressure zone in the recirculation region formed due to the change in geometry of the airway causes no collapse due to the solid support on the posterior wall of the airway. The 2D PC-MRI technique was able to visualize the formation of the vortices in the recirculation region very well. This information can add value to the existing clinical assessment. Comparing the 2D PC-MRI data with the CFD data provides a framework for CFD validation using in-vitro MRI velocity data. A voxel-by-voxel comparison of the velocity value from 2D PC-MRI

and CFD for the entire model showed a fair agreement with R^2 value of 0.633, and qualitatively consistent flow patterns were obtained in the simulation.

6

Experimental investigation of flow in stenosis and pharynx model: 4D flow MRI

6.1 Introduction

The flow features in stenosis and pharynx constitute complex flow phenomenons varying in space and time, such as flow separation, formation of vortices, periodic oscillations, and vibrations. These phenomenons have significant implications for cholesterol deposition in the stenosis and collapse of the pharynx during OSA [137] [138]. In the previous chapters 4 and 5, these flow phenomenons were investigated in the 3D volume by measuring the time-average velocity only in the direction of the flow. Although such an evaluation gives a good understanding of the flow phenomenon and average minimum-maximum velocity values in the region of interest, the characteristics and contribution of the other velocity components in the flow dynamics and pathophysiology cannot be measured or visualized. Therefore, this chapter investigates the use of 4D flow MRI to study the flow dynamics in stenosis and pharynx.

The goals of the chapter are as follows,

1. Application of 4D flow MRI to measure all the three velocity components and

calculate WSS in 16-time steps (each time step has a duration of 64 ms) at steady laminar flow (Re 500) in the stenosis model.

2. Statistical evaluation of the reliability of the 4D flow MRI technique using ICC.

3. Validation of the measured velocities and calculated WSS with published data by Ahmed and Giddens [120].

4. Use of 4D flow MRI technique validated with the stenosis model to measure velocities and calculate wall shear stress (WSS) in 16-time steps in the pharynx model at an average inspirational flow rate.

5. Check of reliability of the 4D flow MRI technique in the pharynx model using intraclass correlation coefficient (ICC).

6. Verification of CFD results of airflow in the pharynx model with the 4D flow MRI results.

7. Comparison of 4D flow MRI data with the 2D PC-MRI data in both stenosis and pharynx to analyze the feasibility of 4D flow MRI application in the investigation of flow dynamics in flow models.

6.2 Experiment setup and inlet conditions

6.2.1 Stenosis model

The 3D printed cosine curve stenosis with 75% occlusion from chapter 4 was used for the 4D flow MRI experiment. The experimental setup remained the same as in chapter 4, subsection 4.2.3. Measurements were taken at a steady flow rate of 59.17 ml/s (Re 500). The test fluid used was a water-glycerol mixture (55.27% glycerol by weight) at 25°C.

6.2.2 Pharynx model

The 3D printed pharynx model developed from the reconstructed CBCT image of a patient suffering from OSA (Chapter 5) was used to study pharyngeal flow dynamics. The experiment was conducted with the water-glycerol mixture (55.27% glycerol by weight) at 25°C at an average inspirational flow rate of 88.62 ml/s. The experimental setup was as described in chapter 5, subsection 5.1.3.

6.2.3 MRI acquisition

The 4D flow MRI experiments were performed with a 3T Ingenia Philips MR system with a maximum gradient strength of 45 mT/m using a 108-channel flexible body coil. A three-dimensional, three directionally velocity-sensitive, time-resolved phase-contrast sequence was used for the experiment. The velocity encoding was adapted to the maximal velocity. The sequence was retrospectively electrocardiogram-gated. Synchronizing MR data acquisition with the cardiac cycle is called gating. In retrospective gating, the data acquisition window covers a specific cardiac phase of limited duration, allowing for reconstructing a series of images of the object/ subject. No automated correction of eddy currents and Maxwell terms was performed during online reconstruction.

Imaging parameters used for the scan were as given in table 6.1, table 6.2 and table 6.3.

Table 6.1: Imaging parameters used for the 4D flow MRI experiment.

Scan mode	3D	**Scan technique**	Fast field echo
Contrast enhancement	T1	**Acquisition mode**	Cartesian
Fast imaging mode	Turbo field echo	**Gradient mode**	Enhanced
Flow compensated	No	**SENSE**	Yes
SMART	Yes	**Local phase correction**	No
Quantitative flow	Yes	**Voxel size**	$1.3 \times 1.3 \times 1.3$ mm^3
Cardiac synchronization	Retrospective	**Number of heart phases**	16

6.2.4 Post-processing in MATLAB and Paraview

The measurements obtained in the experiment: magnitude, phase difference, and velocity images, were saved in DICOM format. These DICOM files were then processed in MATLAB R2020b. Thresholding based on the magnitude image was

Table 6.2: Imaging parameters for stenosis model at Re 500.

Slice orientation	Sagittal	**FOV**	$350mm \times 116mm \times 31$ mm
Number of averages	1	**TE**	2.8 ms
TR	6.8 ms	**Flip angle**	7°
Flow rate	59.17 ml/s	$\mathbf{V_{enc}}$	70 cm/s

Table 6.3: Imaging parameters for pharynx model at average inspirational flow rate.

Slice orientation	Coronal	**FOV**	$150mm \times 99mm \times 52$ mm
Number of averages	1	**TE**	1.9 ms
TR	4.1 ms	**Flip angle**	7°
Flow rate	88.62 ml/s	$\mathbf{V_{enc}}$	220 cm/s

done to remove calculation errors due to the variation in the area. Equation 4.13 was used to calculate the velocities (Ux, Uy, and Uz) from the stored values at all 16-time steps. The voxels were reconstructed as hexahedral mesh, and the calculated velocities were stored in the cells of the meshes. The quantification and visualization of the velocities were performed in Paraview.

6.2.5 Post-processing in GTFlow

WSS is the tangential force of the flowing blood or air on the vessel or airway wall. The WSS quantification and visualization were performed using GTFlow, Gyrotools, Zurich, Switzerland (version 3 and version 4). The WSS was calculated as follows; manual segmentation of the images was performed in GTFlow by thresholding the magnitude images. B-splines were then used to choose the region of interest (ROI) in the axial slices for which the WSS was calculated 6.1.

$$\overrightarrow{\tau} = 2\mu \overrightarrow{\epsilon} \cdot \overrightarrow{n} \tag{6.1}$$

The μ corresponds to the dynamic viscosity of the water-glycerol mixture used in the experiment, $\overrightarrow{n}$ is the inward unit normal, and $\overrightarrow{\epsilon}$ is the deformation tensor. The deformation tensor was calculated from the derivative of the velocity on the segmented contour.

6.2.6 Statistical analysis

A voxel-by-voxel comparison of all three velocity components was made at all chosen slices to check the agreement of the velocity values between the three experiments. This agreement of the values was quantified with the intraclass correlation coefficient (ICC) using a 2-way mixed-effects model with an absolute agreement (95% confidence interval) in IBM SPSS software (version 28). Bland-Altman chart and linear regression were used to assess the correlation between 4D flow MRI and 2D PC-MRI measurements in MATLAB R2020b.

6.3 Results and analysis

The 4D flow MRI experiment was conducted at laminar flow condition (Re 500) in stenosis and average inspirational flow rate in the pharynx. After the MRI acquisition, the images were saved as DICOM images and were transferred to a local computer for post-processing with MATLAB and Paraview. The commercially available software GTFlow was used to calculate the WSS values. The experiment was conducted and analyzed three times for both models to check the reliability of the measurement technique. The flow analysis in the stenosis model was done at chosen slices -1d (inlet), 0d, 1d, 2.5d, 4d, 5d, and 6d, where d is the unoccluded diameter of the stenosis. These distances are calculated from the throat of the stenosis (Chapter 4, figure 4.3). As for the pharynx model, 11 slices along the model was chosen (Chapter 5, figure 5.4).

6.3.1 Stenosis model

6.3.1.1 Reliability analysis

The voxel-by-voxel analysis for all the three components of velocities (time-averaged) in the entire stenosis is given in table 6.4.

In the stenosis, an excellent reliability (ICC $>$ 0.843) is obtained between the three models for all the components of velocities. However, the x-component had a slightly lower ICC value in comparison to the other two components.

Table 6.4: ICC with lower and upper bound (LB and UB) values for x-, y- and z-component in the stenosis model at Re 500.

Component	ICC	LB	UB
x-component	0.843	0.839	0.846
y-component	0.935	0.934	0.935
z-component	0.996	0.996	0.996

6.3.1.2 Velocity analysis in the stenosis model at Re 500

Figure 6.1, represents the 3D model of the stenosis at Re 500 as visualized in Paraview. Each voxel in the model represents the magnitude of velocity averaged over 16 time steps (each time step is 64 ms). As in chapter 4, figure 4.4, the velocities at the throat of the stenosis are higher in comparison to the rest of the model. The velocities on the surface of the model are not null due to the bigger voxel size.

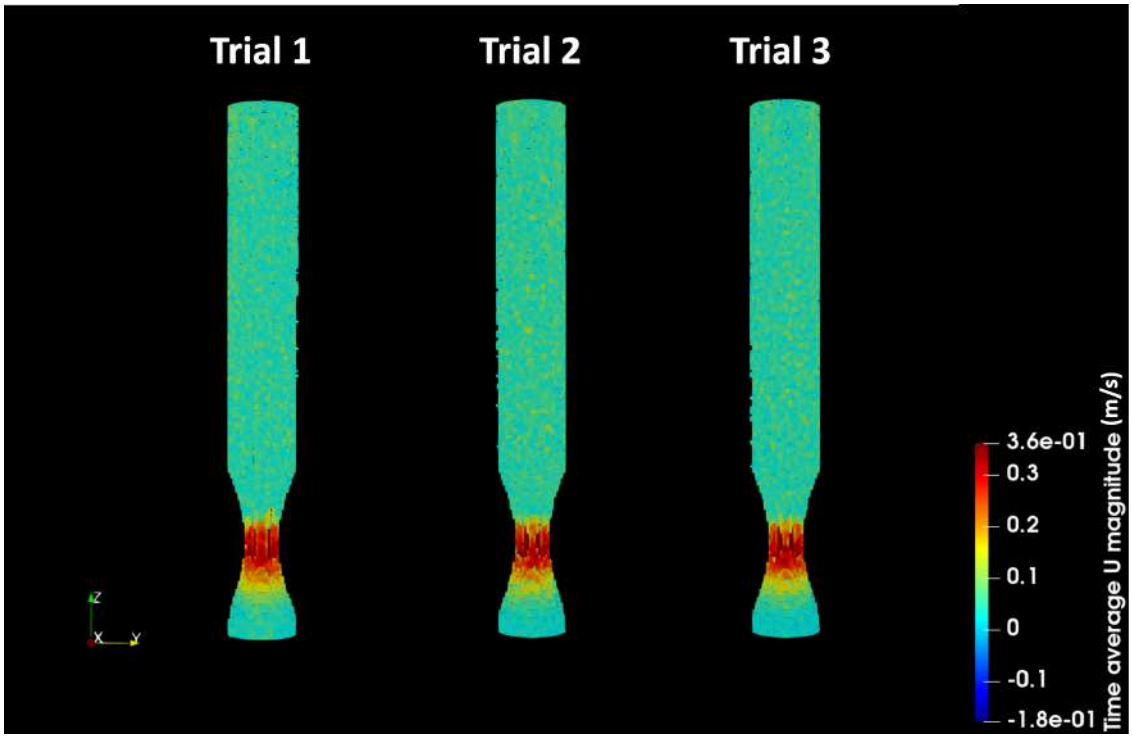

Figure 6.1: 3D model of the stenosis model at Re 500 obtained from the three trials as visualized in Paraview.

The time-average inlet magnitude of velocity are 0.103 m/s, 0.103 m/s, and 0.100 m/s (Figure 6.2). These are 10.8 %, 10.8 %, and 13.6 % lower than the theoretical

velocity, 0.112 m/s calculated from the prescribed flow rate (Equation 4.12). The average velocities of the x-, y- and z-component are 0.002 m/s, 0.008 m/s and 0.099 m/s, respectively The values show that the flow is majorly in z-direction. The variation of the time-averaged velocity magnitude within the 16 time steps in each trial is given by the standard deviation values 0.407 m/s (with the velocity varying between a minimum and maximum velocity value of 0.094 - 0.108 m/s), similarly 0.299 m/s (with the velocity varying between a minimum and maximum velocity value of 0.095 - 0.107 m/s) and 0.225 m/s (with the velocity varying between a minimum and maximum velocity value of 0.091 - 0.102 m/s) at trial 2 and trial 3. The values indicate that the inlet flow is not perfectly steady, but there are minor variations with time. Figure 6.3 shows the velocity (magnitude) profile along the diameter in x-direction. The magnitude of the velocity at 16 time steps and the time-average velocity are depicted. The velocity profile is a parabolic curve at all steps, indicating laminar flow.

In figure 6.4 the magnitude of velocity in the sagittal slice is presented. The flow pattern is similar to that measured by the 2D PC-MRI method (Chapter 4, figure 4.9). The flow at the inlet is parabolic, and the velocity increases as it flows through the stenosis. The maximum velocity is achieved at the center of the stenosis. The flow separates as it flows out of the stenosis due to the abrupt increase in area. The jet formed travels down the pipe, and as seen in the 2D PC-MRI figure, the tip of the jet slightly orients itself towards the wall of the pipe. The same observation is made for velocity patterns generated by z-component in figure 6.7. The velocity pattern generated by x- and y- velocity components are visualized in figures 6.5 and 6.6. Velocity in the x-direction is low; however, significant x-component contribution is seen along the wall downstream to the throat up to 1.5d. After this point, the x-component distributes uniformly until approximately 8.5d. The y-component of the velocity is high at the inlet. Inside the stenosis, the y-component is seen moving along the walls (south-west direction) and then towards the center of the stenosis till 2.5d before dissipating. Around 7.5d, the y-component is high along both sides of the wall. The length of the jet is observed to be 9.5d - 10d. The time variation of the velocity in the sagittal view shows the z-component oscillating at the tip of the jet. The x- and y-component both show slight variations. The centerline velocity profile for all the three trials show a steady velocity value of varying between 0.490 - 0.500 m/s from 0d to 6d (Figure 6.8).

The time-averaged magnitude of velocity for all three trials is given in the table 6.5. At all the chosen slices, the velocity values obtained are congruent. The velocity

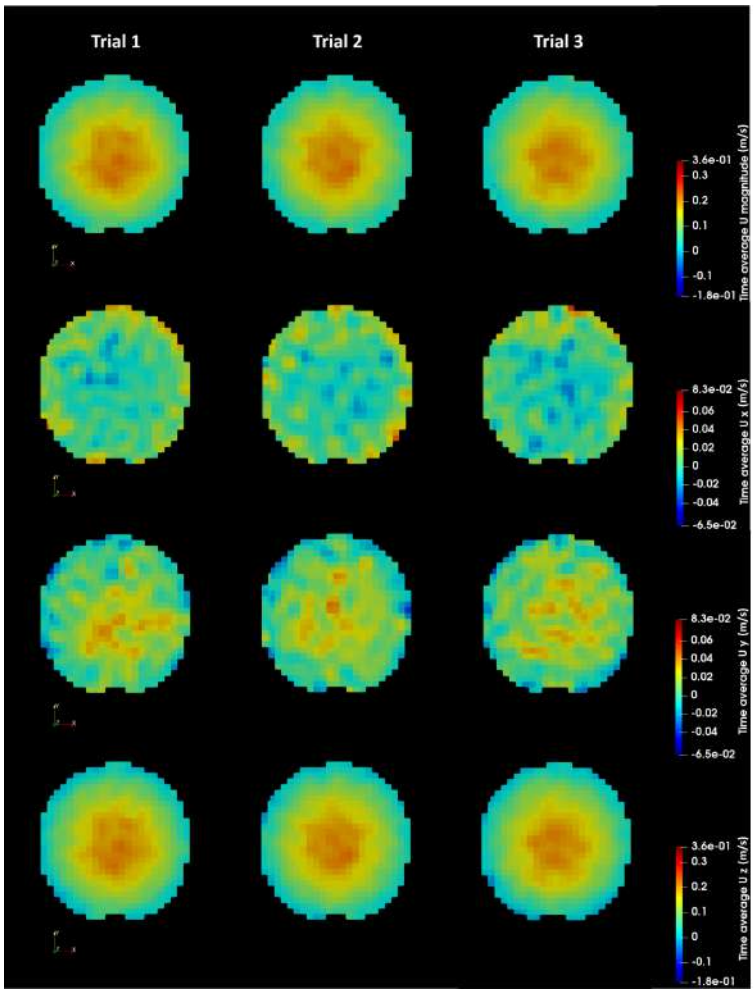

Figure 6.2: Velocity distribution (magnitude, x,y,z-component, m/s) at inlet in all three trials.

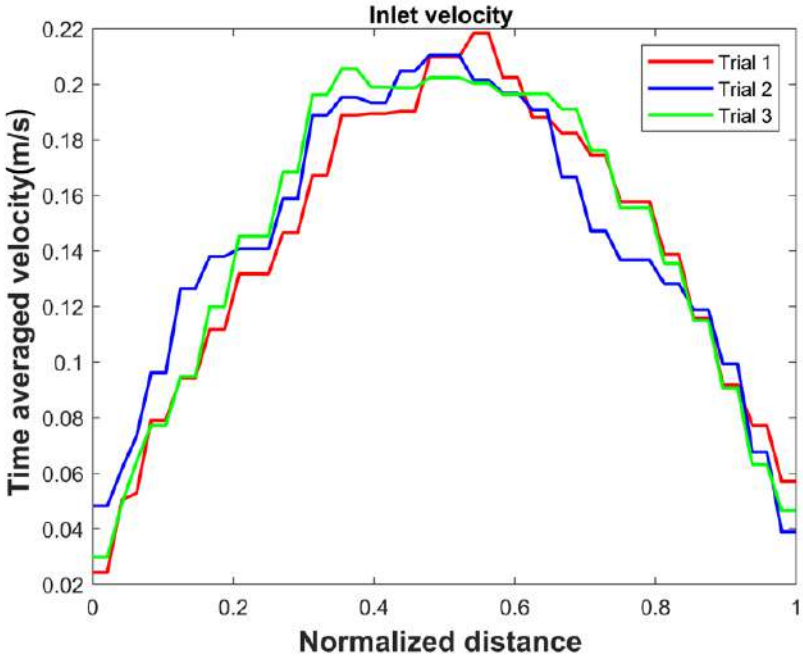

Figure 6.3: Plot of the time-averaged inlet velocity (magnitude of velocity, m/s) profile at Re 500 obtained in all three trials.

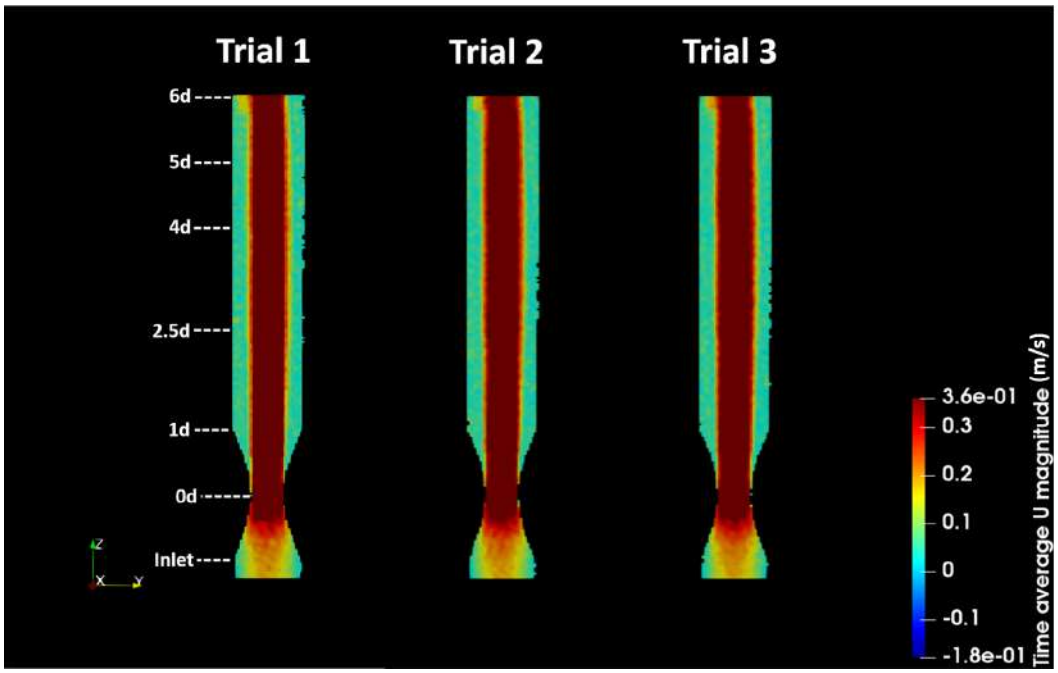

Figure 6.4: Time-averaged velocity distribution (magnitude of velocity, m/s) showing flow separation in the sagittal slice (y-z view) of the stenosis model at Re 500 at all three trials.

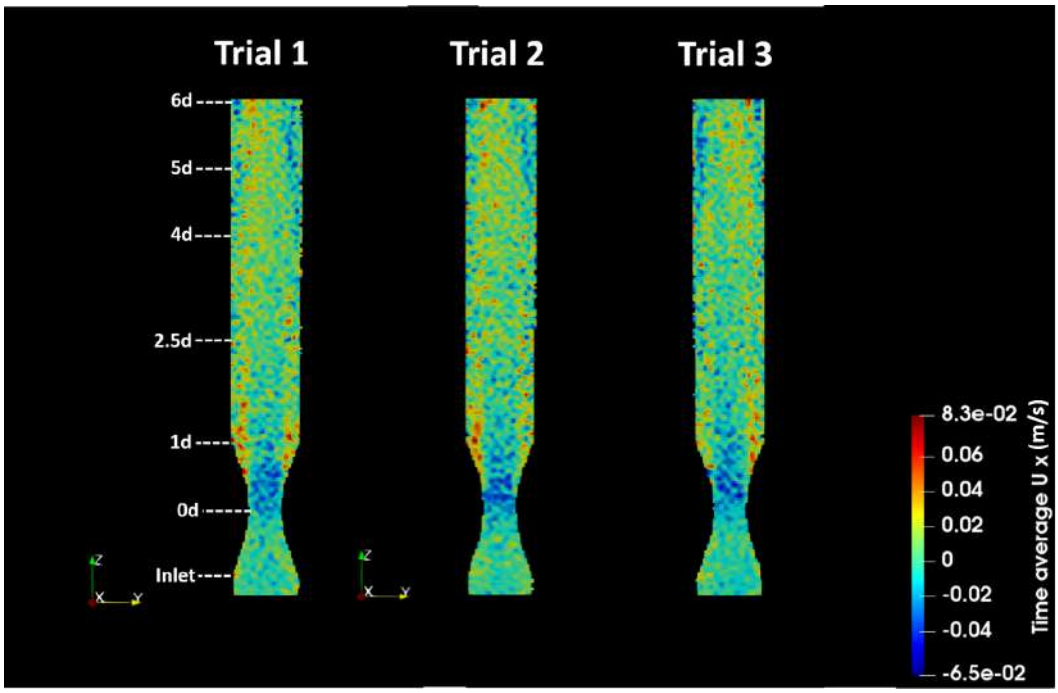

Figure 6.5: Time-averaged velocity distribution (x-component of velocity, m/s) showing flow separation in the sagittal slice (y-z view) of the stenosis model at Re 500 at all three trials.

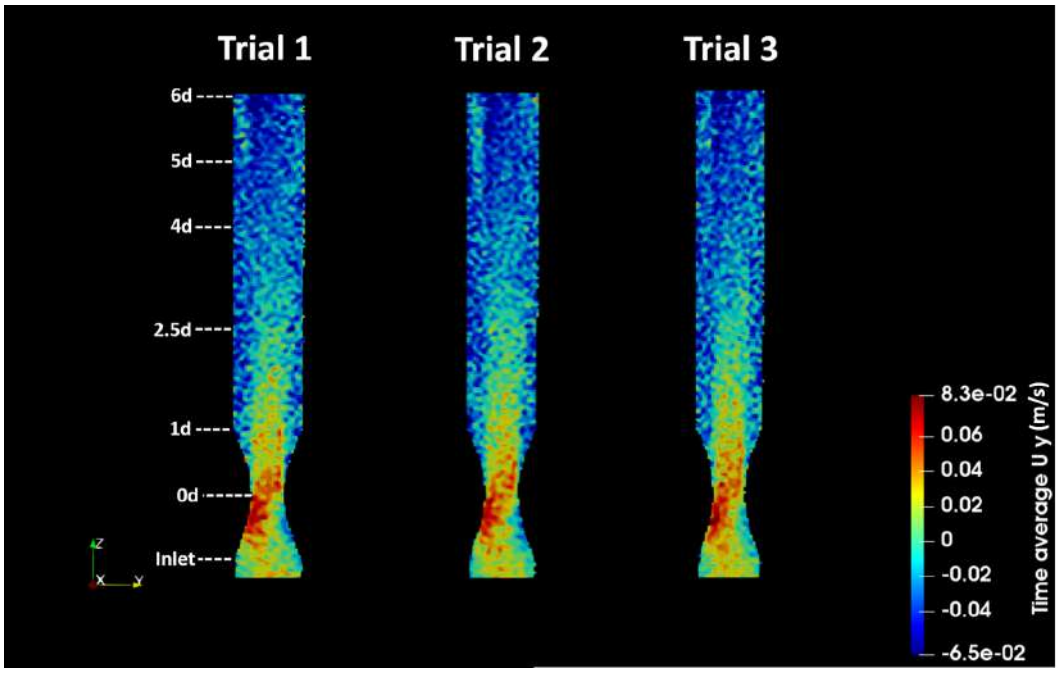

Figure 6.6: Time-averaged velocity distribution (y-component of velocity, m/s) showing flow separation in the sagittal slice (y-z view) of the stenosis model at Re 500 at all three trials.

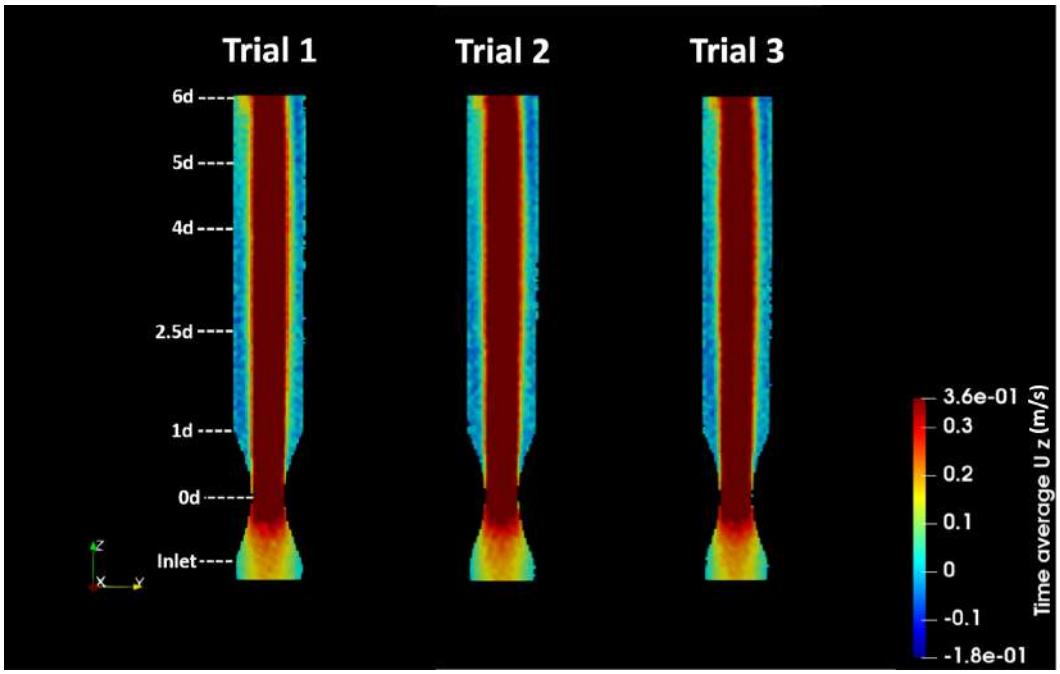

Figure 6.7: Time-averaged velocity distribution (z-component of velocity, m/s) showing flow separation in the sagittal slice (y-z view) of the stenosis model at Re 500 at all three trials.

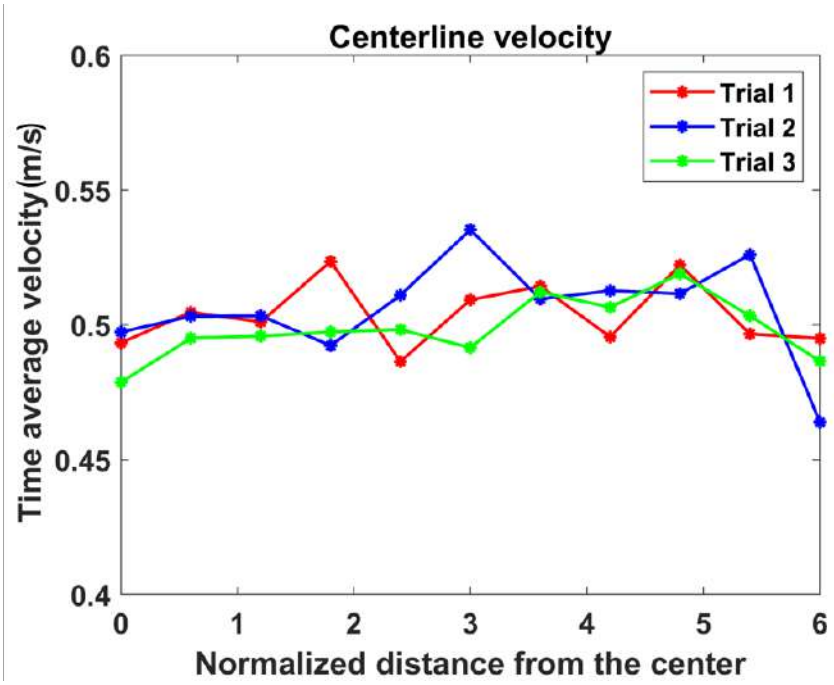

Figure 6.8: Centerline time-averaged velocity (z-component of velocity) profile plotted from 0d to 6d of the stenosis model at Re 500 for all three trials.

value at 0d is approximately four times higher than the inlet velocity at the center. At 1d and 2.5d, the velocity returns to the velocity value seen at the inlet. A steady increase in the velocity is seen from slices 4d to 6d.

The average time-averaged velocities (all components) from the three trials is presented in table 6.6. The x-component of the velocities values are low except at 0d and 1d. At 0d, the velocity value is relatively high and is opposite to the prescribed flow direction. However, aside from 0d, at all other slices, the x-component of the velocity is in the flow direction. As for the y-component, except for the slice at 0d, the direction of y-component velocity is opposite to the prescribed flow direction in all the chosen slices. The y-component values are higher than the x-component except at 1d. The z-component velocity values are all positive (in the flow direction), significantly higher in value, and follow the pattern of the magnitude of velocities.

The velocity pattern in the chosen slices is examined in the figures 6.9 to 6.14. At 0d, the velocity is maximum with a significant contribution from z-component. At 1d, the jet is formed at the center of the slice with a recirculation region around it. In this slice, the z-component has a significant contribution, and the y-component is prominently observed at the center of the jet. A similar pattern is also observed at 2.5d, but here the shape of the jet changes from circular to almost elliptical,

Table 6.5: Time-average velocity (magnitude of velocity) and standard deviation values measured at Re 500 in all three trials.

Slice number	**Trial 1 (m/s)**	**Trial 2 (m/s)**	**Trial 3 (m/s)**	**Average (m/s)**	**Standard deviation (m/s)**
0d	0.435	0.427	0.430	0.430	0.166
1d	0.117	0.120	0.116	0.118	0.405
2.5d	0.116	0.116	0.115	0.116	0.201
4d	0.129	0.125	0.123	0.127	0.092
5d	0.132	0.129	0.130	0.130	0.178
6d	0.140	0.126	0.137	0.138	0.157

Table 6.6: Time-average velocity magnitude and velocity value in all three directions measured at Re 500 in all three trials.

Slice number	**Ux (m/s)**	**Uy (m/s)**	**Uz (m/s)**	**Umag (m/s)**
0d	-1.921	3.700	42.828	43.074
1d	1.242	-1.200	11.657	15.172
2.5d	0.805	-2.365	11.281	15.350
4d	0.628	-3.365	12.279	15.555
5d	0.500	-3.812	12.700	15.808
6d	0.451	-3.829	13.226	16.163

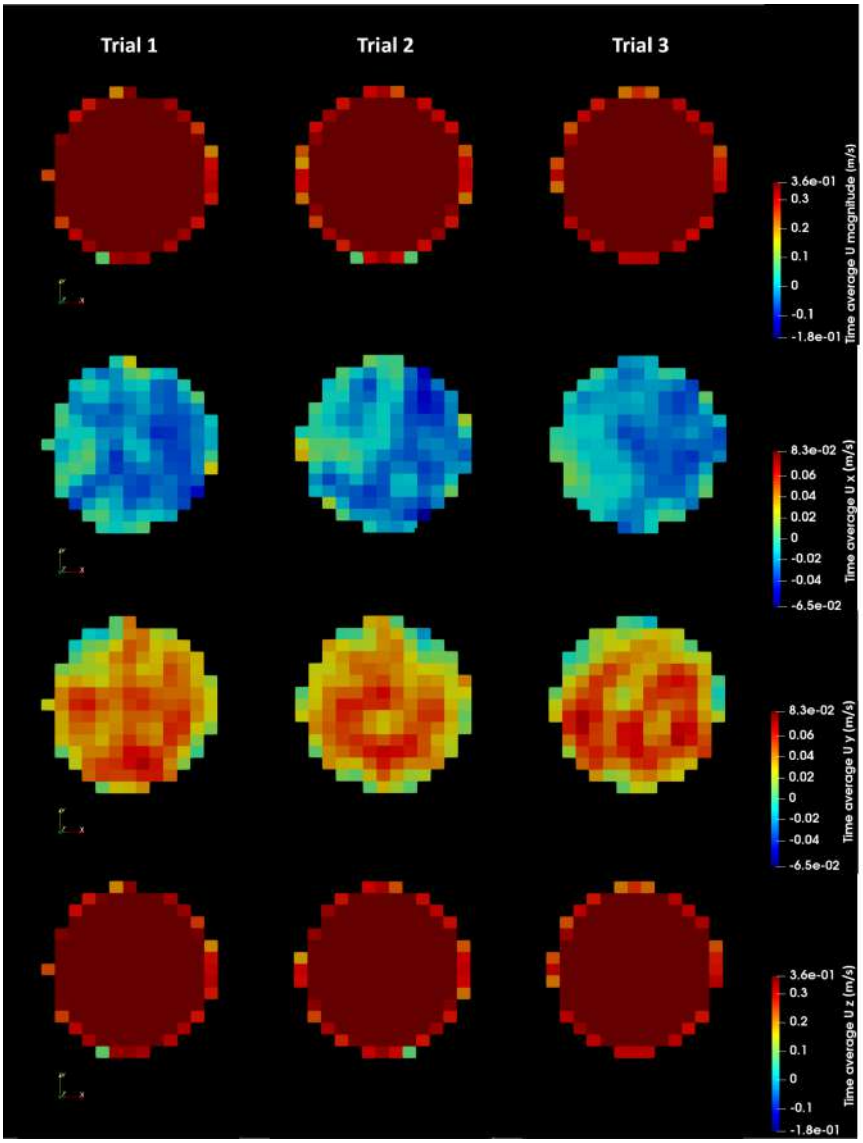

Figure 6.9: Velocity distribution (magnitude, x,y,z-component (m/s) at slice 0d in all three trials.

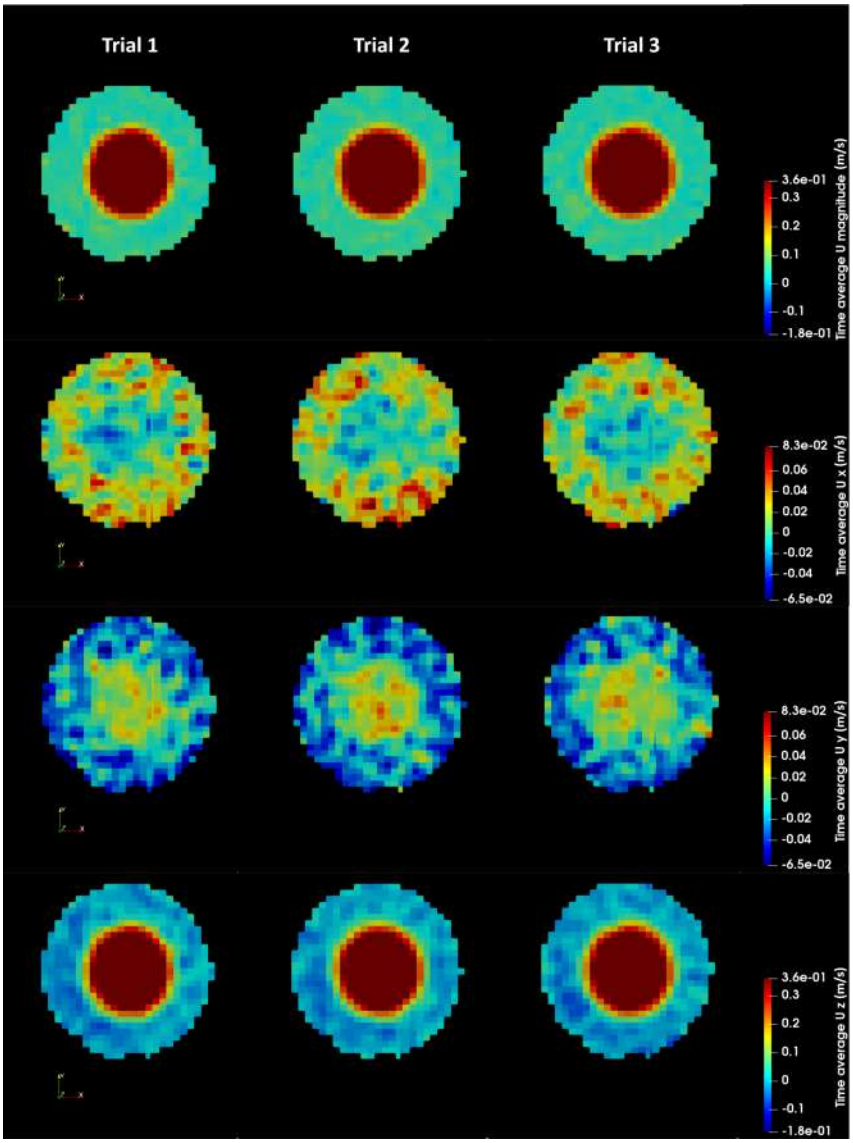

Figure 6.10: Velocity distribution (magnitude, x,y,z-component (m/s) at slice 1d in all three trials.

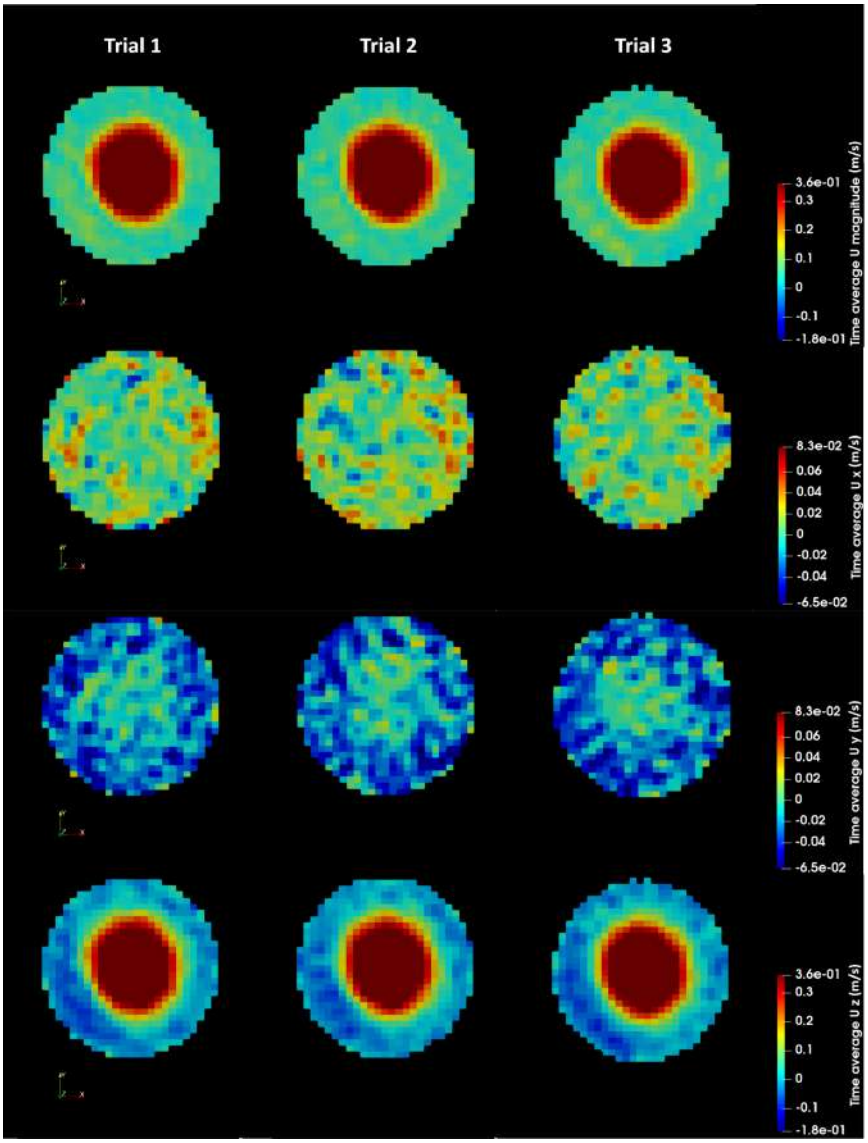

Figure 6.11: Velocity distribution (magnitude, x,y,z-component (m/s) at slice 2.5d in all three trials.

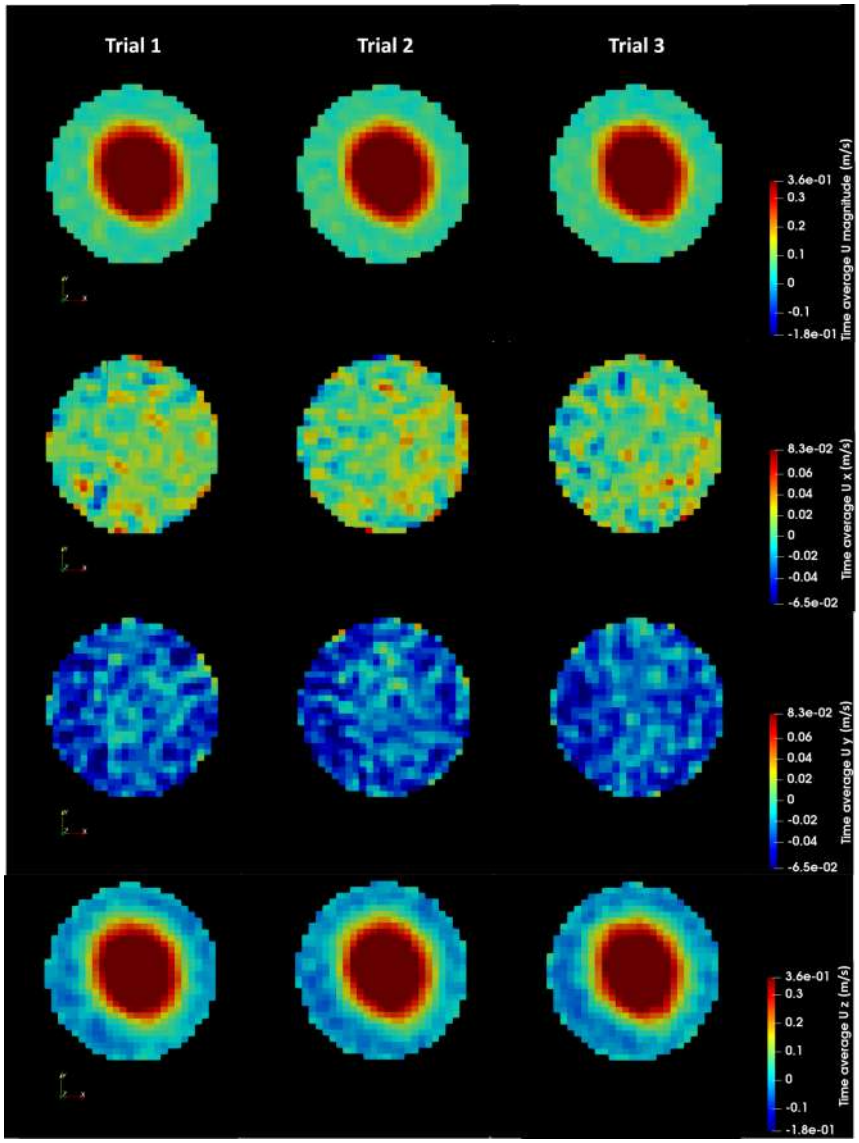

Figure 6.12: Velocity distribution (magnitude, x,y,z-component (m/s) at slice 4d in all three trials.

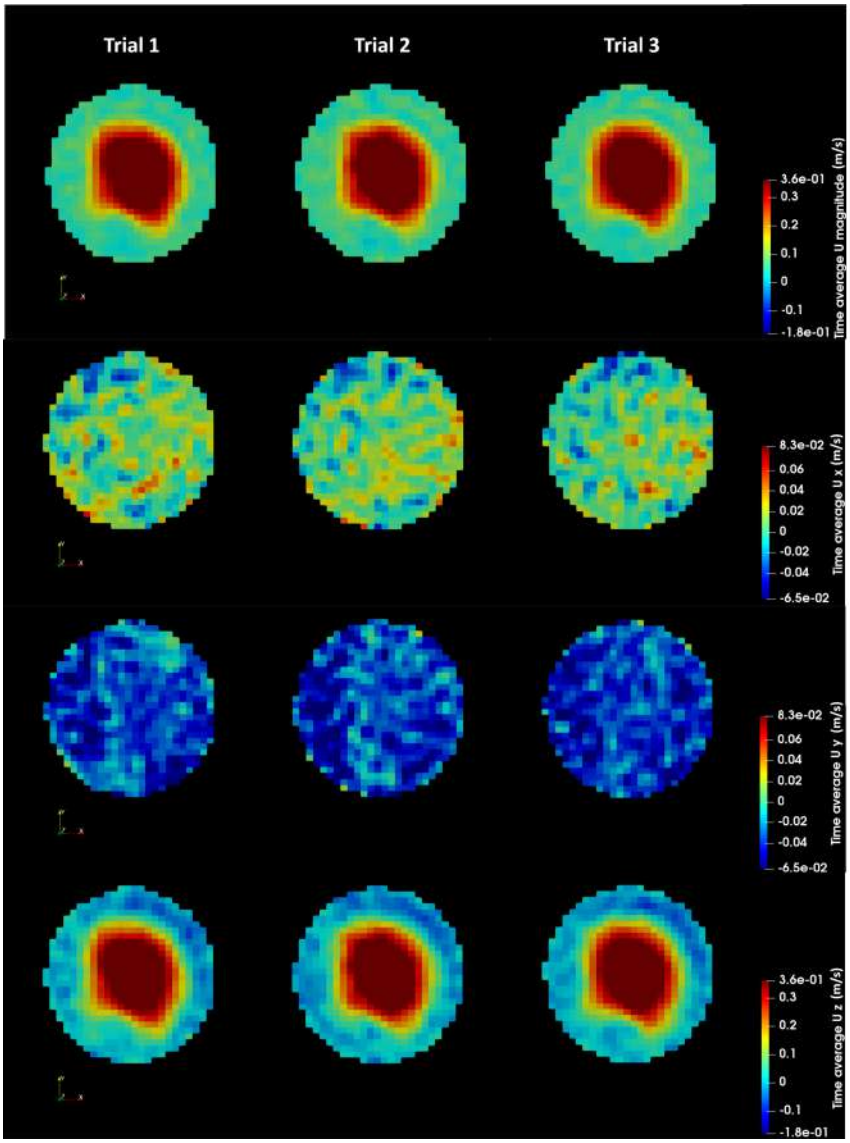

Figure 6.13: Velocity distribution (magnitude, x,y,z-component (m/s) at slice 5d in all three trials.

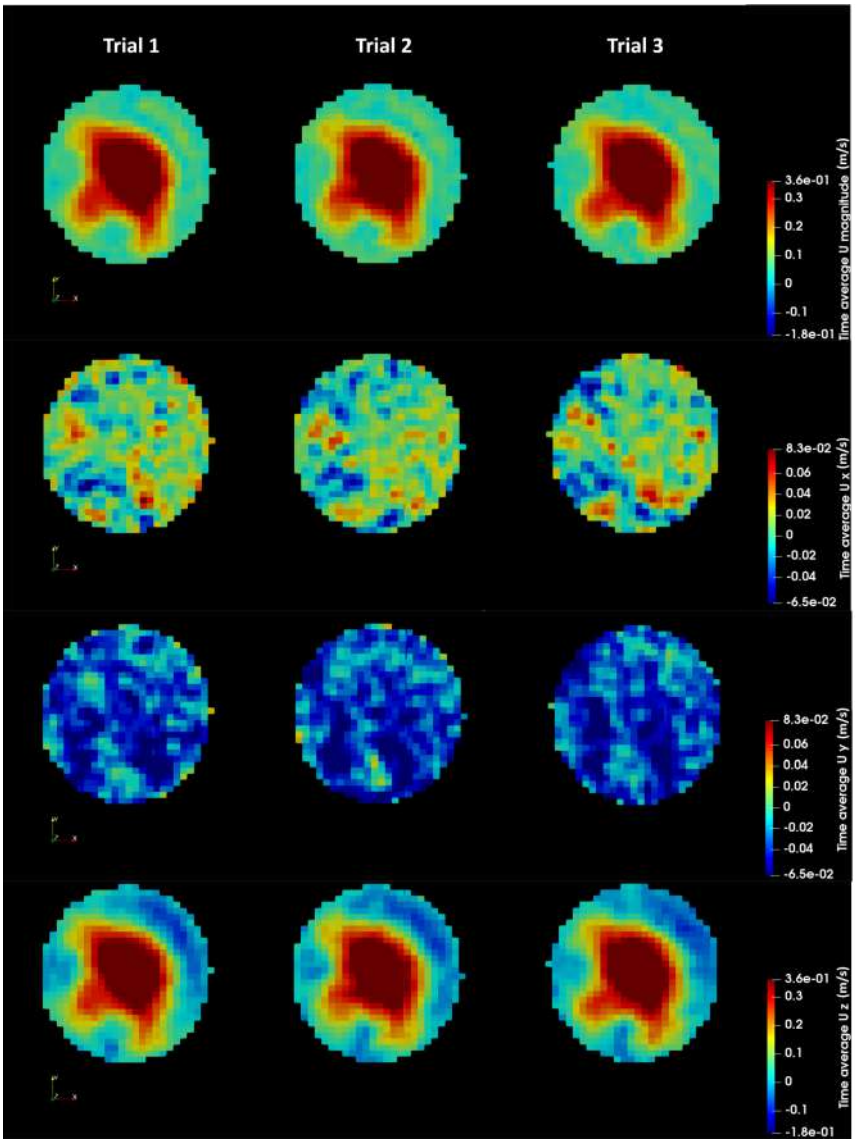

Figure 6.14: Velocity distribution (magnitude, x,y,z-component (m/s) at slice 6d in all three trials.

suggesting the branching out of the jet as observed in chapter 4. At 2.5d, the x-component has a higher contribution compared to the y-component. The jet and the shear layer at 4d are unstable, and x-components are low with some high values across the slice. At 5d, the pattern seen in 4D continues but three branches emerge from the jet. At 6d, the branching is more prominent, and the velocities' x- and y-components are very high. The temporal change in flow was very prominently observed in the post-stenotic region. Slight variations in the flow were observed at the center of 0d at different time steps. At 1d, variations in the recirculation region are observed. Small vortex-like structures start to appear at 2.5d, 4d, and 5d. At 6d, the south and northeast branches both form a vortex-like structure.

In order to check the accuracy of the 4D flow MRI measurements, the velocity values were compared with the values obtained from 2D PC-MRI and LDA (values presented in chapter 4, figure 4.31) (Figure 6.15).

The plots 6.15 shows that the velocity profiles obtained from all the modalities are comparable. At 0d, the LDA has the lowest measured velocity. Compared to the velocity measured by the 2D PC-MRI, the z-component of velocity measured by 4D flow MRI was higher. At 1d and 2.5d, the LDA values were lower from the center of the slice to half of the radius of the slice; beyond this, all three methods showed the same profile and values. At 4d and 5d, from the center of the slice to three-fourths of the radius, LDA was low, then as in 1d and 2.5d, all the modalities had the same profile and similar velocity values. The LDA profile is seen switching velocity values sooner than 2D PC-MRI and 4d flow MRI values. At 6d, a deviation in the velocity profile was observed. Here, LDA showed a blunt velocity profile indicating the end of the jet and higher turbulence. 2D PC-MRI and 4D flow MRI have a fuller profile and have comparable velocity values.

A statistical comparison using linear regression of the z-component of velocity in every voxel on the chosen slice obtained from 2D PC-MRI and 4D flow MRI is given below (Figure 6.16 and table 6.7). Due to the change in the voxel size between 4D flow MRI and 2D PC-MRI, 2D PC-MRI was resampled before the comparison. The data from linear regression suggests a high coincidence of the values obtained from the two techniques.

Additionally, ICC value was calculated for 4D (z-component of velocity) and 2D PC-MRI velocity values at chosen slices. The values are presented in table 6.8.

From the obtained ICC values (ICC $>$ 0.907), it can be implied that the correlation between the 4D flow MRI and 2D results is excellent.

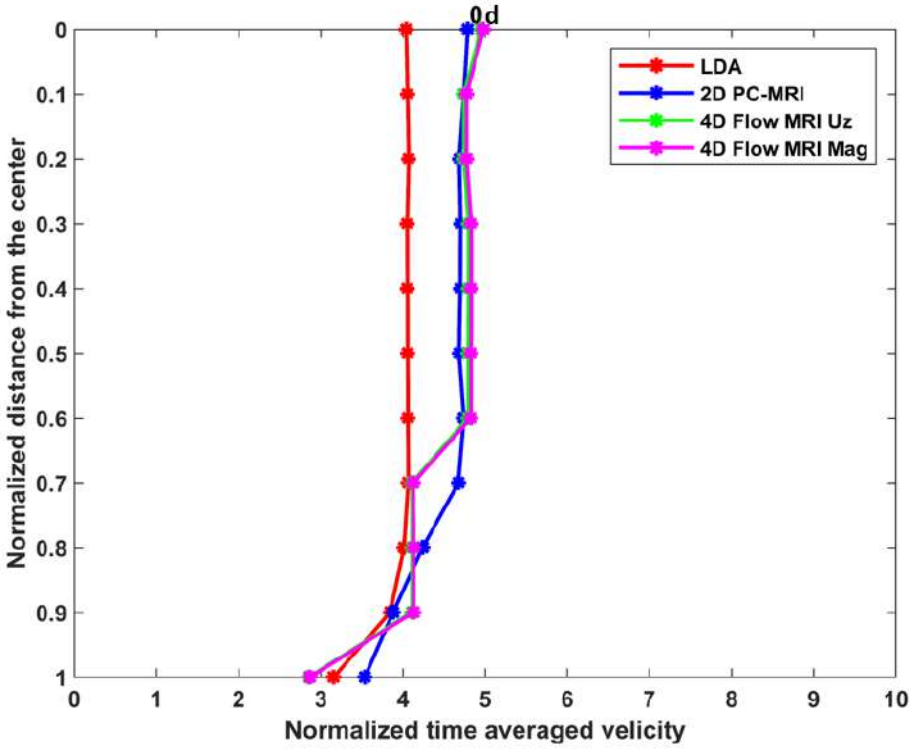
0d
LDA
2D PC-MRI
4D Flow MRI Uz
4D Flow MRI Mag
Normalized distance from the center
Normalized time averaged velicity
0
0.1
0.2
0.3
0.4
0.5
0.6
0.7
0.8
0.9
1
0
1
2
3
4
5
6
7
8
9
10

(a)

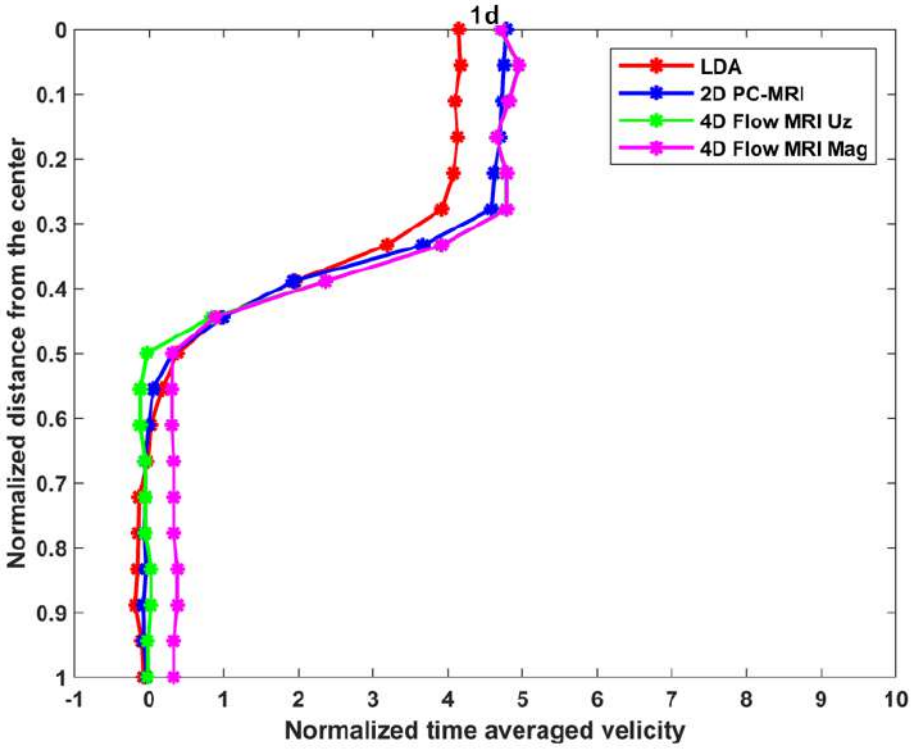
1d
LDA
2D PC-MRI
4D Flow MRI Uz
4D Flow MRI Mag
Normalized distance from the center
Normalized time averaged velicity
0
0.1
0.2
0.3
0.4
0.5
0.6
0.7
0.8
0.9
1
-1
0
1
2
3
4
5
6
7
8
9
10

(b)

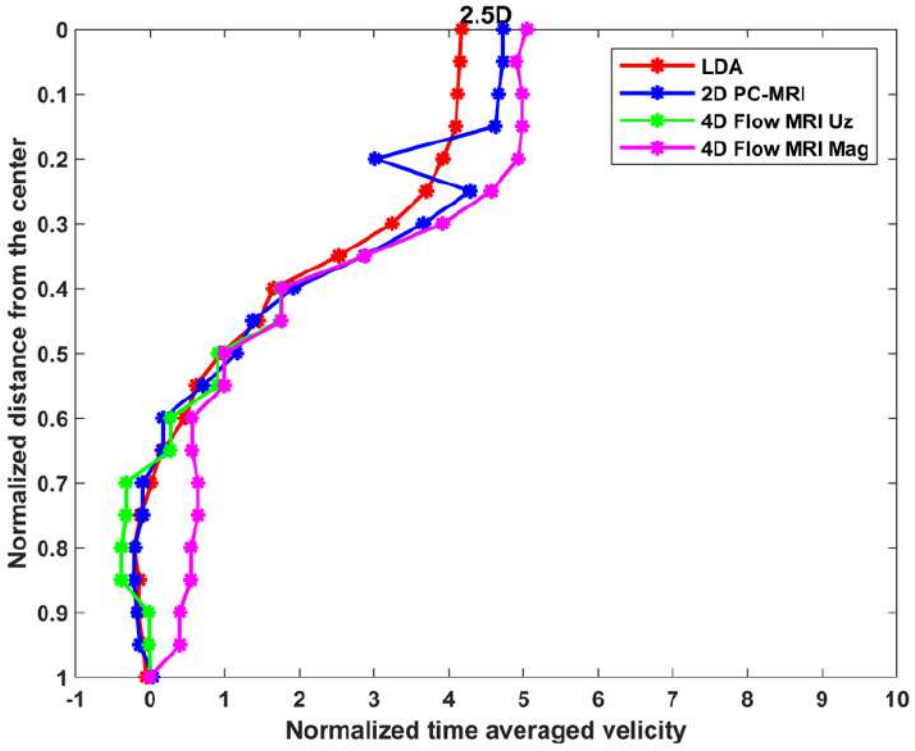
2.5D
LDA
2D PC-MRI
4D Flow MRI Uz
4D Flow MRI Mag
Normalized distance from the center
Normalized time averaged velicity
0
0.1
0.2
0.3
0.4
0.5
0.6
0.7
0.8
0.9
1
-1
0
1
2
3
4
5
6
7
8
9
10

(c)

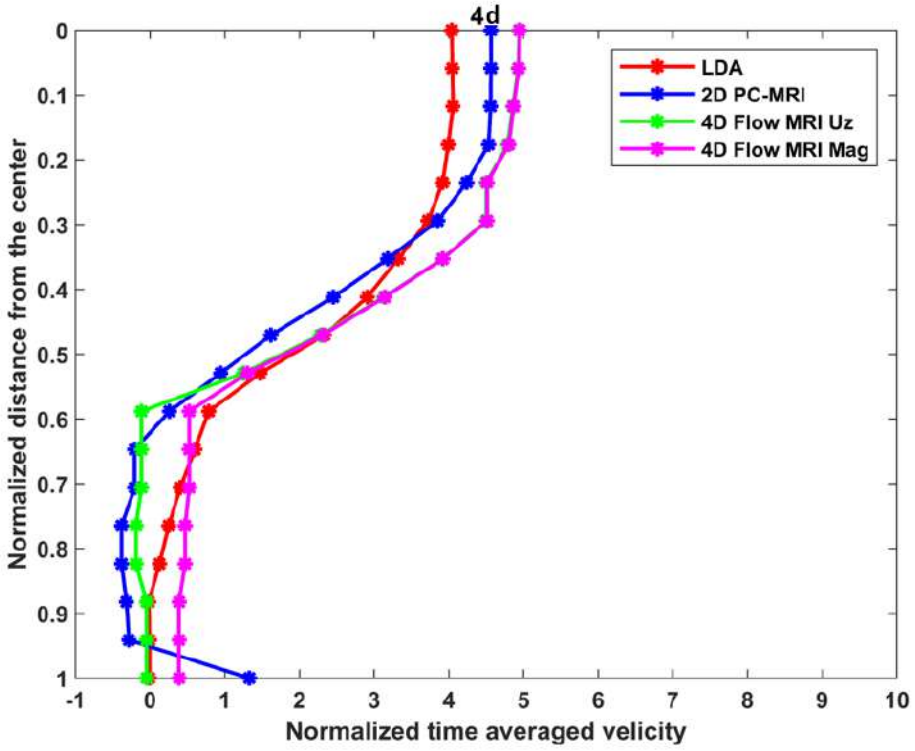
4d
LDA
2D PC-MRI
4D Flow MRI Uz
4D Flow MRI Mag
Normalized distance from the center
Normalized time averaged velicity
0
0.1
0.2
0.3
0.4
0.5
0.6
0.7
0.8
0.9
1
-1
0
1
2
3
4
5
6
7
8
9
10

(d)

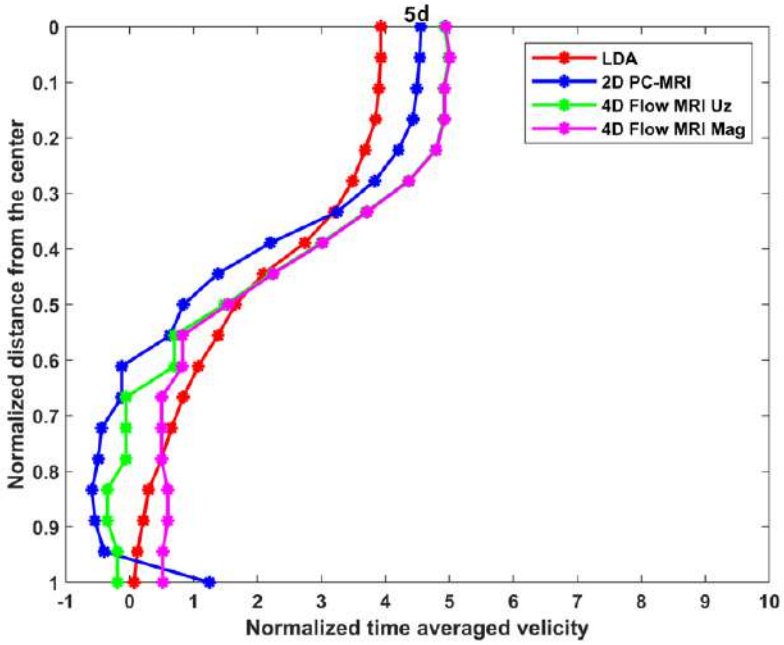

(e)

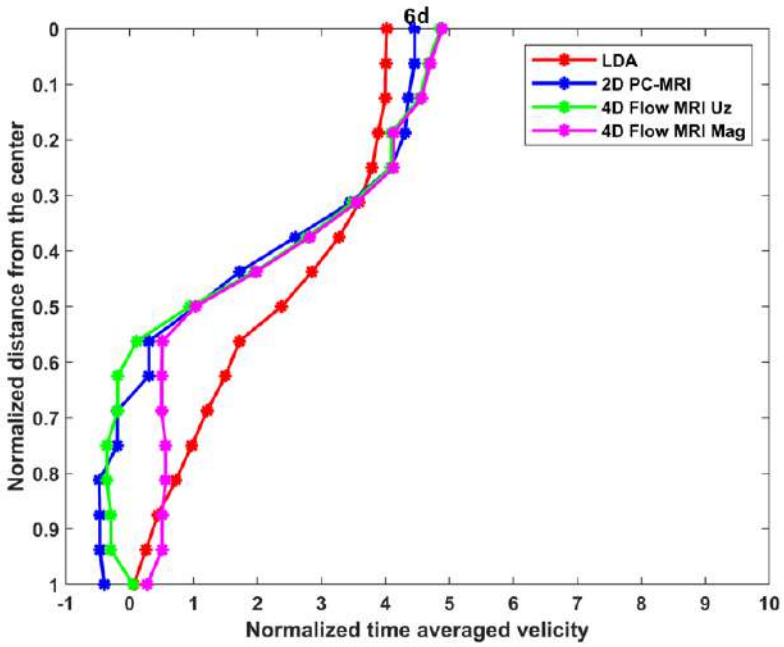

(f)

Figure 6.15: Figures a to f presents the axial velocity profile along the radius of the chosen slice at Re 500 obtained from 4D flow MRI (magnitude of velocity and z-component), 2D PC-MRI and LDA.

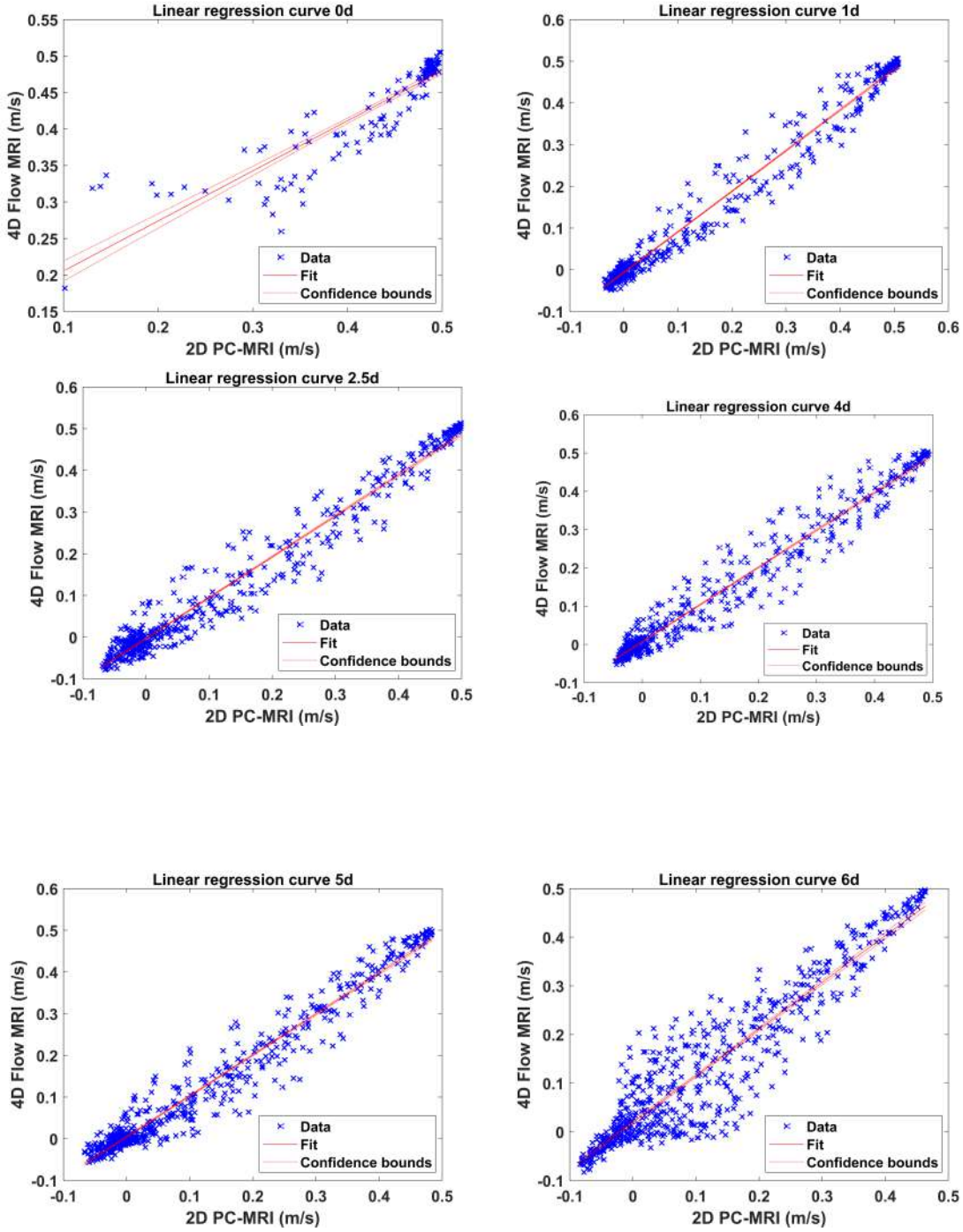

Figure 6.16: Linear regression line of comparison of 4D flow MRI (z-component of velocity) and 2D PC-MRI velocity values at chosen slices at Re 500.

Table 6.7: Linear regression values from the comparison of 4D flow MRI (z-component of velocity) and 2D PC-MRI velocity values at Re 500.

Slice number	**Slope**	**Intercept (m/s)**	**R ^{2}**	**p-value**
0d	0.690	0.137	0.797	<0.001
1d	0.974	-0.006	0.980	<0.001
2.5d	0.980	-0.003	0.965	<0.001
4d	0.973	0.006	0.958	<0.001
5d	0.981	0.005	0.956	<0.001
6d	0.960	0.019	0.863	<0.001

Table 6.8: ICC with lower and upper bound (LB and UB) values for 4D flow MRI (z-component of velocity) and 2D PC-MRI at Re 500 for chosen slices.

4D-2D	**ICC**	**LB**	**UB**
0d	0.926	0.907	0.942
1d	0.994	0.992	0.996
2.5d	0.991	0.990	0.992
4d	0.989	0.988	0.990
5d	0.988	0.987	0.990
6d	0.961	0.952	0.967

6.3.1.3 WSS in the stenosis at Re 500

The derived parameter WSS was calculated and visualized in GTFlow software. Table 6.9 presents the velocities obtained from all the three trials at chosen slices as calculated by GTFlow. These velocities are calculated in the marked area in the chosen slice. No additional corrections were performed in GTFlow. It is to be noted that in GTFlow, the y-coordinate is the z-coordinate in Paraview.

Table 6.9: Time-average velocity magnitude and velocity value obtained from GTFlow in all three directions measured at Re 500 in all three trials.

Slice number	**Ux (m/s)**	**Uy (m/s)**	**Uz (m/s)**	**Umag (m/s)**
Inlet	0.787	9.261	-0.263	9.299
0d	3.590	40.412	1.851	40.613
1d	-1.094	10.715	-1.159	10.832
2.5d	-2.307	22.484	-0.883	11.747
4d	-3.205	12.354	-0.775	12.787
5d	-3.813	12.609	-0.485	13.184
6d	-3.755	13.105	-0.450	13.641

Velocities calculated in MATLAB (Table 6.6) and in GTFlow (Table 6.9) show a high coincidence. Only the z-component of velocity at 0d had a slightly lower value in GTFlow compared to the one obtained in MATLAB. Based on the velocity values calculated above, GTFlow derives the WSS values.

The figure 6.17 shows the WSS on the surface of the stenosis calculated with GTFlow version 4. It can be seen that the WSS starts to increase as it enters the stenosis and is the highest at the center. As it progresses out of the throat, the WSS reduces.

Figure 6.18 shows the WSS vectors calculated in GTFlow version 3 across the circumference of all the chosen slices (additionally WSS is calculated at -1.5d, -1d, -0.35d and -0.01d). Figure 6.19 shows the segments across the circumference of one of the chosen slices over which the WSS is calculated. Table 6.10 and 6.11 presents the WSS axial and magnitude values in the chosen slices.

Observations from WSS vectors (Table 6.10 and 6.11) at all the chosen slices (obtained across 8 segments in each slice), show that at slice -0.35d, -0.001d, and 0d, the WSS is the highest. It is also observed that in these slices the WSS vectors are oriented in the direction of flow, unlike in the other slices where they are randomly

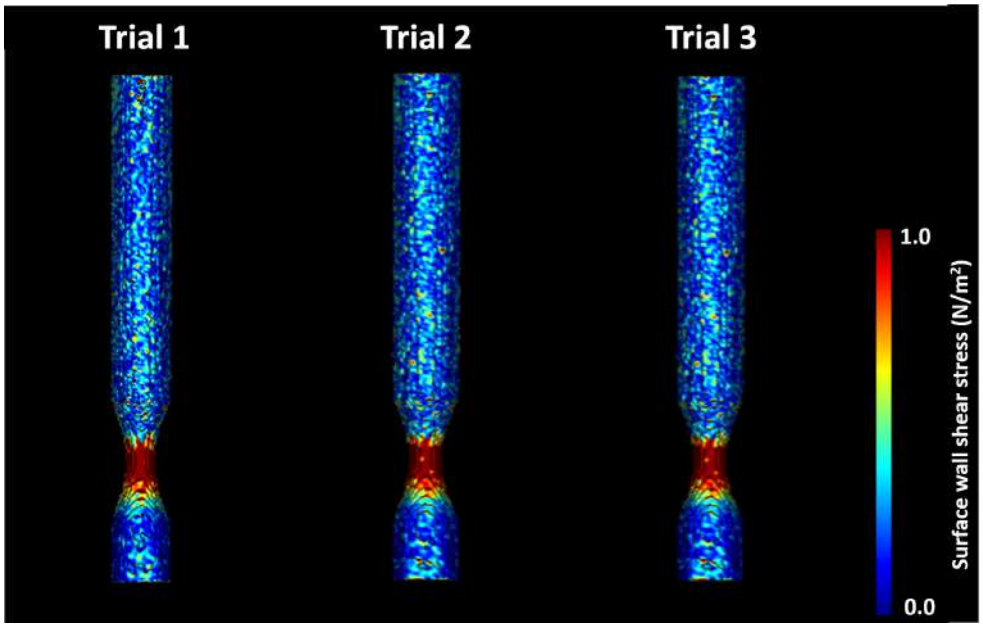

Figure 6.17: Surface WSS distribution (N/m^2) in the stenosis model at Re 500 and at all three trials.

Table 6.10: WSS magnitude and average axial values calculated at Re 500 by GT-Flow from the 4D flow MRI measurements in all three trials at Re 500.

Slice number	**Trial 1 WSS mag (N/m^2)**	**WSS axial (N/m^2)**	**Trial 2 WSS mag (N/m^2)**	**WSS axial (N/m^2)**	**Trial 3 WSS mag N/m^2**	**WSS axial (N/m^2)**
-1.5d	0.113	0.009	0.126	0.010	0.117	-0.009
-1d	0.161	0.987	0.184	0.066	0.144	0.003
-0.35d	1.487	1.475	1.586	1.572	1.492	1.475
-0.01d	2.182	2.166	2.237	2.221	2.244	2.226
0d	1.860	1.846	2.070	2.054	2.016	2.000
1d	0.205	-0.009	0.219	0.011	0.250	-0.018
1.5d	0.336	-0.082	0.349	-0.126	0.295	-0.051
2.5d	0.274	-0.089	0.340	-0.108	0.286	-0.100
4d	0.294	-0.044	0.333	-0.076	0.286	-0.027
5d	0.301	-0.026	0.280	-0.036	0.316	-0.025
6d	0.321	0.114	0.284	0.078	0.313	0.013

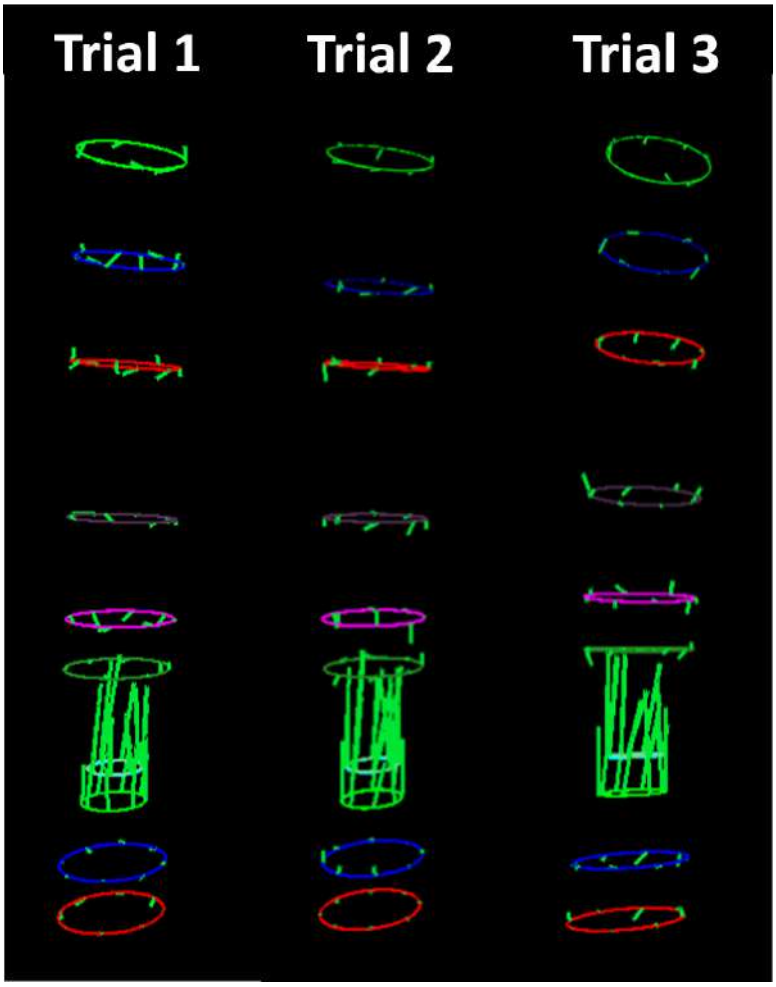

Figure 6.18: WSS vectors (N/m^2, vector length magnified by a factor of 10) across 8 segments of the circumference of the chosen slices in the stenosis model at Re 500 and at all three trials at Re 500.

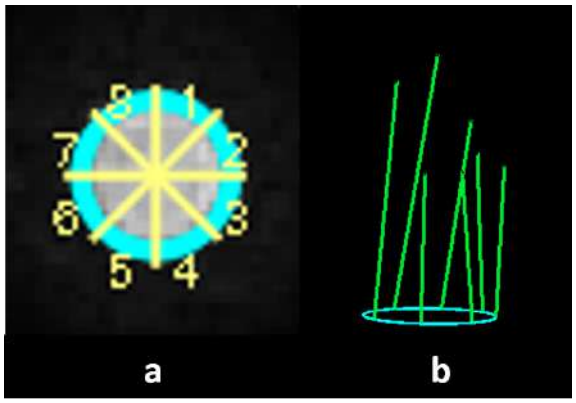

Figure 6.19: Illustration of the segments created across the circumference of the chosen slice (slice 4, in the given illustration) over which the WSS is calculated.

Table 6.11: WSS magnitude and average axial values calculated at Re 500 by GT-Flow from the 4D flow MRI measurements averaged across all three trials at Re 500.

Slice number	**WSS mag (N/m^2)**	**WSS axial (N/m^2)**
-1.5d	0.118	0.003
-1d	0.163	0.031
-0.35d	1.522	1.507
-0.001d	2.221	2.204
0d	1.983	1.967
1d	0.225	-0.005
1.5d	0.327	-0.086
2.5d	0.300	-0.098
4d	0.305	-0.049
5d	0.299	-0.029
6d	0.306	0.069

oriented.

A closer look at the slice -1d, -0.001d, and 1d, shows that, across the circumference of the slice, the vectors are all not uniform (Figures 6.20).

To validate the WSS values obtained from the 4D Flow MRI, they are compared with WSS obtained from published LDA data (Figure 6.21). The WSS in the Ahmed and Giddens paper was calculated from the velocity measured at three radial positions and then fitting a least squared error straight line through the three positions [120]. The qualitative and quantitative analysis is provided below (Figure 6.22 and table 6.12). The plot shows that LDA WSS values are higher from the inlet to the end of the stenosis than the calculated 4D flow MRI WSS values. After this, the 4D flow MRI WSS values are higher than LDA WSS values till 6d. The LDA WSS is highest at 0d and is 23.63 times higher than at the inlet, but WSS obtained by 4D flow MRI at 0d is only 16.76 times higher than inlet WSS. The maximum WSS achieved in 4D flow MRI is at -0.001d, about 18.78 times higher than the inlet WSS. At 1d, it is observed that the WSS values in 4D flow MRI are slightly higher than at the inlet as opposed to the LDA data. Also, at 1.5d, the WSS peaks slightly and then attains a stable value further downstream.

The deviations of WSS observed in the above plot justifies the lower slope value and high bias value in the quantitative analysis (Figure 6.22 and Table 6.12).

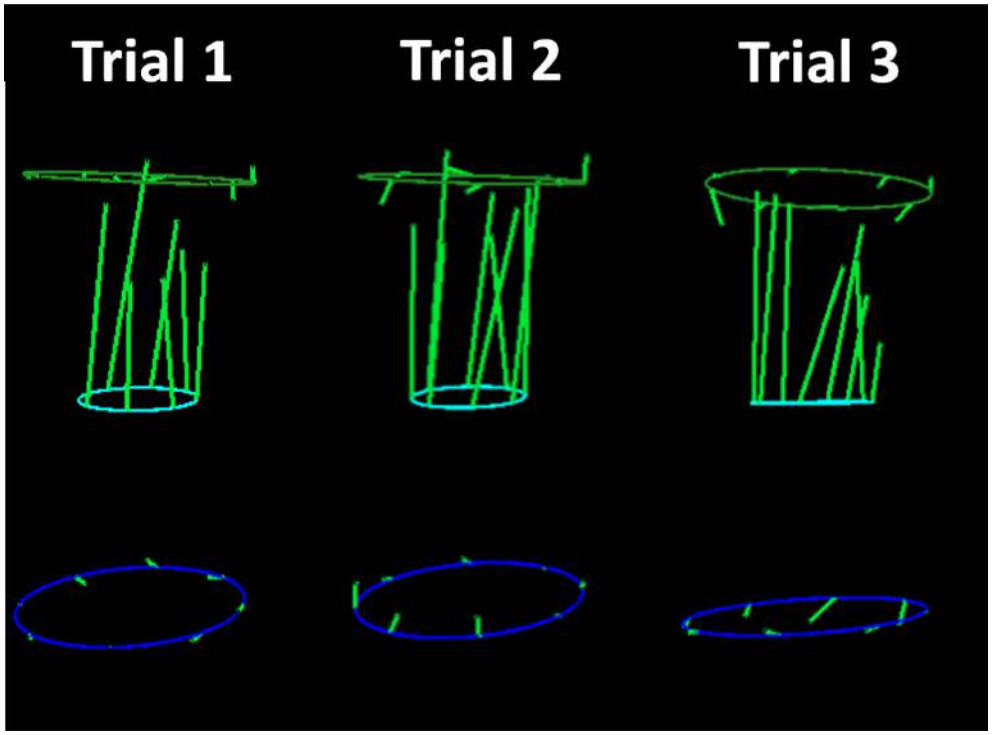

Figure 6.20: WSS vectors (N/m^2, vector length magnified by a factor of 10) across 8 segments in the chosen slice 2,4 and 6 at Re 500.

Table 6.12: Bland-Altman and linear regression values from the comparison of 4D flow MRI (average of the three trials) and LDA WSS values at chosen slices at Re 500.

Slice number	**Slope**	**Intercept (N/m^2)**	**R ^{2}**	**p-value**	**Bias (N/m^2)**
LDA-4D	0.701	2.285	0.978	<0.001	-1.411

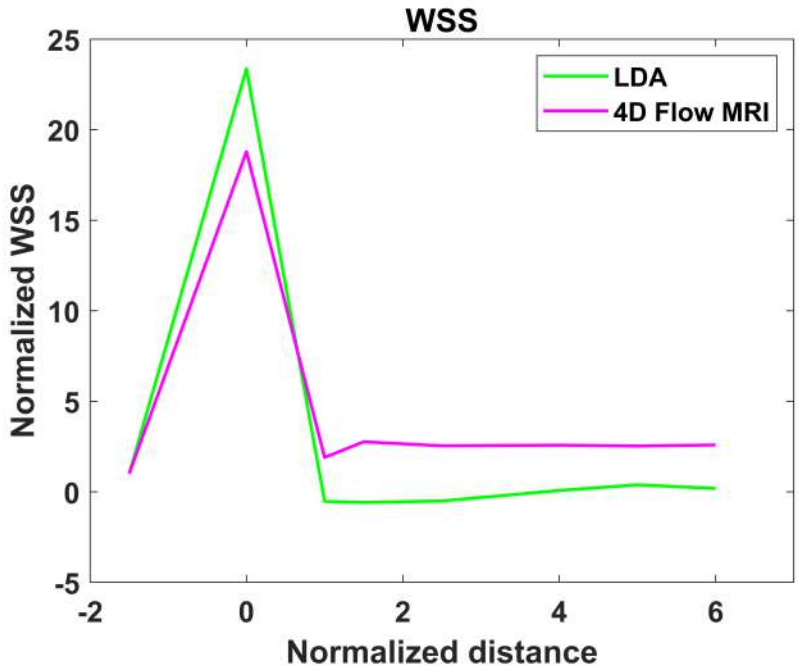

Figure 6.21: Plot of comparison of WSS obtained from 4D flow MRI (average of all three trials) and LDA at across the entire stenosis model.

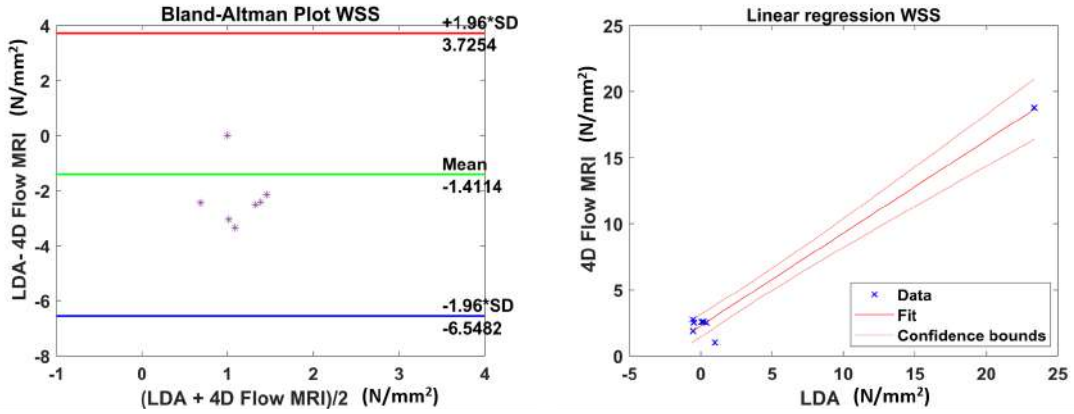

Figure 6.22: Bland-Altman plot and linear regression line of comparison of 4D flow MRI (average of the three trials) and LDA WSS values at chosen slices at Re 500.

6.3.2 Pharynx model

6.3.2.1 Reliability analysis

The voxel-by-voxel analysis for all the three components of velocities (time-averaged) in the entire pharynx model is given in table 6.3.

Table 6.13: ICC with lower and upper bound (LB and UB) values for x-, y- and z-component in the pharynx model at average inspirational flow rate.

Components	ICC	LB	UB
x-component	0.967	0.966	0.967
y-component	0.969	0.968	0.969
z-component	0.993	0.993	0.995

An excellent correlation (ICC $>$ 0.967) is observed in pharynx models for all the three velocity-components.

6.3.2.2 Velocity analysis in the pharynx at average inspirational flow rate

The DICOM images obtained in the experiment were analyzed in MATLAB and visualized in Paraview. Statistical analysis using ICC was done to check the test-retest reliability. According to the results presented in the table 6.13 it is evident that all the values of velocities in the three sets have an excellent agreement. This fortifies the ability of the technique to measure velocity consistently.

The following images show the 3D model of the pharynx with the colormap denoting the magnitude of the velocity at all three trials in figure 6.23. The model surface has non-zero velocity due to the use of large voxel size representing flow within the model aswell. Here, it is observed that velocities are high in the front wall of the oropharynx. Downstream from oropharynx the higher velocities were mainly observed at front wall of the hypopharynx.

The following images show the velocity distribution in the inlet slice in all directions (Figures 6.24). Visually, the velocities appear to be the same throughout the slice. The average velocities were calculated in all three trials and were compared against the theoretical value of 0.058 m/s obtained from equation 4.12. The values obtained were as follows, trial 1: 0.130 m/s (123% higher), trial 2: 0.123 m/s (112% higher) and trial 3: 0.122 m/s (110% higher). The time-averaged inlet velocity magnitude

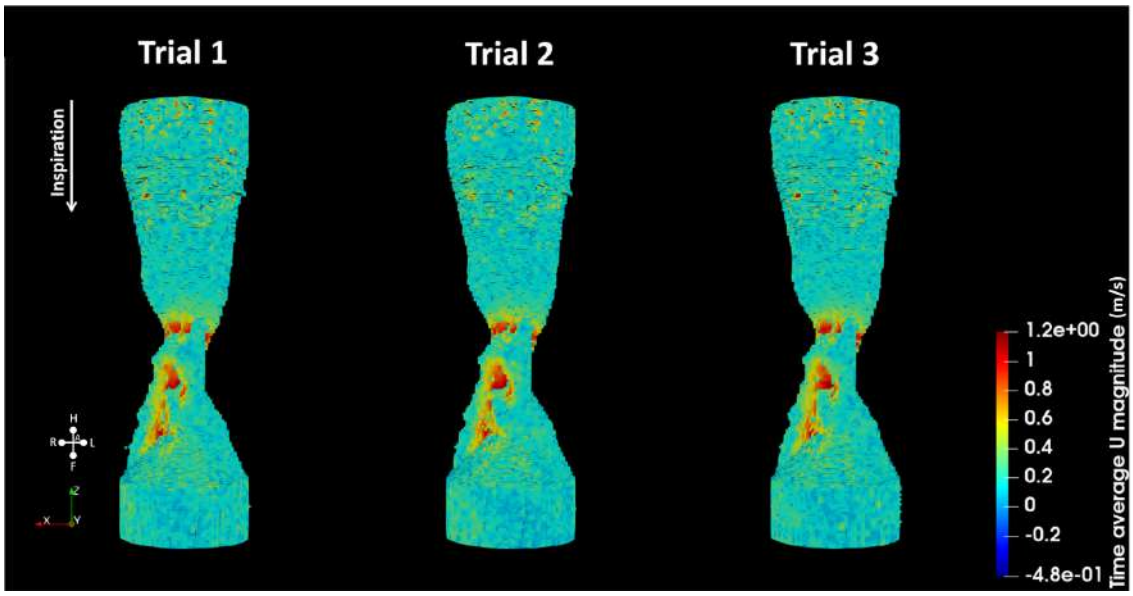

Figure 6.23: 3D model of the pharynx during inspiration obtained from all three trials as visualized in Paraview.

is significantly higher than the velocity calculated from the prescribed flow rate. Therefore, the same is calculated using only the z-component. Here average values 0.030 m/s, 0.037 m/s and 0.033 m/s were obtained for the three trials respectively. Compared to the theoretical value of 0.058 m/s, the z-component values are more appropriate. This implies that the inlet velocity is high due to the significant contribution from the x- (approx -0.09 m/s) and y- (approx -0.01 m/s) component of velocities; that is, the flow is not completely laminar. The plotted velocity profile further supports this observation (Figure 6.25). The velocity profile plotted with the magnitude of the velocity has a top-hat profile.

The coronal and sagittal view of the pharynx model shows the complex flow phenomenon occurring in the pharynx (Figures 6.26 and 6.30). In the coronal slice, the velocity increases as the cross-sectional area reduce in the oropharynx. As the area increases again, flow separation occurs downstream, causing a region recirculation only on the front and side wall of the oropharynx. The jet formed impinges on the front wall of the hypopharynx. At the epiglottis, as the area reduces, the velocity peaks again, and downstream flow separation causes the formation of the recirculation region on the front and back wall again. The jet continues to impinge on the front wall. The x-component of the velocity in sagittal view is as shown in figure 6.27. It is seen that the x-component is prevalent, from just above the epiglottis to the end of the hypopharynx. The y-component is significantly seen

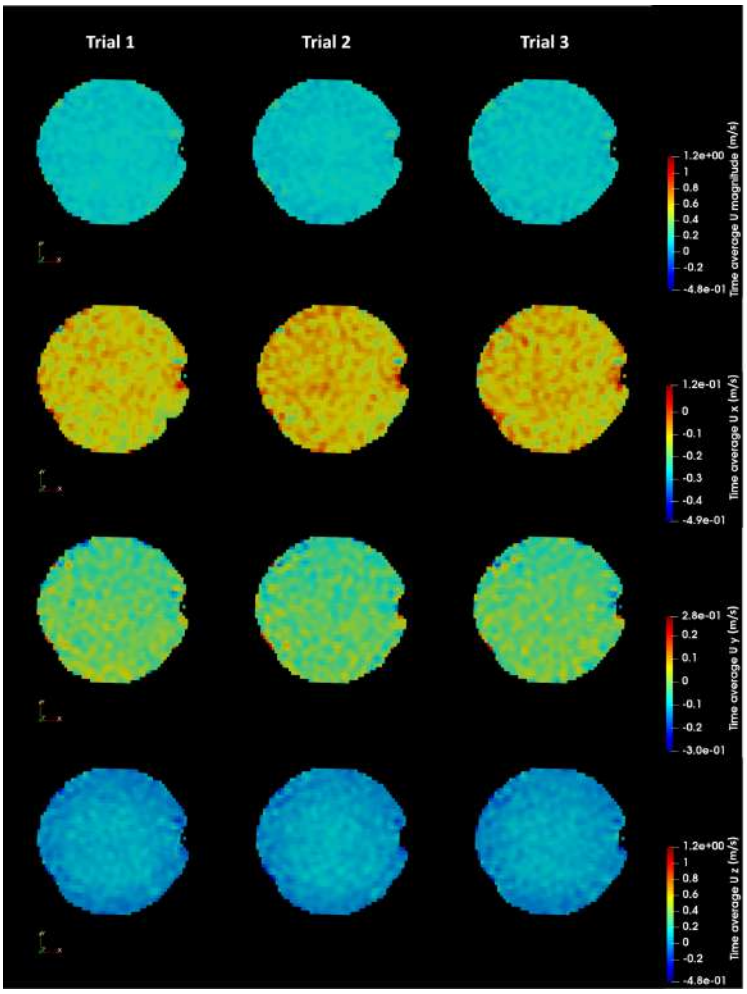

Figure 6.24: Velocity distribution (magnitude of velocity, m/s) in the inlet slice of the pharynx model during inspiration at all three trials.

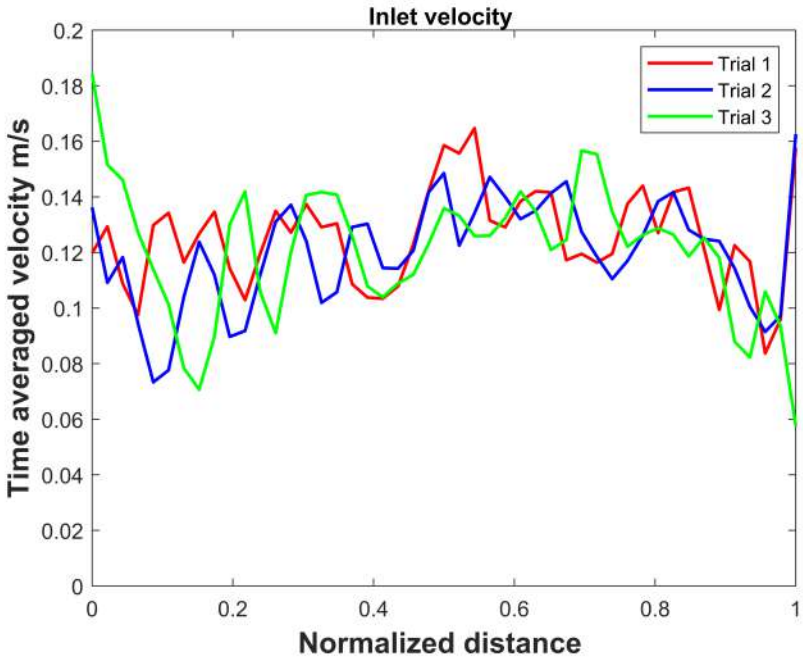

Figure 6.25: Plot of the inlet velocity profile during inspiration obtained in all three trials.

from the minimum cross-sectional area in the oropharynx and traces the path of the jet until the end of the hypopharynx (Figure 6.28). The z-component pattern coincides with that of the magnitude (Figure 6.29). In the time variation of the velocities, variation in the length of the jet is observed. The jet formed in the y normal plane is seen impinging down (Figure 6.30). The x-component traces the path of the jet, and the y-component is high at the minimum cross-sectional area and also along the path of the jet (Figures 6.31 and 6.32). After the epiglottis, the y-component of velocity seems to be higher near the wall. The time variation of the z-component of velocities shows the jet impinging down, hitting the outlet adapter, and then turning up to the front wall (Figure 6.33).

The time-averaged velocity magnitude for all three trials for the eleven chosen slices is given in the table 6.14. The flow pattern shows the velocity increase till slice 6 (slice 6 has the maximum velocity) and then a reduction. Due to the second constriction, the velocity increases at slice eight. The values obtained in all three trials coincide very well, except for slice 10 of trial 1, which has a higher value.

Time-averaged values of all the velocity components are provided in the table 6.15. It is seen that the x-component is always negative, the y-component is positive till slice 5 and then reverses its direction, and the z-component of the velocity is always positive.

Table 6.14: Time-average velocity (magnitude of velocity) and standard deviation values measured during inspiration by 4D flow MRI in all three trials.

Slice number	**Trial 1 m/s**	**Trial 2 m/s**	**Trial 3 m/s**	**Average m/s**	**Standard deviation**
1	0.165	0.165	0.160	0.164	0.003
2	0.194	0.192	0.188	0.191	0.003
3	0.226	0.221	0.216	0.221	0.005
4	0.295	0.291	0.285	0.291	0.005
5	0.509	0.504	0.507	0.506	0.002
6	0.741	0.737	0.731	0.736	0.005
7	0.649	0.639	0.640	0.642	0.006
8	0.677	0.677	0.669	0.674	0.004
9	0.497	0.499	0.494	0.497	0.003
10	0.677	0.412	0.412	0.500	0.153
11	0.393	0.404	0.407	0.402	0.007

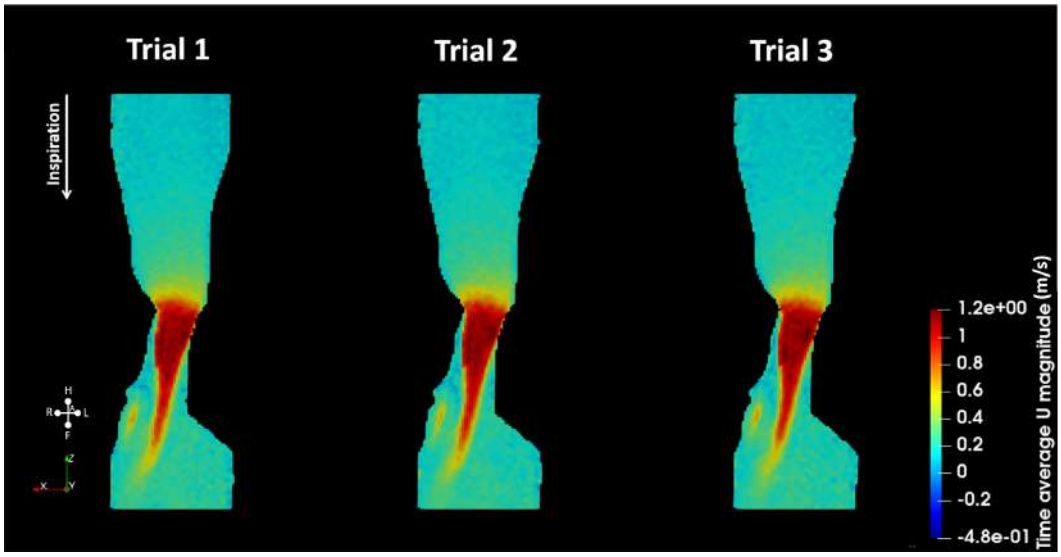

Figure 6.26: Coronal slice of the pharynx model showing velocity distribution (magnitude of velocity, m/s) during inspiration.

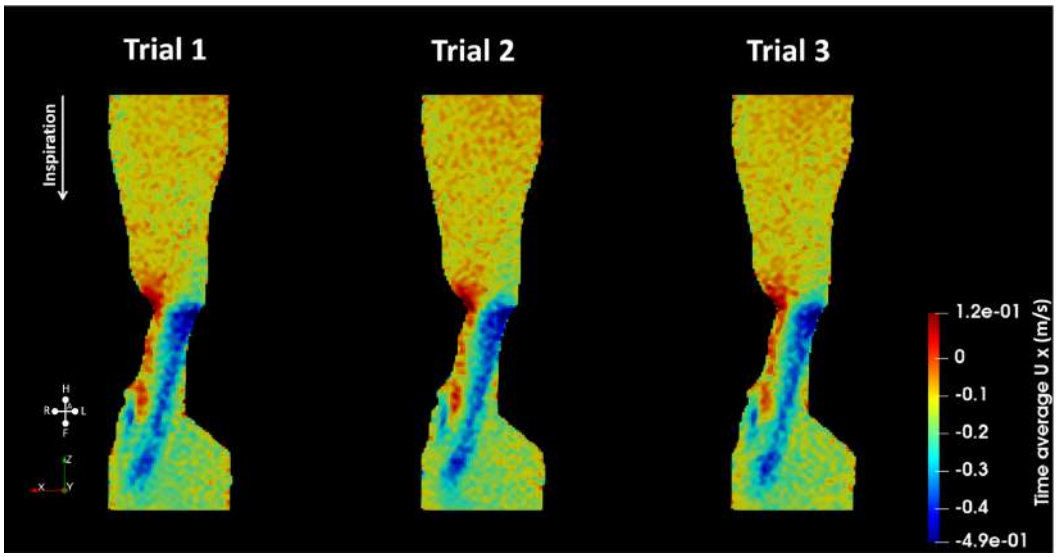

Figure 6.27: Coronal slice of the pharynx model showing velocity distribution (x-component of velocity, m/s) during inspiration.

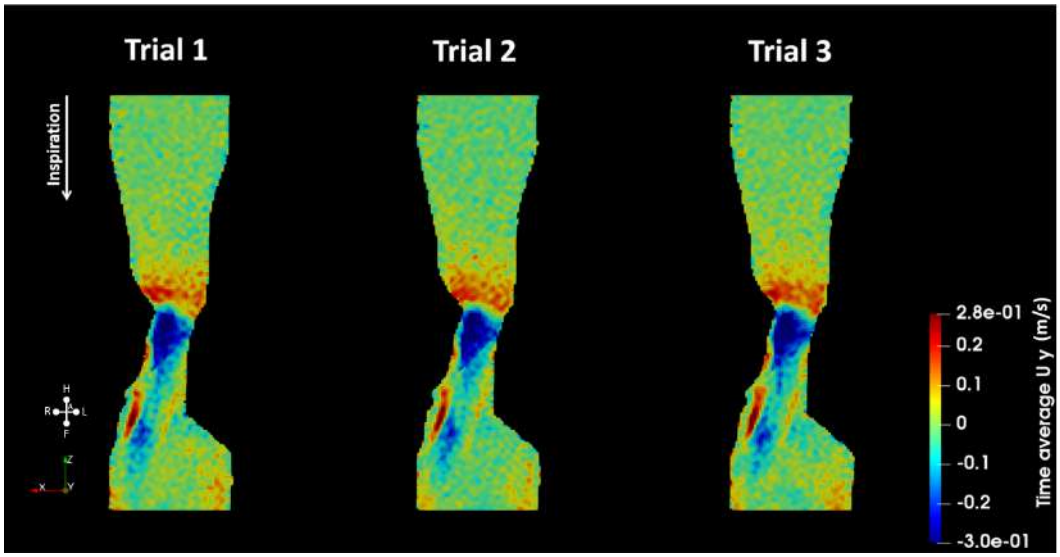

Figure 6.28: Coronal slice of the pharynx model showing velocity distribution (y-component of velocity, m/s) during inspiration.

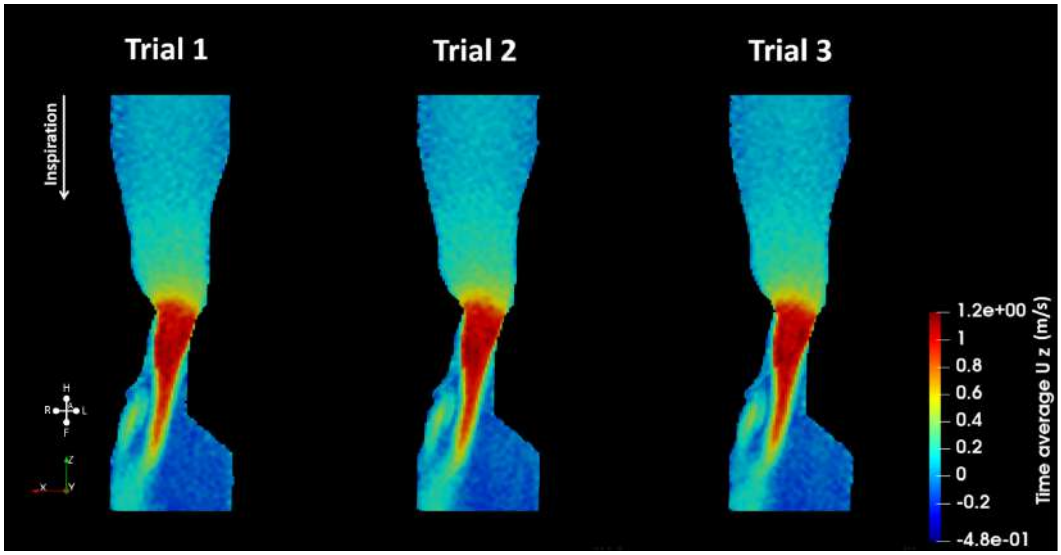

Figure 6.29: Coronal slice of the pharynx model showing velocity distribution (z-component of velocity, m/s) during inspiration.

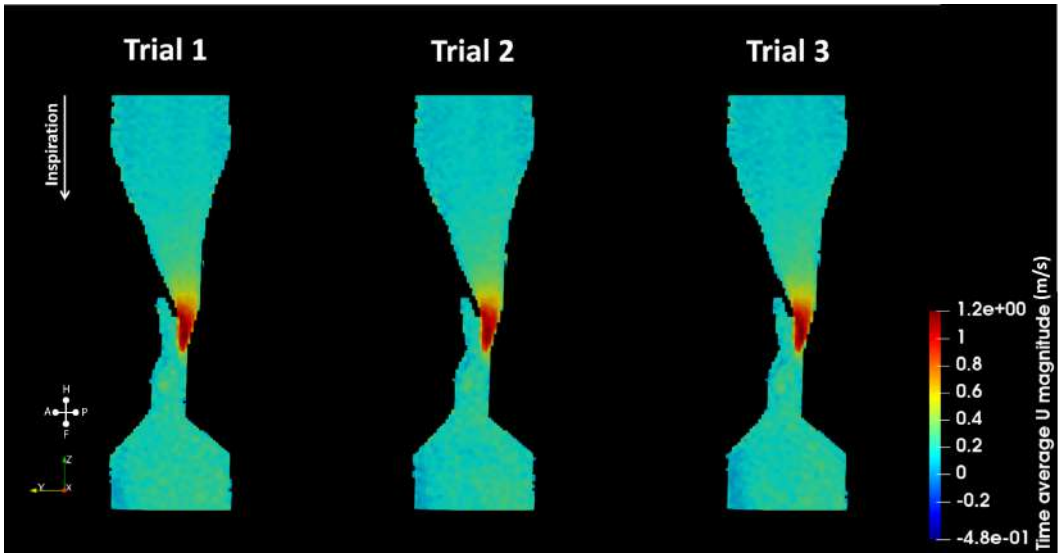

Figure 6.30: Sagittal slice of the pharynx model showing velocity distribution (magnitude of velocity, m/s) during inspiration.

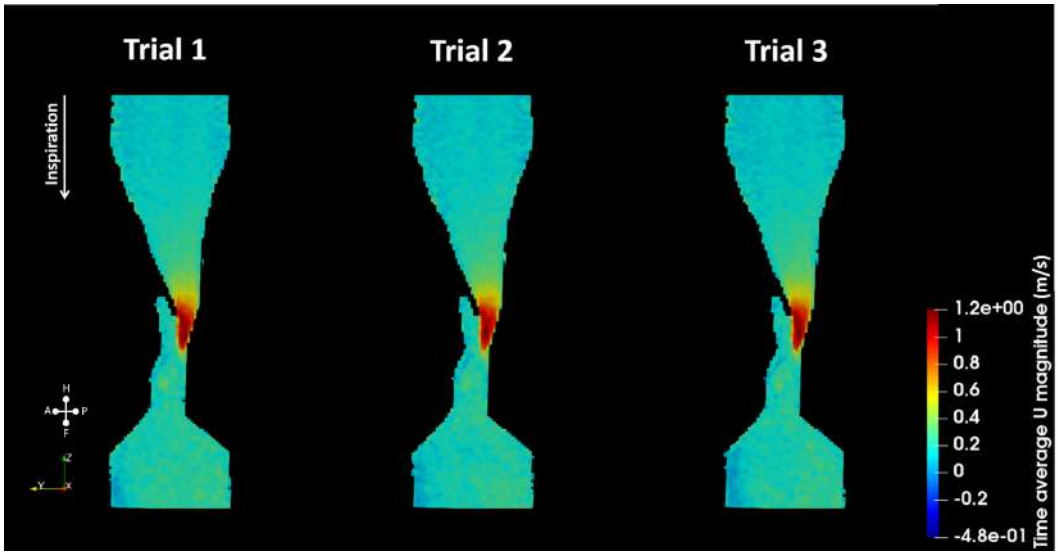

Figure 6.31: Sagittal slice of the pharynx model showing velocity distribution (x-component of velocity, m/s) during inspiration.

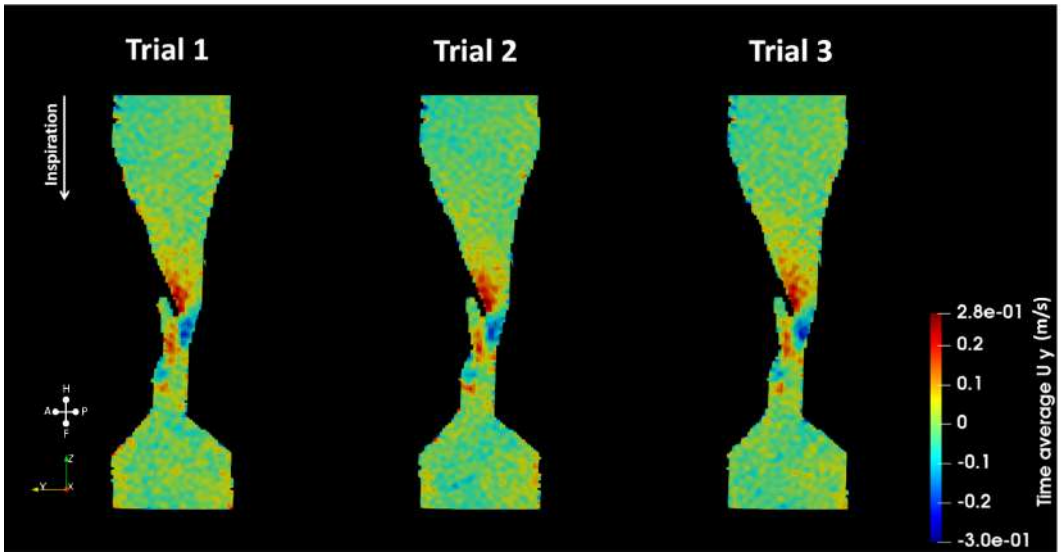

Figure 6.32: Sagittal slice of the pharynx model showing velocity distribution (y-component of velocity, m/s) during inspiration.

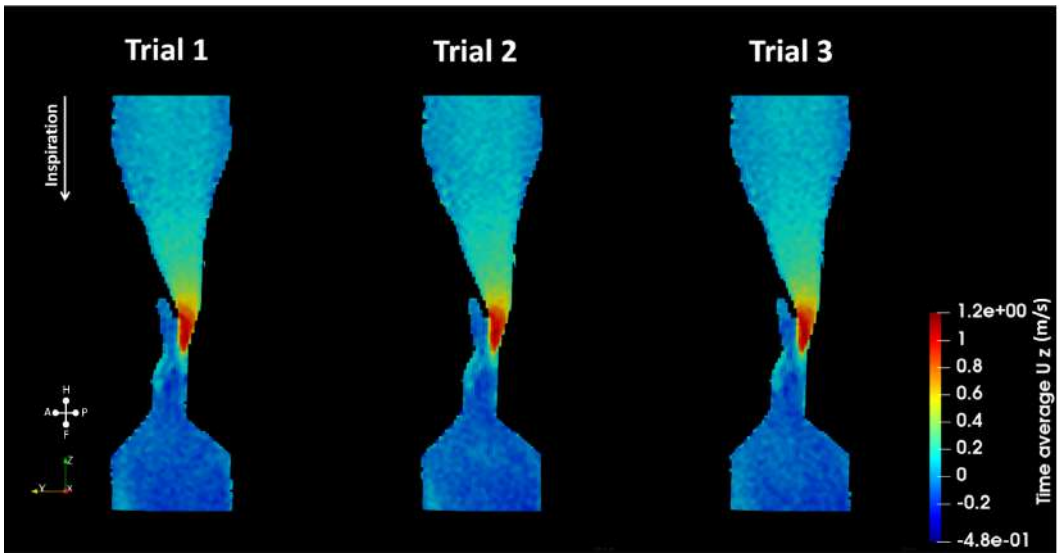

Figure 6.33: Sagittal slice of the pharynx model showing velocity distribution (z-component of velocity, m/s) during inspiration.

Table 6.15: Time-average velocity magnitude and velocity value in all three directions measured during inspiration by 4D flow MRI in all three trials.

Slice number	**Ux m/s**	**Uy m/s**	**Uz m/s**	**Umag m/s**
1	-0.112	0.004	0.098	0.164
2	-0.113	0.010	0.139	0.191
3	-0.113	0.030	0.171	0.221
4	-0.104	0.068	0.246	0.291
5	-0.121	0.091	0.458	0.506
6	-0.236	-0.099	0.639	0.736
7	-0.221	-0.140	0.497	0.642
8	-0.216	-0.088	0.576	0.674
9	-0.213	-0.073	0.364	0.497
10	-0.195	-0.038	0.364	0.500
11	-0.192	-0.032	0.226	0.402

To further analyze the flow phenomenon, all the components of the velocities at the chosen slices are visualized (Figures 6.34 to 6.37). The x-component in all the slices shows the following characteristic (Figure 6.35). Initially, the x-component is low, but it increases with the decrease in area. The x-component is significantly observed towards the air pocket, and as the jet traverses down, it is seen in the direction of the jet. A small vortex-like structure starts to form from slice 7 onwards in the recirculation regions. The time variation of this component shows the formation and dissolving of these structures. The y-component also increases starting slice 6 and then follows the path of the jet (Figure 6.36). Slices 9, 10, and 11 have more vortex-like structures. The z-component contributes to the prominent recirculation region and jet formation (Figure 6.37). The vortex formation and dissolving are seen in slices 7, 8, 9, and 10.

The z-component velocity of the 4D flow MRI and 2D PC-MRI are compared statistically to analyze the similarities and differences.

The linear regression values are given below (Figure 6.38 and 6.16). For the comparison, the 2D PC-MRI data are resampled to match the voxel size of the 4D flow MRI data. An excellent correlation with slope values close to unity is observed in the comparison. An exception was seen at slice 5, where the correlation is low.

Additionally, ICC was calculated for the z-component of velocity measured by 4D

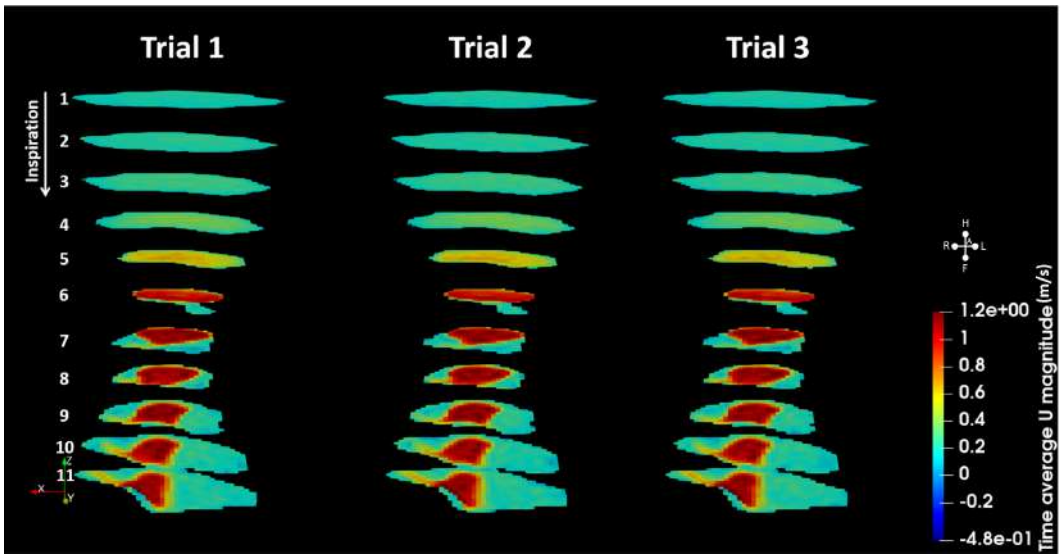

Figure 6.34: Velocity distribution (magnitude of velocity, m/s) in all chosen slices of the pharynx model during inspiration at all three trials.

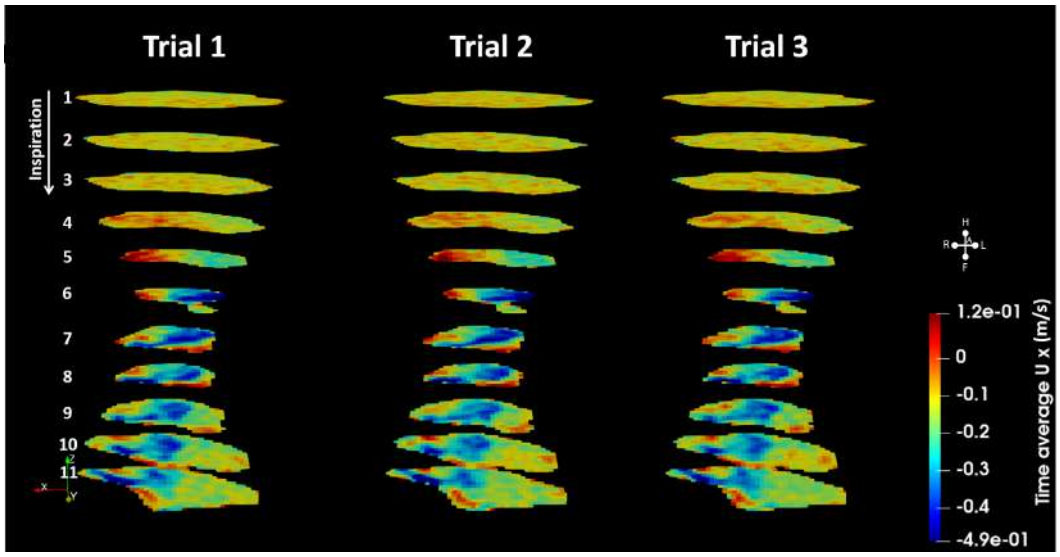

Figure 6.35: Velocity distribution (x-component of velocity, m/s) in all chosen slices of the pharynx model during inspiration at all three trials.

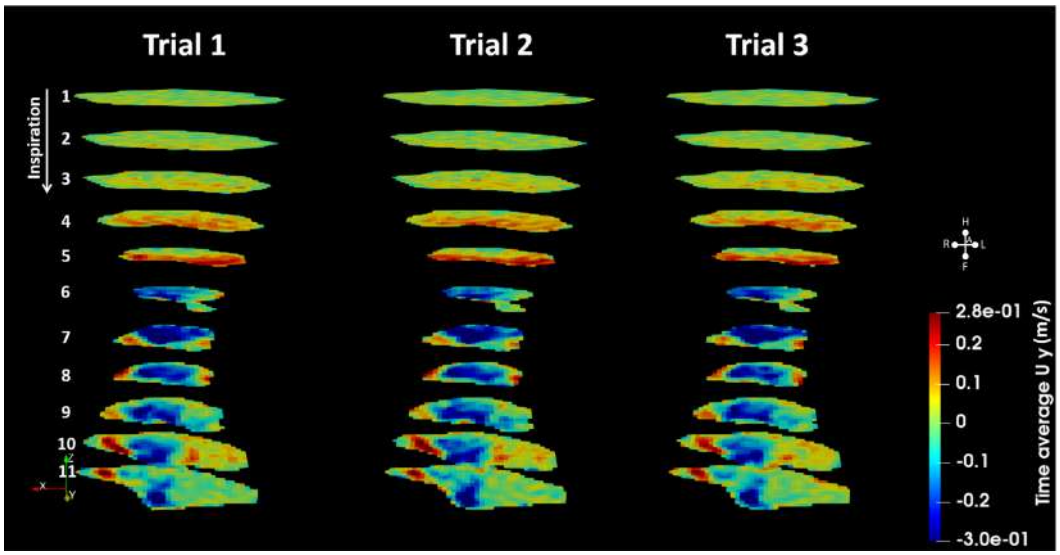

Figure 6.36: Velocity distribution (y-component of velocity, m/s) in all chosen slices of the pharynx model during inspiration at all three trials.

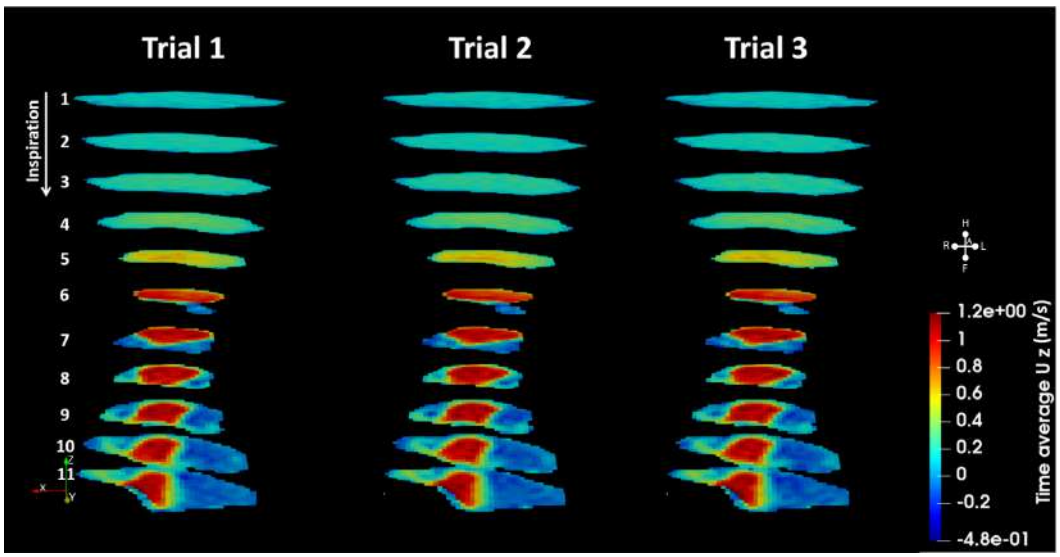

Figure 6.37: Velocity distribution (z-component of velocity, m/s) in all chosen slices of the pharynx model during inspiration at all three trials.

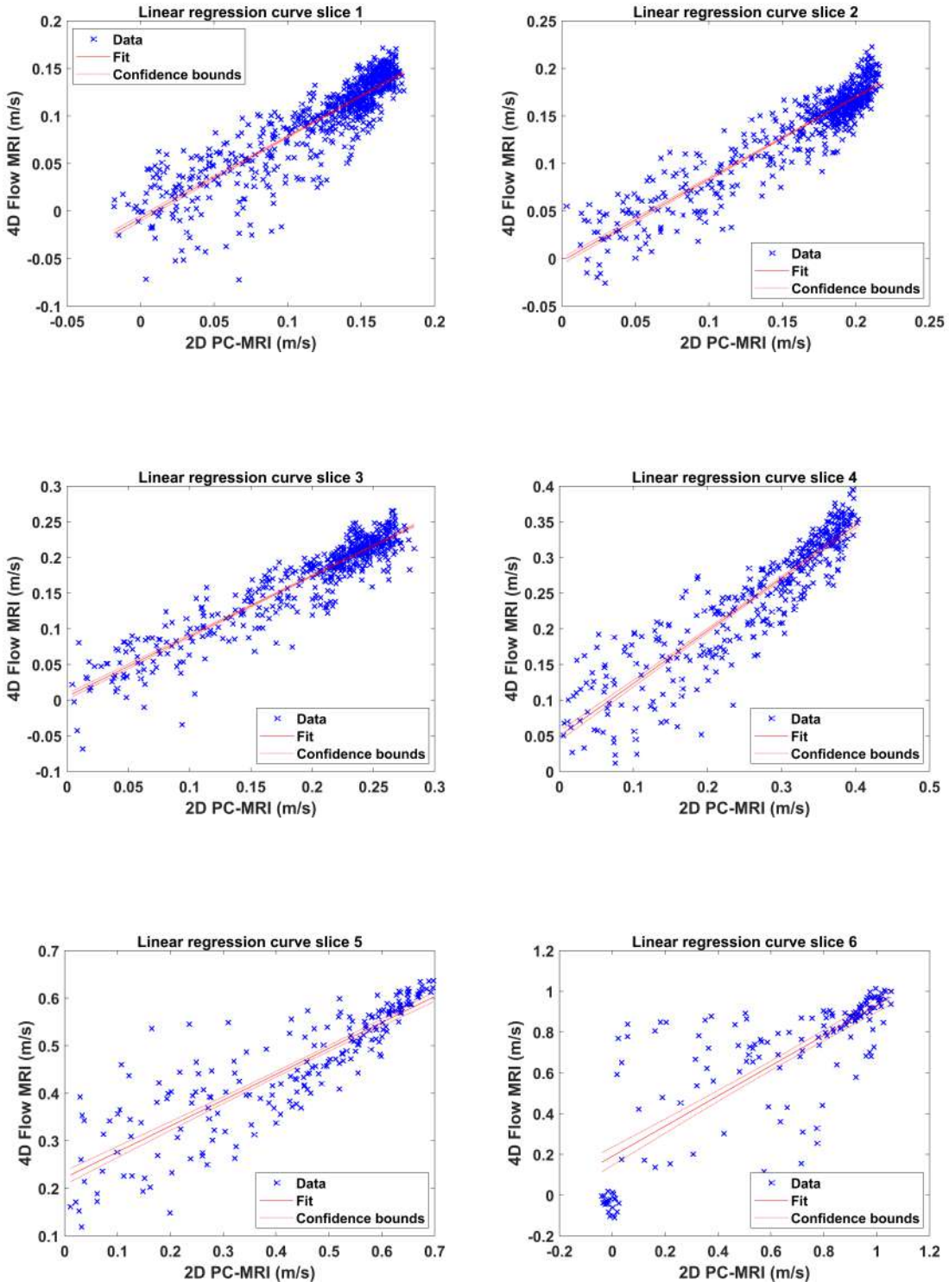

Linear regression line of comparison of 4D flow MRI (z-component of velocity) and 2D PC-MRI velocity values in slices 1 to 6 during inspiration.

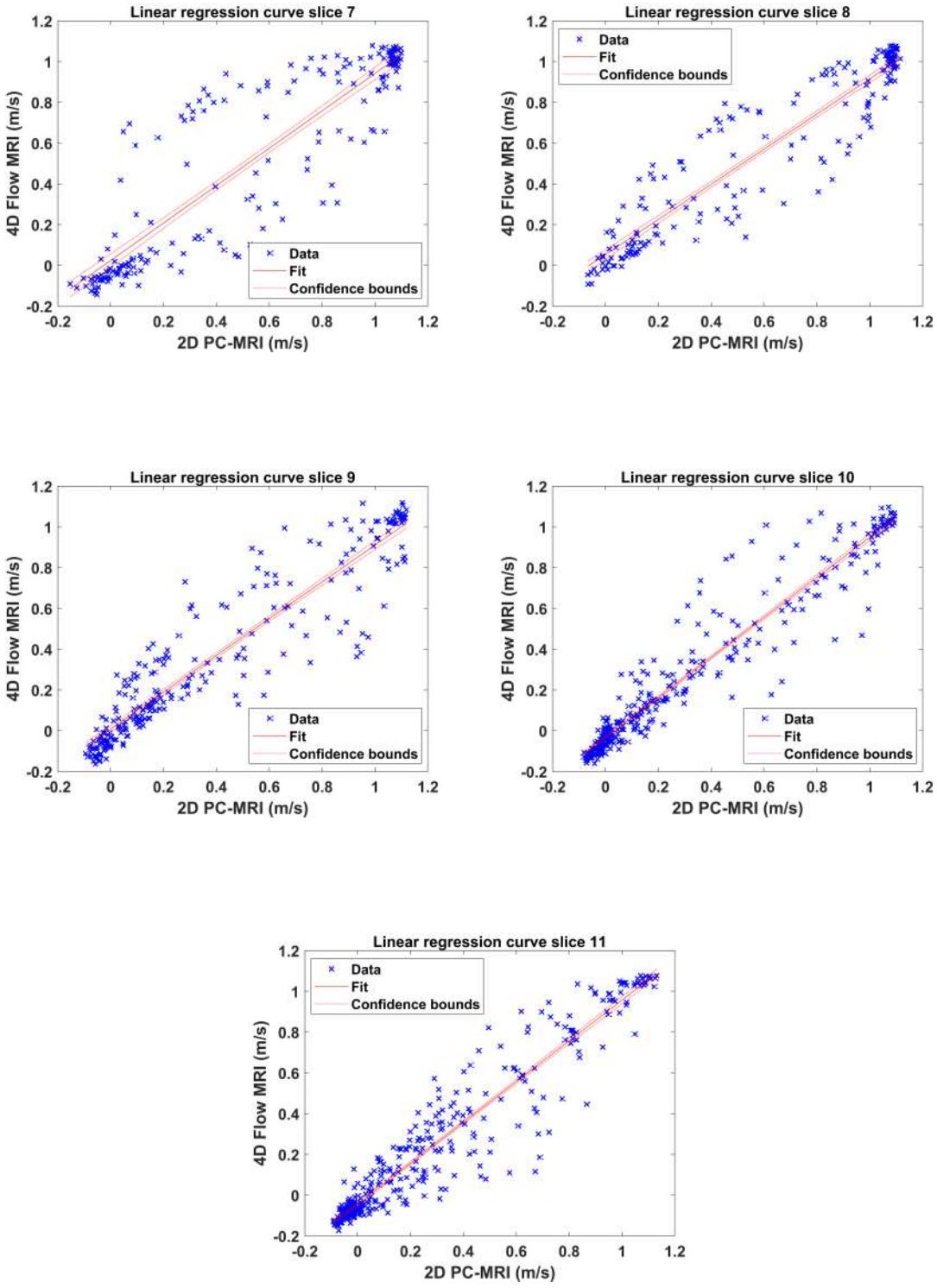

Figure 6.38: Linear regression line of comparison of 4D flow MRI (z-component of velocity) and 2D PC-MRI velocity values in slices 7 to 11 during inspiration.

Table 6.16: Linear regression values from the comparison of 2D PC-MRI (average of the three trials) and CFD velocity values for the entire model during inspiration 4D flow MRI (z-component of velocity) and 2D PC-MRI velocity values at chosen slices during inspiration.

Slice number	**Slope**	**Intercept (m/s)**	**R^2**	**p-value**
1	0.859	-0.008	0.786	<0.001
2	0.863	-0.002	0.860	<0.001
3	0.846	0.005	0.870	<0.001
4	0.738	0.049	0.827	<0.001
5	0.545	0.222	0.747	<0.001
6	0.741	0.191	0.639	<0.001
7	0.918	0.024	0.790	<0.001
8	0.863	0.053	0.877	<0.001
9	0.902	0.009	0.876	<0.001
10	0.982	-0.033	0.926	<0.001
11	1.000	-0.043	0.913	<0.001

flow MRI and 2D PC-MRI (Table 6.17).

Table 6.17: ICC values with lower and upper bound values for the pharynx model for z-component in 4D Flow MRI and 2D PC-MRI.

4D-2D	**ICC**	**LB**	**UB**
Slice 1	0.876	0.279	0.954
Slice 2	0.903	0.187	0.969
Slice 3	0.927	0.547	0.973
Slice 4	0.931	0.890	0.954
Slice 5	0.870	0.837	0.896
Slice 6	0.885	0.856	0.909
Slice 7	0.941	0.928	0.952
Slice 8	0.964	0.955	0.971
Slice 9	0.965	0.958	0.971
Slice 10	0.978	0.968	0.984
Slice 11	0.973	0.960	0.981

The ICC for all the chosen slices (z-component) shows that the values are all excellent. The ICC is slightly lower at slices 1, 5, and 6. The ICC value is the least at slice 5.

6.3.2.3 Comparison of 4D Flow MRI and CFD results

The following section validates the simulation data (Chapter 5, subsection 5.2.4 and subsection 5.3.3) with 4D flow MRI data. The 3D model of the pharynx obtained from the simulation is presented in figure 6.39. As expected, the surface of the model has null velocity. Figure 6.42 shows the velocity pattern obtained by each velocity component in all the 11 chosen slices. A qualitative comparison shows that the velocity pattern of the x- and y-components are similar. However, noticeable changes are observed in velocity patterns of z-component and magnitude. That is the vortices seen starting slice 7 in the 4D flow MRI results are not observable in the simulation result. Additionally, it is seen that the jet is much broader in the simulation than in the experiment.

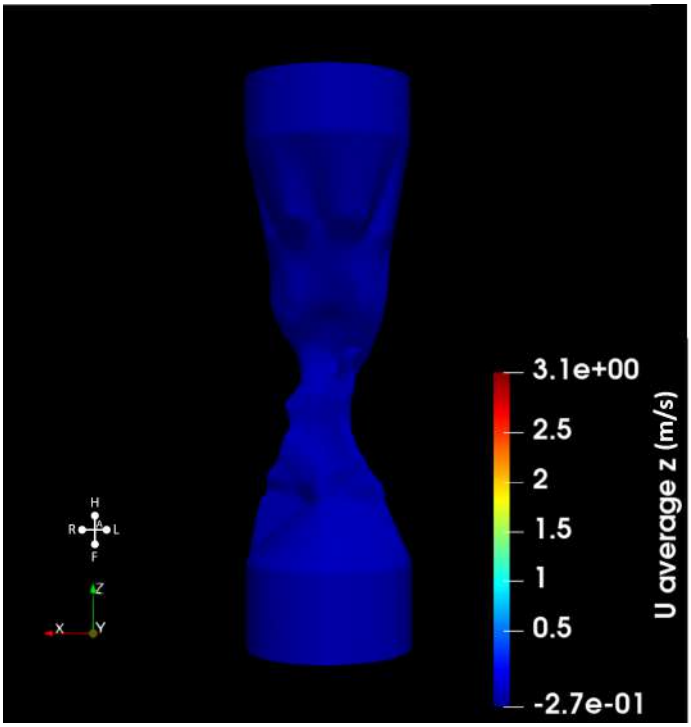

Figure 6.39: 3D model of the pharynx during inspiration obtained from CFD as visualized in Paraview.

A simulation was performed with the same model but without the adapters to check

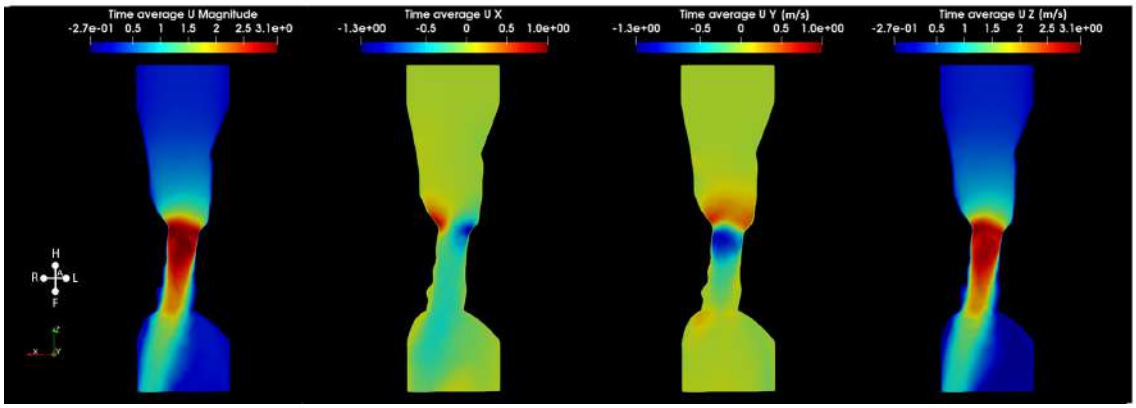

Figure 6.40: Sagittal slice of the pharynx model showing velocity distribution (m/s) during inspiration.

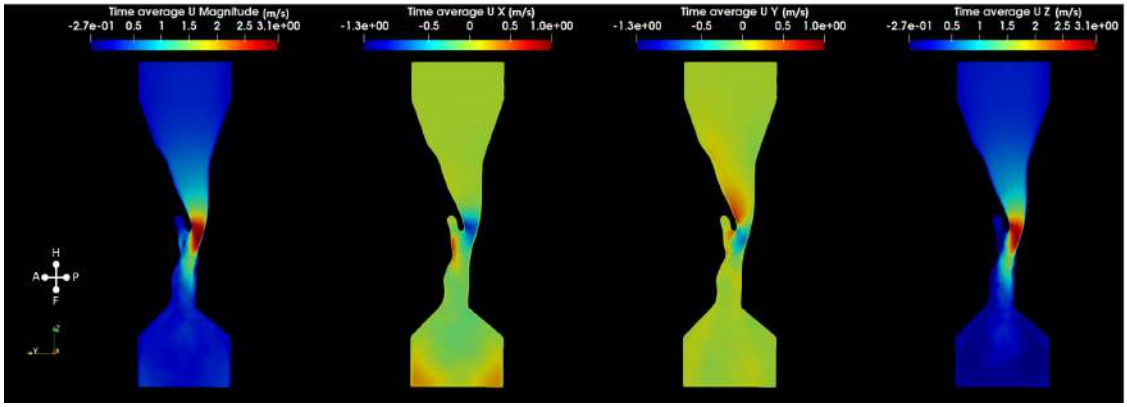

Figure 6.41: Coronal slice of the pharynx model showing velocity distribution (m/s) during inspiration.

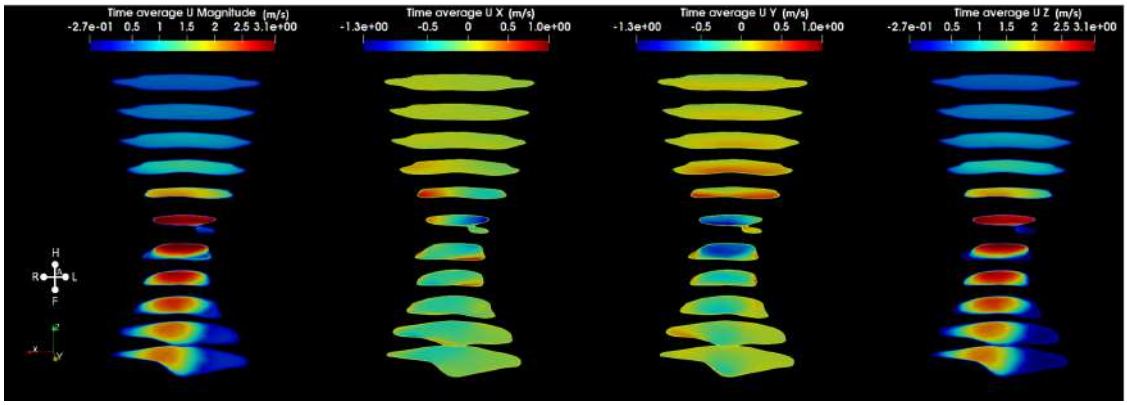

Figure 6.42: Velocity distribution (m/s) in all chosen slices of the pharynx model during inspiration.

the influence of the adapters on pharyngeal flow. These adapters were originally attached to the segmented pharynx inorder to avoid turbulence of the flow during entrance. Figure 6.46 shows that the similarities of the simulation results with no adapter to the experiment are slightly less compared to the model with adapters, but in the z-component and magnitude images, the vortices observed in the 4D flow MRI measurements are present.

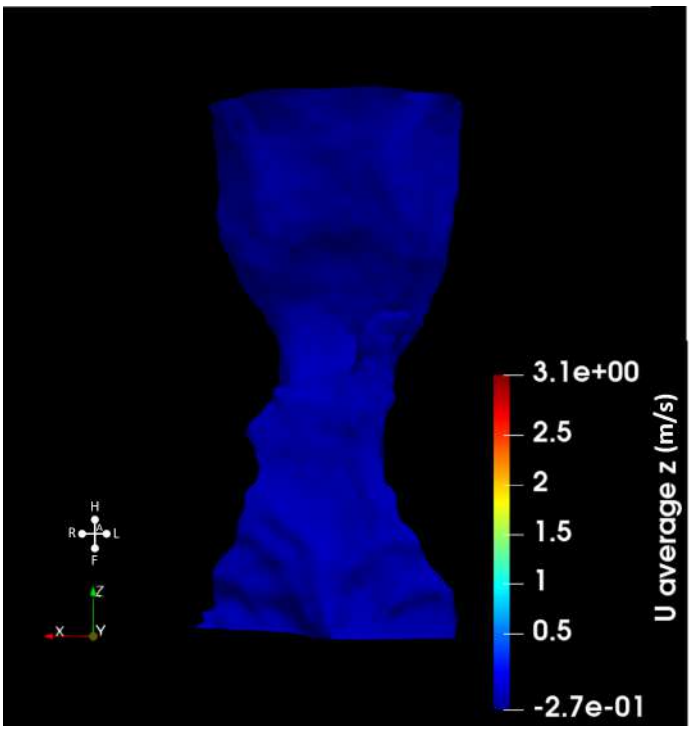

Figure 6.43: 3D model of the pharynx model with no adapters during inspiration obtained from CFD as visualized in Paraview.

The average value of the velocities obtained from 4D flow MRI and the two simulation models (model with adapter and model without adapter) are compared in table 6.18. The two simulation models were resampled to 4D flow MRI data, and a linear regression was performed for a voxel-by-voxel comparison. The regression values are provided in table 6.19.

Comparing the average values shows that both simulations follow the general trend seen in MRI trials. The velocity accelerates as the area reduces downstream of the model and reaches its maximum value at slice 6. Below this slice, the value reduces as the area increases. At slice 8, the value increases again due to a second area reduction. The variations observed in the simulation model with adapter was that the values at the constrictions slice 6 and 7 were significantly higher. The

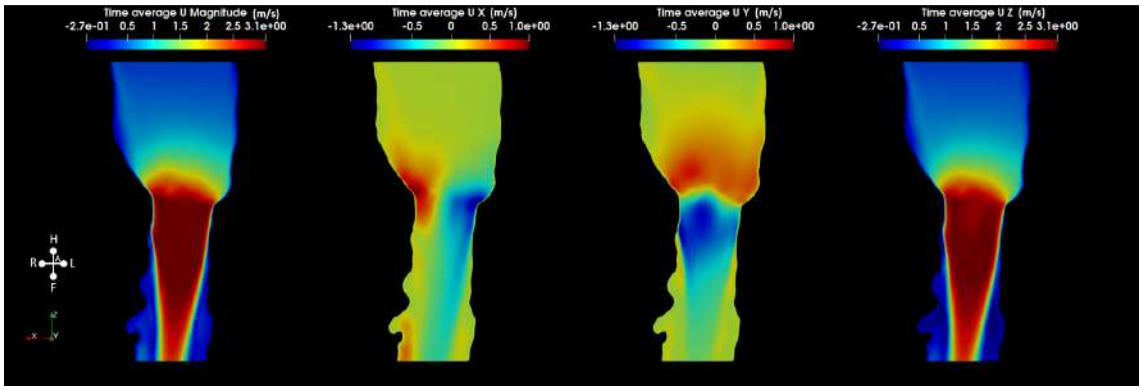

Figure 6.44: Sagittal slice of the pharynx model with no adapters showing velocity distribution (m/s) during inspiration.

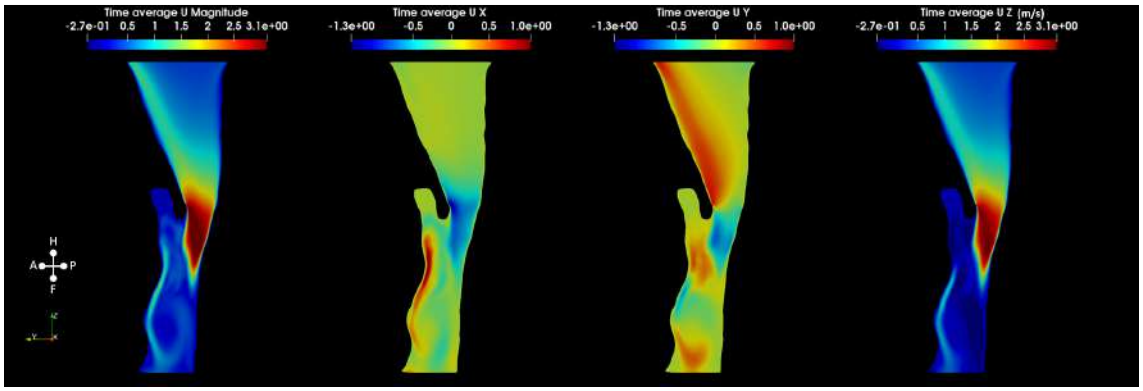

Figure 6.45: Coronal slice of the pharynx model with no adapters showing velocity distribution (m/s) during inspiration.

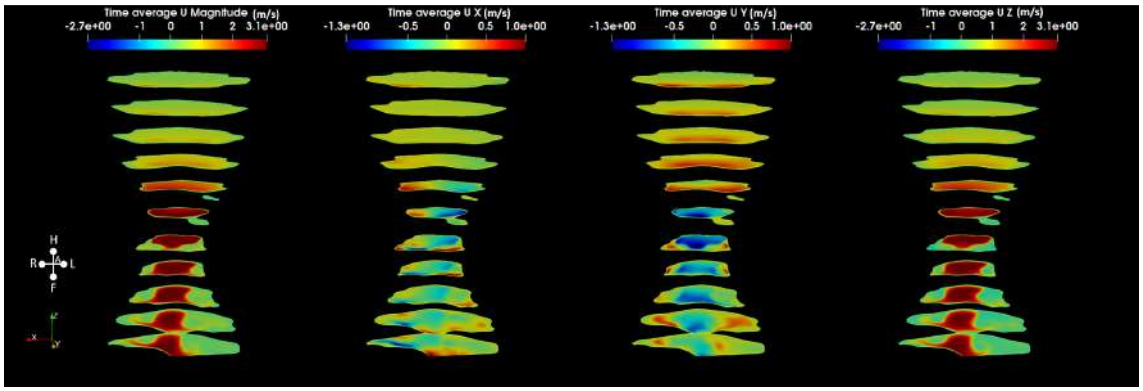

Figure 6.46: Velocity distribution (m/s) in all chosen slices of the pharynx model with no adapters during inspiration.

Table 6.18: Comparison of velocity values obtained from 4D flow MRI and CFD of airflow in the pharynx model with-without adapters during inspiration.

Slice number	**4D flow MRI**				**CFD adapter**				**CFD no adapter**			
-	Ux	Uy	Uz	Umag	Ux	Uy	Uz	Umag	Ux	Uy	Uz	Umag
Slice 1	1	1	1	1	1	1	1	1	1	1	1	1
Slice 2	1.005	2.535	1.414	1.179	4.065	0.476	1.316	1.263	2.127	2.194	1.087	1.036
Slice 3	1.001	6.740	1.749	1.362	6.552	1.295	1.544	1.487	3.133	3.665	1.265	1.210
Slice 4	0.927	14.890	2.506	1.800	13.554	4.302	2.420	2.444	3.676	7.456	1.820	1.800
Slice 5	-0.004	0.002	0.014	0.016	0.001	0.006	0.031	0.033	-0.001	0.005	0.0290	0.031
Slice 6	2.097	-21.963	6.573	4.602	-162.57	-7.766	5.691	6.022	-39.755	-12.018	3.797	3.810
Slice 7	1.965	-31.487	5.141	4.000	-12.915	-5.981	3.756	5.127	-7.554	-10.059	2.664	3.502
Slice 8	1.878	-19.258	5.854	4.143	-53.423	-0.820	4.833	4.822	-14.356	-5.468	3.325	3.450
Slice 9	1.872	-15.705	3.711	3.0516	-57.593	0.030	1.798	2.132	-10.346	-6.772	2.0939	2.270
Slice 10	1.673	-2.131	2.645	2.556	-57.592	0.030	1.798	2.132	-1.927	-0.206	1.509	1.813
Slice 11	1.691	-7.218	2.293	2.449	-75.961	0.0362	2.004	2.338	-10.974	-1.552	1.906	2.000

Table 6.19: Linear regression values from comparison of 4D flow MRI and CFD (with adapter and without adapter) velocity values during inspiration.

Parameters	**Ux**	**Uy**	**Uz**	**Ux**	**Uy**	**Uz**
Intercept (m/s)	27.320	-0.217	0.761	21.459	0.114	0.429
Slope	-29.099	0.193	0.516	-19.143	0.352	0.688
R-squared	0.638	0.608	0.633	0.588	0.607	0.665

rest of the slices showed similar values. The x- and y-components obtained in CFD significantly differ from the 4D flow MRI values. Although the z-component is similar, the values at slices 7 and 8 in the simulation are less than 4D flow MRI values. A comparison with simulation without adapter shows that the magnitude and the z-component of the velocity were lower than that of the MRI's. The x- and y-components were again quite different from the MRI values.

Linear regression is performed to compare the velocity values in each voxel in simulation and MRI. The values suggest that, as seen in the table of averages, the x velocity component is not congruent. However, the y- and the z-component have better congruence. The model with no adapter has a better fit of y- and z-component values.

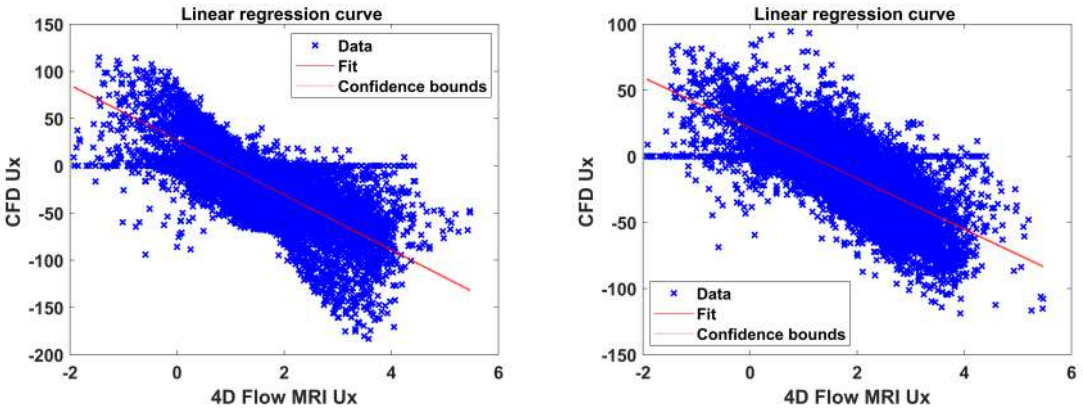

Figure 6.47: Linear regression line of comparison of 4D flow MRI and CFD with adapter and without adapter velocity values in x-component during inspiration.

The ICC values were obtained by comparing the velocity in each voxel of the 4D flow MRI model with the velocity obtained in the corresponding cell in the resampled simulation model with adapter (Table 6.20). The x- and y-component has a very poor correlation but the z-component ICC value is excellent.

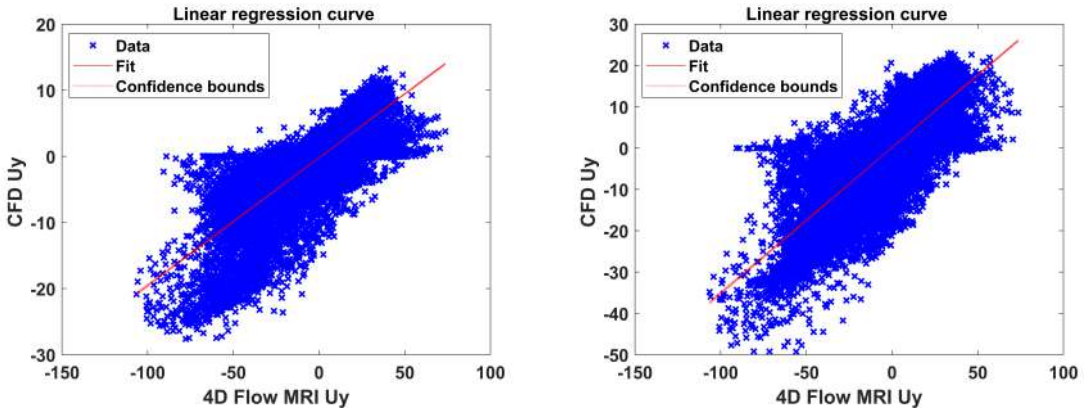

Figure 6.48: Linear regression line of comparison of 4D flow MRI and CFD with adapter and without adapter velocity values in y-component during inspiration.

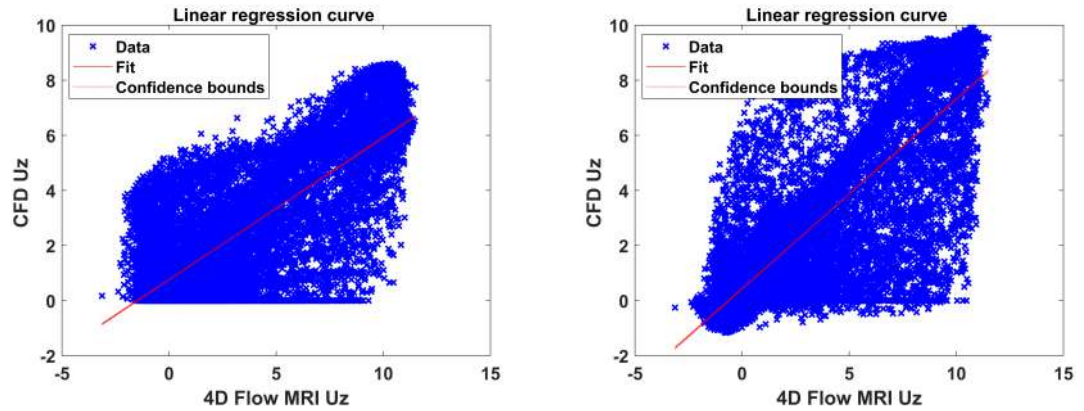

Figure 6.49: Linear regression line of comparison of 4D flow MRI and CFD with adapter and without adapter velocity values in z-component during inspiration.

Table 6.20: ICC for 4D and CFD with and without adapter.

Adapter/ No adapter	**ICC**	**LB**	**UB**	**ICC**	**LB**	**UB**
x-component	-0.076	-0.119	-0.035	-0.121	-0.156	-0.087
y-component	0.534	0.522	0.544	0.738	0.731	0.744
z-component	0.830	0.784	0.863	0.885	0.865	0.900

The simulation without the adapter shows a very poor correlation for the x-component and an excellent correlation for the y- and z-component. The ICC for y- and z- in this model is better than the simulation model with the adapter.

6.3.2.4 WSS in the Pharynx

GTFlow software was used to calculate the WSS on the surface of the pharynx. The velocity values were calculated in individual slices as mentioned above for stenosis in section 6.3.1.3. The values obtained are presented below in the table 6.21. The velocity values compared to the values obtained in MATLAB are slightly higher. The streamlines generated in the software (Figure 6.50) show the vortices formed in slice 7, where the flow separation has happened. Vortices are also seen in the front-right and back walls of the pharynx.

Table 6.21: Time-average velocity magnitude and velocity value obtained from GTFlow in all three directions measured during inspiration in all three trials.

Slice number	**Trial 1 m/s**	**Trial 2 m/s**	**Trial 3 m/s**	**Average m/s**	**Standard deviation m/s**
1	0.207	0.207	0.206	0.206	0.000
2	0.241	0.231	0.230	0.234	0.006
3	0.267	0.261	0.266	0.265	0.003
4	0.310	0.305	0.303	0.306	0.004
5	0.473	0.465	0.463	0.467	0.006
6	0.856	0.819	0.871	0.849	0.026
7	0.672	0.658	0.675	0.668	0.009
8	0.704	0.682	0.677	0.687	0.014
9	0.605	0.577	0.587	0.590	0.014
10	0.473	0.458	0.461	0.464	0.008
11	0.470	0.465	0.470	0.468	0.003

With velocity values, WSS values are derived. The WSS on the front and back surface of the pharynx are depicted in figures 6.51 and 6.52. High WSS values are seen at minimum cross-sectional area and below oropharynx.

The WSS vectors in all chosen slices are illustrated in figure 6.53. Moving downstream from the inlet of the pharynx, the WSS increases significantly. Looking at

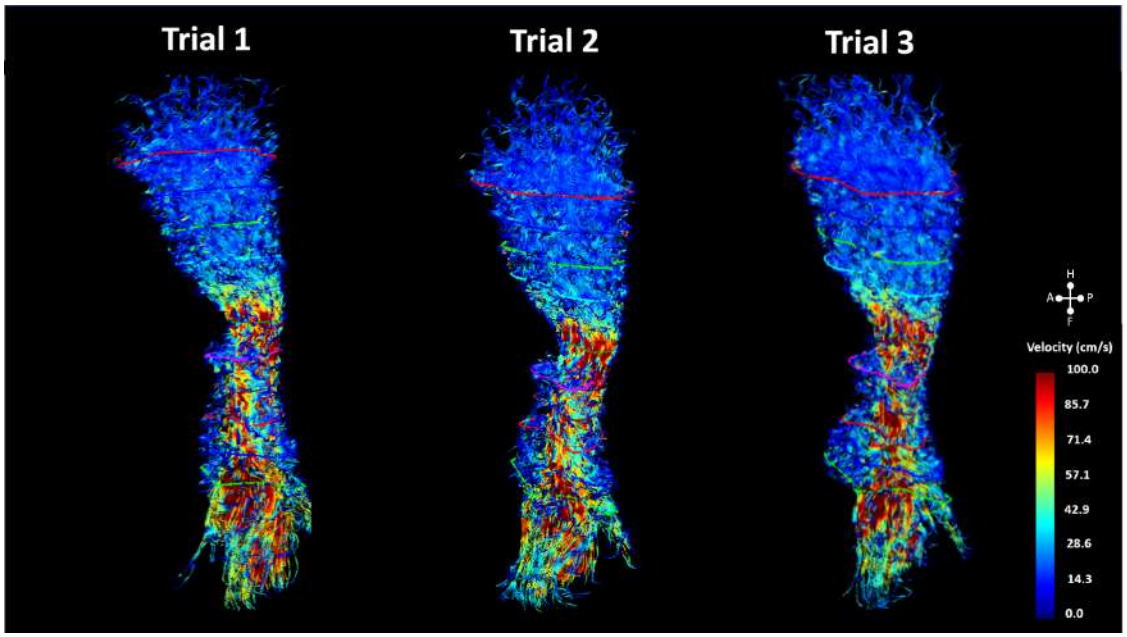

Figure 6.50: Streamlines in the pharynx model visualized in Paraview.

the time-average magnitude and axial WSS values across the eight segments, it is seen that at slice 6, the WSS values are the maximum, approximately 6.5 times higher than at slice 1. Slice 7, 8, and 9 have three times higher WSS than slice 1 (Table 6.22). At slice 10, the WSS decreases and increases again at slice 11.

In almost all the chosen slices, the direction of the WSS vectors is in the direction of flow. However, a closer look at the WSS vectors in slices 6, 7, and 8 segments shows that some of the WSS vectors in slice 7 are in the opposite direction (Figure 6.54). These vectors lie on the front-right side of the pharynx.

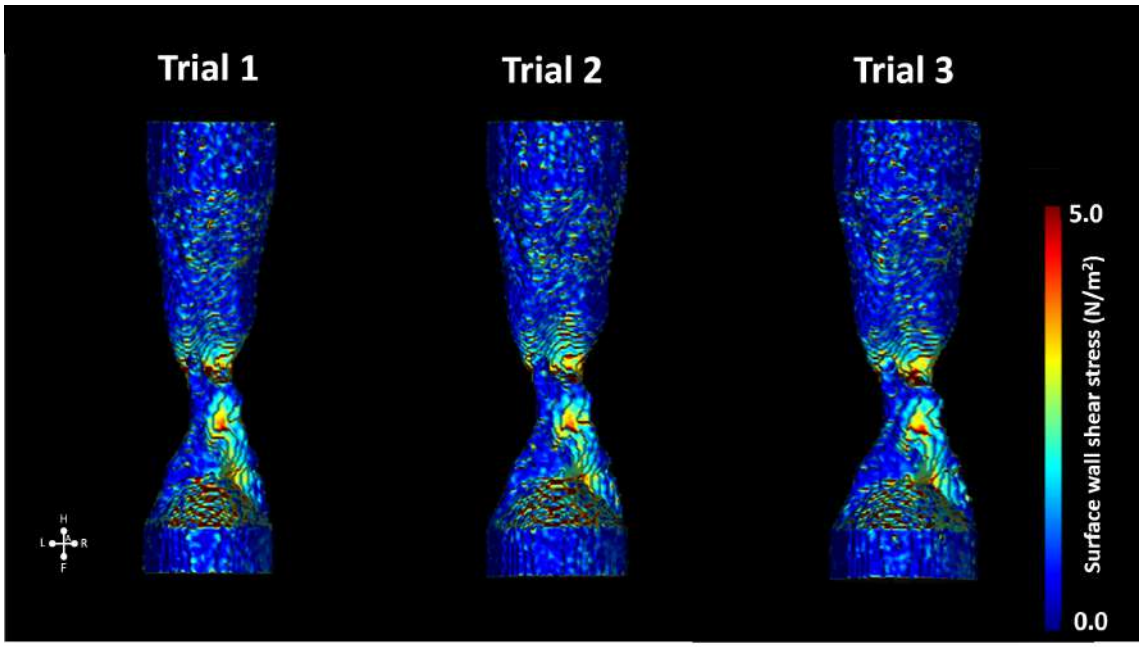

Figure 6.51: Surface WSS distribution (N/m^2) in the pharynx model (front) during inspiration and at all three trials.

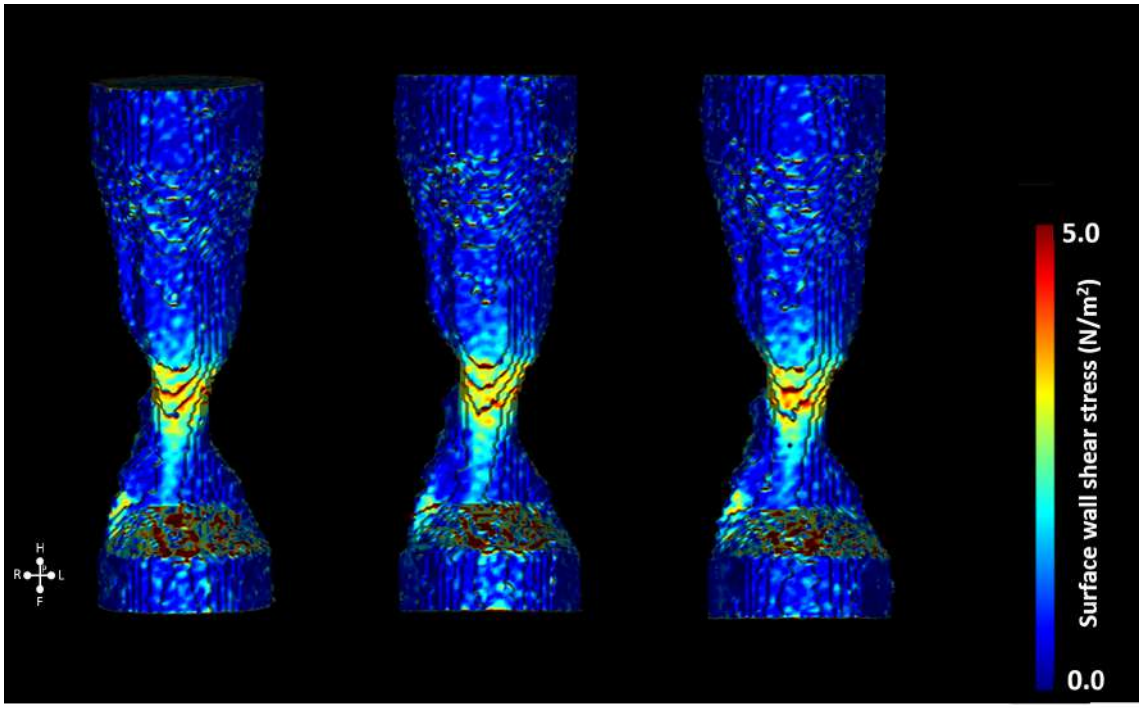

Figure 6.52: Surface WSS distribution (N/m^2) in the pharynx model (back) during inspiration and at all three trials.

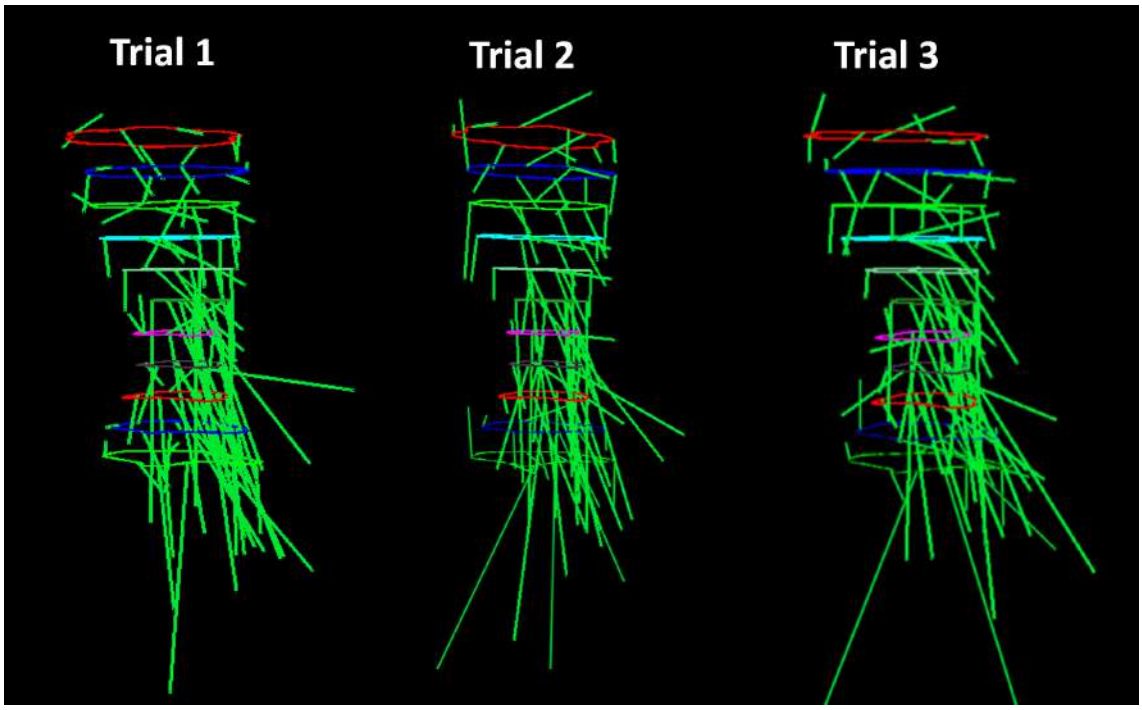

Figure 6.53: WSS vectors (N/m^2, vector length magnified by a factor of 10) across 8 segments of the circumference of the chosen slices in the pharynx model during inspiration and at all three trials at Re 500.

Table 6.22: WSS magnitude and average axial values calculated by GTFlow from the 4D flow MRI measurements in all three trials during inspiration.

Slice number	**Trial 1 WSS mag N/m²**	**WSS axial N/m²**	**Trial 2 WSS mag N/m²**	**WSS axial N/m²**	**Trial 3 WSS mag N/m²**	**WSS axial N/m²**
1	0.729	0.199	0.703	0.186	0.610	0.176
2	0.787	0.441	0.831	0.337	0.791	0.374
3	0.919	0.529	0.874	0.459	0.954	0.498
4	0.976	0.584	1.094	0.752	1.127	0.781
5	1.832	1.601	2.059	1.840	1.921	1.641
6	4.768	4.476	4.818	4.522	3.972	3.779
7	2.719	2.080	2.519	1.842	2.840	2.189
8	2.536	1.725	2.577	2.012	2.271	1.828
9	2.137	1.786	2.324	2.020	1.857	1.288
10	1.413	0.878	1.386	0.745	1.319	0.647
11	2.041	1.520	2.371	1.855	2.344	1.844

Slice number	WSS mag	WSS axial
1	0.680	0.187
2	0.803	0.384
3	0.916	0.496
4	1.066	0.705
5	1.937	1.694
6	4.520	4.259
7	2.693	2.037
8	2.461	1.855
9	2.106	1.698
10	1.373	0.757
11	2.52	1.739

Table 6.23: WSS magnitude and average axial values calculated by GTFlow from the 4D flow MRI measurements averaged across all three trials during inspiration.

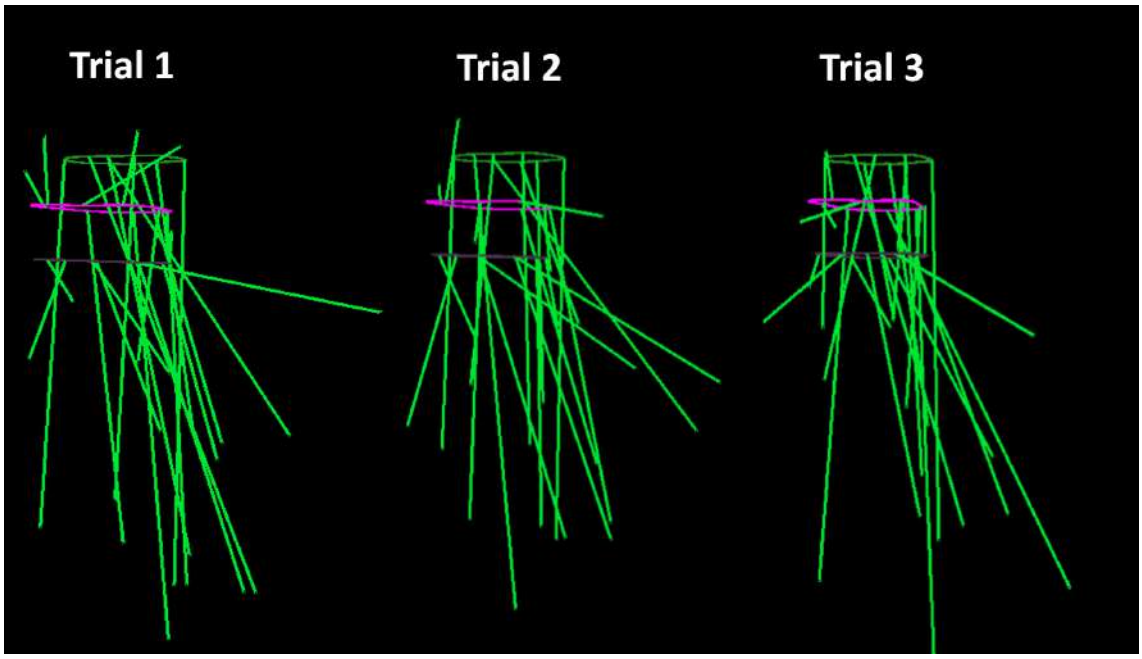

Figure 6.54: WSS vectors (N/m^2, vector length magnified by a factor of 10) across 8 segments in the chosen slice 6,7 and 8 during inspiration.

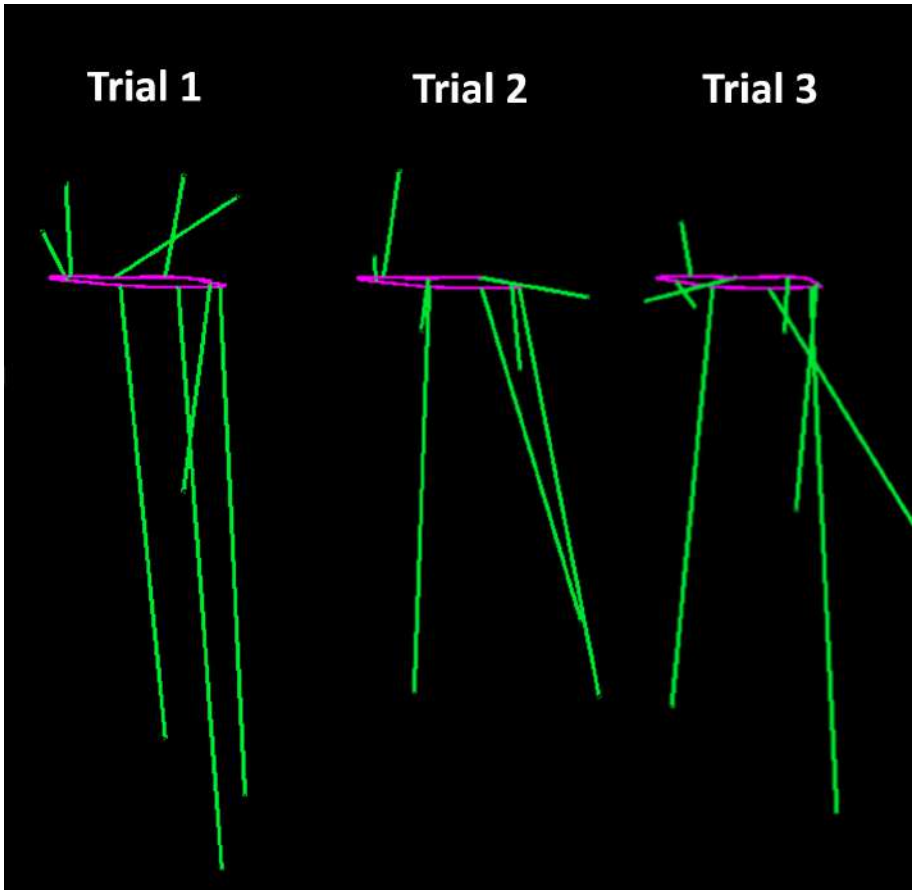

Figure 6.55: WSS vectors (N/m^2, vector length magnified by a factor of 10) across 8 segments in the chosen slice 7 during inspiration.

6.4 Discussion

This chapter aimed at illustrating the application of 4D flow MRI in investigation and validation of flow dynamics in stenosis and pharynx. The results, interpretation, advantages and disadvantages of the technique is provided below.

Reliability analysis

The ability of the 4D flow MRI technique to produce consistent results in both stenosis and pharynx models was well demonstrated by statistically comparing all the three components of measured velocity in three trials using ICC. Both the models have ICC above 0.800, indicating an excellent correlation. Only the x-component of velocity in the stenosis had an ICC value in the range of 0.839 - 0.846. Apart from this, the other components of velocities in the stenosis model and pharynx model had ICC $>$ 0.934. These values suggest that 4D flow MRI can consistently measure velocities in all directions, independent of the model.

Flow dynamics in the stenosis

Although the stenosis model has a simple geometry, the converging and diverging area produces complex flow phenomenons. These flow phenomenons, such as the flow separation, recirculation region, and jet formation, were well observed in 4D flow MRI measurements. A closer look at the velocity patterns observed by plotting the x-, y-, and z-component velocities shows the flow instabilities in the post-stenotic region, the Coanda wall attachment, and branching of the jet occurring due to the unsteady inlet flow. The flapping of the trailing edge of the jet that was previously unseen by 2D PC-MRI measurements was seen by the 4D flow measurements. The formation and dissipation of large vortices right below the stenosis, mainly in slices, were visualized.

Visually, the magnitude and the z-component velocity pattern images were very similar to the patterns obtained by the 2D PC-MRI measurements. A numerical comparison of the z-component values of 2D PC-MRI and 4D flow MRI data shows a good correlation. However, it is to be noted that the 4D flow MRI values in all the slices were higher than the ones obtained by 2D PC-MRI despite having similar inlet values. A similar observation was made comparing the 4D flow MRI z-component results with the LDA results.

The measurement of all the three velocity components presented the possibility of

calculating wall shear stress. This was calculated in the GTFlow software. The WSS was calculated on the entire stenosis surface and the chosen slices' circumference. This analysis showed that the WSS was maximum at the throat of the stenosis, and immediately downstream, the WSS drops. These results were also compared to the published LDA for validation. This comparison showed an underestimation of the WSS value in GTFlow at 0D (LDA: 23 times higher than at inlet, GTFlow: 16 times higher than at the inlet). The maximum WSS was obtained at position -0.01 d and not 0D. It is to be noted that this calculation of the WSS on the chosen slice had its circumference chosen manually. Therefore, it could be subjected to some manual error. Also, the velocity value at the throat was less in GTFlow than in Paraview or the theoretical value.

The knowledge of the flow phenomenon, instabilities, turbulence, and WSS received from the 4D flow MRI in the stenosis and post-stenosis helps better understand the cause of the effects, progression, and location detection of atherosclerosis. That is, it is known from several research that low WSS is the leading hemodynamic parameter promoting atherosclerotic plaque growth, which in turn influences the blood flow and WSS distribution [139] [140]. That is, downstream of the stenosis, the back flow in the recirculation region with low WSS might lead to further accumulation of the near-wall LDL, progressing atherosclerosis further. As seen in the WSS images, the WSS is uneven across the circumference, and the values vary with time. Such oscillating values have a detrimental impact on the wall of the lumen. Flow instability such as the Coanda effect can cause higher pressure and stress on one side of the wall than the other.

Flow dynamics in the pharynx

As in stenosis, the converging-diverging areas in the pharynx produce complex 3D flow patterns. Due to the complexity of the geometry post-constriction in the pharynx, the flow patterns and their effects are more prominent. As in the stenosis, the x- and y-component's role in the flow is seen in 4D flow MRI. In the current case, this was majorly seen at the inlet (This variation possibly occurs from unsteady flow generation by the pump or short entrance length). Although the component of the velocity value matched perfectly with the theoretically expected value and 2D PC-MRI, it was observed that the flow was higher upon the inclusion of the x- and y-component of the velocity component. The x- and y-component velocities were significantly higher, causing the velocity magnitude to be higher. Qualitatively the velocity flow pattern in the entire model looked very similar to 2D PC-MRI.

In both, the formation of small vortices, slice 7 onwards, was observed. With the help of 4D flow MRI, the formation and dissipation of the vortices formed in the recirculation were well captured. The velocity component's contribution to this turbulence was also measured and visualized. Most vortices had a significant contribution from the z-component of the velocity, and the x- and y-component of velocities were seen in smaller vortices. The variation in the jet length and its impingement asymmetrically on the wall of the pharynx was well visualized. The 4D flow MRI and 2D PC-MRI z-component of velocity's numerical comparison shows a perfect coincidence. However, as in the case of stenosis, the velocity values obtained in 4D Flow MRI were slightly higher. The WSS was calculated for the pharynx with the help of GTFlow. The WSS on the surface was as expected, high at the smaller cross-section and on the wall with jet impingement. On calculating the WSS on the circumference of the chosen slice, it was seen that at slice 7, where recirculation occurs due to flow separation, the WSS vectors reverse their direction on the front wall. High WSS values are associated with increased friction between flow and the airway lumen. This reversal of the WSS vectors would cause additional strain on the airway lumen and directly affect the pressure distribution to cause deformation or collapse. The vortices and the jet impingement seen during the time evolution of the velocity pattern on the anterior wall is speculated to cause soft tissue damage and aid in snoring. These additional information help in localizing the cause of sleep apnea in a given patient and also change flow parameters or the geometry to understand to help rectify or alleviate the problem.

Comparison of 4D flow MRI results with CFD in the pharynx

The experimental results of the pharynx model were used to validate the simulation results in the same model. The qualitative comparison revealed that the prominently seen recirculation regions in the 4D flow MRI measurements were not present in the simulation results. Quantitatively the z-component results were congruent, but the x-component results showed stark differences. In order to further investigate these differences, flow in the model with no adapters attached was studied and compared; the results of this simulation were closer to the one obtained by 4D Flow MRI. However, the x- and y-components of the velocities still had differences. In both the models, the differences were seen in the post-stenotic region, where the flow is turbulent. This deviation seen in the comparison could be coming from the higher and non-uniform inlet flow.

4D flow MRI

The 4D flow MRI undoubtedly provides a comprehensive evaluation of the flow dynamics in the stenosis and pharynx. The test-retest reliability analysis showed that the method is very stable. By comparing the results with that obtained from 2D PC-MRI, it was seen that both z-component of the velocity values were comparable, showing the accuracy of the measured values. However, consistently all the z-component of velocity values obtained in 4D flow MRI were slightly higher. The various reasons contributing to this might be the decreased spatio-temporal resolution or the acquisition technique. The higher spatio-temporal resolution was linked to a large amount of data is produced in this method. Due to the limitation of the computer, a comprise on the time, spatial resolution, and memory for the data had to be done. However, the amount of signal received has to be also considered, a higher spatial resolution might lead to a very little signal received.

GTFlow for post-processing of the data was suitable for a quick analysis and provided valuable information in understanding the mechanics of the wall deformation. However, as choosing of ROI is prone to errors due to manual intervention. Therefore, further development of post-processing in a form allowing use in a consistent workflow would be desirable. It is also necessary to establish standardized analysis methods with limit values for various parameters allowing differentiation between pathological and healthy in order to obtain reproducible and comparable results.

Due to better signal averaging and higher spatial resolution, 2D PC-MRI 1-direction provides accurate results and therefore is an excellent PC-MRI technique to validate simulation results. However, 2D PC-MRI does not give the whole picture about the flow dynamics, and all that can be compared is the velocity in one direction. Using 4D flow MRI, one can compare all the components of velocities and their derived parameters with the simulation data. As seen, the flow is turbulent, complex, and varies with time in both stenosis and the pharynx. Although velocity in the z-component is the main contributor to the flow, the other two components play a significant role in the turbulence, instabilities, and WSS.

6.5 Conclusion

The quantitative comparison of the voxel-by-voxel velocity values (all three components) between the three trials in the stenosis and pharynx model showed excellent reliability. The 4D flow MRI analysis of the flow in the stenosis again measured

and visualized the flow separation and Coanda effect prominently seen in the 2D PC-MRI experiment (Chapter 4). With the time evolution of the velocity pattern, the flapping jet and formation-decay of the vortices are well visualized. The WSS distribution calculated in GTFlow showed the critical changes in the WSS value in the stenosis model. The 4D flow MRI velocity and WSS values were well validated with the published data. The same technique was then extended to the pharynx model. The reliability of 4D flow MRI in measuring velocities in the complex model in all three trials was also excellent. The flow pattern and velocity values measured in 4D flow MRI were congruent with the 2D PC-MRI results (Chapter 5). With the help of 4D flow MRI, the vortices formed in the recirculation region were visualized. Further, the WSS calculation and visualization showed the reversal of WSS in the recirculation region, making the airway more susceptible to collapse. In conclusion, our study confirms the applicability of the 4D flow MRI technique as a validation technique. Despite the potential overestimation of velocity, 4D flow MRI promises the most comprehensive evaluation of the flow in the stenosis and pharynx provided by a single diagnostic technique, assessing anatomy and time evolving primary and secondary flow patterns non-invasively. This information helps understand the problem's cause, effect, and better localization.

7

Summary, conclusion and future work

7.1 Summary

The present thesis demonstrates the use of MRI-based methods, 2D PC-MRI, and 4D flow MRI as an investigative tool to study flow patterns in-vitro and as a validation tool for CFD simulation. A stenosis model with 75% occlusion to study the stenotic flow at laminar and turbulent flow conditions and a subject-specific, anatomically accurate pharynx model from CBCT image to study flow dynamics during inspiration and expiration were additively manufactured. The reliability of the experiment setup and PC-MRI technique were established with reliability tests performed on three experiments for each technique, model, and boundary condition. The accuracy of 2D PC-MRI results in the stenosis model was checked by comparing 2D PC-MRI results with previously published LDA data. This validated technique was also extended to study flow dynamics in the pharynx model during average inspirational and expiration flow rates. Prominent flow phenomenons occurring in both models, such as flow separation with instabilities like the Coanda effect and large vortex formation in the stenosis and pharynx models, were well measured and visualized. This demonstrated the use of the technique as an investigative tool. The application of the technique as a validation tool was showcased by statistically comparing the LES model at Re 2000 in the stenosis model and CFD of airflow in

the pharynx model at an average inspirational flow rate with 2D PC-MRI data. Further, 4D flow MRI was applied to measure the time variation of velocities in all three directions at Re 500 in the stenosis model and the average inspirational flow rate in the pharynx model. The velocities and WSS in the stenosis model were again validated with published LDA data. A comprehensive flow study was done by measuring all the components of the velocities and investigating the WSS derived from the measured velocities. The velocities in all three directions showed the influence of the velocities in components perpendicular to the flow direction for the flow separation and its effect on soft tissue damage or snoring. The analysis of WSS in both models gave vital information about the progression of atherosclerosis and collapse of the airway in stenosis and pharynx models, respectively. These results were also compared with the 2D PC-MRI and simulation results to understand further the advantages and disadvantages of the techniques as an investigative and validation tool.

7.1.1 Findings

The following are the main achievements of the study.

- Demonstration of feasibility of 3D printed rigid anatomical models for MRI investigations

  3D printing is an innovative, and rapidly growing technology to produce custom anatomical models and medical conditions models for medical education and treatment planning. Such models can also be used for magnetic resonance experimental design. This work demonstrates that the 3D printing technology (3D printer used: ProJet 3510HD, material: VisijetX) can be successfully used to fabricate an accurate (0.001-0.002 inch per inch of part dimension) idealised stenosis model and a patient customised obstructive sleep apnea diseased pharynx model. These models were used to study the flow dynamics in stenosed artery and pharynx using the PC-MRI technique. For this in-vitro measurement of blood flow in the stenosed artery and airflow in the pharynx, a water-glycerol mixture was used. By varying the proportion of water and glycerol a suitable density and viscosity of the fluid mixture can be obtained that maintains dynamic similarity with either blood or airflow. During the measurement of velocity in these models with the water-glycerol mixture, no artifacts arising due to the model material and water-glycerol mixture was found. Additionally, in every trial the measured velocity value was compared

with the theoretical velocity value at the inlet of the model to ensure that the experimental setup is accurate and reliable.

- Establishment of test-retest reliability of the 2D PC-MRI and 4D flow MRI technique

  PC-MRI is a non-invasive imaging technique that enables quantitative measurement of flow in the direction of flow and 4D flow MRI measures the velocity in the three spatial and temporal dimension. Although PC-MRI has shown a lot of utility in measuring flow, there are several potential sources of error that can significantly affect the accuracy and precision of flow measurements. Therefore, all the flow measurements using 2D PC-MRI and 4D flow MRI in stenosis and pharynx model at all defined boundary conditions were performed in triplicate. In this study the test-retest repeatability for velocity value measured in three was assessed using intraclass correlation coefficients (ICC) calculated using 2-way mixed model with 95% confidence interval.That is velocity measurement in every voxel of one trial was compared with the velocity value in the corresponding voxel of the other to trials using ICC. The ICC value for velocity measured by 2D PC-MRI in stenosis (at Re 500 and Re 2000) and pharynx model were above 0.8 and were therefore characterized as excellent. Similarly, the velocity measured using 4D flow MRI in the stenosis (Re 500) and pharynx model showed excellent realiability with ICC value $>$ 0.8. This showed the ability of the techniques to measure velocity accurately and reliably every time.

- Validation of 2D PC-MRI technique to measure velocity with published and well accepted velocity values measured using laser doppler anemometry

  The velocity in the stenosis model (75% occlusion model) was measured at Re 500 and Re 2000 using 2D PC-MRI. The flow dynamics in the stenosis, including flow instabilities such as Coanda flow, were well visualized and measured. The evaluation of the accuracy of 2D PC-MRI velocity values by validating it with published data by Ahmed and Giddens [120] using Bland-Altman plot and linear regression analysis. A good correlation was obtained between the 2D PC-MRI and LDA measurements with linear regression values ranging from 0.767-0.998 for Re 500 and 0.543-0.983 for Re 2000. The feasibility of the 2D PC-MRI technique as a tool for reliable velocity measurement was demonstrated, and a statistical framework was provided for further comparisons.

- Validation of numerical simulations of flow in stenosis model at Re 2000 with 2D PC-MRI data

  Flow in the stenosis model at Re = 2000 was simulated with LES at Re 2000. LES is a turbulence model used in CFD. In LES, the large-scale motions of the large eddies of turbulent flow are computed directly, and only small-scale or sub-grid-scale motions are modeled. The voxel-by-voxel comparison of 2D PC-MRI and LES data (for a detailed comparison, the LES data is resampled to the spatial resolution of the PC-MRI data) in the stenosis model showed agreement with a slope and R^2 values of 1.030 and 0.827, respectively. These results support using 2D PC-MRI as an investigative tool for studying flow dynamics and a validation tool for numerical simulations.

- Investigation of flow in the pharynx model during inspiration and expiration using the validated 2D PC-MRI technique

  The flow analysis during inspiration showed, a negative pressure zone in the recirculation region on the anterior wall caused due to the geometry of the airway; this coupled with the intrinsic lack of solid support in the anterior wall-flow phenomenon makes the anterior airway more susceptible to a collapse. Conversely, during expiration, a negative pressure zone in the recirculation region formed due to the change in geometry of the airway causes no collapse due to the solid support on the posterior wall of the airway. The 2D PC-MRI technique was able to visualize the formation of the vortices in the recirculation region very well. This valuable information can add value to the existing clinical assessment.

- Validation of numerical simulations of flow in pharynx model during inspiration with 2D PC-MRI data

  Comparing the 2D PC-MRI data with the CFD data provides a framework for CFD validation using in-vitro MRI velocity data. A voxel-by-voxel comparison of the velocity value from 2D PC-MRI and CFD for the entire model showed a fair agreement with R^2 value of 0.633, and qualitatively consistent flow patterns were obtained in the simulation.

- Investigation of evolution of the flow along with wall shear stress in the stenosis and pharynx model at laminar and average inspirational flow rate using 4D flow MRI.

  The 4D flow MRI analysis of the flow in the stenosis again measured and visualized the flow separation and Coanda effect prominently seen in the 2D

PC-MRI experiment (Chapter 4). With the time evolution of the velocity pattern, the flapping jet and formation-decay of the vortices are well visualized. The WSS distribution calculated in GTFlow showed the critical changes in the WSS value in the stenosis model. The 4D flow MRI velocity and WSS values were well validated with the published data. The flow pattern and velocity values measured in 4D flow MRI were congruent with the 2D PC-MRI results (Chapter 5). With the help of 4D flow MRI, the vortices formed in the recirculation region were visualized. The same technique was then extended to the pharynx model. Further, the WSS calculation and visualization showed the reversal of WSS in the recirculation region, making the airway more susceptible to collapse. In conclusion, our study confirms the applicability of the 4D flow MRI technique as a validation technique. Despite the potential overestimation of velocity, 4D flow MRI promises the most comprehensive evaluation of the flow in the stenosis and pharynx provided by a single diagnostic technique, assessing anatomy and time evolving primary and secondary flow patterns non-invasively. This information helps understand the problem's cause, effect, and better localization.

- The application of 4D flow MRI as a validation tool was shown by comparing the CFD results in the pharynx with 4D flow MRI results.

  The experimental results of the pharynx model were used to validate the simulation results in the same model. The qualitative comparison revealed that the prominently seen recirculation regions in the 4D flow MRI measurements were not present in the simulation results. Quantitatively the z-component results were congruent, but the x-component results showed stark differences. In order to further investigate these differences, flow in the model with no adapters attached was studied and compared; the results of this simulation were closer to the one obtained by 4D Flow MRI. However, the x- and y-components of the velocities still had differences. In both the models, the differences were seen in the post-stenotic region, where the flow is turbulent. This deviation seen in the comparison could be coming from the higher and non-uniform inlet flow.

7.1.2 Concluding remarks

2D PC-MRI and 4D flow MRI are promising techniques to accurately and reliably measure the flow in circulatory and respiratory structures. For such an investigation

3D printing is a feasible technique for producing highly accurate 3D anatomical model generated from segmentation of MRI images of the patients. Furthermore the material of the model and the water-glycerol mixture used to mimic blood flow and airflow are completely compatible to the MRI and no artifacts or inaccuracies in the velocity measurement arising from magnetic properties of the material and fluid was found.

The investigation of flow in the stenotic model at laminar and turbulent region shows that the 2D PC-MRI can visualize the steady and unsteady flow. The velocity measured by PC-MRI showed good agreement to the well accepted velocity measurements in the stenotic model measured using laser doppler anemometry. This validated 2D PC-MRI method was then used to measure the velocity in the patient customized pharynx model accurately, showcasing the capabilitiy of the technique to measure and visualize complex flow. The 2D PC-MRI data was used successfully to validate the numerical simulation of flow in the stenosis and the pharynx by comparing the data using t-test, Bland-Altman anylsis and linear regression.

The flow features in stenosis and pharynx constitute complex flow phenomenons varying in space and time, such as flow separation, formation of vortices, periodic oscillations, and vibrations. Although 2D PC-MRI gives a good understanding of the flow phenomenon and average minimum-maximum velocity values in the region of interest, 4D flow MRI was used study the contribution of the other velocity components and the wall shear stress to the flow dynamics and pathophysiology. Using this the development of turbulence and variation of wall shear stress was identified. The so measured velocity was compared to the validated 2D PC-MRI data and the laser doppler anemometry data. The comparison showed that the 4D flow MRI overestimates the velocity value slightly probably owing to the lower spatial resolution. However, the additional information received in the 4D flow MRI gives a much deeper insight into the dynamic relationship of the geometry, flow and pathophysiology. Moreover, this method provides an opportunity to validate numerically simulated velocity measurements in all spatial and temporal dimension.

Thus, all of our findings support the use of 2D PC-MRI and 4D flow MRI techniques to investigate flow dynamics in various flow models and serve as a good validation tool for numerical simulation.

7.2 Future work

For future work, the following investigations are proposed.

- Imaging of the upper airway The stenosis studies can be extended to anatomically accurate stenotic models to further explore the hemodynamics and effect of geometries and bifurcations in atherosclerosis. For this imaging of the stenotic arteries is required. High quality of the imaging would aid in better segmentation and better 3D printing. Likewise for the imaging of the pharynx better resolution and CT images of patients in the supine position with the inclusion of the nasal cavity would help to get the most accurate representation of the upper airway during OSA. Additionally, this would provide more realistic boundary conditions for the flow studies. However, segmentation of the upper airway, particularly the nasal cavity and the surrounding tissues, is subjective and requires extensive manual intervention. A better automatic method is thus required. Furthermore, other imaging modalities such as MRI could be explored to acquire upper airway images.

- Development of compliant models The 3D printed models used for the current study were rigid models. Building a compliant stenosis and pharynx model using materials with properties similar to the physiological component. Elastic properties of the tissues and arteries can be determined by mechanical testing. For example muscles around the upper airways havea E-modulus of 10^3 and these can be simulated using silicone with similar E- modulus. With such models the dynamic interaction of the fluid structure and the fluid can be investigated.

- Improvements in experiment setup and inlet conditions To ensure steady flow at the inlet of the model a laminizer can be included. Further inclusion of fluid temperature controller can ensure that the properties of the of the fluid does not change during the long measurement period. As such a change in the fluid properties can have an effect on the velocity. In the current study, the flow at the ilet of the stenosis and the pharynx was asssumed to be steady. However, to mimic the blood flow or airflow and make more accurate predictions of flow phenomenon use of oscillatory or pulsatile or customized breathing patterns flow is recommended.

- MRI acquisition and post-processing Variations in acquisition parameters such as voxel size, number of signal averages, velocity encoding influence the ac-

curacy and precision of the velocity measurements. Therefore, optimization of the imaging parameters to increase SNR and reduces noise in velocity images would further improve the quality of the images and for more accurate of velocity measurements. Artifact reduction, particularly for turbulent flow conditions with post-processing is encouraged for future studies.

- Additional studies As much as the geometry of the arteries or the airway has an impact flow of the fluid, the wall and surface properties of the arteries or pharynx also has an effect on the flow dynamics. Conversely, the flow dynamics also has the potential to deform the physiological structure and/ or damage it. Therefore, when investigating the flow dynamics in compliant models additionally studying the wall deformation will provide valuable information.

  Also, study of pressure drop within the models can also give further insight. For such a study use of a pressure transducer can be used. Using novel techniques such as pressure-sensitive paint (PSP) can give information about the surface pressure. Pressure sensitive paints is a method for measuring surface pressure by measuring the luminescence of the paint excited with LED lamp using a camera (luminescent response is a function of the local barometric pressure at the surface). This technique provides a non-intrusive full-field surface pressure.

  Alternatively, calculating surface pressure from the surface velocity measured in 4D Flow MRI can be done in software such as MevisFlow.

  More case studies with and without MAD is required.

Publication List

P1. P. Gurumurthy, P. Ulloa, C. Kluck, T. M. Buzug, and M. A. Koch, "Study of fluid flow patterns in a human pharynx phantom using phase contrast-mri," *Magnetic Resonance Materials in Physics, Biology and Medicine*, vol. 29, no. 1, pp. 201–202, 2016.

P2. P. Gurumurthy, C. Hagen, P. Ulloa, M. A. Koch, and T. M. Buzug, "Session 53. modelling and simulation iv," *Biomedical Engineering/Biomedizinische Technik*, vol. 62, no. s1, pp. s507–s510, 2017.

P3. C. Hagen, P. Gurumurthy, and T. M. Buzug, "Effects of replacing the nasal cavity with a simple pipe like structure in cfd simulations of the airflow within the upper airways of osa patients with patient individual flow rates," *Current Directions in Biomedical Engineering*, vol. 3, no. 2, pp. 795–798, 2017.

P4. A. Ibbeken, P. Gurumurthy, F. Zell, C. Hagen, and T. M. Buzug, "Fabrication of a flexible stenosis phantom for flow measurements using additive manufacturing," *Transactions on Additive Manufacturing Meets Medicine*, vol. 1, no. 1, 2019.

P5. A. Ibbeken, P. Gurumurthy, F. Zell, C. Hagen, M. A. Koch, and T. M. Buzug, "Mri flow measurements with a flexible stenosis phantom," *Current Directions in Biomedical Engineering*, vol. 5, no. 1, pp. 565–568, 2019.

P6. N. Abrams, P. Gurumurthy, A. Frydrychowicz, T. Buzug, D. Pawlak, K. Hasselbacher, M. Suurna, and A. Steffen, "Can the therapy outcome of upper airway stimulation (uas) be predicted by a preoperative mri?" *Laryngo-Rhino-Otologie*, vol. 98, no. S 02, p. 10849, 2019.

Bibliography

[1] J. L. Sobiesk and S. Munakomi, "Anatomy, head and neck, nasal cavity," *StatPearls Publishing: Treasure Island, FL, USA*, 2022.

[2] N. Mygind and R. Dahl, "Anatomy, physiology and function of the nasal cavities in health and disease," *Adv. Drug Deliv. Rev.*, vol. 29, no. 1-2, pp. 3–12, 1998.

[3] National Cancer Institute. Anatomical plane definition. https://training.seer.cancer.gov/anatomy/body/terminology.html. Accessed: 2022-05-16.

[4] C. J. T. Spence, "Experimental investigations of airflow in the human upper airways during natural and assisted breathing," Ph.D. dissertation, University of Canterbury, Mechanical Engineering, 2011.

[5] C. S. Van Holsbeke, S. L. Verhulst, W. G. Vos, J. W. De Backer, S. C. Vinchurkar, P. R. Verdonck, J. W. van Doorn, N. Nadjmi, and W. A. De Backer, "Change in upper airway geometry between upright and supine position during tidal nasal breathing," *J. Aerosol Med. Pulm. Drug Deliv.*, vol. 27, no. 1, pp. 51–57, 2014.

[6] Open Anesthesia. Anatomy of the pharynx. https://www.openanesthesia.org/upper-airway-anatomy/. Accessed: 2022-05-19.

[7] K. P. Strohl, J. P. Butler, and A. Malhotra, "Mechanical properties of the upper airway," *Compr. Physiol.*, vol. 2, no. 3, pp. 1853–1872, 2012.

[8] I. Ayappa and D. M. Rapoport, "The upper airway in sleep: physiology of the pharynx," *Sleep Med. Rev.*, vol. 7, no. 1, pp. 9–33, 2003.

[9] A. C. F. Suárez-Quintanilla and S. Sharma. (2024) Anatomy, head and neck, larynx.

[10] R. Courtney, "The functions of breathing and its dysfunctions and their relationship to breathing therapy," *Int. J. of Osteopath. Med.*, vol. 12, no. 3, pp. 78–85, 2009.

[11] T. Stedman, *Stedman's medical dictionary*. Dalcassian publishing company, 1920.

[12] Division of Sleep Medicine at Harvard Medical School. Sleep, learning and memory. http://healthysleep.med.harvard.edu/healthy/matters/benefits-of-sleep/learning-memory. Accessed: 2022-05-19.

[13] T. W. Kim, J.-H. Jeong, and S.-C. Hong, "The impact of sleep and circadian disturbance on hormones and metabolism," *Int. J. Endocrinol.*, vol. 2015, no. 1, 2015.

[14] J. G. Park, K. Ramar, and E. J. Olson, "Updates on definition, consequences, and management of obstructive sleep apnea," *Mayo Clin. Proc.*, vol. 86, no. 6, pp. 549–555, 2011.

[15] 3D Systems Inc. Collapse of soft tissue into the airway. https://www.tmjsleepma.com/tmj-apnea-services/sleep-apnea-in-adults. Accessed: 2022-05-16.

[16] A. V. Benjafield, N. T. Ayas, P. R. Eastwood, R. Heinzer, M. S. Ip, M. J. Morrell, C. M. Nunez, S. R. Patel, T. Penzel, J.-L. Pépin *et al.*, "Estimation of the global prevalence and burden of obstructive sleep apnoea: a literature-based analysis," *Lancet Respir. Med.*, vol. 7, no. 8, pp. 687–698, 2019.

[17] A. Malhotra, I. Ayappa, N. Ayas, N. Collop, D. Kirsch, N. Mcardle, R. Mehra, A. I. Pack, N. Punjabi, D. P. White *et al.*, "Metrics of sleep apnea severity: beyond the apnea-hypopnea index," *Sleep*, vol. 44, no. 7, 2021.

[18] M. M. Lyons, N. Y. Bhatt, A. I. Pack, and U. J. Magalang, "Global burden of sleep-disordered breathing and its implications," *Respirology*, vol. 25, no. 7, pp. 690–702, 2020.

[19] L. M. Stephanie Watson, Reviewed by Elaine K. The effects of sleep apnea on the body. https://www.healthline.com/health/sleep-apnea/effects-on-body#Takeaway. Accessed: 2022-05-19.

[20] N. E. Morsy, N. S. Farrag, N. F. Zaki, A. Y. Badawy, S. A. Abdelhafez, A.-H. El-Gilany, M. M. El Shafey, S. R. Pandi-Perumal, D. W. Spence, and A. S. BaHammam, "Obstructive sleep apnea: personal, societal, public health, and legal implications," *Rev. Environ. Health*, vol. 34, no. 2, pp. 153–169, 2019.

[21] K. Sutherland and P. A. Cistulli, "Recent advances in obstructive sleep apnea pathophysiology and treatment," *Sleep and Biological Rhythms*, vol. 13, no. 1, pp. 26–40, 2015.

[22] R. Arens and C. L. Marcus, "Pathophysiology of upper airway obstruction: a developmental perspective," *Sleep*, vol. 27, no. 5, pp. 997–1019, 2004.

[23] J. H. Walsh, M. S. Leigh, A. Paduch, K. J. Maddison, J. J. Armstrong, D. D. Sampson, D. R. Hillman, and P. R. Eastwood, "Effect of body posture on pharyngeal shape and size in adults with and without obstructive sleep apnea," *Sleep*, vol. 31, no. 11, pp. 1543–1549, 2008.

[24] D. J. Eckert and A. Malhotra, "Pathophysiology of adult obstructive sleep apnea," *Proc. Am. Thorac. Soc.*, vol. 5, no. 2, pp. 144–153, 2008.

[25] L. V. Pham and A. R. Schwartz, "The pathogenesis of obstructive sleep apnea," *J. Thorac. Dis.*, vol. 7, no. 8, pp. 1358–1372, 2015.

[26] M. Goyal and J. Johnson, "Obstructive sleep apnea diagnosis and management," *Mo Med*, vol. 114, no. 2, pp. 120–124, 2017.

[27] V. K. Kapur, D. H. Auckley, S. Chowdhuri, D. C. Kuhlmann, R. Mehra, K. Ramar, and C. G. Harrod, "Clinical practice guideline for diagnostic testing for adult obstructive sleep apnea: an american academy of sleep medicine clinical practice guideline," *J. Clin. Sleep Med.*, vol. 13, no. 3, pp. 479–504, 2017.

[28] M. Kapoor and G. Greenough, "Home sleep tests for obstructive sleep apnea (osa)," *J. Am. Board. Fam. Med.*, vol. 28, no. 4, pp. 504–509, 2015.

[29] B. Pivetta, L. Chen, M. Nagappa, A. Saripella, R. Waseem, M. Englesakis, and F. Chung, "Use and performance of the stop-bang questionnaire for obstructive sleep apnea screening across geographic regions: a systematic review and meta-analysis," *JAMA Netw. Open*, vol. 4, no. 3, 2021.

[30] B. Amra, B. Rahmati, F. Soltaninejad, and A. Feizi, "Screening questionnaires for obstructive sleep apnea: an updated systematic review," *Oman Med. J.*, vol. 33, no. 3, pp. 184–192, 2018.

[31] D. J. Gottlieb and N. M. Punjabi, "Diagnosis and management of obstructive sleep apnea: a review," *JAMA*, vol. 323, no. 14, pp. 1389–1400, 2020.

[32] B. Carvalho, J. Hsia, and R. Capasso, "Surgical therapy of obstructive sleep apnea: a review," *Neurotherapeutics*, vol. 9, no. 4, pp. 710–716, 2012.

[33] M. Friedman and O. Jacobowitz, *Sleep Apnea and Snoring E-Book: Surgical and Non-Surgical Therapy.* Elsevier Health Sciences, 2018.

[34] A. E. Sher, "Upper airway surgery for obstructive sleep apnea," *Sleep Med. Rev.*, vol. 6, no. 3, pp. 195–212, 2002.

[35] S. Nordgård, B. K. Stene, and K. W. Skjøstad, "Soft palate implants for the treatment of mild to moderate obstructive sleep apnea," *Otolaryngolog. Head Neck Surg.*, vol. 134, no. 4, pp. 565–570, 2006.

[36] R. N. Aurora, K. R. Casey, D. Kristo, S. Auerbach, S. R. Bista, S. Chowdhuri, A. Karippot, C. Lamm, K. Ramar, R. Zak *et al.*, "Practice parameters for the surgical modifications of the upper airway for obstructive sleep apnea in adults," *Sleep*, vol. 33, no. 10, pp. 1408–1413, 2010.

[37] W. J. Randerath, J. Verbraecken, S. Andreas, G. Bettega, A. Boudewyns, E. Hamans, F. Jalbert, J. R. Paoli, B. Sanner, I. Smith *et al.*, "Non-cpap therapies in obstructive sleep apnoea," *Eur. Respir. J.*, vol. 37, pp. 1000–1001, 2011.

[38] W. Kukwa, E. Migacz, T. Lis, and S. L. Ishman, "The effect of in-lab polysomnography and home sleep polygraphy on sleep position," *Sleep Breath.*, vol. 25, no. 1, pp. 251–255, 2021.

[39] A. M. Osman, S. G. Carter, J. C. Carberry, and D. J. Eckert, "Obstructive sleep apnea: current perspectives," *Nat. Sci. Sleep.*, vol. 10, pp. 21–34, 2018.

[40] E. Borsini, F. Nogueira, and C. Nigro, "Apnea-hypopnea index in sleep studies and the risk of over-simplification," *Sleep Sci*, vol. 11, no. 1, pp. 45–48, 2018.

[41] G. J. Garcia and B. T. Woodson, "The collapsing anatomical structure is not always the primary site of flow limitation in obstructive sleep apnea," *J. Clin. Sleep Med.*, vol. 16, no. 3, pp. 345–346, 2020.

[42] K. Sutherland, K. Kairaitis, B. J. Yee, and P. A. Cistulli, "From cpap to tailored therapy for obstructive sleep apnoea," *Multidiscip. Respir. Med.*, vol. 13, no. 1, pp. 1–13, 2018.

[43] M. Dieltjens, M. J. Braem, S. Op de Beeck, A. V. Vroegop, E. Kazemeini, E. Van de Perck, J. Beyers, C. Kastoer, K. Wouters, M. Willemen *et al.*, "Remotely controlled mandibular positioning of oral appliance therapy during polysomnography and drug-induced sleep endoscopy compared with conventional subjective titration in patients with obstructive sleep apnea: protocol for a randomized crossover trial," *Trials*, vol. 20, no. 1, pp. 1–10, 2019.

[44] W. Randerath, C. L. Bassetti, M. R. Bonsignore, R. Farre, L. Ferini-Strambi, L. Grote, J. Hedner, M. Kohler, M.-A. Martinez-Garcia, S. Mihaicuta *et al.*, "Challenges and perspectives in obstructive sleep apnoea: report by an ad hoc working group of the sleep disordered breathing group of the european respiratory society and the european sleep research society," *Eur. Respir. J.*, vol. 52, no. 3, 2018.

[45] S. Taherian, H. Rahai, S. Lopez, J. Shin, and B. Jafari, "Evaluation of human obstructive sleep apnea using computational fluid dynamics," *Commun. Biol.*, vol. 2, no. 1, pp. 1–7, 2019.

[46] G. Mylavarapu, "Computational flow modeling of human upper airway breathing," Ph.D. dissertation, University of Cincinnati, 2013.

[47] C. Hagen, P. Gurumurthy, and T. M. Buzug, "Effects of replacing the nasal cavity with a simple pipe like structure in cfd simulations of the airflow within the upper airways of osa patients with patient individual flow rates," *Current Directions in Biomedical Engineering*, vol. 3, no. 2, pp. 795–798, 2017.

[48] H. C. N. Nguyen, "Model-based analysis of respiratory mechanics for diagnosis of cardiopulmonary diseases," Ph.D. dissertation, Rheinisch-Westfälische Technische Hochschule Aachen, 2019.

[49] T. Pedley and X. Luo, "Modelling flow and oscillations in collapsible tubes," *Theor. Comput. Fluid Dyn.*, vol. 10, no. 1, pp. 277–294, 1998.

[50] R. Fodil, C. Ribreau, B. Louis, F. Lofaso, and D. Isabey, "Interaction between steady flow and individualised compliant segments: application to upper airways," *Med. Biol. Eng. Comput.*, vol. 35, no. 6, pp. 638–648, 1997.

[51] B. T. Woodson, "Expiratory pharyngeal airway obstruction during sleep: a multiple element model," *Laryngoscope*, vol. 113, no. 9, pp. 1450–1459, 2003.

[52] W. A. Conrad, "Pressure-flow relationships in collapsible tubes," *IEEE Trans. Biomed. Eng.*, no. 4, pp. 284–295, 1969.

[53] J. B. Grotberg and O. E. Jensen, "Biofluid mechanics in flexible tubes," *Annu. Rev. Fluid Mech.*, vol. 36, pp. 121–147, 2004.

[54] G. Macdonald, *On the Respiratory Functions of the Nose and Their Relation to Certain Pathological Conditions*. Watt, 1889.

[55] C. A. Parker, "Some observations and remarks on the air-currents in nasal respiration," *J. Laryngol. Otol.*, vol. 16, no. 7, pp. 345–355, 1901.

[56] L. Silverman, R. C. Lee, C. K. Drinker, F. M. Rackemann *et al.*, "A new method for studying breathing, with observations upon normal and abnormal subjects," *J. Clin. Invest.*, vol. 23, no. 6, pp. 907–913, 1944.

[57] L. Silverman, "Respiratory air flow characteristics and their relation to certain lung conditions occurring in industry," *J. Indust. Hyg. & Toxico.*, vol. 28, no. 5, pp. 183–96, 1946.

[58] M. Rao and L. Silverman, "Respiratory patterns in pulmonary tuberculosis," *Am. Rev. Tuherc.*, vol. 54, no. 6, pp. 574–581, 1946.

[59] A. Otis and D. Proctor, "Measurement of alveolar pressure in human subjects," *Am. J. Physiol.*, vol. 152, no. 1, pp. 106–112, 1947.

[60] B. Shevrygin, "The movement of air to the olfactory region of the nose in man," *Fiziol. Zh.*, vol. 19, no. 2, pp. 247–249, 1973.

[61] R. B. Schlesinger and M. Lippmann, "Particle deposition in the trachea: in vivo and in hollow casts," *Thorax*, vol. 31, no. 6, pp. 678–684, 1976.

[62] P. AW, "Air currents in the upper respiratory tract and their clinical importance," in *Trans Am Laryngol Assoc. Annual Meeting of the American Laryngological Association. American Laryngological Association. Annual Meeting*, vol. 53, no. 72nd Meeting, 1952, pp. 73–103.

[63] H. Masing, "Experimentelle untersuchungen über die strömung im nasenmodell," *Arch. Klin. Exp. Ohren-, Nasen- Kehlkophheilk.*, vol. 189, no. 1, pp. 59–70, 1967.

[64] D. F. Proctor, "Airborne disease and the upper respiratory tract," *Bacteriol. Rev.*, vol. 30, no. 3, pp. 498–513, 1966.

[65] D. L. Swift and D. F. Proctor, "Access of air to the respiratory tract," *Respir. Defense Mech.*, vol. 5, no. part 1, pp. 63–93, 1977.

[66] D. E. Hornung, D. A. Leopold, S. L. Youngentob, P. R. Sheehe, G. M. Gagne, F. D. Thomas, and M. M. Mozell, "Airflow patterns in a human nasal model," *Arch. Otolaryngol. Head Neck Surg*, vol. 113, no. 2, pp. 169–172, 1987.

[67] M. Girardin, E. Bilgen, and P. Arbour, "Experimental study of velocity fields in a human nasal fossa by laser anemometry," *Ann. Otol. Rhinol. Laryngol.*, vol. 92, no. 3, pp. 231–236, 1983.

[68] S. E. Churchill, L. L. Shackelford, J. N. Georgi, and M. T. Black, "Morphological variation and airflow dynamics in the human nose," *Am. J. Hum. Biol.*, vol. 16, no. 6, pp. 625–638, 2004.

[69] G. Von Hagens, K. Tiedemann, and W. Kriz, "The current potential of plastination," *Anat. Embryol*, vol. 175, no. 4, pp. 411–421, 1987.

[70] C. Croce, R. Fodil, M. Durand, G. Sbirlea-Apiou, G. Caillibotte, J.-F. Papon, J.-R. Blondeau, A. Coste, D. Isabey, and B. Louis, "In vitro experiments and numerical simulations of airflow in realistic nasal airway geometry," *Ann. Biomed. Eng.*, vol. 34, no. 6, pp. 997–1007, 2006.

[71] P. W. Scherer, I. I. Hahn, and M. M. Mozell, "The biophysics of nasal airflow," *Otolaryngologic Clin. N. Am.*, vol. 22, no. 2, pp. 265–278, 1989.

[72] J. Leiter, "Analysis of pharyngeal resistance and genioglossal emg activity using a model of orifice flow," *J. Appl. Physiol.*, vol. 73, no. 2, pp. 576–583, 1992.

[73] S. Schreck, K. Sullivan, C. Ho, and H. Chang, "Correlations between flow resistance and geometry in a model of the human nose," *J Appl Physiol*, vol. 75, no. 4, pp. 1767–1775, 1993.

[74] I. Hahn, P. W. Scherer, and M. M. Mozell, "Velocity profiles measured for airflow through a large-scale model of the human nasal cavity," *J. Appl. Physiol.*, vol. 75, no. 5, pp. 2273–2287, 1993.

[75] C. Brucker and K.-l. Park, "Experimental study of velocity fields in a model of human nasal cavity by dpiv," in *First Symposium on Turbulence and Shear Flow Phenomena*. Begel House Inc., 1999, pp. 831–836.

[76] K. W. Stapleton, E. Guentsch, M. Hoskinson, and W. H. Finlay, "On the suitability of k–ε turbulence modeling for aerosol deposition in the mouth and throat: a comparison with experiment," *J. Aerosol Sci.*, vol. 31, no. 6, pp. 739–749, 2000.

[77] J. Kelly, A. Prasad, and A. Wexler, "Detailed flow patterns in the nasal cavity," *J. Appl. Physiol.*, vol. 89, no. 1, pp. 323–337, 2000.

[78] L. Hopkins, J. Kelly, A. Wexler, and A. Prasad, "Particle image velocimetry measurements in complex geometries," *Exp. Fluids*, vol. 29, no. 1, pp. 91–95, 2000.

[79] A. Heenan, E. Matida, A. Pollard, and W. Finlay, "Experimental measurements and computational modeling of the flow field in an idealized human oropharynx," *Exp. Fluids*, vol. 35, no. 1, pp. 70–84, 2003.

[80] S. Kim and S. Chung, "An investigation on airflow in disordered nasal cavity and its corrected models by tomographic piv," *Meas. Sci. Technol.*, vol. 15, no. 6, pp. 1090–1096, 2004.

[81] I. Hörschler, C. Brücker, W. Schröder, and M. Meinke, "Investigation of the impact of the geometry on the nose flow," *Eur. J. Mech. - B/Fluids*, vol. 25, no. 4, pp. 471–490, 2006.

[82] M. Brouns, S. Verbanck, J. Van Beeck, S. Vanlanduit, J. Vanherzeele, and C. Lacor, "Piv on the flow of a simplified upper airway model," in *Proceedings of the 13th International Symposium on Applications of Laser Techniques to Fluid Mechanics.*, 2006.

[83] C. Xu, S. Sin, J. M. McDonough, J. K. Udupa, A. Guez, R. Arens, and D. M. Wootton, "Computational fluid dynamics modeling of the upper airway of children with obstructive sleep apnea syndrome in steady flow," *J. Biomech.*, vol. 39, no. 11, pp. 2043–2054, 2006.

[84] D. Doorly, D. Taylor, and R. Schroter, "Mechanics of airflow in the human nasal airways," *Respir. Physiol. Neurobiol.*, vol. 163, no. 1-3, pp. 100–110, 2008.

[85] S. K. Kim and S.-K. Chung, "Investigation on the respiratory airflow in human airway by piv," *J. Visual.*, vol. 12, no. 3, pp. 259–266, 2009.

[86] G. Mylavarapu, S. Murugappan, M. Mihaescu, M. Kalra, S. Khosla, and E. Gutmark, "Validation of computational fluid dynamics methodology used for human upper airway flow simulations," *J. Biomech*, vol. 42, no. 10, pp. 1553–1559, 2009.

[87] A. Pollard and A.-M. Shinneeb, "Oro-pharangeal-laryngeal flow physics," in *Proceedings of the 17th Australasian Fluid Mechanics Conference, Auckland, New Zealand*, 2010.

[88] F. Chouly, A. Van Hirtum, P.-Y. Lagrée, X. Pelorson, and Y. Payan, "Modelling the human pharyngeal airway: validation of numerical simulations using in vitro experiments," *Medical & biological engineering & computing*, vol. 47, no. 1, pp. 49–58, 2009.

[89] ——, "Numerical and experimental study of expiratory flow in the case of major upper airway obstructions with fluid–structure interaction," *J. Fluids Struct.*, vol. 24, no. 2, pp. 250–269, 2008.

[90] A. Pollard, M. Uddin, A.-M. Shinneeb, and C. Ball, "Recent advances and key challenges in investigations of the flow inside human oro-pharyngeal-laryngeal airway," *Int. J. Comput. Fluid Dyn.*, vol. 26, no. 6-8, pp. 363–381, 2012.

[91] M. Zhao, T. Barber, P. A. Cistulli, K. Sutherland, and G. Rosengarten, "Simulation of upper airway occlusion without and with mandibular advancement in obstructive sleep apnea using fluid-structure interaction," *J. Biomech.*, vol. 46, no. 15, pp. 2586–2592, 2013.

[92] T. B. Le, M. G. Moghaddam, B. T. Woodson, and G. J. Garcia, "Airflow limitation in a collapsible model of the human pharynx: physical mechanisms studied with fluid-structure interaction simulations and experiments," *Physiol. Rep.*, vol. 7, no. 10, 2019.

[93] Y. Fan, J. Dong, L. Tian, K. Inthavong, and J. Tu, "Numerical and experimental analysis of inhalation airflow dynamics in a human pharyngeal airway," *Int. J. Environ. Res. Public Health*, vol. 17, no. 5, 2020.

[94] X. Xu, J. Wu, W. Weng, and M. Fu, "Investigation of inhalation and exhalation flow pattern in a realistic human upper airway model by piv experiments and cfd simulations," *Biomech. Model. Mechanobiol.*, vol. 19, no. 5, pp. 1679–1695, 2020.

[95] L. de Rochefort, X. Maître, R. Fodil, L. Vial, B. Louis, D. Isabey, C. Croce, L. Darrasse, G. Apiou, G. Caillibotte *et al.*, "Phase-contrast velocimetry with hyperpolarized 3he for in vitro and in vivo characterization of airflow," *Magn. Reson. Med.*, vol. 55, no. 6, pp. 1318–1325, 2006.

[96] G. J. Collier, M. Kim, Y. Chung, and J. M. Wild, "3d phase contrast mri in models of human airways: Validation of computational fluid dynamics simulations of steady inspiratory flow," *J. Magn. Reson. Imaging.*, vol. 48, no. 5, pp. 1400–1409, 2018.

[97] R. H. Hashemi, W. G. Bradley, and C. J. Lisanti, *MRI: the basics: The Basics*. Lippincott Williams & Wilkins, 2012.

[98] J. W. Akitt and B. E. Mann, *NMR and Chemistry: An introduction to modern NMR spectroscopy*. Crc Press, 2017.

[99] V. Mlynárik, "Introduction to nuclear magnetic resonance," *Anal. Biochem.*, vol. 529, pp. 4–9, 2017.

[100] A. D. Elster. Distribution of energy states. https://mriquestions.com/fall-to-lowest-state.html. Accessed: 2022-05-19.

[101] R. A. Pooley, "Fundamental physics of mr imaging," *Radiographics*, vol. 25, no. 4, pp. 1087–1099, 2005.

[102] B. Köhler, "Guided qualitative and quantitative analysis of cardiac 4d pc-mri blood flow data," Ph.D. dissertation, Dissertation, Magdeburg, Universität, 2016, 2016.

[103] F. Bloch, "Nuclear induction," *Phys. Rev.*, vol. 70, no. 7-8, p. 460, 1946.

[104] F. Lugauer and J. Wetzl, "6.1 nuclear magnetic resonance (nmr)."

[105] D. Firmin, P. Gatehouse, J. Konrad, G. Yang, P. Kilner, and D. Longmore, "Rapid 7-dimensional imaging of pulsatile flow," in *Proceedings of Computers in Cardiology Conference*. IEEE, 1993, pp. 353–356.

[106] M. Markl, S. Schnell, C. Wu, E. Bollache, K. Jarvis, A. Barker, J. Robinson, and C. Rigsby, "Advanced flow mri: emerging techniques and applications," *Clin. Radiol.*, vol. 71, no. 8, pp. 779–795, 2016.

[107] Z. Stankovic, B. D. Allen, J. Garcia, K. B. Jarvis, and M. Markl, "4d flow imaging with mri," *Cardiovasc. Diagn. Ther*, vol. 4, no. 2, pp. 173–192, 2014.

[108] M. Markl, "Velocity encoding and flow imaging," *University Hospital Freiburg, Dept of Diagnostic Radiology, Germany*, 2005.

[109] V. Sochat. Watershed algorithm. https://vsoch.github.io/2013/meyer-watershed-segmentation/. Accessed: 2022-05-19.

[110] F. Meyer, "The watershed concept and its use in segmentation: a brief history," *arXiv preprint arXiv:1202.0216*, 2012.

[111] M. V. M. Cirne and H. Pedrini, "Marching cubes technique for volumetric visualization accelerated with graphics processing units," *J. Braz. Comput. Soc.*, vol. 19, no. 3, pp. 223–233, 2013.

[112] M. Garland and P. S. Heckbert, "Surface simplification using quadric error metrics," in *Proceedings of the 24th annual conference on Computer graphics and interactive techniques*, 1997, pp. 209–216.

[113] T. Liu, M. Chen, Y. Song, H. Li, and B. Lu, "Quality improvement of surface triangular mesh using a modified laplacian smoothing approach avoiding intersection," *PLoS One*, vol. 12, no. 9, 2017.

[114] TMJ & Sleep Therapy Centre of New England. Multijet printing. https://www.3dsystems.com/multi-jet-printing. Accessed: 2022-05-16.

[115] J. D. Anderson, "Governing equations of fluid dynamics," in *Computational fluid dynamics*. Springer, 1992, pp. 15–51.

[116] R. Bhaskaran and L. Collins, "Introduction to cfd basics," *Cornell University-Sibley School of Mechanical and Aerospace Engineering*, pp. 1–21, 2002.

[117] P. H. Geoghegan, "In vitro experimental investigation into the effect of compliance on models of arterial hemodynamics," Ph.D. dissertation, University of Caunterbury. Mechanical Engineering, 2012.

[118] O. Veselỳ, L. Nováková, and J. Adamec, "Experimental study of effect of stenosis geometry on flow parameters," in *EPJ Web of Conferences*, vol. 92. EDP Sciences, 2015.

[119] M. Thiriet, M. Delfour, A. Garon, and P. Lanzer, "Vascular stenosis: An introduction," *PanVascular medicine*, pp. 781–868, 2015.

[120] S. A. Ahmed and D. P. Giddens, "Velocity measurements in steady flow through axisymmetric stenoses at moderate reynolds numbers," *J. Biomech.*, vol. 16, no. 7, pp. 505–516, 1983.

[121] N.-S. Cheng, "Formula for the viscosity of a glycerol- water mixture," *Ind. Eng. Chem. Res*, vol. 47, no. 9, pp. 3285–3288, 2008.

[122] A. D. Elster. Velocity encoding. https://mriquestions.com/what-is-venc.html. Accessed: 2022-11-30.

[123] C. Schareck, T. Oechtering, A. Frydrychowicz, and M. Koch, "Development of a graphical user interface and cross manufacturer adaptation of a program for determining the pulse wave velocity in the aorta from phase-contrast magnetic resonance images," *Curr. Dir. Biomed. Eng.*, vol. 4, no. 1, pp. 477–480, 2018.

[124] L. Daly and G. J. Bourke, *Interpretation and uses of medical statistics*. John Wiley & Sons, 2008.

[125] T. K. Koo and M. Y. Li, "A guideline of selecting and reporting intraclass correlation coefficients for reliability research," *J. Chiropr. Med.*, vol. 15, no. 2, pp. 155–163, 2016.

[126] J. M. Bland and D. Altman, "Statistical methods for assessing agreement between two methods of clinical measurement," *Lancet*, vol. 327, no. 8476, pp. 307–310, 1986.

[127] J. Ludbrook, "Confidence in altman–bland plots: a critical review of the method of differences," *Clin. Exp. Pharmacol. Physiol.*, vol. 37, no. 2, pp. 143–149, 2010.

[128] M. Pollock, S. Jefferson, J. Kane, K. Lomax, G. MacKinnon, and C. Winnard, "Method comparison - a different approach," *Ann. Clin. Biochem.*, vol. 29, no. 5, pp. 556–560, 1992.

[129] D. Giavarina, "Understanding bland altman analysis," *Biochem. Med.*, vol. 25, no. 2, pp. 141–151, 2015.

[130] A. R. Sakhare, G. Barisano, and J. Pa, "Assessing test–retest reliability of phase contrast mri for measuring cerebrospinal fluid and cerebral blood flow dynamics," *Magn Reson Med.*, vol. 82, no. 2, pp. 658–670, 2019.

[131] J. Doke. Grabit function. https://www.mathworks.com/matlabcentral/fileexchange/7173-grabit. Accessed: 2022-11-22.

[132] S. J. Sherwin and H. M. Blackburn, "Three-dimensional instabilities and transition of steady and pulsatile axisymmetric stenotic flows," *J. Fluid Mech.*, vol. 533, pp. 297–327, 2005.

[133] J. Vétel, A. Garon, D. Pelletier, and M.-I. Farinas, "Asymmetry and transition to turbulence in a smooth axisymmetric constriction," *J.Fluid Mech.*, vol. 607, pp. 351–386, 2008.

[134] S. S. Varghese, S. H. Frankel, and P. F. Fischer, "Direct numerical simulation of stenotic flows. part 1. steady flow," *J.Fluid Mech.*, vol. 582, pp. 253–280, 2007.

[135] X. Liu, W. Yan, Y. Liu, Y. S. Choy, and Y. Wei, "Numerical investigation of flow characteristics in the obstructed realistic human upper airway," *Comput. Math. Methods Med.*, vol. 2016, 2016.

[136] V. N. Riazuddin, M. Zubair, M. Z. Abdullah, R. Ismail, I. L. Shuaib, S. A. Hamid, and K. A. Ahmad, "Numerical study of inspiratory and expiratory flow in a human nasal cavity," *J. Med. Biol. Eng.*, vol. 31, no. 3, pp. 201–206, 2011.

[137] B. Zhuang, A. Sirajuddin, S. Zhao, and M. Lu, "The role of 4d flow mri for clinical applications in cardiovascular disease: current status and future perspectives," *Quant. Imaging Med. Surg.*, vol. 11, no. 9, pp. 4193–4210, 2021.

[138] W. Faizal, N. N. N. Ghazali, C. Khor, I. A. Badruddin, M. Zainon, A. A. Yazid, N. B. Ibrahim, and R. M. Razi, "Computational fluid dynamics modelling of human upper airway: A review," *Comput. Methods Program Biomed.*, vol. 196, pp. 105 627–105 622, 2020.

[139] A. Arzani, "Coronary artery plaque growth: A two-way coupled shear stress–driven model," *Int. J. Numer. Methods Biomed. Eng.*, vol. 36, no. 1, 2020.

[140] T. Chaichana, Z. Sun, and J. Jewkes, "Computation of hemodynamics in the left coronary artery with variable angulations," *J. Biomech.*, vol. 44, no. 10, pp. 1869–1878, 2011.

List of abbreviations

AHI Apnea-hypopnea index

AT Arousal threshold

BMI Body mass index

CAD Computer aided design

CBCT Cone-beam computed tomography

CFD Computational fluid dynamics

COPD Chronic obstructive pulmonary disease

CV Coefficient of variation

d Diameter

D Dimension

DNS Direct numerical simulation

DPIV Digital particle image velocimetry

DTI Diffusion tensor imaging

EMG Electromyography

ESS Epworth sleepiness scale

FDM Finite difference method

FEM Finite element method

FH Foot head

fMRI Functional magnetic resonance imaging

FOV Field of view

FSI Fluid structure interaction

FVM Finite volume method

HD High definition

HGNS Hypoglossal nerve stimulation

HOP Human oropharynx

ICC Intraclass correlation coefficient

k-t BLAST Broad-use linear acquisition speed-up technique

k-t GRAPPA Generalized autocalibrating partial parallel acquisition

LAUP Laser-assisted uvulopalatoplasty

LB Lower bound

LDA Laser doppler anemometry

LDL Low-density lipoprotein

LES Large eddy simulation

LG Loop gain

MAD Mandibular advancement device

MJP Multijet printing

MMA Maxillomandibular advancement surgery

MRI Magnetic resonance imaging

NMR Nuclear magnetic resonance

ODE Ordinary differential equation

OPL Oro-pharyngeal-laryngeal

OSA Obstructive sleep apnea

PC-MRI Phase contrast- magnetic resonance imaging

PC-VIPR Phase contrast vastly undersampled isotropic projection reconstruction

PCV-MRI Phase contrast velocimetry - magnetic resonance imaging

PDE Partial differential equation

PIV Particle image velocimetry

PSG Polysomnography

RANS Reynolds-averaged Navier Stokes

RDI Respiratory disturbance index

Re Reynolds number

RF Radio frequency

RI Rescale intercept

RMS Root mean square

RNG Renormalization group

ROI Region of interest

RS Rescale slope

SMART simultaneous multiangular relaxometry of tissue

SNR Signal-to-noise ratio

SST Shear stress transport

SS Scale slope

SV Stored values

TE Time of echo

TPIV Tomographic particle image velocimetry

TR Repetition time

UB Upper bound

UPPP Uvulopalatopharyngoplasty

Venc Velocity encoding

WSS Wall shear stress